CRITICAL QUALITY ATTRIBUTES OF HOT MELT EXTRUDED AMORPHOUS SOLID DISPERSIONS

by

Dana Moseson

A Dissertation

Submitted to the Faculty of Purdue University

In Partial Fulfillment of the Requirements for the degree of

Doctor of Philosophy

Department of Industrial and Physical Pharmacy

West Lafayette, Indiana

December 2020

THE PURDUE UNIVERSITY GRADUATE SCHOOL
STATEMENT OF COMMITTEE APPROVAL

Dr. Lynne S. Taylor, Chair
Department of Industrial and Physical Pharmacy

Dr. Stephen R. Byrn
Department of Industrial and Physical Pharmacy

Dr. Zoltan K. Nagy
Davidson School of Chemical Engineering

Dr. Qi (Tony) Zhou
Department of Industrial and Physical Pharmacy

Approved by:
Dr. Rodolfo Pinal

Dedicated to Henry and Audrey

ACKNOWLEDGMENTS

First and foremost, I feel like I hit the lottery to have such a wonderful advisor, Professor Lynne Taylor. I appreciate her scientific guidance, mentorship, and support through all of the fun science and tough life-stuff. She always pushed me to dig deeper, try new things, take risks, and seize opportunities. I would also like to thank my thesis advisory committee members Stephen Byrn, Qi (Tony) Zhou, and Zoltan Nagy for their helpful guidance and service.

I am grateful to the Department of Industrial and Physical Pharmacy, department heads Elizabeth Topp and Eric Munson, and its faculty for accepting me into the Ph.D. program, and enabling me to develop academically and professionally, and for providing a teaching assistantship, research facilities, and administrative support during my graduate studies. Special thanks to Mary Ellen Hurt, Nancy Cramer, Jen Gray, and Erin Hartman for endless patience and administrative support.

This research would not have been as successful without the input of many collaborators and their technical expertise. First, I would like to thank my research collaborators Naila Mugheirbi, Andrew Parker, Andrew Stewart, Christopher Gilpin, Stephen Beaudoin, Ayse Eren, Zoltan Nagy, Andres Lust, Tze Ning Hiew, Benedito Alvarenga, and Dishan Shah for their valuable and innovative contributions. Research assistants Kevin Altman, Isaac Corum, and Madison Jordan are especially thanked for their time and dedication to the work, and for enriching discussions and growth. Purdue staff Laurie Mueller, Robert Seiler, Dhananjay Pai, and Matthias Zeller are also thanked for their technical assistance. And lastly, I'd like to thank Julie Calahan, Eric Munson, Sugandha Saboo, Siddhi Hate, Mingyue Li, and Yongchao Su for pursuing research ideas with me that didn't make it to the finished product.

I am grateful to the friendship and support of my Taylor lab colleagues, especially Naila Mugheirbi, Tze Ning Hiew, Clara Correa-Soto, Sugandha Saboo, Siddhi Hate, Hanh Thuy Nguyen, Tu Van Duong, Andres Lust, Vivek Bhardwaj, Ahmed Elkhabaz, and Kevin Altman. It has been wonderful to work alongside you all for the past four years.

I would like to thank the following institutions for funding support: National Science Foundation Graduate Research Fellowship program (NSF GRFP) under grant award DGE-1333468, Center for Pharmaceutical Processing Research (CPPR), Food and Drug Administration (FDA) grant award 1U01FD005259-01, Purdue University summer research grant, and the College

of Pharmacy travel award. I would also like to thank American Chemical Society (ACS) and Elsevier for reprint permission of the manuscripts included in this dissertation.

This journey would not have been possible without the support of family and friends. To my parents, who have always pushed me and believed in me. To my sisters Shelley and Jen, thank you for your friendship and encouragement. I am also grateful to Bill Tarrh for his love and tech support and Laura Elicker for her friendship and adventures.

TABLE OF CONTENTS

LIST OF TABLES

LIST OF FIGURES

ABSTRACT

The success of an amorphous solid dispersion (ASD) formulation, consisting of a homogeneous molecular dispersion of drug and polymer, relies on its ability to create and maintain a supersaturated solution. However, supersaturated solutions are metastable and prone to crystallization. In solution, crystals are expected to serve as a template for crystal growth, depleting achieved supersaturation. Thus, in an ASD product, ideally no crystallinity should be present. However, technical challenges exist in both processing and characterization to routinely ensure this is achieved. The presented studies follow the process design, characterization, and dissolution performance of hot melt extruded amorphous solid dispersions, seeking insight into the significance of critical quality attributes of resulting extrudates, namely residual crystallinity and thermal degradation.

Selection of hot melt extrusion (HME) processing conditions to prepare ASDs is governed by thermodynamic and kinetic attributes of the drug and polymer system. Mapping the temperature-composition phase diagram to HME processing conditions provides a processing design strategy to prevent residual crystallinity while simultaneously avoiding thermal degradation. Through processing temperatures below the drug's melting point (T_m) and above the formulation critical temperature (T_c), fully amorphous systems could be generated if sufficient kinetics were provided. The utility of thermogravimetric analysis was critically examined for prediction of the chemical stability processing window for HME formulations.

For characterization and product performance characterization, residual crystalline content in HME ASDs can be anticipated and tailored to various levels. Several HME ASDs were characterized by a range of analytical techniques, highlighting the sensitivity of available techniques to qualitatively or quantitatively detect crystalline content (depending on limitations which stem from properties of the instrument or sample). Transmission electron microscopy (TEM) was found to identify low levels of crystallinity not observed by other technique and provide insight into crystal dissolution mechanisms. A defect-site driven dissolution and fragmentation model was suggested, and supported by a Monte Carlo simulation, underscoring that crystal defect sites, either intrinsic to the crystals or formed during processing, expedite dissolution rates and generation of new surfaces for dissolution.

Non-sink dissolution was performed for indomethacin/PVPVA HME ASD samples with residual crystallinity ranging from 0-25% crystalline content. Due to effective crystal growth inhibition by the polymer, crystals had little impact on dissolution performance. Achieved supersaturation was reduced approximately by the level of crystallinity present, i.e. a lost solubility advantage. These studies have significance for HME processing design and risk assessment of crystallinity within ASD formulations.

CHAPTER 1. INTRODUCTION

1.1 Research Significance and Objectives

1.1.1 Background

Physiochemical properties of drug molecules drive biopharmaceutical performance.[1–4] Due to advances in drug discovery technologies, new drugs are becoming larger and more lipophilic, resulting in poor aqueous solubility.[2–6] As 90% of current pipeline compounds are classified as BCS Class 2 or 4, and therefore have low solubility, solubility enhancing strategies are essential, since the ability of the drug to dissolve in aqueous biologic fluids is a key precursor to bioavailability.

A popular strategy to overcome poor aqueous solubility and slow dissolution rates is through the amorphous solid dispersion (ASD), in which an amorphous drug is stabilized by an amorphous polymer as a homogenous molecular mixture.[7,8] There are two major manufacturing methods to prepare an ASD: spray drying (SD) or hot melt extrusion (HME). HME was introduced to the pharmaceutical industry as a solubility enhancement manufacturing technology in 1991, when it was used to prepare a troglitazone solid dispersion without the use of solvents.[9] The pace of drug product approvals has accelerated in the last several years, highlighting the applicability of this technology and growing industry interest.[8,10]

As of 2017, there have been ten approved drug products which utilize an ASD formulation platform in combination with HME processing (Table 1.1).[8,10] A few trends and limitations to the HME process are identified by this set of drug products. First, suitable drugs have melting points below approximately 200°C. This limitation stems from the availability of pharmaceutically-acceptable thermally-stable polymers. Second, polyvinylpyrrolidone/vinyl acetate copolymer (PVPVA) is the most common polymer used in extrusion processes for amorphous solid dispersions, although three products have been commercialized using polyvinylpyrrolidone (PVP), hydroxypropyl methylcellulose (HPMC), or hydroxypropyl methylcellulose acetate succinate (HPMCAS). Viscosity and thermal stability are key parameters for a polymer used in an extrusion process, in addition to the requirements that it impart physical stability to and dissolution enhancement of the ASD formulation. Lastly, drug product approvals using this technology are dominated by just two companies. While the pharmaceutical industry is generally slow to adapt to

new technologies, it can be inferred that the technological complexity dissuades companies from pursuing this processing method.[9]

Table 1.1. Approved amorphous solid dispersion drug products produced by hot melt extrusion.

Drug Product Brand Name	Drug	Drug Melting Point (°C)	Polymer	Company	Year Approved
Rezulin	Troglitazone	185	PVP	Warner-Lambert	1997
Kaletra	Ritonavir/lopinavir	122/125	PVPVA	AbbVie	2005
Norvir	Ritonavir	122	PVPVA	AbbVie	2010
Onmel	Itraconazole	166	HPMC	Merz NA	2010
Noxafil	Posaconazole	171	HPMCAS	Merck	2013
Viekira Pak	Ombitasvir/paritaprevir/ ritonavir	160/140/122	PVPVA	AbbVie	2014
Belsomra	Suvorexant	153	PVPVA	Merck	2014
Zepatier	Elbasvir/grazoprevir	Unknown/185	PVPVA	Merck	2016
Venclexta	Venetoclax	138	PVPVA	AbbVie	2016
Mavyret	Glecaprevir/pibrentasvir	Unknown/ unknown	PVPVA	AbbVie	2017

1.1.2 Research Objectives

The research objectives in this thesis are to investigate the impact of critical quality attributes of hot melt extruded (HME) amorphous solid dispersion (ASD) formulations. Too often, a trial-and-error approach is used to find the "sweet spot" for processing to prevent thermal degradation of drug and/or polymer and residual crystallinity.[11–13] Therefore, this research project focuses on three objectives:

(1) understanding the relationship of thermodynamic and kinetic criteria in hot melt extrusion (HME) process and formulation design to critical quality attributes of amorphous solid dispersions (ASDs): degradation and residual crystallinity

(2) seeking insight into crystallization mechanisms during non-sink dissolution of HME ASDs containing residual crystallinity

(3) investigating the mechanism of crystal dissolution into a polymer melt using innovative characterization techniques

The International Council for Harmonisation (ICH) Pharmaceutical Development Q8(R2) guideline[14] states that studies should provide "scientific understanding to support the establishment of the design space, specifications, and manufacturing controls." As both stability and dissolution performance may be affected by the presence of crystallinity within the ASD, the manufacturing process must be designed to generate a fully amorphous system.[15] Therefore, our first goal is to provide a process design strategy to eliminate or minimize residual crystallinity in HME ASDs, while simultaneously avoiding thermal degradation.

Specific Aim 1: Demonstrate that residual crystallinity can be rationalized based on the thermodynamic phase diagram and kinetic considerations.
Hypothesis 1: Below the formulation critical temperature, it will not be possible to prepare a fully amorphous extrudate. At or above the formulation critical temperature, crystalline content will be a function of processing temperature and residence time.

Commonly, thermogravimetric analysis (TGA) methods are used to define the degradation temperature of pharmaceutical materials. However, this method is challenging to apply to amorphous materials, due to their tendency to crystallize. Additionally, a review of the literature has found that experimental determinations of degradation temperature using nonisothermal heating methods are based on qualitative degradation curve interpretation. Hence, our second goal is to critically evaluate nonisothermal and isothermal TGA methods to enable degradation predictions for pharmaceutical materials.

Specific Aim 2. Validate thermogravimetric analysis methods as a surrogate to assess the likelihood of degradation of amorphous materials during HME.
Hypothesis 2. Volatile weight loss during isothermal heating of amorphous materials will provide a direct indication of chemical stability during HME processing.

Specifications must be set for allowable crystallinity (typically on a mass basis), as it is not always practical to completely avoid residual crystallinity, or prevent crystallization upon product storage. However, as many factors contribute to crystallization, such as crystallization tendency, polymer type, and crystal properties, the degree of crystallinity is an arbitrary indicator of product

quality.[16–21] Given this knowledge gap around the impacts of residual crystallinity on product performance, the third goal is to elucidate the critical factors of residual crystals and drug-polymer interactions which influence to the performance of HME ASDs, specifically non-sink dissolution.

Specific Aim 3. Demonstrate that residual crystals have a negative impact on non-sink dissolution performance.
Hypothesis 3. Residual crystals will impact solution in one or both ways: (1) through loss of solubility advantage or (2) seed crystal growth, leading to desupersaturation.

Solid state characterization techniques underpin drug development and manufacturing. A recent news article highlighted the need for advanced characterization methods to detect and avoid failure modes such as crystallization of amorphous systems, thus linking physical changes to measures of performance and quality.[22] Therefore, the last goal is to apply innovative analytical techniques to image and characterize crystals found with HME ASDs to understand the effects of processing conditions on residual crystals.

Specific Aim 4. Apply an innovative analytical method, transmission electron microscopy, to image and characterize crystals found within HME ASDs present as a result of incomplete phase transformation.
Hypothesis 4. Residual crystals will be highly defective, as a result of thermally- and mechanically-induced structural deformation.

Following successful completion of this research, greater insight into the interplay between processing conditions, formulation composition/selection, and product performance will be achieved. This, together with application of advanced characterization approaches will enable rational design of hot melt extrusion amorphous solid dispersion products and processes based on thermodynamic and kinetic considerations.

1.2 Amorphous Solid Dispersions as a Formulation Strategy

1.2.1 Crystalline and Amorphous Solids

A crystalline solid is characterized by a three-dimensional long-range lattice arrangement of molecules.[23] Many substances have multiple crystal structures, known as polymorphs. As a result of these structural differences, polymorphic forms may have distinct physical and chemical properties, such as solubility, dissolution, density, mechanical attributes, and stability.[24] The amorphous form of a drug is characterized by the lack of three-dimensional long-range order found in crystalline forms.[25] Amorphous forms can be obtained by vapor condensation, supercooling of the melt, precipitation from solution, and by mechanically destroying the crystal structure.[26] Crystalline and amorphous materials have many pharmaceutically relevant differences.[23,27] Typically, crystalline solids are more physically and chemically stable, have higher purity, lower solubility, lower hygroscopicity, and have a melting point. Additionally, they are harder, more brittle, less compressible, and have directionally dependent properties (anisotropy). Crystalline materials often have better flow and handling characteristics. Unless the molecule has insufficient solubility to generate adequate bioavailability, the crystalline material is generally more desirable.

In thermodynamic terms, the amorphous form has a higher free energy and enthalpy than the stable crystalline form (Figure 1). These differences translate into properties of pharmaceutical importance. Because of the disruption of the crystal lattice, the apparent solubility of the amorphous form exceeds that of the crystalline form. Correspondingly, the thermodynamic driving force for crystallization in both the supercooled liquid and glassy state is increased due to the higher energy state. Amorphous forms can also be expected to have increased chemical instability.[28]

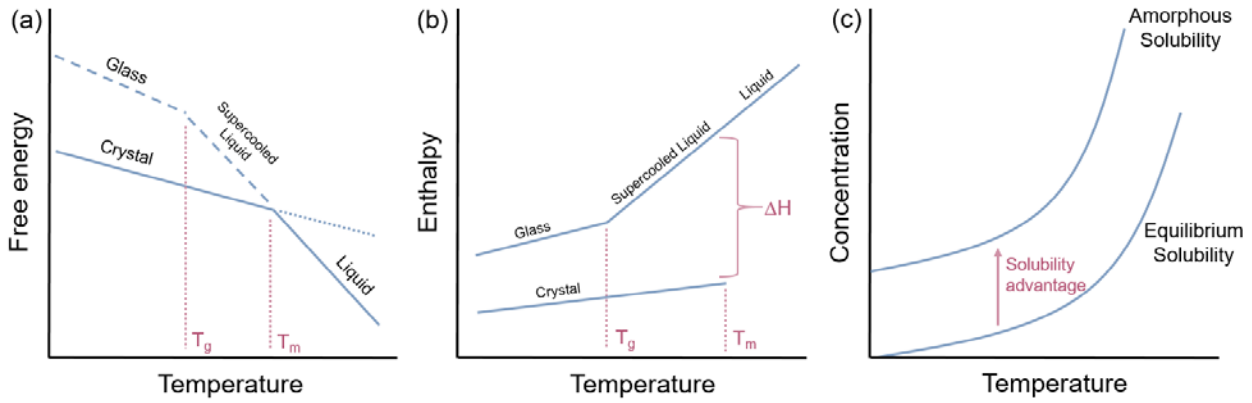

Figure 1.1. Amorphous forms have higher free energy and enthalpy than crystalline forms, which translates to a solubility advantage.

Gibbs free energy can be represented by Eq. 1, and is schematically shown for crystalline and liquid forms in Figure 1.1a.

$$G = H - TS \qquad \text{Eq. 1}$$

Above the melting temperature (T_m), the solid exists at a lower free energy, and is therefore the thermodynamically stable form. As the sample is heated, the solid will spontaneously melt to form the liquid. If the liquid is cooled below T_m, crystallization would be expected to occur, to restore the thermodynamically stable crystalline state. However, if the liquid is cooled quickly enough to avoid the formation of crystal nuclei, a supercooled liquid can form having increased viscosity upon decreased temperature. Upon continued cooling, a glassy state will form upon cooling below the glass transition temperature T_g. The glass transition represents a kinetically-induced transition, because it depends on the rate of temperature change.[28] Below the glass transition temperature, kinetic stability is imparted to the amorphous solid.[26]

The liquid, crystalline, and amorphous states can also be described in terms of enthalpy (ΔH), which is a result of interactions between molecules (Figure 1.1b). As the liquid is cooled, the supercooled liquid and glassy amorphous solid can be formed. The amorphous form is metastable to the crystalline form, thus there is a driving force for crystallization. A crystallization event results in a discontinuous transition to a lower enthalpic state.

Dissolving a crystalline solid involves breaking the intermolecular interactions in the crystal lattice and forming new interactions between molecules of the solute and solvent.[29] The pharmaceutical relevance of the amorphous form stems from the theoretical solubility advantage

that can be achieved over the crystalline form (Figure 1.1c), as the amorphous form lacks the directional energetic interactions which form the crystal lattice. The typical solubility advantage of the amorphous form is 2-20 fold over the crystalline form.[30] Practically, this solubility advantage can be difficult to achieve and sustain due to crystallization.[31]

An amorphous solid or supersaturated solution will ultimately crystallize to the stable form. This conversion will happen over a timescale depending on the crystallization tendency of the compound, as well as thermodynamic driving forces and kinetic factors.[16,19,32,33] The crystallization process primarily consists of two phenomena: nucleation and subsequent growth of solute nuclei. Nucleation or growth can compete for the consumption of supersaturation in the solid or solution state.[34]

1.2.2 Amorphous Solid Dispersions

Amorphous solid dispersions (ASDs) consist of an amorphous drug dispersed in an amorphous polymer as a homogenous molecular mixture. Most commonly, ASDs are binary systems consisting of drug and polymer, although multi-component systems are possible. The polymer serves to inhibit crystallization of the amorphous drug both in the solid and solution states, enabling the solubility advantage to be achieved and enhanced bioavailability to be realized. In a recent commentary by Newman et al, it was found that bioavailability achieved with ASD systems was improved over the reference crystalline system in 80% of cases.[1] For example, Yamashita and coworkers observed a 10-fold increase in C_{max} and AUC with a solid dispersion of tacrolimus and HPMC over the reference crystalline drug.[35]

The incorporation of a polymer provides physical stability by decreasing the chemical potential of the drug as a result of molecular level mixing (Figure 1.2). The polymer acts to inhibit nucleation (and crystal growth) by decreasing drug mobility, through specific interactions, providing steric hindrance, and by acting as a solvent for the drug. The second major role of the polymer is to enhance the dissolution performance of the drug by increasing the rate and extent of dissolution under non-sink conditions, as well as inhibition of solution crystallization.

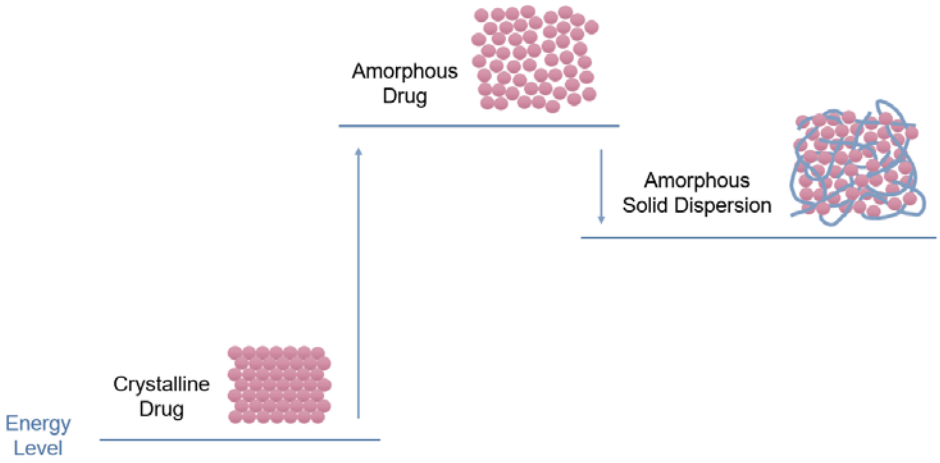

Figure 1.2. The thermodynamic energy level of the amorphous forms is higher than that of the crystalline drug. By dispersing the amorphous form in an amorphous polymer, the energy level is reduced.

1.2.3 Preparation Methods

The preparation process contributes to the chemical and physical stability as well as dissolution performance of the ASD.[36] ASD preparation methods can be broadly classified as solvent-based or thermal-based processes.[37] Solvent-based ASD manufacturing processes typically consists of three major steps: (1) dissolving the drug and polymer components in a volatile solvent, (2) removing the bulk of the solvent to produce solids, and (3) secondary drying to further remove any residual solvent.[36] Solvent-based processes used to produce ASDs include spray drying, co-precipitation, rotary evaporation, vacuum drying, freeze-drying, and the use of supercritical fluids.[36,38] Solvent-based processes are material-sparing in early phase development and applicable to a wide range of compounds; thus, spray drying dominates the field.[38,39]

Thermal-based ASD manufacturing methods consist of two major steps: (1) melting or dissolving the drug within the polymer at elevated temperature and (2) rapid cooling of the molten material so it solidifies into a one-phase system.[15,36] Thermal-based methods include hot melt extrusion (HME) and KinetiSol Dispersing Technology.[36] For thermally stable systems, HME offers several advantages over solvent-based processing: it is solvent-free, inexpensive, continuous, high-throughput, easily scalable, and requires only a small facility footprint, enabling batch size flexibility and fast production.[40,41] HME to prepare ASDs will be the focus of this review.

1.3 Hot Melt Extrusion

1.3.1 Equipment

A hot melt extruder consists of a feeding system, heated barrel system, and die, as well as downstream processing equipment for cooling or milling.[15,36] Twin-screw extruders are typically used to prepare pharmaceutical formulations, because of ease of material feeding, high kneading/dispersing capabilities, and shorter transit time.[15] Twin-screw extruders can be further classified by screw size, direction of screw rotation, and configuration of mixing elements.[42] Counter-rotating screw designs impart very high shear to the melt, but suffer from potential air entrapment, generation of high pressures, and low maximum screw speeds and throughput. Co-rotating screw designs are self-wiping, maintain good mixing and conveying characteristics, and can achieve high screw speeds and throughput.[15] The co-rotating design is of greatest interest for pharmaceutical applications, because of their efficient mixing capabilities, narrow residence time distributions (RTD), and low material stagnation.[43] Twin-screw extruders offer modular design of screw elements. Highly efficient mixing and uniformity are a result of intense mixing associated with short inter-screw mass transfer distances.[43] The short residence times offered by this process (commonly under 2 minutes) are advantageous for heat- or shear-sensitive formulations.[44] A schematic of a co-rotating twin-screw extruder is found in Figure 14.[43]

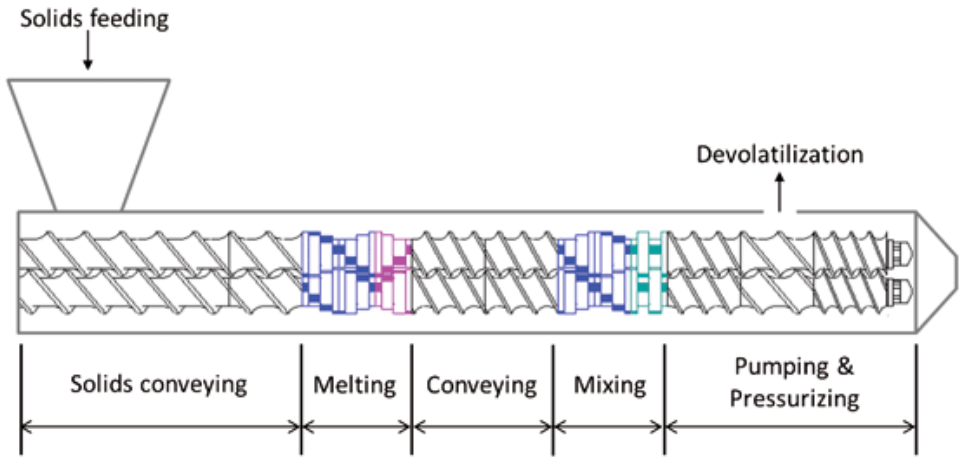

Figure 1.3. Schematic representation of a twin-screw extruder and elementary processing steps.[43]

1.3.2 ASD Formation by Hot Melt Extrusion

During HME, the crystalline drug and polymer are transformed into a single phase, homogenous melt due to thermal and mechanical input. First, the powder components are fed into the heated barrel and screw system. High temperatures and mixing in the screws generate a molten phase, created by softening the polymer (when heated above its glass transition temperature T_g). Next, the dispersed drug crystals melt and/or dissolve into the polymer, depending on the temperature profile provided to the system. If the drug and polymer are miscible and adequate mixing is provided, the process results in a single phase viscous liquid of drug and polymer, which is then extruded through a die, cooled, and subjected to downstream processing.[15,42] When the extrudate is cooled quickly to ambient temperatures, the drug is kinetically trapped in the high energy amorphous state, although it is thermodynamically unstable/metastable.[10]

Conductive melting of the drug and polymer is localized at the barrel surface and takes place throughout length of the screw. Since drug crystal dissolution and mixing only take place when the polymer is molten, limited dissolution may take place in polymer which softened late in the process, resulting in product inhomogeneity. The portion of polymer which melted early may be more susceptible to thermal degradation.[45]

1.3.3 Formulation and Process Design

1.3.3.1 Material Science Tetrahedron Framework for HME

The inter-related design parameters of hot melt extrusion product and process can be described by the materials science tetrahedron framework developed by Sun,[46] and described for HME by Evans et al.[47] Equipment variables include the extruder geometry, screw design (e.g. co-rotating vs. counter-rotating, incorporation of mixing elements), and die geometry. Material variables include the rheological and thermal properties of the drug and polymer (as well as other included excipients), miscibility of drug and polymer, the drug loading, and the drug's particle size distribution. Process variables include feed rates, screw speed, temperature profile, and residence time distribution. These factors, among many others, govern the resulting critical quality attributes (CQAs) and performance of the HME intermediate.

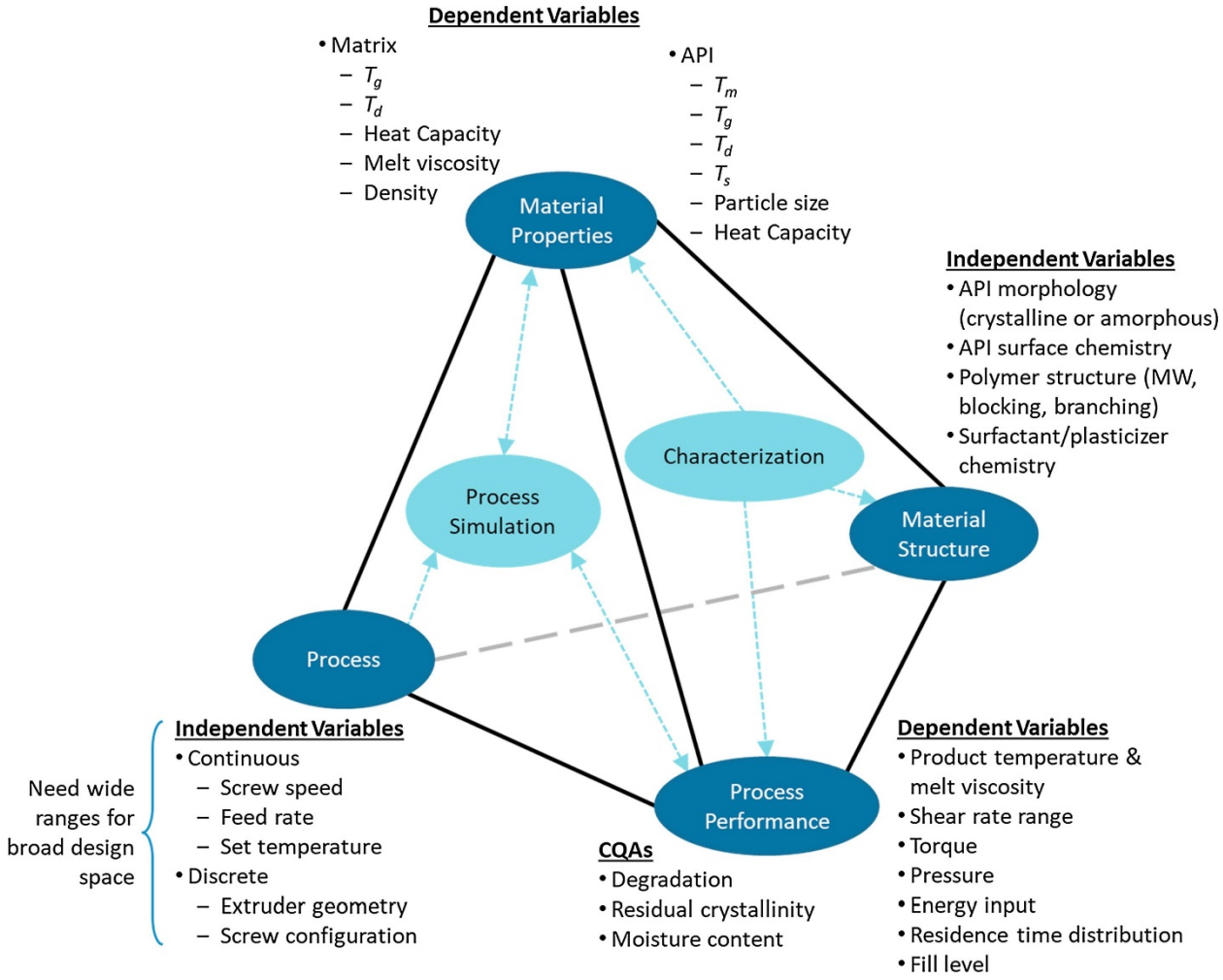

Figure 1.4. The materials science tetrahedron as applied to hot-melt extrusion for ASD formation. T_g = glass transition temperature, T_m = melting temperature, T_d = degradation temperature, T_s = solubility temperature (temperature at which a given concentration of API is thermodynamically soluble in the matrix).[47]

1.3.3.2 Relationship of Material and Process Attributes to Critical Quality Attributes

The relationship of many independent and dependent variables contribute to resultant product characteristics.[48] The complex interplay of selected material attributes and process parameters are highlighted in Figure 1.5. Each independent variable (pink), affects several dependent variables (green), which then impact the critical quality attributes (CQAs) of the ASD intermediate (orange, blue, yellow), which in turn affect the Quality Target Product Profile attributes (QTPP) (white). To illustrate this interplay, residence time can be followed through the flow chart as a surrogate for many kinetic factors. Residence time is impacted directly by screw

speed, screw type/configuration/size, and feeding rate/type and indirectly by temperature and shear due to their impact on melt viscosity. These factors then influence the homogeneity of the ASD, chemical degradation of drug or polymer, and whether or not the crystalline-to-amorphous phase transformation has completed. These critical quality attributes then contribute to the performance, efficacy, and safety of the dosage form.

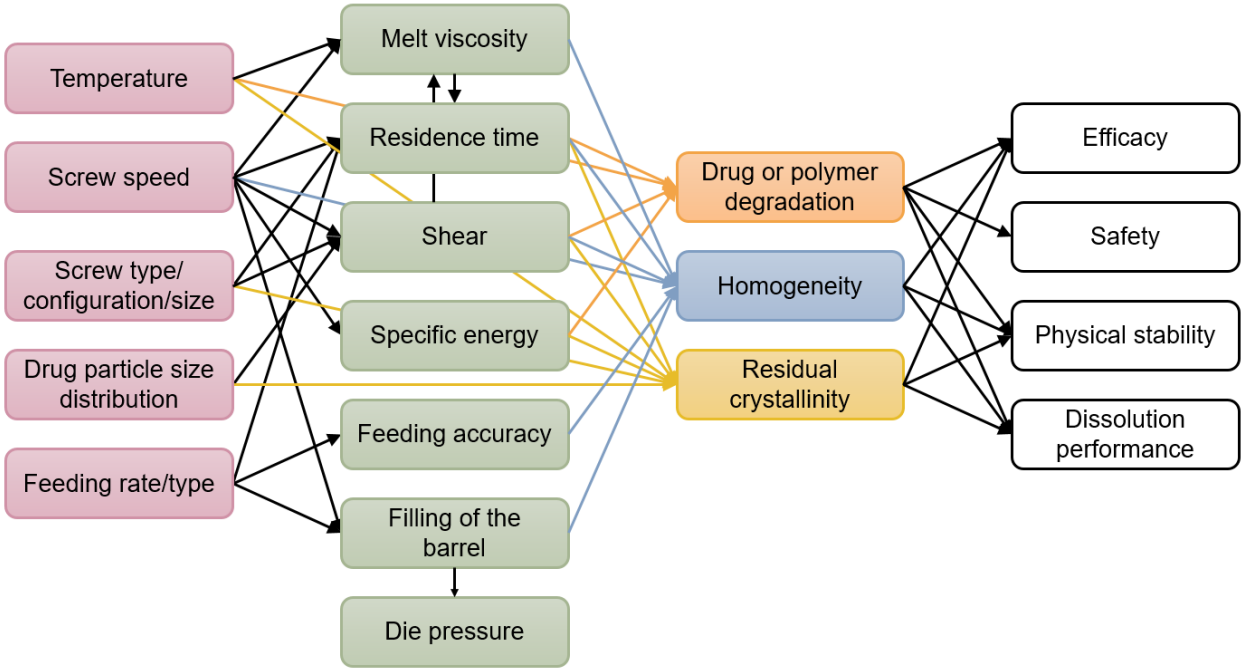

Figure 1.5. Complex interplay of the material attributes and process parameters to HME intermediate critical quality attributes (CQAs) and quality target product profile (QTPP) influenced by material, equipment, and process variables.

1.3.3.3 Processing Regimes

Hot melt extrusion processes for amorphous solid dispersions can be classified based on the relationship of the processing temperature profile used to the melting temperature of the drug.[49] When a temperature at or above the T_m is used, both drug and polymer transform into the liquid state, based on thermal input, and undergo liquid-liquid mixing, assuming a miscible system. At temperatures below the T_m, the drug crystal must dissolve into a miscible polymer in order to successfully prepare a single-phase amorphous system. Typical process attributes used in each regime are described in Table 1.2.[50]

Table 1.2. Attributes of a hot melt extrusion process for production of ASDs based on processing temperature classification.[50]

Process attribute	Processing Temperature At or Above T_m	Processing Temperature Below T_m
Feed rate	Higher	Lower
Shear	Low	Higher shear from dispersive mixing
Process length	Shorter	Longer
Specific energy	Lower	Higher
Bulk API properties	Less critical	Critical
Bulk excipient properties	Less critical	Can be critical
Mixing required	Primarily distributive mixing	Primarily dispersive mixing

1.3.3.4 Downstream Processing

The HME ASD intermediate is subsequently subject to downstream processing, such as milling, blending, compression, and/or encapsulation, in order to form the drug product, typically a tablet or capsule. These processes may alter the attributes of the amorphous solid dispersion, such as crystallinity or phase separation, and therefore alter the performance of the drug product.[51–53]

1.3.4 Phase Diagrams

1.3.4.1 Melting Point Depression

The Flory-Huggins theoretical framework can be used to describe the well-known phenomenon of melting point depression.[54–59] A miscible drug-polymer system is one in which the (supercooled) liquid form of the drug homogenously mixes with the polymer across all compositions.[60] Miscible drug-polymer systems exhibit melting point depression because the chemical potential of the drug in the drug-polymer system is reduced relative to that of the pure drug due to favorable exothermic mixing and entropy of mixing. This relationship is described by Eq. 2

$$\frac{1}{T_c}-\frac{1}{T_m}=-\frac{R}{\Delta H}\left[\ln\phi+\left(1-\frac{1}{m}\right)(1-\phi)+\chi(1-\phi)^2\right] \qquad \text{Eq. 2}$$

where the T_m is the melting temperature of the pure drug (in Kelvin), T_c is the depressed melting point of the drug-polymer system (in Kelvin), R is the gas constant, ΔH is the enthalpy of fusion

of the drug, ϕ is the volume fraction of the drug, m is the ratio of the polymer segment to drug molecular volume, and χ is the Flory-Huggins interaction parameter. A negative χ indicates a miscible system. Limitations of this approach and further discussion of the interaction parameter can be found in the literature.[61–64]

The solubility of the drug in the polymer, refers to the ability of the crystalline form of the drug to be solubilized in a polymer.[54] In a miscible drug-polymer system, solubility determination by multiple methods are considered to be thermodynamically equivalent.[65] In the melting point depression method by differential scanning calorimetry (DSC), the solubility equilibrium is approached by heating a fixed composition to determine the temperature at which dissolution is complete (melting point offset temperature) (Figure 1.6, line c → e). In the hot melt extrusion process, complete solubility is achieved by solute dissolution into the molten polymer from an under-saturated state under isothermal conditions (Figure 1.6, line b → e).

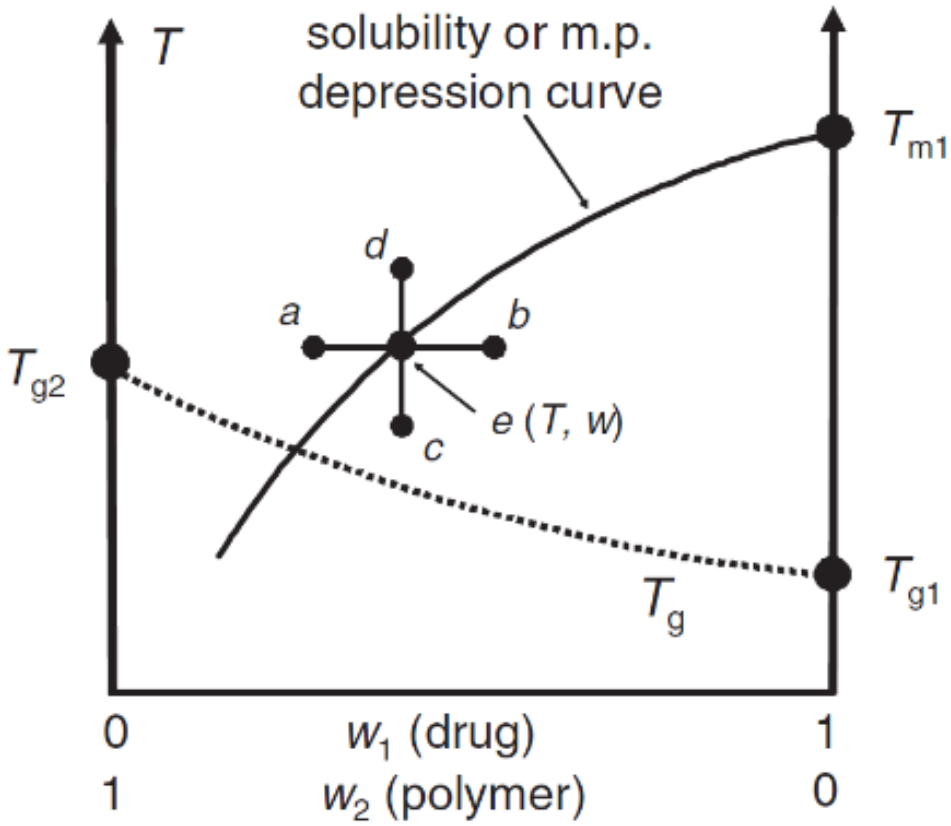

Figure 1.6. Thermodynamic equivalence of solubility curve determination.[65]

Phase diagrams can be readily constructed by thermal analysis methods such as the melting point depression DSC method or recrystallization method.[66–68] Besides Flory-Huggins, other approaches are commonly used to determine the solubility temperature and building phase diagrams, such as PC-SAFT and an empirical model.[69,70]

1.3.4.2 Glass Transition

The glass transition temperature marks the transition between the supercooled liquid and glassy state of an amorphous material. The high glass transition temperature of polymer carriers typically increases the T_g of the ASD compared to the T_g of the amorphous drug alone. The Gordon-Taylor equation is commonly used to predict the composite T_g (Eq. 3)

$$T_g = \frac{w_1 T_{g1} + K w_2 T_{g2}}{w_1 + K w_2}, \text{ where } K = \frac{\rho_1 T_{g1}}{\rho_2 T_{g2}} \qquad \text{Eq. 3}$$

where w is the weight fraction, where ρ is the true density, and the subscripts *1* and *2* represent each component. Typically, a miscible drug-polymer system will display a single, concentration-dependent T_g.[60,71] T_g values which deviate from the concentration-dependent relationship may indicate other phenomena, such as plasticization or anti-plasticization.[72,73]

1.3.4.3 Phase Behavior

The phase diagram shown in Figure 1.7 identifies the composition and temperature regions where the mixture is thermodynamically and/or kinetically stable.[69] Above the solubility line, the mixture is thermodynamically stable, wherein all components are molten and homogenously mixed. Below the glass transition (formulation T_g), the mixture is kinetically stabilized due to high viscosity and may be thermodynamically stable, based on composition and temperature above or below the solubility line. In the region below the solubility line and above the glass transition, the mixture is thermodynamically and kinetically unstable, and prone to phase separation and/or crystallization. Flory-Huggins solution theory has been used to model the melting point depression phenomena in drug-polymer blends, and also has been used to predict ASD physical stability and phase behavior.[68,69,74–78]

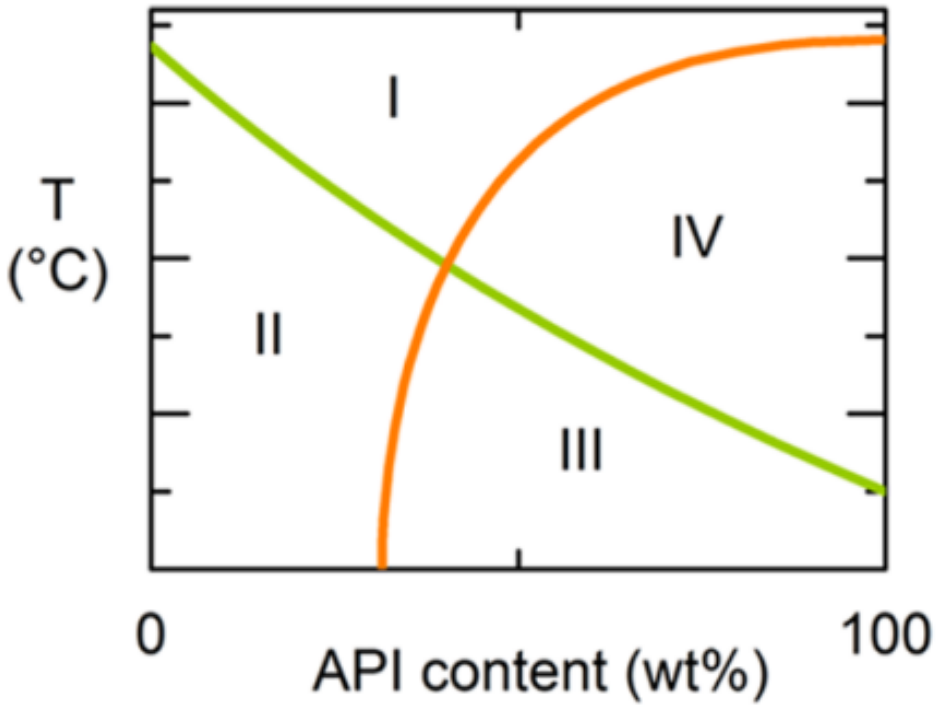

Figure 1.7. Phase behavior of an amorphous solid dispersion. The solubility (orange) and glass transition (green) curves divide the phase diagram into four areas: (I) thermodynamically stable melt, (II) thermodynamically stable glass, (III) kinetically stable glass, and (IV) thermodynamically and kinetically unstable melt.[69]

1.4 Critical Quality Attributes of HME ASDs

Aside from the expected attributes of physical, chemical, or microbiological purity that are expected of a drug product, several critical quality attributes (CQAs) play a significant role in the performance of ASDs manufactured by HME. Three CQAs will be highlighted here, along with the two methods of performance evaluation. The successful formation of an ASD, as determined by its CQAs and resulting performance attributes, is dependent on the interplay of many material, equipment, and processing variables.

1.4.1 Degradation

At some elevated temperature range, depending on residence time, thermal degradation of the drug or polymer may result from the extrusion process. Thermal degradation is typically thought to be a result of cumulative exposure.[79] The range where a formulation is susceptible to thermal degradation should be experimentally determined. In the literature, thermal degradation is

commonly investigated using thermal gravimetric analysis and HPLC.[79–83] Raman spectroscopy has also been employed on-line to monitor drug degradation.[11] In a recent study, Evans et al demonstrated a "dissolve-then-degrade" mechanism for a model compound, torasemide, in Soluplus.[83] In addition to temperature, some compounds may be sensitive to shear.[49,83] Strategies for mitigating thermal degradation investigated in the literature include plasticization of the melt,[84] drug-polymer interactions,[85] adjusting the chemical microenvironment,[86] or modifying process parameters or equipment setup.[86–88]

While each drug has a unique chemical stability profile, the limited availability of thermally stable and pharmaceutically acceptable polymers also limits the temperature range of most HME processes. The most commonly used polymers have degradation temperatures between 175-250°C.[50] Mechanical shear stresses imposed by the rotating screw and high processing temperatures may cause chain scission, depolymerization, or thermal degradation of polymers.[15] Serajuddin and coworkers have extensively studied the rheological and degradation properties of common polymers to provide processing recommendations.[81,89–91]

1.4.2 Crystallinity

Crystallinity in the ASD may be from one of two formation pathways: (1) a result of recrystallization from the matrix or (2) residual from the process.[92] These crystals directly result in lost solubility advantage,[93] and may have additional product performance implications. Physical instability (i.e. phase separation or crystallization) upon storage or exposure to moisture is affected by the inherent crystallization tendency of the drug, polymer type, miscibility, drug loading, T_g, and particle surface area,[60,92,94–98] and may be accelerated due to the presence of crystallinity.[99] In solution, desupersaturation results due to nucleation or crystal growth in a reduced levels of dissolved drug available for absorption.[17,100,101]

1.4.3 Homogeneity

A fully miscible ASD system contains molecularly dispersed drug and polymer. However, phase separation can occur when a system is supersaturated with respect to the liquid-liquid mixing phase diagram, forming amorphous drug-rich and polymer-rich domains throughout the ASD matrix. Discrete drug-rich domains are found to crystallize faster than single phase systems.[96]

Phase separation can be induced by water, temperature changes, or processing factors.[51,52,102–104] Detection of phase separation on varying domain length scales can be accomplished with techniques such as ssNMR, DSC, TEM, and Raman spectroscopy.[98,102–106] In the literature, homogeneity of ASDs is typically improved by the use of vigorous mixing conditions.[102,107]

1.5 Performance Evaluation

1.5.1 Critical Quality Attribute Detection Methods

A complementary set of methods are typically used to characterize the critical quality attributes of a formulation. Crystallinity detection and quantification in ASD formulations is commonly performed using X-ray powder diffraction (XRPD).[108] However, the technique has several limitations stemming from formulation and method parameters. In particular, detectability of crystalline peaks above baseline noise is limited by crystal mass fraction which may be reduced by dilution with a polymer, as well as crystal quality/size.[27,108,109] High sensitivity to crystalline content is achieved with polarized light microscopy (PLM), even when XRPD has determined a sample to be amorphous.[92] However, PLM is limited by spatial resolution caused by the diffraction limitation, only detecting crystals greater than approximately 0.5-1 μm. Differential scanning calorimetry (DSC) for detection of crystallinity or inhomogeneity is limited primarily by the dynamic heating process, as well as crystal mass fraction within the overall sample and crystal or phase separated domain size.[65] More sensitive techniques, such as Raman spectroscopy, have observed molecular-level differences in the amorphous phase, even when DSC and XRPD have failed to identify these differences.[102,106]

1.5.2 Stability Testing

Physical stability of ASDs is typically assessed by storing a fresh sample, presumably completely amorphous, at defined temperature and humidity conditions, then investigated with respect to crystallization. Lin et al have contributed an excellent review of factors affecting physical stability of amorphous solid dispersions.[19]

1.5.3 Dissolution Testing

Dissolution behavior of ASDs is typically assessed under non-sink conditions in simple or biorelevant media. Sink conditions are commonly defined as having a volume of solvent at least 3 times greater than that present in a saturated solution.[110] In order to achieve sink conditions for a poorly water soluble drug, large media volumes or high levels of surfactant may be required. However, such conditions are not useful for investigating a formulation's potential for supersaturation, because the drug concentrations will remain below the equilibrium (crystalline) solubility. In the context of bioavailability enhancement, amorphous solid dispersions generate a transient supersaturated drug solution, where the concentrations achieved are significantly higher than the equilibrium solubility. Thus, testing under "non-sink" conditions is an important way to measure the performance of an amorphous solid dispersion, as both the achievable supersaturation can be characterized, as well the kinetics of nucleation and growth.[111] This competition between dissolution and crystallization is illustrated by Figure 8a. The drug can enter the solution state and be absorbed or crystallize. The drug can also crystallize directly from the solid state (matrix crystallization), ultimately decreasing the achievable supersaturation.

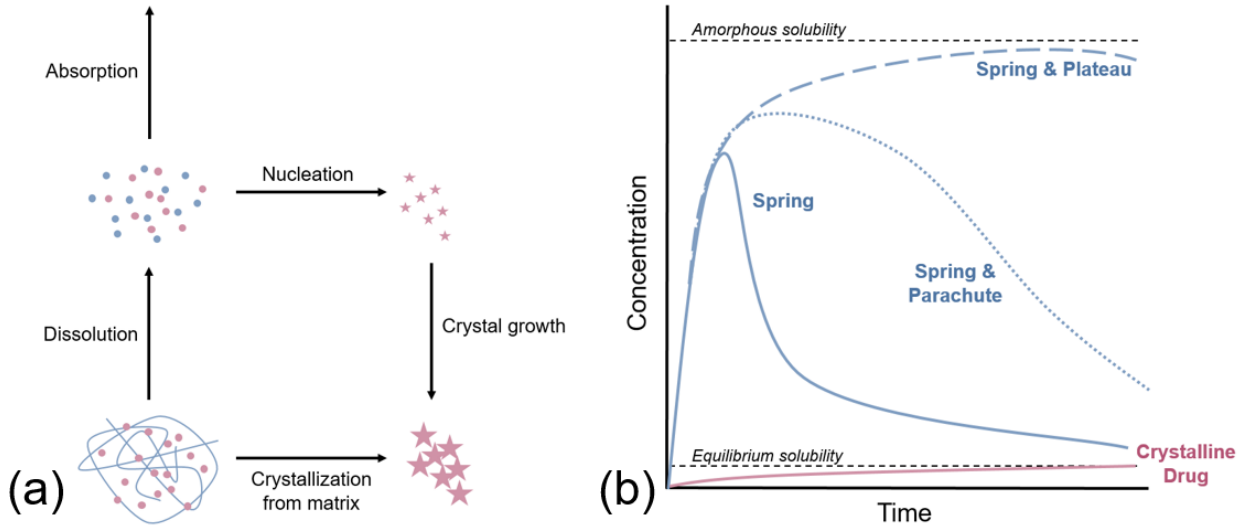

Figure 1.8. (a) Schematic illustrating the competition between dissolution and crystallization from the solid or solution states from an amorphous solid dispersion (adapted).[112] (b) Theoretical dissolution profiles of amorphous solid dispersions relative to that of the crystalline drug (adapted).[30,113]

Under non-sink conditions, the dissolution profile may follow one of several motifs, based on the drug's solid state form and ability of the polymer to promote dissolution and inhibit crystallization (Figure 8b).[30,113] The ability of the amorphous drug to form a colloidal phase (liquid-liquid phase separation, or LLPS) at concentrations above the amorphous solubility is beyond the scope of this literature review.[30,114] The crystalline drug is characterized by a limited extent of dissolution, constrained by the equilibrium solubility. Generally, the dissolution rate of the crystalline form is comparatively slower than that of the amorphous form for an equivalent surface area of dissolving material. An amorphous form may achieve a faster rate and extent of dissolution, creating a supersaturated state with respect to the equilibrium solubility. As any attained supersaturation is metastable with respect to the equilibrium solubility, rapid desupersaturation may result due to crystallization (the "spring" profile). This profile may also occur in ASD systems with a polymer which is an ineffective crystallization inhibitor. By incorporating a polymer capable of inhibiting crystallization, the achieved supersaturation can be prolonged and onset of crystallization delayed (the "spring & parachute" profile).[113] The "spring & plateau" profile represents the ideal dissolution profile, where supersaturation is rapidly achieved and solution crystallization is completely prevented during transit through the gastrointestinal tract.[30] The amorphous solubility limits the maximum possible molecularly dissolved drug concentration. By maximizing molecularly dissolved drug concentrations, *in vivo* exposure is also maximized.[114]

1.6 Research Overview

In chapter 1, an overview of the fundamental aspects of amorphous solid dispersions as a formulation strategy, hot melt extrusion, and performance evaluation is provided.

In chapter 2, the description and application of temperature-composition phase diagrams as related to hot melt extrusions, with specific focus on identifying and validating the formulation critical temperature T_c as the minimum processing temperature which can be used to prepare amorphous solid dispersions are reported.

In chapter 3, characterization of an X-ray amorphous hot melt extruded formulation by transmission electron microscopy (TEM) to detect and characterize low levels of residual crystallinity is described. Two populations of residual crystals were identified: single crystals mid-dissolution (<100 nm) and nanocrystalline domains of 5-10 nm in size.

In chapter 4, mechanisms of crystal dissolution of indomethacin crystals into polymer melts are elucidated. A defect-site driven dissolution and fragmentation model was proposed to describe experimental and simulated evidence of irregular dissolution patterns.

In chapter 5, non-sink dissolution testing of a model amorphous solid dispersion system manufactured by hot melt extrusion was performed. Supersaturation profiles of indomethacin/PVPVA ASDs containing 0-25% residual crystallinity demonstrated lost solubility advantage. Evidence of polymer adsorption onto indomethacin crystals formed a mechanistic hypothesis to describe the highly effective crystal growth inhibition observed.

In chapter 6, nonisothermal and isothermal TGA heating methods were validated as a surrogate to assess the likelihood of degradation of amorphous materials during hot melt extrusion. The results indicate that TGA mass loss of volatiles should be considered only an approximate indicator of degradation, as actual potency loss is likely to be significantly higher.

CHAPTER 2. THE APPLICATION OF TEMPERATURE-COMPOSITION PHASE DIAGRAMS FOR HOT MELT EXTRUSION PROCESSING OF AMORPHOUS SOLID DISPERSIONS TO PREVENT RESIDUAL CRYSTALLINITY

This chapter is a reprint with minor modifications of a manuscript published in *International Journal of Pharmaceutics* in October 2018 with the same title by: Dana E. Moseson and Lynne S. Taylor. Reprinted with permission from Elsevier. DOI: 10.1016/j.ijpharm.2018.10.055.

2.1 Abstract

Hot melt extrusion (HME) can be used to produce amorphous solid dispersions (ASDs) at temperatures below the drug's melting point if the drug and polymer exhibit melting point depression. However, the risk of residual crystallinity becomes significant. The purpose of this study was to apply the temperature-composition phase diagram to the HME process, correlating process conditions to ASD residual crystallinity, and identifying the formulation critical temperature, which defines the theoretical minimum processing temperature. The phase diagram of indomethacin (IDM) and polyvinylpyrrolidone/vinyl acetate copolymer (PVPVA) was generated using melting point depression measurements coupled with Flory-Huggins theory. Extrudates were manufactured above, at, and below the formulation critical temperature (T_c) as identified from the phase diagram, with a range of residence times, and characterized for crystallinity. Below the T_c, a fully amorphous sample could not be prepared. Above T_c, sufficient residence time led to amorphous samples. A processing operating design space diagram with three regimes was generated to correlate temperature and residence time factors with process outcome. In conclusion, phase diagrams provide a rational basis for designing hot melt extrusion processes of amorphous solid dispersions to minimize residual crystalline content, delineating the minimum processing temperature based on thermodynamic considerations.

2.2 Introduction

When choosing a commercial amorphous solid dispersion (ASD) manufacturing process, there are two leading choices: spray drying or hot melt extrusion (HME).[37] Solvent-based processes are more common because they are applicable to a wide range of compounds, and are

material-sparing in early phase development.[38,39] However, HME offers several advantages for thermally stable systems; it is solvent-free, continuous, high-throughput, easily scalable, inexpensive, and requires only a small footprint.[40]

Detailed descriptions of the HME process can be found in the literature.[15,42] First, the powder components are fed into the extruder, then conveyed into a heated barrel by a screw system. A molten phase is generated by means of high temperatures and mixing in the screws. The first stage of the molten phase is created by softening the polymer by heating to above its glass transition temperature (T_g). Next, dispersed crystalline drug particles melt and/or dissolve into the polymer. If the drug and polymer are miscible and adequate mixing is provided, a single phase, homogenous viscous liquid consisting of drug and polymer results, which is then extruded through a die, cooled, and subjected to downstream processing. Pharmaceutical hot melt extrusion processes have been widely investigated using considerations such as equipment configuration and design,[12,115] rheology,[116–119] formulation,[85,86,120–122] and process analytical technology.[11,123,124]

Avoidance of thermal degradation and an absence of residual crystallinity are two critical quality attributes of hot melt extruded ASDs.[11,83,125] To preclude thermal degradation of drug and/or polymer, lower processing temperatures are desirable, albeit accompanied by a risk of residual crystalline content, if the crystals do not fully melt or dissolve during the process. Hot melt extrusion processing at temperatures below the drug's melting point has been extensively documented with the majority of studies utilizing melting point depression to reduce thermal degradation.[72,79,85–87] Studies providing strategies to mitigate the corresponding risk of crystallinity have thus far been limited to equipment setup (screw configuration) and drug particle size reduction.[13,126] Risk-based strategies are of considerable importance to formulation and process development scientists because residual crystalline content directly results in lost solubility advantage,[93] but also impacts product performance in other ways. Physical instability upon storage or exposure to moisture is affected by many parameters, such as drug loading, polymer type, miscibility, T_g, particle surface area, and the inherent crystallization tendency of the drug,[60,92,94–98] and may be accelerated due to the presence of seed crystals.[99] In solution, as a consequence of secondary nucleation or growth of seed crystals, desupersaturation results in a reduced amount of dissolved drug available for absorption.[17,100,101,111,127,128] As both stability and dissolution performance may be undermined by the presence of seed crystals, it is considered critical to design the ASD manufacturing process to generate a fully amorphous system.[15]

Melting point depression occurs for many systems, most famously ice,[129] and has been documented for drug-polymer systems.[66,74,75,130,131] Flory-Huggins solution theory has been used to model melting point depression in drug-polymer blends, and also has been used to predict ASD phase behavior and physical stability.[68,69,74–78] Melting point depression in a drug-polymer blend is most commonly depicted using a temperature-composition phase diagram. The phase diagram has been conceptually proposed as a methodology for identifying the solubility line and thus suitable HME processing temperatures,[43,49,125] although the validity of this approach has not been extensively demonstrated in the literature. Several studies have evaluated HME in the context of the phase diagram and shown some evidence of residual crystals for samples processed below the solubility line.[12,130,132] However, because little melting point depression was observed in these particular systems, the validity of utilizing melting point depression to extend the processing window to considerably lower temperatures, while simultaneously avoiding residual crystalline content remains an open question.

The goal of this study was to demonstrate the applicability of the temperature-composition phase diagram to guide the HME processing design space for ASD manufacture. We hypothesize that, for a system exhibiting substantial melting point depression, processing can be carried out at temperatures considerably below the melting point and still lead to an amorphous extrudate, as long as factors impacting the kinetics of drug crystal dissolution are also taken into account. This provides a processing strategy for thermally labile systems or for drugs with high melting points. By defining the lower temperature of processing based on the solubility line, and considering mechanical, material, and kinetic variables, this approach provides a rational basis for minimization or, more desirably, elimination of residual crystalline content. Indomethacin (IDM) and polyvinylpyrrolidone/vinyl acetate copolymer (PVPVA) were used as the model drug and polymer. IDM, a BCS Class 2 compound with low aqueous solubility and a melting point of 161°C, is representative of the types of compounds processed by HME. PVPVA is the most common polymer used with ASDs processed by HME.[10] Our approach involved constructing a phase diagram using melting point depression measurements obtained with differential scanning calorimetry (DSC) coupled with Flory-Huggins theory. Extrudates were then prepared at a range of temperature and residence times, assessed for crystallinity, with results explained based on the obtained phase diagram.

2.3 Experimental

2.3.1 Materials

Indomethacin (IDM), verified to be the thermodynamically stable γ polymorph by XRPD and DSC (data not shown), was obtained from ChemShuttle (Hayward, CA) and used as-is unless otherwise noted. Polyvinylpyrrolidone/vinyl acetate copolymer (PVPVA, Kollidon VA64) was a gift from BASF (Florham Park, NJ). The key material attributes of IDM and PVPVA are listed in Table 2.1. All other materials used were of suitable reagent grade. Particle size analysis of the IDM and PVPVA powders was performed in triplicate using a Malvern Mastersizer 3000 particle size analyzer with Aero S attachment (Worcestershire, UK).

Table 2.1. Physiochemical properties of indomethacin (IDM) and polyvinylpyrrolidone/vinyl acetate copolymer (PVPVA). Error is reported as one standard deviation, n=3.

Component	Molecular weight (g/mol)	Melting point, T_m (°C)	Glass transition, T_g (°C)	Enthalpy of fusion, ΔH (kJ/mol)	True density (g/mL)	Molecular volume (cm^3/mol) [3]	Particle size (μm)
IDM	357.8	160.64 ± 0.04	43.7 ± 0.5	37.8 ± 0.6	1.31 (amorphous form) [2]	273	D10: 6.3 ± 0.1 D50: 21.9 ± 0.3 D90: 63.4 ± 0.9
PVPVA	55,000 [1]	---	104.2 ± 0.4	---	1.18 [2]	46,610	D10: 24.1 ± 0.5 D50: 72 ± 3 D90: 169 ± 14

[1] Polymer molecular weight is an estimate from the manufacturer's specification range of 45000-70000.
[2] True density values taken from literature.[133]
[3] Calculated by dividing molecular weight by true density.

2.3.2 Melting Point Depression

2.3.2.1 Theoretical Concepts

Melting point depression is a well-known phenomenon, which can be described within the Flory-Huggins theoretical framework.[54–59] The free energy of mixing of polymer and small molecule is described by Equation 1

$$\Delta G = RT\left[\phi \ln \phi + \frac{(1-\phi)}{m}\ln(1-\phi) + \chi\phi(1-\phi)\right] \quad (4)$$

where ΔG is the Gibbs free energy, R is the gas constant, T is the temperature in Kelvin, ϕ is the volume fraction of the drug, m is the ratio of the polymer segment to drug molecular volume, and χ is the Flory-Huggins interaction parameter.

The melting point of a drug occurs when the chemical potential of the crystalline and molten forms are equal. In the presence of a miscible polymer, favorable exothermic mixing in combination with a favorable entropy of mixing will result in a depressed melting point, as the chemical potential of the drug-polymer system is reduced relative to that of the pure drug.[74,75] Therefore, miscible drug-polymer systems will exhibit melting point depression. If the drug and polymer are immiscible, melting point depression will not occur, since the presence of the polymer does not alter the chemical potential of the drug.[75] The relationship between the melting temperature of the pure drug, T_m, and the depressed melting point of the drug in the drug-polymer system, herein referred to as the critical temperature, T_c, is shown by Equation 2, where ΔH is the heat of fusion of the drug.

$$\frac{1}{T_c} - \frac{1}{T_m} = -\frac{R}{\Delta H}\left[\ln\phi + \left(1 - \frac{1}{m}\right)(1-\phi) + \chi(1-\phi)^2\right] \tag{5}$$

The Flory-Huggins interaction parameter, χ, is an indication of the non-ideality of mixing, and can display non-trivial dependence on temperature, chain length, and composition. A negative χ indicates a favorable enthalpy of mixing and results in additional melting point depression beyond that driven by the combinatorial entropy. Additional discussion of the interaction parameter, as well as the limitations of this approach can be found in the literature.[61,62]

A miscible drug-polymer system is one in which the (supercooled) liquid form of the drug mixes with the softened polymer across all compositions.[60] The solubility of the drug in the polymer, refers to the ability of the crystalline form of the drug to be solubilized in a polymer.[54] In a miscible drug-polymer system, solubility determination of crystalline drug in the polymer by multiple methods is considered to be thermodynamically equivalent.[65] Two approaches are applied herein which seek to determine this solubility equilibrium: melting point depression and hot melt extrusion. In the melting point depression method, the solubility equilibrium is measured by heating a fixed composition to determine the dissolution temperature. In the hot melt extrusion process, the solubility equilibrium is determined by monitoring solute dissolution from an under-saturated state under isothermal conditions.

2.3.2.2 Phase Diagram Construction

The melting point depression DSC method developed by Tao et al.[66] was used, with several modifications, to build a thermodynamic temperature-composition phase diagram that can be correlated to HME process design. Physical mixtures of IDM and PVPVA of compositions every 10% drug loading from 40%-90% were prepared in triplicate by cryomilling (6750 Freezer/Mill, SPEX, Metuchen, NJ) approximately 1 g of sample under liquid nitrogen using 5 minutes of pre-cooling time, followed by 2 minutes of grinding time at 10 Hz. Samples were then brought to room temperature and stored under desiccant until analysis.

A Q2000 differential scanning calorimeter equipped with a refrigerated cooling accessory (TA Instruments, New Castle, DE) purged with nitrogen at 50 mL/min was used to analyze physical mixtures of IDM and PVPVA as well as their constituent components. The instrument was calibrated for temperature and enthalpy using indium and tin. Since the dissolution of the crystalline drug into the molten polymer is a dynamic measurement, the melting point offset temperature depends on heating rate.[66,131] Physical mixtures of 3-5 mg were loaded into standard aluminum pans and heated from 25-180°C at various heating ramp rates, then cooled to 25°C at 10°C/min, followed by a second heating ramp at 10°C/min. In the first heating ramp, six heating rates of 0.5-10°C/min were used to determine the relationship of melting point offset temperature to heating rate.

The melting point offset temperature was selected as the most relevant parameter to understand the system, as it represents the temperature at which the composition is fully solubilized. Thus, the melting point offset temperature most accurately reflects the goals of this study, i.e. to determine the lower bound of HME processing temperature to generate a fully amorphous system. As the change in melting point offset temperature is nonlinear with respect to heating rate, the data were fit to a second order polynomial curve and extrapolated to zero heating rate. The intercept of melting point offset temperature at 0°C/min heating rate was used as the equilibrium critical temperature (T_c) for a given composition. By rearrangement of Equation 2, the interaction parameter can then be calculated across the range of compositions to model the solubility line. The drug molecular volume was used as the lattice volume.

The second heating ramp was used to determine the onset dry glass transition (T_g) temperature. The Gordon-Taylor relationship (Equation 3) was used to model the formulation glass

transition, where *w* is the weight fraction, where ρ is the true density, and the subscripts *1* and *2* represent each component.[73]

$$T_g = \frac{w_1 T_{g1} + K w_2 T_{g2}}{w_1 + K w_2}, \text{ where } K = \frac{\rho_1 T_{g1}}{\rho_2 T_{g2}} \quad (6)$$

Enthalpy of fusion (ΔH), melting point offset temperature (T_m), and onset T_g temperature were determined in triplicate for IDM using the approach described for the physical mixtures. The onset T_g temperature of PVPVA was determined using the procedure described above using heating and cooling rates of 10°C/min (n=6).

2.3.3 Processing

2.3.3.1 Preparation of Amorphous Solid Dispersions by Hot Melt Extrusion

A 50% drug loading level of IDM in PVPVA was selected for investigation, as a range of processing conditions are accessible within the phase diagram (above polymer glass transition T_g and minimum processing temperature T_{min}). Being a fairly high drug loading level, this composition is also relevant to certain marketed ASD formulations. A physical mixture of IDM and PVPVA was prepared at 1:1 water corrected weight ratio by blending 200 g for 10 minutes at 20 rpm in a 1 liter Dott-Bonapace tumble blender (Limbiate, Italy). Prior to blending, a 60 mesh sieve was used to separate any agglomerated material from the bulk IDM powder.

Extrudates were prepared using temperatures above, at, and below the formulation critical temperature T_c (131°C for the 1:1 IDM:PVPVA system), so as to characterize the impact of process temperature and kinetic factors on product characteristics. An Xplore Pharma Melt Extruder (Geleen, The Netherlands), assembled with a 5 mL co-rotating conveying screw and barrel set (refer to the schematic in Appendix A Figure A.1), was used to prepare 10 g batch sizes of the 1:1 IDM:PVPVA premix with a screw speed of 20 rpm.[134] A water bath set to 10°C cooled the hopper to prevent powder melting and blockage of the feeding zone. The processing temperature of all heating zones was set per the conditions in Table 2.2, so as to achieve the desired product melt temperature as monitored by an in-line thermocouple located between screws and recirculation channel or die. The process set temperature was always higher than the bulk product melt temperature. The residence time, as noted by the time to first appearance of the extrudate, was controlled using one of two methods. First, the instrument was set in continuous mode (the

recirculation channel was closed), yielding a residence time of approximately 2 minutes. Second, the recirculation channel valve was in the open position to control the residence time; the valve was then closed to stop the recirculation and begin extruding the melt. In all experiments, the total extrusion time ranged from the noted time until 2-4 minutes later (depending on material flow). The extrudates were allowed to cool at room temperature. The selected screw configuration and speed was intended to provide moderate mixing without excessive heat generation, and to prioritize the conductive heating effects on the crystal dissolution process. Increased local temperatures due to viscous dissipation may yet be significant, and impacted by the shear imparted and composition,[135] but not detected here due to the extruder size and thermocouple placement. Further, variation in shear experienced by the melt may also occur due to the crystal dissolution and subsequent plasticization process.[136]

A portion of each extrudate was cryomilled for 60 seconds of grinding time at 10 Hz to form a fine powder. Powders were then brought to room temperature and sieved to achieve particle size fractions of 100-250 μm and <100 μm. Extrudates and powders were stored in a refrigerator under desiccant until analysis.

Table 2.2. Hot melt extrusion processing conditions and sample appearance. Error of product melt temperature range is reported as the actual temperature range during the experiment. The sample ID is reported as Temp-Time.

Sample ID	Process Set Temperature (°C)	Product Melt Temperature Range (°C)	Residence Time (min)	Appearance[1]
161-2	166	161 ± 1	2	Clear
141-10	145	141 ± 1	10	Clear
141-2	145	141 ± 1	2	Clear with visible crystals
138-2	142	138 ± 1	2	Clear with visible crystals
134-2	138	134 ± 1	2	Cloudy
134-10	138	134 ± 1	10	Clear
131-2	135	131 ± 1	2	Very cloudy
131-5	135	131 ± 1	5	Cloudy
131-10	135	131 ± 1	10	Clear with visible crystals
131-20	135	131 ± 1	20	Clear
126-2	130	126 ± 1	2	Very cloudy
126-10	130	126 ± 1	10	Cloudy
121-2	126	121 ± 1	2	Opaque
121-20	126	121 ± 1	20	Cloudy with visible crystals
117-2	122	117 ± 1	2	Opaque

[1] Images of the representative extrudates are found in Appendix A Figure A.2.

2.3.3.2 Preparation of Amorphous Solid Dispersions by Solvent Evaporation

An amorphous solid dispersion of 1:1 IDM:PVPVA was prepared by the solvent evaporation method. The drug and polymer were dissolved in a mixture of methylene chloride and methanol (2:1 v:v). The ASD was prepared with a Brinkmann Rotavapor-R (Buchi, New Castle, DE) under reduced pressure at 60°C to remove the solvent. The sample was then dried under vacuum to remove residual solvent and cryomilled for 60 seconds of grinding time at 10 Hz to form a fine powder.

2.3.4 Characterization

2.3.4.1 Determination of Crystalline Content by XRPD

X-ray powder diffraction (XRPD) patterns were collected using a Rigaku SmartLab diffractometer (Rigaku Americas, The Woodlands, Texas) in Bragg-Brentano mode with a Cu-kα radiation source and d/tex ultra detector. Using a glass sample holder, the patterns were obtained from 5-40° 2θ, using a step size of 0.02° and a 0.5°/min scan rate. A calibration curve ($R^2 = 0.985$) covering the range 0-100% crystalline content was prepared by geometric mixing of various amounts of crystalline IDM with a fully amorphous IDM:PVPVA sample (prepared by solvent evaporation). Each calibration sample was prepared in triplicate. The raw intensity data was processed using a moving average filter in order to maximize the signal-to-noise ratio, then subtracted from the baseline in order to calculate the peak area of 11.7°, 21.7°, and 26.8° 2θ. A fully amorphous 1:1 IDM:PVPVA ASD prepared by solvent evaporation was measured in triplicate, and the response was used to calculate the baseline noise. The LOD and LOQ were determined to be approximately 0.4% and 1% based on a 3:1 and 10:1 signal-to-noise ratio of intensity of the 11.7° 2θ peak. Each extrudate powder (100-250 μm size fraction) was analyzed and the total peak area used to determine the % crystallinity.

2.3.4.2 Imaging of Extrudate Powders by Polarized Light Microscopy (PLM)

Each powder sample (100-250 μm size fraction) was loaded in mineral oil on a glass slide and visually observed for birefringence using a Nikon Eclipse E600 POL cross-polarized light microscope (20X objective) with Nikon DS-Ri2 camera (Melville, NY).

2.3.4.3 Determination of Extrudate Thermal Properties

The thermal properties of the extrudate powders, the 1:1 IDM:PVPVA physical mixture and solvent evaporation preparations, as well as the constituent components were analyzed by DSC. Each sample (3-5 mg, <100 μm size fraction) was loaded into standard aluminum pans and heated from 0-180°C at 5°C/min with modulation of ±0.796 every minute, then cooled to 0°C at 10°C/min, followed by a second heating ramp at 10°C/min.

2.3.5 Crystal Dissolution in Polymer Visualized by Hot Stage Microscopy

A Nikon Eclipse E600 POL cross-polarized light microscope (20X objective) with Nikon DS-Ri2 camera (Melville, NY) and Linkam TMS93 hot stage accessory (Surrey, United Kingdom) was used to characterize the isothermal dissolution process of the crystalline drug into the molten polymer. A small amount of HME 117-2 powder (<100 μm size fraction) was placed on a glass coverslip and heated at 100°C/min to the target temperature, and held for up to 24 hours. Images were periodically captured using NIS-Elements D software to monitor the dissolution process of the IDM into PVPVA in the absence of mechanical mixing.

Since the IDM:PVPVA physical mixture did not have sufficient contact surface area for heat transfer between the glass slide, drug, and polymer particles to conduct the experiment, the 117-2 HME sample was used to visualize the dissolution kinetics in the absence of mixing. This sample (<100 μm size fraction) was used for all experiments, as it had the highest crystalline content but had undergone intimate mixing and possible crystal size reduction due to shear or partial dissolution. Also, since the ASD is partially formed, its composite glass transition temperature is lower, quickly decreasing the viscosity of the surrounding matrix so as to promote the formation of the dissolution boundary layer of the suspended crystals, in the absence of mixing.

2.4 Results

2.4.1 Temperature-Composition Phase Diagram

IDM demonstrated melting point depression in the presence of PVPVA across the range of compositions, as demonstrated in Figure 2.1a, confirming drug-polymer miscibility at elevated temperatures. The 50% drug loading composition shows approximately 30°C of melting point depression relative to the melting point offset temperature of the pure drug. Compositions with lower polymer content showed moderate melting point depression (1-4°C), while polymer amounts above 30% enhanced the ability of the drug to be solubilized, resulting in greater melting point depression (6-30°C).

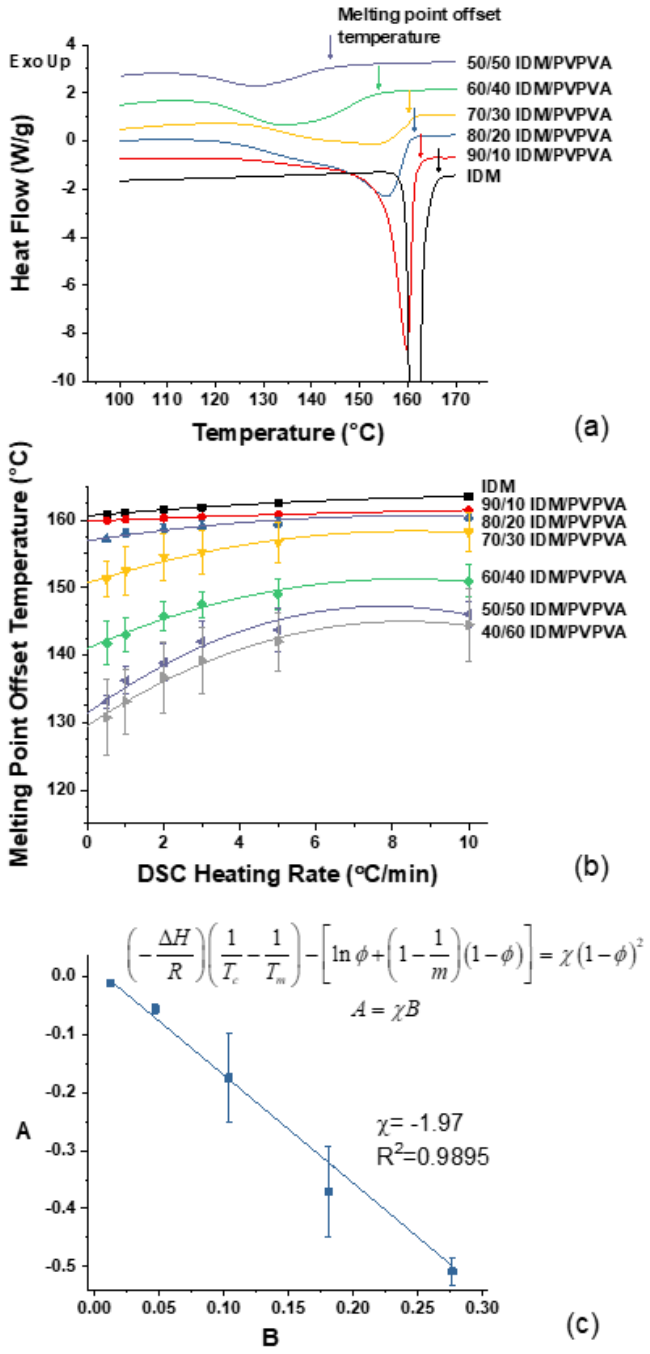

Figure 2.1. (a) Representative DSC thermograms of the dissolution/melting endotherms of IDM:PVPVA compositions and pure IDM heated at 10°C/min. Melting point offset temperature reflects the point at which all crystalline drug has dissolved into the molten polymer, or all crystalline drug has melted. (b) Melting point offset temperature vs. DSC heating rate for IDM:PVPVA compositions and pure IDM at 10°C/min scanning rate. Second order polynomial regression was used to calculate the melting point offset temperature. (c) The χ interaction parameter is calculated as the slope by rearrangement of Equation 2 into linear A=χB form. Error is reported as one standard deviation of triplicate preparations.

The effect of DSC heating rate on melting point offset temperature is shown in Figure 2.1b. Compositions down to 50% drug loading could be analyzed without significant viscosity effects hindering the measurement. High variability between replicates was seen for the 40% drug loading sample, indicating that the high viscosity of the system hindered accurate determination of the melting point offset temperature; as such, this drug loading was not used for further calculations.

The Flory-Huggins interaction parameter, χ, was calculated by rearrangement of Equation 2, where χ is the slope of the linear trend line (Figure 2.1).[74] This approach yields a single interaction parameter that describes the melting point depression across the entire composition range and neglects any temperature- or composition-dependence,[62] good agreement of the experimental data and modeled solubility line is observed (Table 2.3, Figure 2.2). The calculated interaction parameter of χ = -1.97 is comparable with other interaction parameters determined for the same drug-polymer system in other studies (-0.64, -2.06, -2.9, and -4.5).[61,65,68,137] Differences in the value of the interaction parameter can be attributed to various factors, including sample preparation (e.g. cryomilling), DSC method (e.g. heating rate), or choice of melting point onset or offset temperature for the determination; however, all studies similarly conclude that the IND:PVPVA system is miscible based on the negative value of the interaction parameter.

Table 2.3. Experimental and predicted equilibrium critical temperature (Tc) and glass transition (Tg) of IDM, PVPVA, and IDM:PVPVA mixtures. Error is reported as one standard deviation of triplicate preparations.

Sample Description	**Experimental T_c (°C)**	**Predicted T_c (°C)**	**Experimental T_g (°C)**	**Predicted T_g (°C)**
IDM	160.64 ± 0.04	160.6	43.7 ± 0.5	43.7
90/10 IDM/PVPVA	159.9 ± 0.3	159.4	47.0 ± 0.3	49.4
80/20 IDM/PVPVA	157.2 ± 0.4	155.6	52.6 ± 0.4	55.1
70/30 IDM/PVPVA	151 ± 3	149.6	59.7 ± 0.9	61.0
60/40 IDM/PVPVA	141 ± 3	141.4	66.3 ± 0.8	66.9
50/50 IDM/PVPVA	132.3 ± 0.8	131.0	72.2 ± 0.5	72.9
40/60 IDM/PVPVA	129 ± 6	118.5	77.6 ± 0.7	79.0
30/70 IDM/PVPVA	N/A	103.6	N/A	85.2
20/80 IDM/PVPVA	N/A	85.5	N/A	91.4
10/90 IDM/PVPVA	N/A	61.1	N/A	97.8
PVPVA	N/A	N/A	104.2 ± 0.4	104.2

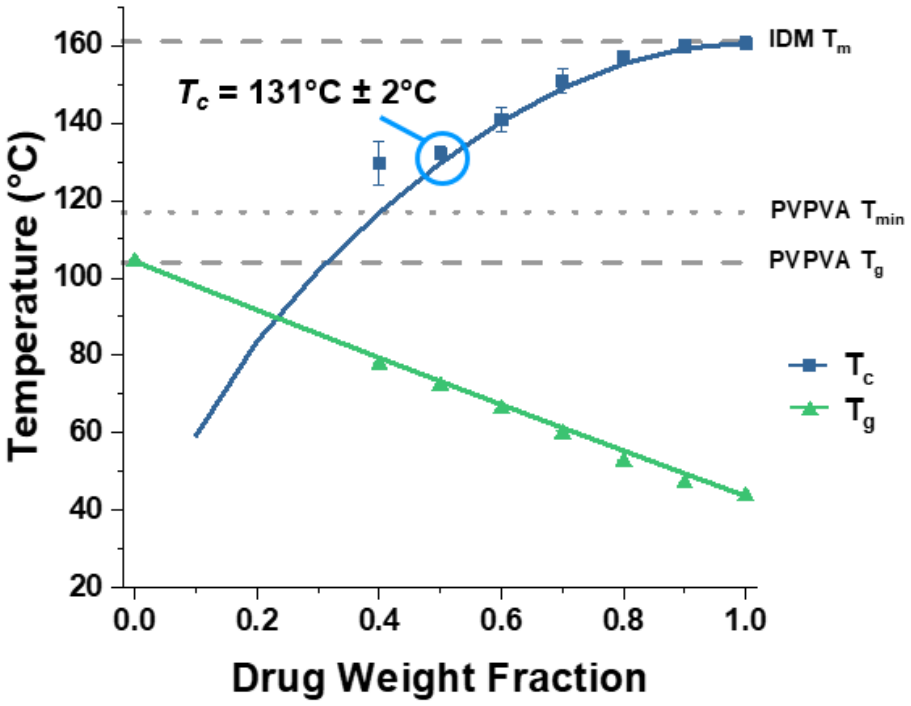

Figure 2.2. IDM:PVPVA temperature-composition phase diagram showing the experimental and predicted critical temperatures T_c (solubility line) and formulation glass transition temperatures T_g. The melting point and glass transition temperature of IDM and PVPVA, respectively, are noted by the dashed lines. The PVPVA minimum processing temperature T_{min} is approximated as 117°C (noted by the dotted line found 10-15°C above the PVPVA T_g). Error bars reflect one standard deviation (n=3); the error bars are too small to see on the experimental T_g results and several experimental T_c compositions.

The equilibrium critical temperature (T_c) for each composition (Table 2.3) was calculated by extrapolating the melting point offset temperature to zero heating rate as described above. The calculated interaction parameter, $\chi = -1.97$, was used in Equation 2 to predict the critical temperature across the entire composition range. Although the 40% drug loading composition is above the polymer T_g, the experimental melting point offset temperature shows a significant deviation from that predicted by Equation 2, due to viscosity effects. Throughout this work, the term critical temperature T_c refers to the solubility temperature at a fixed composition, and not the concept of upper or lower critical solution temperature.

The experimental and predicted IDM:PVPVA temperature-composition phase diagram is shown in Figure 2.2. IDM:PVPVA temperature-composition phase diagram showing the experimental and predicted critical temperatures T_c (solubility line) and formulation glass transition temperatures T_g. The melting point and glass transition temperature of IDM and PVPVA,

respectively, are noted by the dashed lines. The PVPVA minimum processing temperature T_{min} is approximated as 117°C (noted by the dotted line found 10-15°C above the PVPVA T_g). Error bars reflect one standard deviation (n=3); the error bars are too small to see on the experimental T_g results and several experimental T_c compositions.. The predicted formulation critical temperature T_c forms the solubility line. The experimental results above 50% drug loading are in good agreement with the predicted value, while the 40% drug loading composition deviates significantly from the predicted value, as previously discussed. Therefore, above 50% drug loading, the critical temperature T_c = 131°C ± 2°C forms the lower bound of processing temperature wherein all crystalline drug can be dissolved into the molten polymer, if the process were taken to equilibrium. Below 50% drug loading, the polymer's minimum processing temperature T_{min} forms the lower bound of processing temperature. All experimental formulation T_g values (Table III) are in good agreement with the values predicted by the Gordon-Taylor equation (Equation 3).

2.4.2 Characterization of IDM:PVPVA Extrudates

2.4.2.1 Determination of Crystalline Content by XRPD

XRPD was used to identify and quantify the presence of residual crystallinity as a function of sample temperature and residence time (diffractograms of all samples are shown in Appendix A Figure A.3). Figure 3 clearly demonstrates that longer residence time and/or higher temperature reduces the amount of residual crystallinity. At the formulation critical temperature T_c (131°C), the crystalline content decreases from 3% to trace levels within 10 minutes residence time. Above the T_c (>131°C), for equivalent residence times, crystalline content decreases as the processing temperature increases. Below the T_c (<131°C), crystalline content above the limit of quantification is seen in all samples irrespective of residence time, suggesting that the drug loading is above the solubility of the crystalline drug in the polymer for these temperatures. Samples prepared below the T_c (as measured by the bulk product melt temperature) and long residence times have lower crystalline content than expected based on the phase diagram. This may be a result of local heating effects within the extruder causing the melt to experience transiently higher temperatures above that of the measured bulk product melt temperature, driving greater crystal dissolution into the polymer.

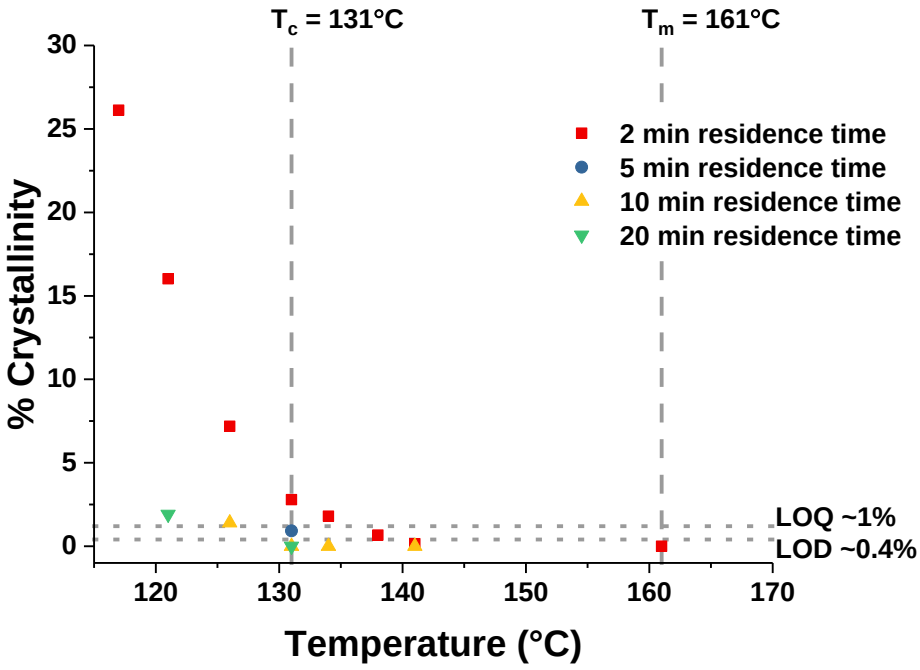

Figure 2.3. Quantification of crystalline content of IDM:PVPVA ASDs (100-250 µm size fraction) by XRPD as a function of product melt temperature. The dashed lines indicate the formulation critical temperature T_c and drug melting point T_m, delineating the processing regime boundaries by temperature. The dotted lines indicate the method limit of detection (LOD) and quantification (LOQ). Above T_m *(melting regime)*, no crystallinity is seen even at short residence times. Between T_c and T_m *(dissolution regime)*, crystalline content quickly falls below the LOD/LOQ with increasing residence time. Below the T_c *(suspension regime)*, crystalline content is seen in all samples, even at long residence times.

2.4.2.2 Imaging of Extrudates by PLM

Non-quantitative, polarized light microscopy was found to be highly sensitive for detection of residual crystals through their birefringent properties (representative images are found in Figure 2.4), even when XRPD suggested an amorphous sample. For samples prepared at 2 minutes of residence time, as the melt temperature was decreased, the level of birefringence increases significantly. As expected, the level of birefringence decreases for samples prepared at longer residence times at the same melt temperatures. Although several samples were identified as X-ray amorphous through the XRPD method, low levels of birefringence are noted in samples prepared at longer residence times and above the T_c (frames B, C, E, and F). Interestingly, a diffuse pattern of birefringence is seen in samples prepared at longer residence times (for example, frames C, E, F, and H), suggesting that the crystals are very small, relative to the optical microscopy detection

limit, possibly containing a high defect density, and well distributed in the samples. The PLM results show good agreement with the XRPD data, in that longer residence times and higher temperatures yield lower levels of residual crystallinity.

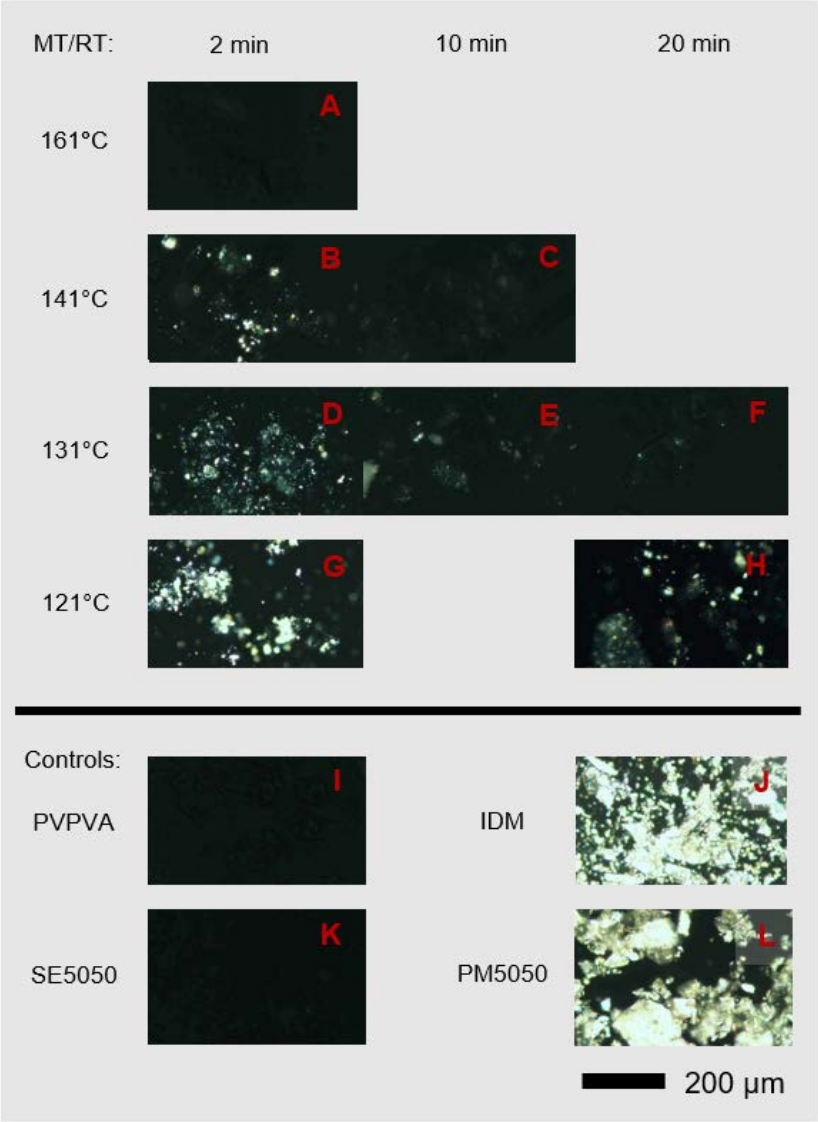

Figure 2.4. Polarized light micrographs of IDM:PVPVA ASDs (100-250 µm size fraction) prepared at operating melt temperatures 161°C (A), 141°C (B-C), 131°C (D-F), and 121°C (G-H). Controls shown include PVPVA (I), IDM (J), 1:1 IDM:PVPVA ASDs prepared by solvent evaporation (SE5050, K), and the 1:1 IDM:PVPVA physical mixture (PM5050, L). Birefringence indicates the presence of crystalline content. MT = melt temperature, RT = residence time.

2.4.2.3 Assessment of Crystalline Content by DSC

DSC was also used to provide a positive, but insensitive identification of crystalline content. The reversing and non-reversing heat flow of several HME ASDs, compared against the pure polymer (PVPVA), the physical mixture, and an ASD prepared by solvent evaporation are found in Appendix A Figure A.4. Above the polymer T_g, during the heating step, the drug crystals, if present, can dissolve into the molten polymer (just as in the melting point depression DSC method used to prepare the phase diagram). Depending on the quantity and characteristics of the crystals, this crystal dissolution endotherm may or may not be detectable. Only four HME batches, those prepared with short residence times (2 minutes) with temperatures at or below the T_c (131°C), had dissolution endotherms that were consistently detectable (greater than approximately 1.5 J/g). Process conditions consisting of higher temperatures and longer residence times provided more mixing and opportunity for crystal size reduction due to shear as well as further crystal dissolution, so all appeared "amorphous" by this technique, even when crystallinity was clearly seen with other techniques. This is because the crystals, although initially present, can dissolve into the molten matrix during the dynamic DSC test, so the method qualitatively and quantitatively under-predicts crystalline content, when compared with the XRPD method.

2.4.3 Crystal Dissolution in Polymer Visualized by Hot Stage Microscopy

The goal of this experiment was to simulate the temperature conditions of the HME process, as an alternate means of understanding the thermodynamic driving force for crystal dissolution into molten polymer. Since this experiment is diffusion-controlled (i.e., there is no mixing), the time to complete dissolution is over-predicted and the process might arrest due to kinetic hindrances (viscosity).

The time to complete dissolution (loss of birefringence) is shown in Figure 2.5a. Representative micrographs are shown of the dissolution process at temperatures above and below the predicted formulation critical temperature T_c (Figure 2.5b). In the sample held at the drug's melting point T_m (161°C), most of the drug had dissolved before the temperature setting was reached (the initial heating step was performed at 100°C/min). Thus, the drug melting was complete in under 30 seconds (Figure 2.5b, Panel A). Between the T_m and T_c, the dissolution process completed between approximately 3 minutes and 2 hours (Figure 2.5b, Panels B-D). In

this temperature range, dissolution is slower than the melting process as a result of decreased thermal input, increased matrix viscosity, and lack of external mixing, demonstrating the impact of kinetic factors on the crystal dissolution process. The extended time frame of these hot stage experiments compared to residence time in an extrusion experiment emphasizes the importance of mixing forces to decrease boundary layers on suspended drug particles to promote dissolution and homogenously distribute the drug and polymer, rather than reliance on diffusion only.

Below T_c, the crystal dissolution process did not complete for up to 8 hours of observation (Figure 5b, Panel E), based on residual birefringence, suggesting that the drug cannot be completely solubilized in the molten polymer at this temperature due to thermodynamic, rather than kinetic limitations. Complete loss of birefringence was observed between approximately 8-20 hours of extended monitoring, however the variation between samples indicates significant dependence on initial particle size, increasing melt viscosity, lack of mixing, and also on limitations introduced by the diffraction barrier.

The data is broadly consistent with the phase diagram generated using the melting point depression DSC method. Longer dissolution times are required as the temperature is reduced. However, a lower critical temperature is predicted with microscopy. This could be due to loss of crystallinity due to sample degradation due to long equilibration times at high temperatures, or a loss of ability to detect crystals less than approximately 600 nm in size. At shorter equilibration times (<2 hours), the critical temperature T_c of 131°C is confirmed.

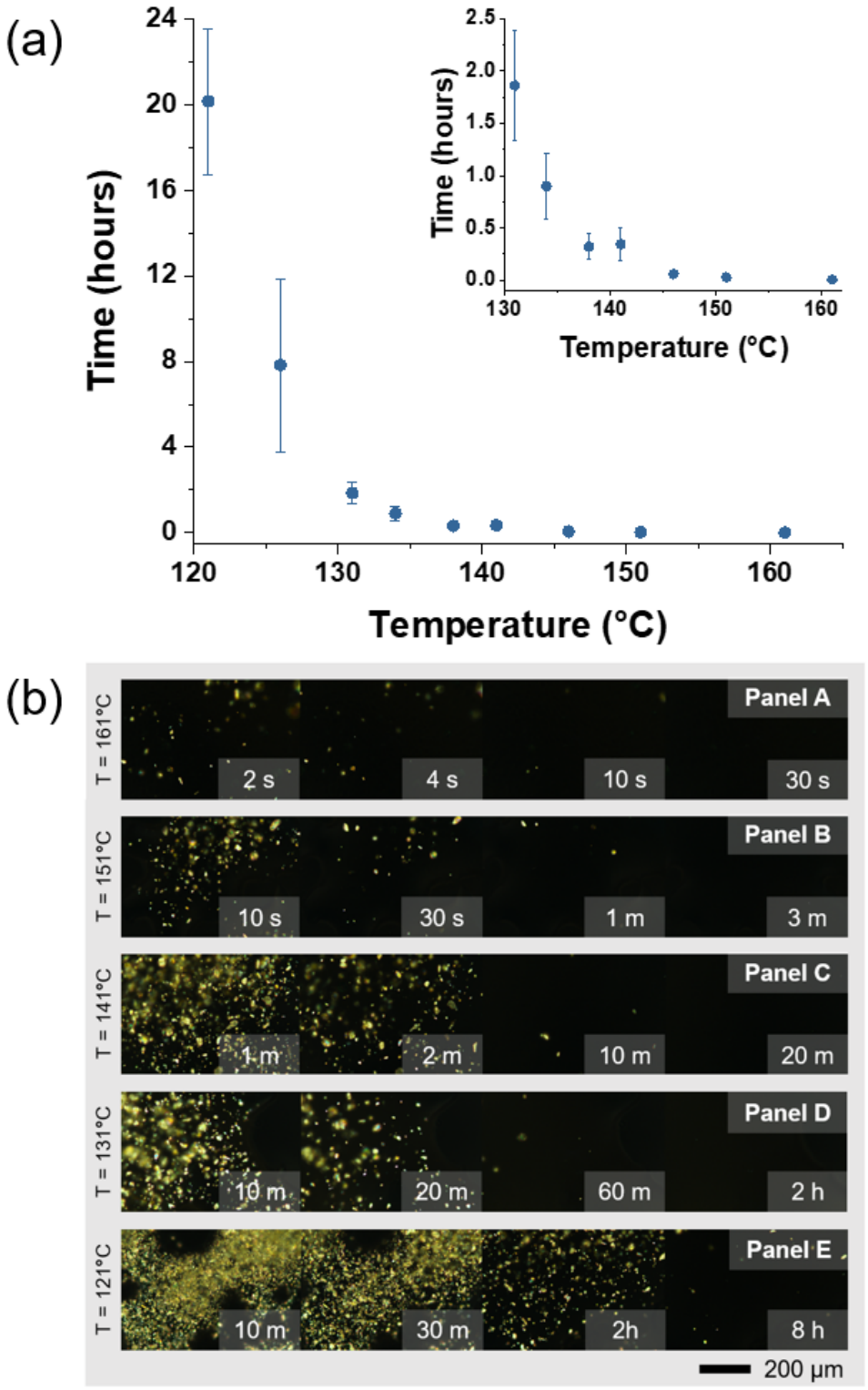

Figure 2.5. (a) Time at hot stage temperature until all crystalline content was dissolved (n=3). (b) Hot stage polarized light micrographs of 1:1 IDM:PVPVA over time at isothermal temperature settings 161°C (Panel A), 151°C (Panel B), 141°C (Panel C), 131°C (Panel D), and 121°C (Panel E). Birefringence indicates the presence of residual crystals. T = isothermal temperature setting.

2.5 Discussion

2.5.1 Application of the Temperature-Composition Phase Diagram to HME

The temperature-composition phase diagram (Figure 2.6a) can be applied to the HME process to understand the complex interplay between formulation, process, and performance. Although the phase diagram has been discussed in the framework of HME processing, little experimental validation of its applicability has been documented in the literature,[12,43,49,125,130,132] in particular to assess the risk of crystalline content that may remain if insufficient thermal or kinetic input are provided. The acceptable temperature design space is bounded by the thermal degradation region and solubility line. The polymer glass transition and minimum processing temperature is added as it provides a viscosity limitation to processing; most pharmaceutical polymers require a temperature of 15-60°C above T_g to be sufficiently molten for processing.[132]

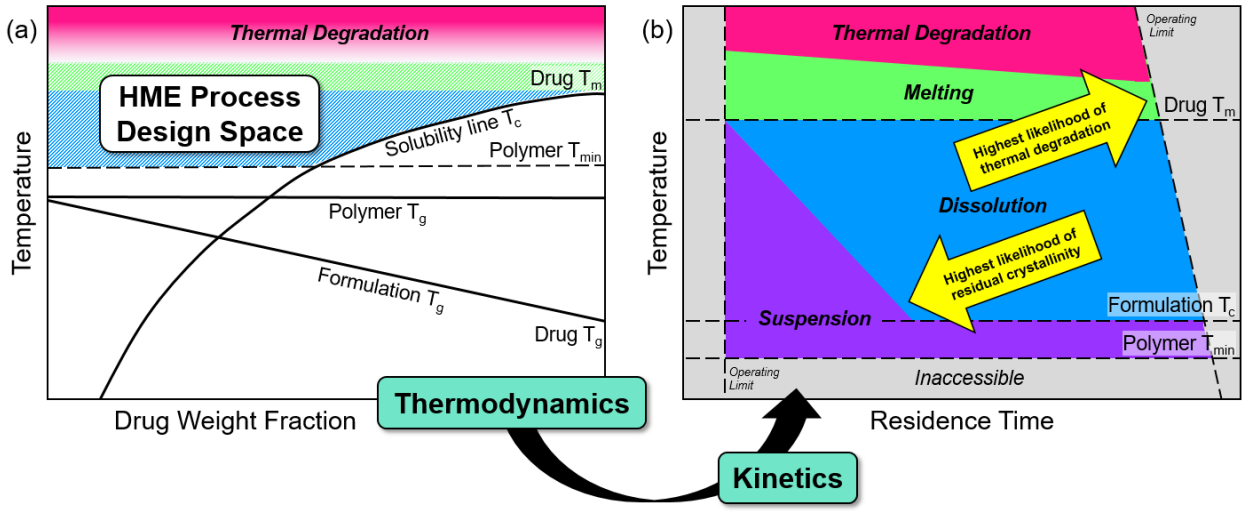

Figure 2.6. (a) The temperature-composition phase diagram as related to the hot melt extrusion process. The temperature design space falls below the thermal degradation temperature and, depending on composition, above the solubility line or polymer's minimum processing temperature T_{min}. Product phase behavior is governed by the solubility line (formulation T_c) and formulation glass transition T_g. (b) Hot melt extrusion process operating design space diagram. Three processing regimes (melting, dissolution, and suspension) can be delineated by temperature and kinetic considerations. Higher temperatures and longer residence times correspond to a greater risk of thermal degradation; lower temperatures and shorter residence times correspond to a greater risk of residual crystallinity.

The temperature-composition phase diagram shows the extent to which the drug's melting point is reduced by increasing amounts of polymer under equilibrium conditions. By exploiting

melting point depression of a miscible drug-polymer system, lower processing temperatures can be used to produce a homogenous, molecularly dispersed ASD, whereby processing conditions must be selected to satisfy both thermodynamic and kinetic criteria. Based on consideration of the phase diagram, residual crystalline content will be present if the processing temperature is lower than the critical temperature for a given composition. For miscible drug-polymer systems that interact strongly in the molten phase, melting point depression can be quite extensive.[66,68,75] For the IDM:PVPVA system investigated here, which has favorable specific interactions,[105] a substantial extent of melting point depression (30°C) was observed at the 50% drug loading level (Figure 2.2). In contrast, for drug-polymer systems with unfavorable interactions, melting point depression may be minor or non-existent, in particular at relatively high drug loadings.[75,77]

In the context of HME, the critical temperature T_c represents the minimum theoretical processing temperature (based on thermodynamic considerations) for a given composition where drug crystals can fully dissolve and mix with the polymer. This value provides the lowest possible bound of product melt temperature when designing an HME process to achieve a completely amorphous mixture, recognizing that the measured product or process set temperature may deviate from the actual temperature experienced by the melt, which in turn may vary in different regions of the extruder. Because kinetic factors are also important, sufficient time and appropriate mixing/mechanical conditions are also required for the crystal dissolution process to complete at the critical temperature.

When the solubility line crosses below the polymer's minimum processing temperature T_{min}, determined as the temperature above the polymer T_g where the polymer has softened to provide a sufficiently low viscosity to initiate the crystal dissolution process, this value now provides the lower bound for successful processing, provided this viscosity is also within the equipment operating limits. A viscosity range of 1000-10,000 Pa s is commonly cited,[81] though the precise viscosity range for successful processing may be formulation- and equipment-dependent. For neat PVPVA, this viscosity range provides an extrusion temperature window of 157-177°C.[81] For any given drug-polymer system, the minimum processing temperature may vary based on the extent of plasticization induced by the drug, but must always be above the polymer's glass transition T_g. Further, although the minimum processing temperature is depicted in the phase diagram as being constant (Figure 2.2, Figure 2.6), it may have compositional dependence based on viscosity (higher viscosities will be observed at lower drug loads). For the extruder and

formulation used in this study, a minimum processing temperature of 117°C was observed, as the matrix viscosity is quickly reduced as indomethacin dissolves into and plasticizes the polymer. For the IDM:PVPVA system, drug loadings below 50% would be governed by this T_{min} (or higher, as required to accommodate the increased viscosity associated with lower drug loadings) as the lower bound of melt temperature for successful processing.

The applicability of the phase diagram for understanding temperature regions where residual crystallinity can be minimized is clearly demonstrated in this study. Amorphous samples with a 50% drug loading were successfully prepared with temperatures at and above the formulation critical temperature T_c when given sufficient mixing/time to achieve equilibrium, convincingly demonstrating that melting point depression can be utilized to reduce processing temperatures. In contrast, residual crystalline content persisted in all samples prepared below the T_c, as insufficient thermal input was provided, whereby the drug content was higher than the solubility limit of the drug in the polymer at these temperatures.

2.5.2 HME Processing Regimes

Regime maps incorporate concepts described in the phase diagram in conjunction with kinetic considerations such as residence time, and can be used to further guide the acceptable process operating design space (Figure 2.6b). DiNunzio and coworkers have classified the acceptable temperature design space into two regimes: miscibility and solubilization.[49,50] Another classification approach uses six categories based on drug melting point, extent of melting point depression, and polymer viscosity, with the objective of guiding risk-based processing decisions.[43] Herein, our regime map builds on this past work and focuses on the thermodynamic and kinetic behavior of a miscible drug-polymer system to classify the design space into three regimes: melting, dissolution, and suspension. A primary focus of our regime map (Figure 2.7) is to describe the consequences of insufficient thermodynamic or kinetic input, namely that residual crystallinity will remain in both the dissolution and suspension regimes. The pure drug melting point T_m, formulation critical temperature T_c, and polymer's minimum processing temperature T_{min} form the major transition temperatures between processing regimes. For a given composition, the polymer T_{min} may be above the T_m or T_c, so this schematic serves to represent a system and drug loading where each of these temperatures are discrete and sufficiently separated.

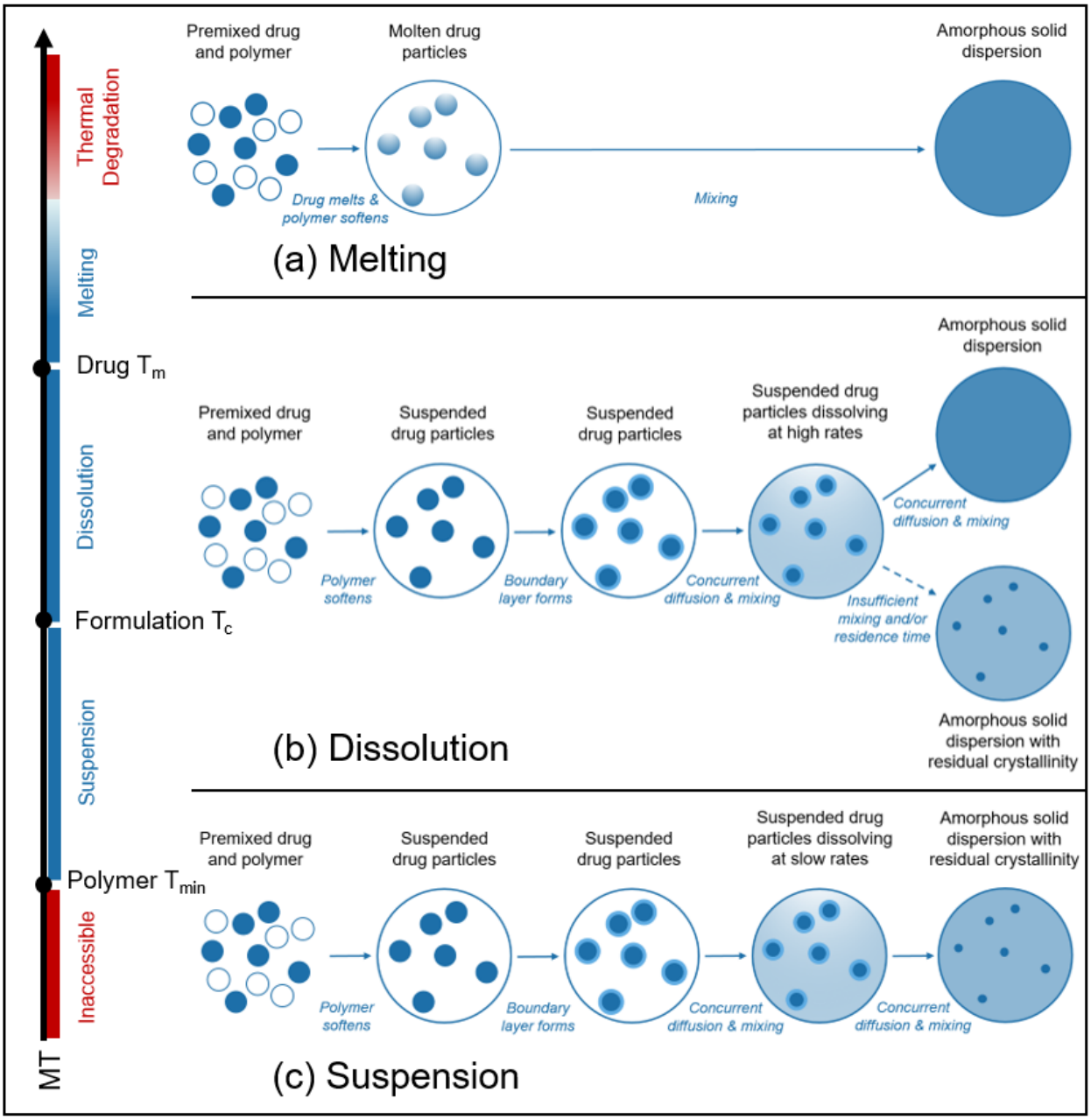

Figure 2.7. HME processing regime scenarios: (a) the melting (or liquid-liquid miscibility) regime occurs above drug T_m, (b) the dissolution (or solubilization) regime occurs between drug T_m and the formulation critical temperature T_c because of the melting point depression phenomenon, and (c) the suspension regime occurs below the formulation critical temperature T_c. In the melting and dissolution regimes, given sufficient mixing time and intensity, a homogenous molecular dispersion can be formed. In the dissolution or suspension regimes, the suspended drug particles may not fully dissolve due to insufficient process kinetics and/or the drug-polymer solubility limit. Blue represents drug, white represents polymer. T_m = drug melting point, T_c = formulation critical temperature, T_{min} = minimum processing temperature of the polymer, MT = melt temperature.

2.5.2.1 Melting Regime

As shown in Figure 2.7a, the melting (or miscibility) regime takes place above the melting point of the pure drug T_m; for indomethacin, this would correspond to temperatures above the melting point of the γ polymorph (161°C). Based on thermal input, both drug and polymer transform into the liquid state and undergo liquid-liquid mixing, assuming a miscible system. Then, given even a minimal amount of mechanical input, a homogenous system will be formed. Because melting is thermodynamically driven, given even a minimal amount of processing time, there is no risk of residual crystallinity, unless the drug recrystallizes during cooling due to insufficient stabilization by the polymer.

2.5.2.2 Dissolution Regime

As shown in Figure 2.7b, the dissolution (or solubilization) regime takes place between the pure drug melting point T_m and the formulation critical temperature T_c, because of the melting point depression phenomenon. For the 1:1 IDM:PVPVA system, this corresponds to product melt temperatures ranging from 131-161°C. A similar solution formation process was presented by Liu et al.[138] In this regime, the extrusion process begins with premixed drug and polymer, the polymer softens into a continuous liquid state with drug particles suspended. A dissolution boundary layer forms at the crystal-polymer interface, which drug molecules diffuse through into the melt. Similarly, heat transfer boundary layer will also exist. These boundary layers are reduced by mixing forces. Thus, the drug crystals decrease in size until all of the drug molecules are molecularly dispersed in the molten polymer. Contributions from dispersive mixing may also cause breakage if the drug particle encounters the impact zone of the mixing elements or if the shear stress exceeds the critical breakage stress of the drug particles. The dissolution regime does not exist for immiscible systems or for systems where the polymer's minimum processing temperature T_{min} is greater than the pure drug melting point T_m.

A homogenous molecular dispersion forms if the system achieves the thermodynamic solubility equilibrium. Hot melt extrusion, due to its continuous and finite nature, is inherently non-equilibrium. However, given the appropriate kinetic conditions, an HME process can approximate this equilibrium condition. In practice, this approximate equilibrium may be difficult

to attain based on the high matrix viscosity. The impact of kinetic factors on the crystal dissolution process can be understood using the Noyes-Whitney equation (Equation 4)

$$\frac{dC}{dt} = \frac{DA}{hV}\left(C_s - C\right) \tag{7}$$

where *dC/dt* is the change in concentration vs. time, *D* is the diffusion coefficient, *A* is the surface area available for dissolution, C_s is the solubility of the crystalline drug in the molten polymer, *C* is the concentration of the dissolved drug in the liquid phase at time *t*, *h* represents the boundary layer thickness at the solid-liquid interface, and *V* is the volume of the liquid phase. The diffusion coefficient will increase due to increased temperature or decreased viscosity. It should be noted that the viscosity of the liquid phase is not constant at a given temperature. As the drug dissolves, the viscosity typically decreases due to the plasticization effect of the drug on the polymer;[136] this is the case for the system studied herein. The use of higher screw speeds and shear will decrease the boundary layer thickness, facilitating dissolution and attainment of a homogenous molecular dispersion.

The particle size distribution provides a critical kinetic variable in a hot melt extrusion process.[126] Smaller particles will dissolve more quickly based on surface area considerations. In this work, the drug lot was used as-received; no particle size modification was performed, aside from sieving to remove very large agglomerates prior to preparing the physical mixture. Although the D_{50} was ~22 micron, many particles over 150 microns were present (data not shown). Because of a reduced surface area-to-volume ratio, these large particles require significantly more time to complete the dissolution process at a given temperature. These large particles are likely the primary reason trace crystallinity may be detected by polarized light microscopy at long residence times (Figure 2.4) at some processing temperatures. Thus, for a process designed with a specific size fraction, crystallinity may be detected when other lots are used which contain larger particles. Hence, it is critical to have particle size control over the starting drug material, to ensure a well-controlled manufacturing process.

Because processing in the dissolution regime is both thermodynamically and kinetically driven, the risk for residual crystallinity is controlled by selection of key process variables. Dissolution rate will depend on temperatures, residence time distribution, screw configuration and speed, relative particle sizes of polymer and drug, and drug-polymer miscibility.[11–13,83,126,132,138,139] The use of a robust screw configuration may be sufficient to overcome particle size and dissolution

rate limitations.[13,126] Vigorous mixing conditions are also an important prerequisite to formation of a homogenous molecular dispersion.[48,102] However, if the process is given insufficient mixing and/or residence time, residual crystalline content will be entrapped in the ASD matrix. Physical stability and/or solution dissolution performance may be compromised if residual crystallinity remains.[17,99,111,127] In order to set appropriate specifications, it is important that these consequences be understood for a given formulation.

2.5.2.3 Suspension Regime

As shown in Figure 2.7c, the suspension regime takes place below the formulation critical temperature T_c. For the IDM:PVPVA system studied herein, this corresponds to product melt temperatures below 131°C. In this temperature range, a completely amorphous dispersion cannot be achieved under any kinetic conditions. The scheme follows that of the dissolution regime, though the diffusion rates of the drug into the matrix would be considerably slower, and terminates with residual crystalline content.

2.5.3 Experimental Process Operating Design Space

The experimental process operating design space diagram for the 1:1 IDM:PVPVA system is shown in Figure 2.8. Herein, screw configuration and speed were held constant, a single drug lot was used, and a single composition was explored. Residence time was the primary kinetic variable used to demonstrate the impact of adequate mixing/time on the residual crystalline content of the extrudate. Residence times employed here are significantly longer than those found in typical continuous extrusion experiments, but serve to highlight the interplay between thermodynamic and kinetic factors on the crystal dissolution process.

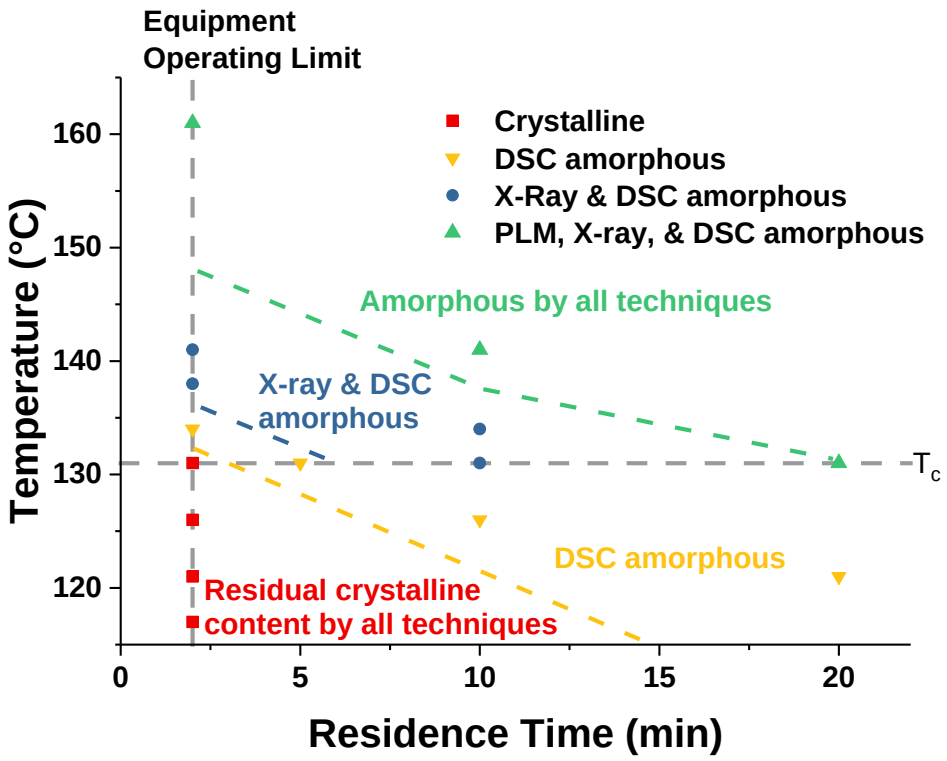

Figure 2.8. HME process operating design space of 1:1 IDM:PVPVA. Based on the sensitivity of the characterization technique, the sample can be classified as amorphous or crystalline. These classifications create zones where the samples can be considered amorphous. The transition between crystalline and amorphous zones are approximated between experimental data points.

Figure 2.8 shows the expected trends between temperature and residence time, with longer residence times being required to produce amorphous samples at lower temperatures. Thus, at a lower temperature (131°C), 20 minutes of residence time was required to generate a sample that was crystal-free, while at a higher temperature (141°C), only 10 minutes was required. However, thermodynamic factors are also highlighted, in that all samples produced below formulation critical temperature T_c show evidence of crystallinity, regardless of residence time.

Of particular note from Figure 2.8 is the dependence of the zone boundaries on the sensitivity of the measurement technique. As the ability of these techniques to detect residual crystallinity differs significantly, the processing zone boundary shifts within the operating space. In Figure 2.8, the placement of the zone boundary is approximated between the experimental data points. Similarly, zone boundaries could be defined by a single quantitative technique such as XRPD, so as to identify process conditions which yield residual crystallinity below certain levels

(e.g. <1%, <2%, <5%). Such an approach would be best done using modeling or statistical experimental design, such as Design of Experiments (DOE), in conjunction with experiments that demonstrate that these levels of crystallinity do not impact product performance.

Control of particle size, equipment configuration, and process parameters are assumed in such a diagram. While an as-received particle size distribution was used in this study, it must be stressed that the actual particle size distribution plays into the required residence time to transition from the residual crystalline to fully amorphous regions. If a smaller particle size distribution is used, the transition line would shift to the left (lower residence times would be adequate). A larger particle size distribution would cause the transition line to shift to the right, which would require potentially significantly longer residence times to complete the crystalline-to-amorphous transition. Changes to screw configuration or other process parameters similarly affect the location of the transition line, thus the complex interplay of these parameters must guide material and process specifications.

2.6 Conclusions

The temperature-composition phase diagram showing the extent of melting point depression of a drug by a polymer provides a rational framework for designing hot melt extrusion processes of amorphous solid dispersions to prevent residual crystalline content, delineating the minimum processing temperature based on thermodynamic considerations. This approach can be further refined by developing a process operating design space diagram which incorporates both thermodynamic and kinetic considerations, wherein processes using lower temperatures and shorter residence times are more susceptible to residual crystallinity. Accurate determination of the processing regime zone boundaries lessens the risk of residual crystallinity, and depends on the analytical approach employed.

The ICH Pharmaceutical Development Q8(R2) guideline states that studies should provide "scientific understanding to support the establishment of the design space, specifications, and manufacturing controls." This study clearly demonstrates that melting point depression can be effectively utilized as a risk-based process design strategy. The approach described thus provides a thermodynamic basis for hot melt extrusion product and process design as well as practical tools for formulation and process development.

CHAPTER 3. NANOMETER-SCALE RESIDUAL CRYSTALS IN A HOT MELT EXTRUDED AMORPHOUS SOLID DISPERSION: CHARACTERIZATION BY TRANSMISSION ELECTRON MICROSCOPY

This chapter is a reprint with minor modifications of a manuscript published in *Crystal Growth & Design* in October 2018 with the same title by: Dana E. Moseson, Naila A. Mugheirbi, Andrew A. Stewart, and Lynne S. Taylor. Reprinted with permission from American Chemical Society (ACS). DOI: 10.1021/acs.cgd.8b01435

3.1 Abstract

Common characterization techniques used to detect crystallinity in amorphous solid dispersions (ASD) typically have detection or quantification limits on the order of 1%. Herein, an amorphous solid dispersion of indomethacin and polyvinylpyrrolidone/vinyl acetate copolymer (PVPVA) produced by hot melt extrusion was determined to be amorphous by X-ray powder diffraction (XRPD) and differential scanning calorimetry (DSC). However, through the use of transmission electron microscopy (TEM), residual crystals of two populations were identified: single crystals mid-dissolution (<100 nm) and nanocrystalline domains of 5-10 nm in size. Both domain types were observed to contain a high defect density. Polarized light microscopy (PLM) and scanning electron microscopy (SEM) techniques supplement these findings by corroborating crystallinity. The use of high resolution analytical techniques to identify and characterize residual crystallinity is considered an important first step to understanding the significance of these residual crystalline populations to ASD performance attributes.

3.2 Introduction

Amorphous solid dispersions (ASDs) are an increasingly popular formulation strategy used to overcome poor aqueous solubility and slow dissolution of many drugs, improving bioavailability and therapeutic efficacy.[7,8] By crystalline-to-amorphous solid state transformation and subsequent stabilization by dispersion within an amorphous polymer, the solubility advantage of the amorphous form often can be realized.[30,93] Hot melt extrusion (HME) processes utilize thermal and mechanical input to form ASDs by melting and/or dissolving the drug into the molten polymer.[15] Given sufficient thermal input and mixing, a homogenous molecular dispersion should result free of residual crystallinity.[140] However, if the transformation is incomplete, residual crystalline content may contribute to potential stability or dissolution performance issues.[17,99,127]

X-ray powder diffraction (XRPD) is the gold standard technique for crystallinity detection and quantification in ASD formulations.[108] However, the technique is limited by mass fraction and dilution, crystal quality, as well as method parameters.[27,108,109] A complementary set of techniques would commonly be used to characterize a formulation, but have their own limitations which stem from properties of the instrument or sample. Polarized light microscopy (PLM) may be highly sensitive for detection of crystalline content, even when XRPD has determined a sample to be amorphous,[92] but this technique is limited by spatial resolution caused by the diffraction limitation. Differential scanning calorimetry (DSC) is limited by mass fraction, domain size, and the dynamic heating process.[65,140] Other studies have demonstrated that molecular-level differences in the amorphous phase can be identified by more sensitive techniques, such as Raman spectroscopy, even when XRPD and DSC have failed to identify these differences.[102,106]

The use of higher resolution analytical techniques may overcome some of these limitations in order to characterize residual crystalline content. Microscopy techniques such as transmission electron microscopy (TEM) have recently been found to be capable of detecting crystalline phases within ASDs.[103,141] Fast Fourier Transform (FFT) analysis reveals periodic structure within TEM images, which may or may not be clearly visible in image space. The Fourier space image will produce sharp spots at frequencies corresponding to the lattice periodicities within the image, which in turn enables crystallinity to be confirmed and domains spatially identified within the micrograph. The inherent challenge of TEM is in preparing an electron-transparent sample on the order of 100 nm in thickness; however the technique allows atomic distances to be visualized.[142,143]

Herein, an X-ray amorphous extrudate of a 1:1 blend of indomethacin (IDM) and polyvinylpyrrolidone/vinyl acetate copolymer (PVPVA) was prepared using HME processing conditions that correspond to the solubility temperature, i.e. the lowest temperature where a homogenous molecular dispersion could theoretically be prepared.[140] Under these conditions, there is a significant risk of residual crystallinity if insufficient time or mixing conditions are provided. By processing for a long residence time to account for the kinetics of drug crystal dissolution, the extrudate was found to be amorphous by XRPD and DSC. However, through the use of high resolution characterization techniques, namely transmission electron microscopy (TEM), evidence of nanometer-scale crystallinity was found.

3.3 Experimental

3.3.1 Materials

Indomethacin (IDM, T_m = 161°C) was obtained from ChemShuttle (Hayward, CA). Polyvinylpyrrolidone/vinyl acetate copolymer (PVPVA, Kollidon VA64, T_g = 104°C) was a gift from BASF (Florham Park, NJ).

3.3.2 Methods

3.3.2.1 Hot Melt Extrusion

An Xplore Pharma Melt Extruder (Geleen, The Netherlands), assembled with the 5 mL co-rotating conveying screw and barrel set, was used at a screw speed of 20 rpm to prepare an extrudate of a 1:1 IDM:PVPVA premix (water corrected weight ratio). A schematic of the extruder used in this study is found in Figure 3.1a, and the temperature and time process conditions used are shown in the process operating design space diagram Figure 3.1b). A water bath set to 10°C cooled the hopper, and the heating zone temperature was set to 134°C, resulting in a bulk product melt temperature of 131°C (as monitored by an in-line thermocouple located after the screw and prior to the recirculation channel or die). The recirculation valve was in the open position to extend the processing time; the valve was closed after 20 minutes to stop the recirculation and begin extruding the melt. The extrudate was allowed to cool at room temperature. A portion of the extrudate was cryomilled using a SPEX 6750 Freezer/Mill (Metuchen, NJ) for 60 seconds of grinding time at 10 Hz under liquid nitrogen to form a fine powder. Powders were then brought to

room temperature and sieved to achieve particle size fractions of 100-250 µm and <100 µm. Extrudates and powders were stored in a refrigerator under desiccant until analysis.

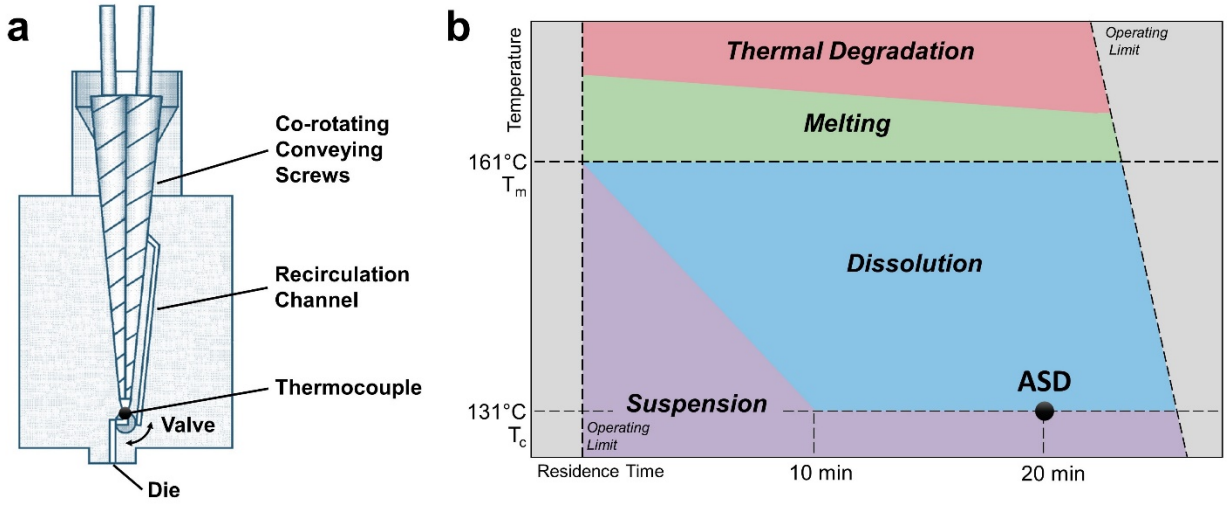

Figure 3.1. (a) Schematic of the hot melt extruder. (b) The process conditions of the IDM:PVPVA extrudate (ASD) are represented within a process operating space diagram, constructed based on the characterization of many samples found in our previous work.[140]

3.3.2.2 X-ray Powder Diffraction (XRPD)

X-ray powder diffraction (XRPD) patterns were collected using a Rigaku SmartLab diffractometer (Rigaku Americas, The Woodlands, Texas) in Bragg-Brentano mode with a Cu-Kα radiation source and a d/tex ultra detector. Using a glass sample holder, the patterns of the extrudate powder (100-250 µm size fraction) were obtained from 5-40° 2θ, using a step size of 0.02° and a scan rate of 0.5° per min. The limits of detection and quantification were found to be 0.4% and 1%, respectively.[140]

3.3.2.3 Differential Scanning Calorimetry (DSC)

A TA Q2000 differential scanning calorimeter equipped with a refrigerated cooling accessory (TA Instruments, New Castle, DE) purged with nitrogen at 50 mL/min was used to detect the T_g of the extrudate powder (<100 µm size fraction), as well as the constituent components. Each sample (3-5 mg, <100 µm size fraction) was loaded into a standard aluminum

pan and heated from 0-180°C at 5°C/min with modulation of ±0.796 every minute, then cooled to 0°C at 10°C/min, followed by a second heating ramp at 10°C/min.

3.3.2.4 Polarized Light Microscopy (PLM)

The 100-250 µm size fraction powder samples or indomethacin particles were loaded in mineral oil on a glass slide and visually observed for birefringence using a Nikon Eclipse E600 POL cross-polarized light microscope (20X objective) with Nikon DS-Ri2 camera (Melville, NY). At least 5 images were captured to characterize the sample.

3.3.2.5 Transmission Electron Microscopy (TEM)

Small pieces of the extrudate or indomethacin particles were sprinkled on a 300 mesh carbon-coated copper TEM grids with 5-6 nm standard thickness (SPI supplies, West Chester, PA). Extrudate pieces were placed on the TEM grid by gently touching/wiping the interior of the vial lid, which contained particulates fragmented from the bulk extrudate rods, with the carbon-coated side of the grid.

Bright-field transmission electron micrographs were acquired in an FEI Tecnai G20 electron microscope (FEI, Hillsboro, Oregon, USA) equipped with a LaB6 source, X-max 80 mm^2 silicon drift detector (Oxford Instruments, Abingdon, Oxfordshire, UK), and operated at 200 keV, 100 µm aperture, and a spot size of 1 (drug crystal images) or 3 (extrudate images). At least three grid squares were analyzed to identify particles that were suitably electron transparent for imaging.

Fast Fourier Transform (FFT) analysis was performed using the Gatan DigitalMicrograph 3.21 software suite (Pleasanton, CA). Fourier filtering was applied using a spot mask symmetric about the origin of the FFT image, which selects only the desired frequencies (in reciprocal space). By then performing an inverse FFT on the masked image, the filtered image is reconstructed (in real space) which reveals only the periodic content associated with the specific FFT spot pair. ImageJ 1.51 (National Institutes of Health, Bethesda, MD) was used to apply false color imaging.

3.3.2.6 Scanning Electron Microscopy

Indomethacin particles or a cross section of the extrudate were fixed on a SEM stub using double sided carbon tape, sputter-coated with platinum target for 60 seconds and examined with a

FEI Nova nanoSEM field emission scanning electron microscope (FEI Company, Hillsboro, Oregon) operating at a 5 kV accelerating voltage, ~5 mm working distance, and a spot size of 3. High resolution through-the-lens detector (TLD) and Everhart Thornley detector (ETD) were used to image the extrudate and indomethacin particles, respectively.

3.4 Results and Discussion

3.4.1 Characterization of Indomethacin Crystals

The IDM starting material was primarily composed of plate-like particles (Figure 3.2a,b), which consist of single crystals coated with smaller crystals as observed by extinguishing birefringence during rotation under polarized light (Figure 3.2a). The crystal lattice planes seen by TEM (Figure 3.2c-e) show microstructure consistent with crystals in a variety of orientations, consistent with the observations from SEM and PLM, where small crystals are agglomerated or electrostatically affixed to the surface of larger crystals, and surface imperfections are evident.

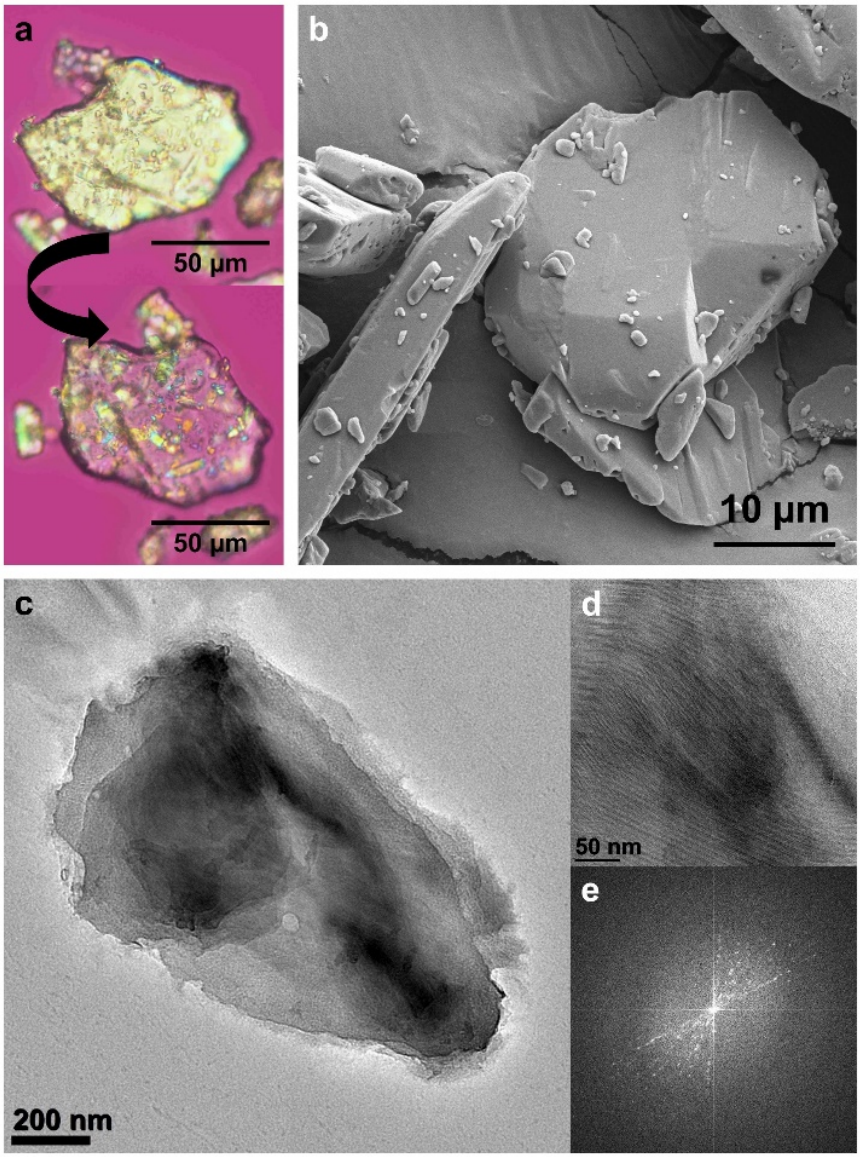

Figure 3.2. (a) Polarized light microscopy images of an IDM crystal, demonstrating extinguishing birefringence upon rotation. (b) Scanning electron microscopy (SEM) image of the IDM particles. (c) BF TE micrograph of an IDM particle. (d, e) BF TE micrograph of the crystalline microstructure and corresponding FFT pattern.

3.4.2 Sample Preparation & Characterization

By applying high temperatures and mixing in an HME process, crystalline drug particles melt and/or dissolve into the molten polymer. Based on the temperature-composition phase diagram constructed previously,[140] processing conditions used to prepare the IDM:PVPVA extrudate were expected to generate a fully amorphous system. As shown in the process operating design space diagram (Figure 3.1b), within the dissolution regime, the crystalline drug can be fully solubilized at or above the formulation critical temperature T_c (131°C), given sufficient mixing and residence time. Samples prepared at this lower bound of processing temperature have the greatest risk of residual crystalline content, because drug crystal dissolution into a polymer melt is both a thermodynamically and kinetically driven process.

An ASD prepared at the formulation critical temperature T_c (131°C) with 10 minutes of residence time was found to be X-ray amorphous, but had some birefringence detected using PLM. Hence, for TEM studies, the processing time was extended to 20 minutes. This extended processing time was selected to achieve complete dissolution of any residual crystals that may have been present after 10 minutes of processing time (below the XRPD limit of detection, 0.4%, but visible by PLM). Characterization by common analytical tools supported this supposition: no evidence of crystallinity is seen by XRPD (Figure 3.3), a single composite glass transition T_g is observed by DSC (Figure 3.3b), trace or no birefringence is seen by PLM (Figure 3.3c), and the extrudate is clear by visual assessment (Figure 3.3d).

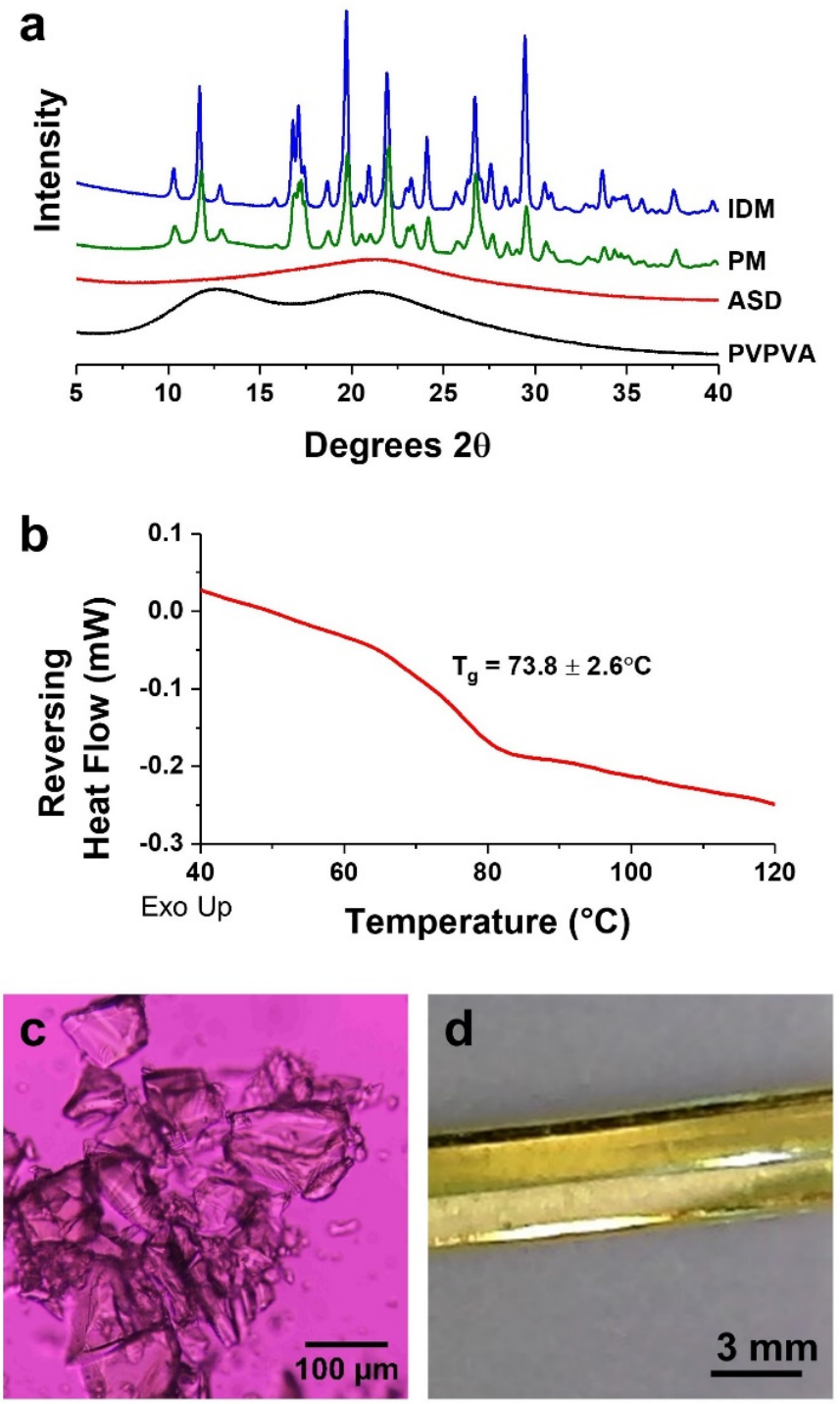

Figure 3.3. Characterization of the IDM:PVPVA extrudate (ASD). (a) X-ray powder diffraction patterns of PVPVA, ASD, physical mixture (PM), and pure IDM. The halo pattern of the ASD pattern indicates the sample is amorphous. (b) Reversing heat flow DSC thermogram of 1:1 IDM:PVPVA showing a single T_g. (c) Polarized light micrograph of 1:1 IDM:PVPVA. Trace birefringence is observed in some images. (d) The 1:1 IDM:PVPVA extrudate appears clear, indicating the sample is amorphous.

3.4.3 Extrudate Characterization by Transmission Electron Microscopy

Multiple particles of the ASD extrudate were imaged using transmission electron microscopy (TEM), and both amorphous and crystalline domains were detected within (Figures 3.4-3.6). Amorphous domains appear as a homogenous continuous phase, while evidence of crystallinity include darker areas within the matrix, diffraction contrast, and lattice planes.[103,141,144] Each of these particles show broadly consistent, yet unique morphology. In particular, highly defective nanometer-scale crystallites of two populations are identified. First, discrete crystals (<100 nm) are observed mid-dissolution. Second, nanocrystalline domains of approximately 5-10 nm in size, commonly in clusters, are observed. When observing small crystalline phases, it is often difficult to confirm the crystallinity by FFT, for a variety of reasons: the crystal orientation may have frequencies beyond those which can be recorded in the image, the specimen thickness may vary causing some areas to be too thick to record a lattice image, the sub-surface placement of the crystal within the particle obscures the lattice, the remaining degree of order in the domain, and the interference of the drug-polymer amorphous matrix.

The ASD particle shown in Figure 3.4a shows evidence of amorphous material and both populations of crystalline domains. The population of nanocrystalline domains is shown in Figure 3.4b. The FFT pattern (inset) confirms that many of the domains in this region are crystalline. The domains are clustered within the particle, suggesting that these domains originated from the same crystal and have not yet distributed and dissolved into the matrix. The domains in this image are 5.8 ± 1.2 nm in size (± SD, n = 20), and are randomly oriented, as demonstrated in the FFT. The random orientation, similarity of domain size, and clustering suggests a mechanical origin of these crystals.

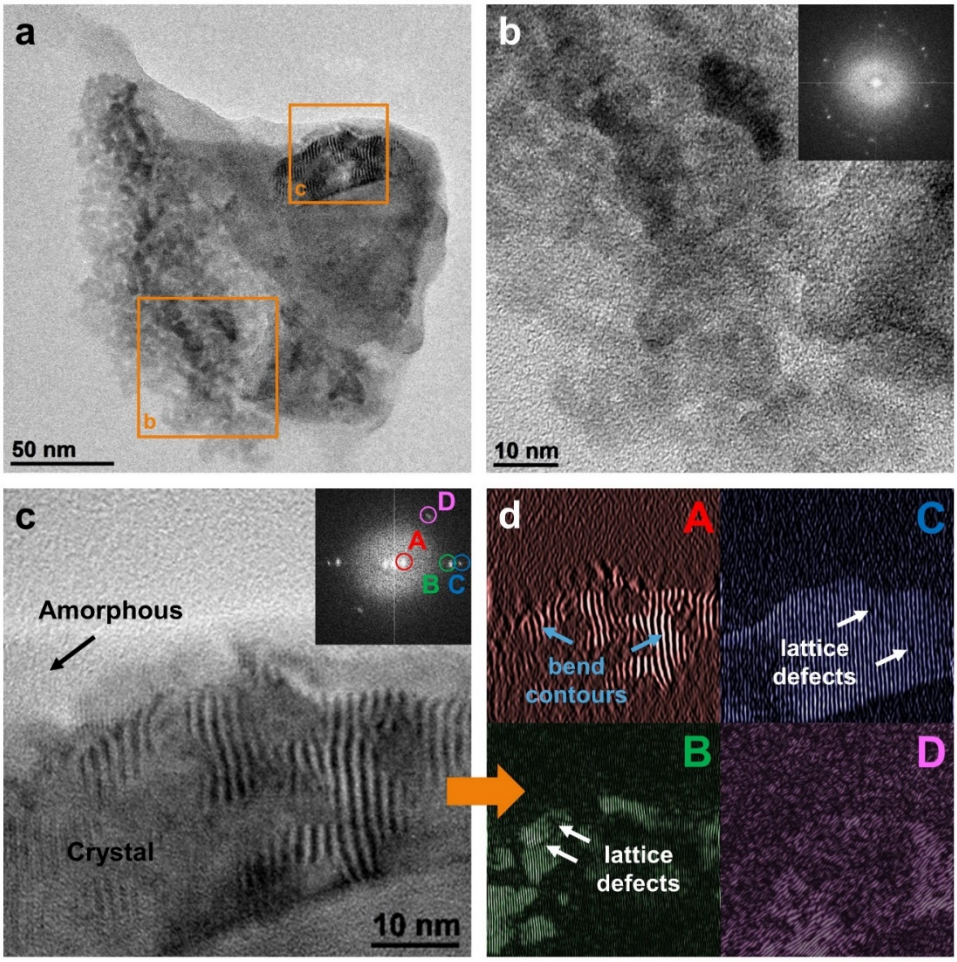

Figure 3.4. (a) BF TE micrograph of an ASD particle with residual crystallinity. (b) BF TE micrograph of the nanocrystalline domains and corresponding FFT pattern (inset). (c) BF TE micrograph of the ~ 26x70 nm discrete crystal and corresponding FFT pattern (inset). (d) Reconstructed BF TE micrographs from the inset of (C) generated using the Inverse FFT function in the Gatan Suite. Each of the areas A-D are colorized to indicate the location where those patterns appear in the original image (c). Bend contours in A are highlighted by blue arrows; lattice defects, such as edge dislocations, are highlighted by white arrows.

A closer view of a discrete 26x70 nm crystal from this ASD particle is shown in Figure 3.4c, which clearly shows both amorphous and crystalline regions (confirmed by the FFT pattern inset). By applying an inverse FFT to each of these spots, the image can be reconstructed to show only the areas producing that order (Figure 3.4d: A-D). The lattice planes, now individually visualized, show dislocations and different degrees of thermally- and/or mechanically-induced structural deformation. The dark interference fringes seen in Figure 3.4d panel A are bend contours, which indicate curvature of the crystal arising due to strain at the interface of the crystal.[145,146] We

hypothesize that this crystal, while defective, is still a single crystal. The reconstructed images Figure 3.4d panels C and D are two lattice planes of the crystal and are found in almost the entire area of the crystal shape, while the planes found in Figure 3.4d panels A and B (if superimposed) form a third, in-focus lattice plane.

Another ASD particle (Figure 3.5a) primarily contains areas that resemble crystalline domains, based on the appearance of the internal structure. A representative region is shown in Figure 3.5b. This partially crystalline area (also seen in the reconstructed false color images found in Figure 3.5c panels A-C) highlights a single lattice spacing in multiple orientations. This suggests that the crystal planes have been sheared with rotation in three distinct orientations. Each plane has a different level of dissolution, most clearly observed in Figure 3.5c panel C.

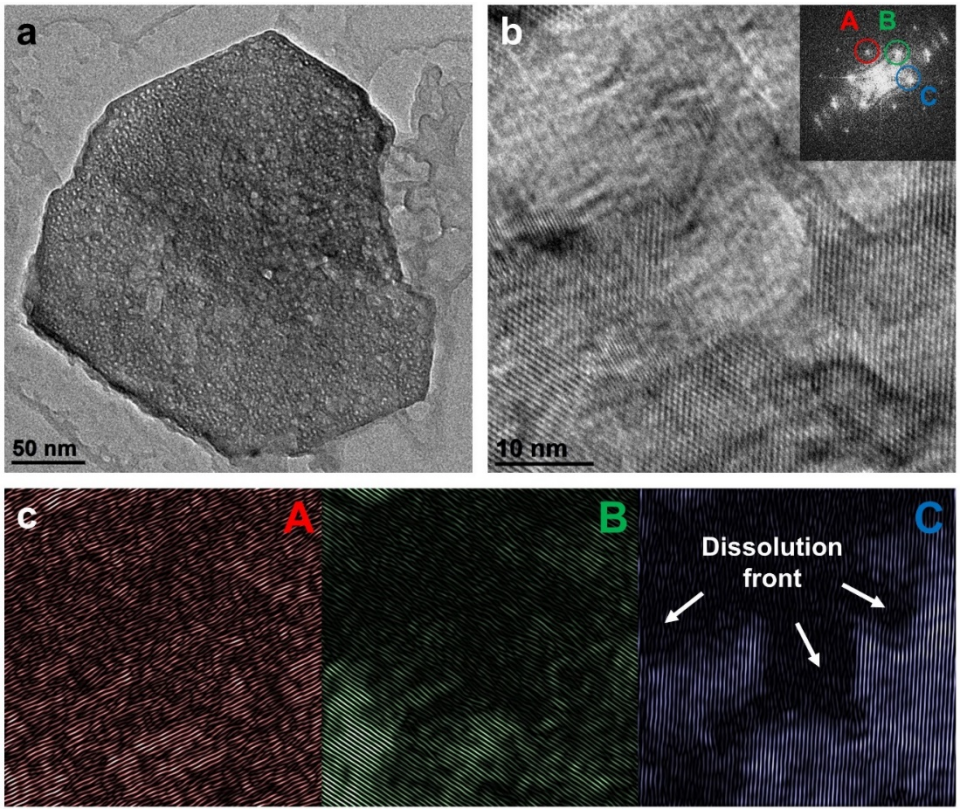

Figure 3.5. (a) TEM image of an ASD particle with residual crystallinity. (b) Representative region of the particle and corresponding FFT pattern (inset). (c) Inverse FFTs of areas A-C colorized to indicate the location where those patterns appear in the original image. The dissolution front is most apparent in C, highlighted by white arrows.

The ASD particle shown in Figure 3.6a is also composed of amorphous and crystalline domains. Channels of amorphous material are observed, where polymer appears to have advanced into the crystalline regions. We hypothesize that the remaining crystalline domains in this particle may have originated from a discrete crystal, now segregated into smaller and partially dissolved domains. The appearance of the bend contours in Figure 3.6b are likely a result of crystal edges formed by dissolution of the crystal and strain at the interface with the amorphous matrix. Figure 3.6c shows a larger crystal with similar bend contours, which are highlighted in the false color reconstructions (Figure 3.6d).

Figure 3.6e contains both single crystals (orange circles) and nanocrystalline domains (yellow circles). The nanocrystalline domains in this region of the particle are more dispersed than those seen in Figure 3.4b, suggesting that, if also formed by the mechanical breakage mechanism, more time has elapsed since the event allowing the nanocrystals to further dissolve or distribute into the surrounding amorphous matrix. In the lower right of the Figure 3.6e, the orientation of the ~60 nm crystal (also seen in the false color reconstructed image found in Figure 3.6f panel B) highlights a single lattice spacing in multiple orientations, suggesting that the crystal planes have been sheared with rotation in multiple orientations. Bend contours are also seen on one edge of the crystal, suggesting strain and deformation at the interface (this crystal edge is also seen in the false color reconstructed image found in Figure 3.6f panel C).

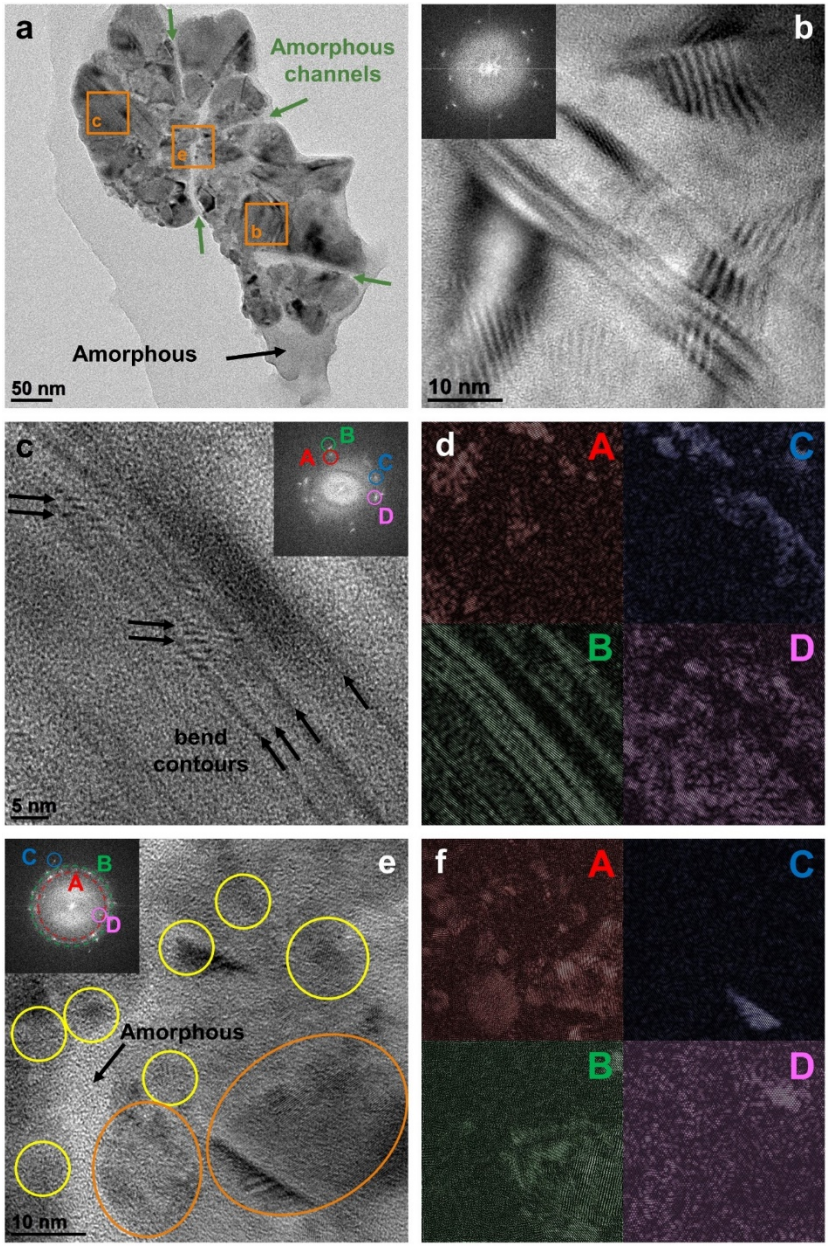

Figure 3.6. (a) BF TE micrograph of an ASD particle with residual crystallinity. Amorphous channels show areas of advancing polymer content. (b) Discrete crystal with bend contours and corresponding FFT pattern (inset). (c) BF TE micrograph of multiple crystals showing strain at the interface. (d) Reconstructed BF TE micrographs from the inset of (c) generated using the Inverse FFT function in the Gatan Suite. Each of the areas A-D are colorized to indicate the location where those patterns appear in the original image (c). (e) BF TE micrograph showing multiple crystals and corresponding FFT pattern (inset). Domains in the 5-10 nm range are highlighted with yellow circles, and larger crystals are highlighted with orange circles. (f) Reconstructed BF TE micrographs from the inset of (e) generated using the Inverse FFT function in the Gatan Suite. Each of the areas A-D are colorized to indicate the location where those patterns appear in the original image (e).

3.4.4 Extrudate Characterization by Scanning Electron Microscopy

The interior of the extrudate rod was imaged for evidence of crystallinity (Figure 3.7) using scanning electron microscopy (SEM). Some regions of the extrudate appear fully amorphous (Figure 3.7a), as no clear features appear on the surface. Some regions have embedded crystals in the size range of 10-1000 nm (Figure 3.7b, c). Due to the resolution capability of the instrument, domains smaller than 10 nm could not be imaged.

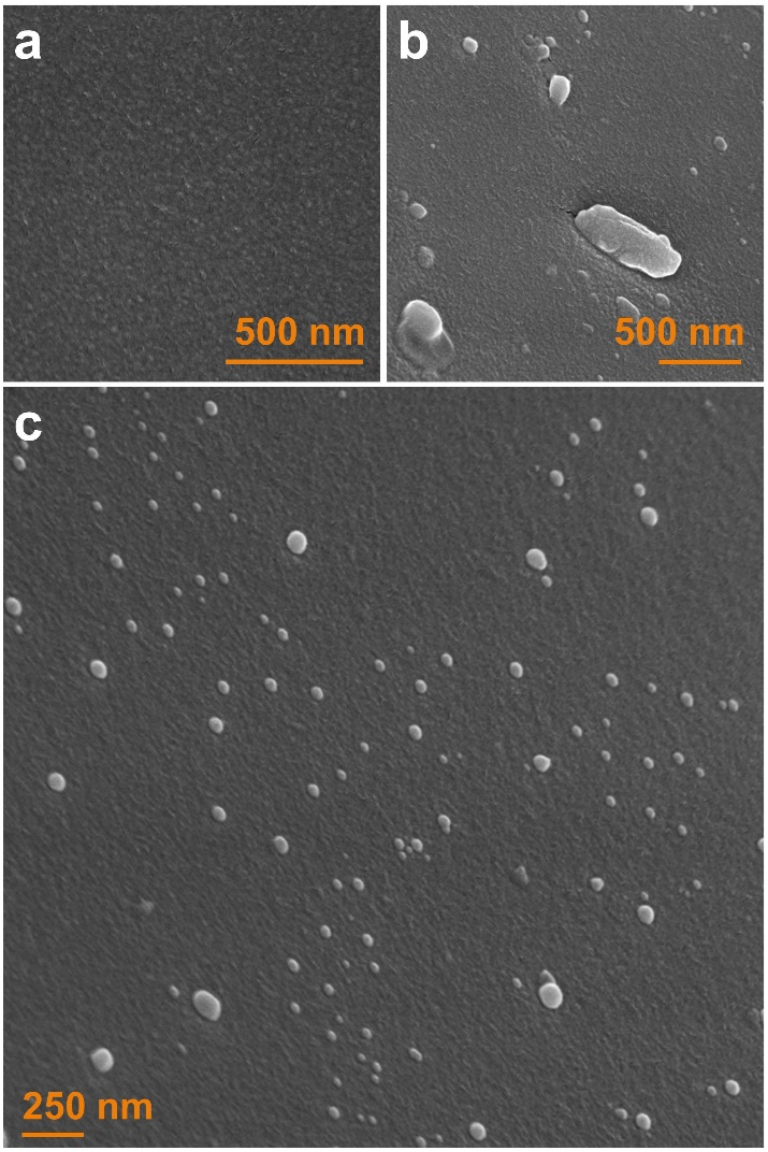

Figure 3.7. Scanning electron microscopy (SEM) images of the ASD extrudate. Some regions appear fully amorphous (a), or contain crystalline domains between 10-1000 nm (b, c). The length distribution of the domains found in (c) were measured as 38 ± 18 nm (± SD, n=100).

3.4.5 Comparison with X-ray Powder Diffraction

Ricarte et al. found that TEM was capable of detecting crystals in an X-ray amorphous physical mixture consisting of 3% crystalline drug,[141] while a much greater degree of sensitivity was found in this analysis. There are many underlying reasons for the sensitivity limitations of X-ray diffraction. Because of the dilution of drug by the polymer in an ASD, crystallinity detection becomes more challenging because of the resulting reduction in signal intensity associated with the crystalline peaks.[109,147] As crystallite size decreases, particularly into the nanometer range, peak broadening may limit detection of otherwise perfect crystals imbedded in an amorphous matrix.[148] Other sources of strain may influence peak detection, such as dislocations, stacking faults, and grain boundaries.[149] In the ASD sample characterized here, as well as many samples in our previous work and others in the literature,[138,140] crystalline content, as quantified by XRPD, may be systematically underestimated based on these factors.

3.4.6 Crystal Dissolution Initiated from Defect Sites

As the starting material of drug crystals is likely to contain imperfections and local disorder at the surface and in the bulk of the crystal,[150,151] these defects are the likely sites for initiation of phase transformation due to thermal or mechanical stresses because of higher overall free energy resulting from the presence of mixed amorphous and crystalline phases. Chemical and thermal etching studies that have demonstrated that dissolution is initiated at defect sites[152,153] and that dissolution rate correlates to defect density.[154] Furthermore, contributions from the crystal structure, solvent-solid interactions, and the adsorption of the solvent molecule onto the crystal surface have been found to influence the dissolution mechanism at the crystal surface.[155,156] The highly defective nanocrystalline domains imaged in this extrudate suggest that defects, both those intrinsic to the crystals and those formed by mechanical damage, propagate as the crystals dissolve into the amorphous matrix, resulting in size reduction of crystals both through dissolution of external crystal surfaces as well as through fragmentation. Thus, due to HME processing under high temperature and shear, loss of crystallinity (i.e. increase in crystal defects) is expected, as an intermediate stage of the crystalline-to-amorphous transformation by mechanical damage and dissolution into the molten polymer.

3.5 Conclusions

Low levels of nanometer-scale residual crystals within a nominally amorphous drug-polymer dispersion prepared by hot melt extrusion were detected by transmission electron microscopy. This technique provided a high degree of sensitivity for the identification and microstructural characterization of two populations of nanocrystalline domains: single crystals <100 nm and clusters of 5-10 nm in size. The residual crystals show little similarity to the bulk crystalline starting material, as a result of thermally- and/or mechanically-induced structural deformation and dissolution into the amorphous matrix.

An open question remains whether or not any level, critical crystal size, or characteristic of residual crystals may be acceptable within ASDs, without causing detrimental stability or dissolution effects. The poor ability of common techniques to detect low levels of crystalline content contributes to the difficulty in addressing this question. The use of high resolution analytical techniques such as transmission electron microscopy to identify and characterize residual crystallinity is considered an important first step to understanding the significance of these residual crystalline populations to ASD performance attributes.

CHAPTER 4. DISSOLUTION OF INDOMETHACIN CRYSTALS INTO A POLYMER MELT: ROLE OF DIFFUSION AND FRAGMENTATION

This chapter is a reprint with minor modifications of a manuscript published in *Crystal Growth & Design* in April 2019 with the same title by: Dana E. Moseson, Andrew S. Parker, Christopher J. Gilpin, Andrew A. Stewart, Stephen P. Beaudoin, and Lynne S. Taylor. Reprinted with permission from American Chemical Society (ACS). DOI: 10.1021/acs.cgd.9b00200.

4.1 Abstract

The dissolution or melting of a crystalline drug into a molten polymeric matrix underpins the fabrication of a number of drug delivery systems. However, little is known about how crystals dissolve in such viscous matrices. Herein, the heat-induced dissolution of indomethacin crystals into a molten polymer, copovidone, was evaluated, probing changes in crystal features at multiple length scales using various microscopy techniques. Diffusion of the drug into the polymer film was observed by elemental composition analysis (scanning electron microscopy with energy-dispersive X-ray analysis). Under polarized light microscopy, irregular dissolution patterns were observed, in which channels and holes were seen forming in the crystals, which then resulted in fragmentation. At shorter length scales by scanning and transmission electron microscopy (SEM and TEM), crystals demonstrated a range of channel formation and fragmentation behaviors. Defect sites intrinsic to the bulk crystals were hypothesized to be the origin of the dissolution-induced fragmentation process. A defect site-driven dissolution and fragmentation model was thus proposed. A Monte Carlo simulation of crystal dissolution under a range of surface energy configurations is also presented. This study has implications for modeling and understanding of dissolution kinetics and pathways of organic crystals in the context of processing operations such as hot melt extrusion.

4.2 Introduction

Crystal dissolution is a fundamentally important process, but is typically studied only by evaluating the rate of appearance of molecules in the solution phase,[157] with little attention paid to the evolving structure of the dissolving crystal.[158,159] This oversight potentially leads to erroneous conclusions about dissolution mechanisms and the implementation of theoretical models that do not appropriately capture dissolution kinetics. In comparison to the body of experimental and theoretical data on crystal growth,[160,161] crystal dissolution kinetics and mechanisms are less well understood.[162,163]

One area where dissolution mechanisms have received little attention is the dissolution of organic crystals into polymers. Polymers are used as functional excipients in pharmaceutical formulations ranging from controlled release delivery systems,[164–166] mucoadhesives,[167,168] nanosuspensions/nanoparticles,[169–171] biopharmaceuticals,[172] transdermal systems,[173] and solid dispersions.[18,174–176] Thermal-based processing, such as hot melt extrusion (HME), has been used manufacture drug-polymer systems for a wide range of formulation applications, including controlled release,[177–179] taste masking,[180] implants,[181,182] and solubility enhancement.[8,183]

The dissolution of crystals into polymers is particularly relevant for hot melt extrusion processing to produce amorphous solid dispersion (ASD) drug formulations.[126,138,140] Amorphous systems are of great interest as a formulation strategy to address low drug solubility.[5,184,185] By dispersing the drug within an amorphous polymer to produce a single phase amorphous blend, a system kinetically stable against crystallization can be produced.[18,19,102] During hot melt extrusion processing, the goal is to transform a powder blend of crystalline drug and amorphous polymer into a single phase, homogenous melt using thermal and mechanical input.[15,36] If performed above the drug's melting point, the transformation can be described as melting, followed by mixing of liquid drug and polymer. If performed below the drug's melting point, the polymer can act as a solvent, allowing the drug to dissolve into the highly viscous matrix.[140] The dissolution process of crystalline drug into polymer melt has been mathematically described by the Noyes-Whitney equation, where dissolution is governed by crystal surface area, solute diffusivity, and solubility.[125,138,140,186] This, however, neglects contributions from drug crystal properties (e.g. defects) or contributions from the mechanical process (e.g. crystal breakage) on the dissolution rate. Despite the practical relevance to the formation of ASDs through the HME process, there is a lack of knowledge around the mechanism of crystal dissolution into polymer melts.

Imperfections and local disorder at crystal surfaces and in the bulk are common in organic crystals, originating during crystallization or other downstream processing operations.[150,151,187,188] Such defects, in the form of vacancies, impurities, dislocations, and grain boundaries, are sites of higher energy and greater molecular mobility, and may contribute to the initiation of physical or chemical transformations, such as melting, solubilization, polymorphic transitions, or mechanical failure.[151] Crystal defects have been linked to increased dissolution rates.[152–154,189] Local stress fields in solids result from virtually all types of reactions, and therefore have important chemical and physical consequences.[190–192] Defects have also been shown to impart localized stress, helping to explain their role in enhancing dissolution rates and facilitating physical or chemical transformations.[193] Crystal faces are known to dissolve at different rates in aqueous solution,[158,159] although most dissolution models typically assume a spherical particle shape.[194–197] Various efforts to study crystallization using Monte Carlo simulations have also revealed the potential for imperfections through the course of crystallization in the form of surface roughening of growing crystal faces.[198,199] These imperfect surfaces are known to exhibit a greater surface energy than their smooth counterparts, as well as heterogeneities in surface energy distribution.[200–202] Monte Carlo simulations have also been used to simulate the statistical processes associated with dissolution of minerals and amorphous solids, highlighting etch pit formation and irregular dissolution associated with defects and surface heterogeneities.[203–206]

Recently, we reported the existence of nanometer-scale residual crystals within a nominally crystal-free hot melt extruded amorphous solid dispersion.[207] These residual crystals were found to contain a range of defects, which we hypothesized had both intrinsic and mechanical origins. Additionally, preliminary evidence of a fragmentation-based dissolution mechanism was observed; however, given the high mechanical input of the HME process, other explanations are also possible. The goal of this study was to explore the dissolution of drug crystals into molten polymer under quiescent conditions, to better understand the crystal-to-solution transformation in the absence of mechanical input, addressing the hypothesis that crystal fragmentation occurs in addition to diffusion-based crystal shrinkage. Copovidone films with suspended indomethacin crystals were heated under quiescent isothermal conditions, at a temperature below the drug's melting point, to initiate the crystal dissolution process. By monitoring changes under multiple length scales, effects of crystal properties and microstructure on the dissolution mechanism were captured. A Monte Carlo simulation of crystal dissolution under a range of surface energy configurations is also

presented. We believe this study is the first to investigate the mechanism of crystal dissolution into a polymer melt and to report a fragmentation-based microstructural progression.

4.3 Experimental Section

4.4 Materials

Indomethacin (IDM, T_m = 161°C) was obtained from ChemShuttle (Hayward, CA). Copovidone (polyvinylpyrrolidone/vinyl acetate copolymer, Kollidon VA64, T_g = 104°C) was a gift from BASF (Florham Park, NJ). Chemical structures and elemental composition are provided in Figure 4.1a. Relative elemental composition refers to the calculated atomic % of the overall composition without hydrogen. The IDM powder has a particle size D50 of 21.9 ± 0.3 μm (Figure 4.1b), determined in triplicate using a Malvern Mastersizer 3000 particle size analyzer with Aero S attachment (Worcestershire, UK).

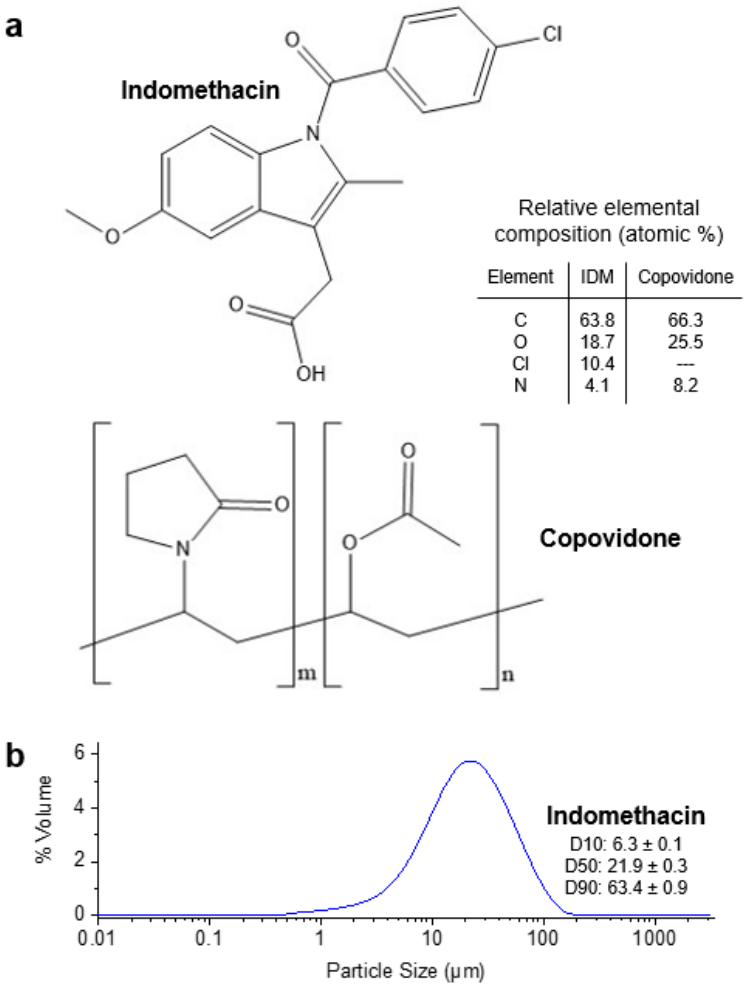

Figure 4.1. (a) Chemical structures and relative elemental composition of indomethacin and copovidone. (b) Particle size distribution of indomethacin crystals.

4.5 Experimental Methods

4.5.1 X-Ray Diffraction (XRD)

Films composed of copovidone and suspended indomethacin (IDM) crystals (5:1 ratio) were deposited from water onto a zero background silicon sample plate. X-ray diffraction patterns were recorded using a Panalytical Empyrean diffractometer (Malvern, United Kingdom) with a Cu-kα radiation source and PIXcel3D detector equipped with an Anton Paar HTK 1200N high temperature chamber (Graz, Austria). Prior to heating, an ambient scan of the film was collected. After heating to 130°C over approximately 10 minutes, patterns were obtained from 10-30° 2θ over 15 minutes and monitored up to 3 hours.

4.5.2 Polarized Light Microscopy (PLM)

Films composed of copovidone and suspended indomethacin (IDM) crystals (5:1 ratio) were deposited from water onto glass slides. Films were held at 130°C for up to 3 hours on an integrated hot stage. During heating on the hot stage, images of the drug crystal dissolution process were periodically captured using a Nikon Eclipse E600 POL cross-polarized light microscope (20X objective) with Nikon DS-Ri2 camera (Melville, NY).

4.5.3 Scanning Electron Microscopy (SEM)

The glass slides from the polarized light microscopy investigation containing the heat-treated films were then fixed on SEM stubs and sputter-coated with platinum for 60 seconds. Imaging was performed with an FEI Nova nanoSEM field emission scanning electron microscope (FEI Company, Hillsboro, Oregon) operated at 10 kV accelerating voltage, ~6 mm working distance, and a spot size of 5. Secondary electron images were captured with the Everhart Thornley detector (ETD) and backscatter electron images were collected using a vCD detector.

To collect elemental data, a ~10 mm working distance and an X-Max energy-dispersive X-ray (EDX) detector was used. The resulting data was analyzed with an Oxford Aztec system (Oxford Instruments, Abingdon, Oxfordshire, UK). The QuantMap and QuantLine functions were used to calculate elemental composition (atomic %).

4.5.4 Transmission Electron Microscopy (TEM)

Films composed of copovidone and suspended indomethacin crystals (5:1 ratio) were deposited from water onto glow-discharged 300 mesh carbon-coated copper TEM grids with 5-6 nm standard thickness (SPI supplies, West Chester, PA). Films were held at 130°C for up to 3 hours on a hot stage (integrated with the polarized light microscope). An FEI Tecnai G20 electron microscope (FEI, Hillsboro, Oregon, USA) equipped with a LaB6 source, X-max 80 mm^2 silicon drift detector (Oxford Instruments, Abingdon, Oxfordshire, UK), and Gatan US1000 2kx2k bottom mount CCD camera, operated at 200 keV, 100 µm aperture, and a spot size of 1, was used to acquire bright-field transmission electron micrographs. At least three grid squares were analyzed to ensure particles characterized were representative of the overall sample.

Fast Fourier Transform (FFT) analysis was performed using the Gatan DigitalMicrograph 3.21 software suite (Pleasanton, CA). Fourier filtering was applied using a spot mask symmetric about the origin of the FFT image, which selects only the desired frequencies (in reciprocal space). By then performing an inverse FFT on the masked image, the filtered image is reconstructed (in real space) which reveals only the periodic content associated with the specific FFT spot pair, not necessarily the atomic columns associated with the crystal. ImageJ 1.51 (National Institutes of Health, Bethesda, MD) was used to apply false color imaging and prepare overlays.

4.6 Computational Methods

4.6.1 Monte Carlo Simulation

Two-dimensional lattice Monte Carlo (MC) simulations were performed in order to model experimental dissolution observations. An initial grid was populated with crystalline sites whereby allowed trial moves consisted of removing crystal sites from the lattice at random. The probability of accepting or rejecting these moves was determined by the change in energy associated with adding or removing interfacial area, where the formation of new interfaces is considered energetically unfavorable. Furthermore, the underlying surface energy distribution of the lattice was also tuned to describe the heterogeneities that may be found in real crystals. Mathematically, the probability for accepting a trial move is expressed as (Eq. 1):

$$P(x) = \exp\left[-\left(E_{surface} + \Delta E_{interfaces}\right)\right] \quad \text{(Eq. 8)}$$

Here, $P(x)$ is the probability of accepting a trial move, $E_{surface}$ is the underlying surface energy of the trial site, and $\Delta E_{interfaces}$ is the energy change from adding or removing the total number of interfaces. Once $P(x)$ is determined, it is compared to a random number between 0 and 1 taken from a uniform distribution; if $P(x)$ is greater than or equal to the random number the trial move is accepted, and if $P(x)$ is less than the random number the trial move is rejected. The simulation is allowed to continue until no crystalline units remain. The dimensionless energy penalty associated with each new interface was chosen to be 4.0 to allow simulations to progress in a reasonable timeframe. Computer code was written in Python and made use of NumPy[208] and Matplotlib[209] libraries for mathematical functions and visualization of results, respectively (found in Appendix B).

4.7 Results

4.7.1 Characterization of Bulk Drug Crystals

Based on characterization by multiple microscopic techniques, the bulk IDM crystals were found to consist of plate-like single crystals, with small crystals adhered to the generally smooth surface.[207] Additionally, surface imperfections and irregular growth are evident (Figure 4.2a,b). When distributed in a copovidone film deposited from water, the plate-like nature of the bulk crystals with associated surface crystals can still be observed (Figure 4.2b,c).

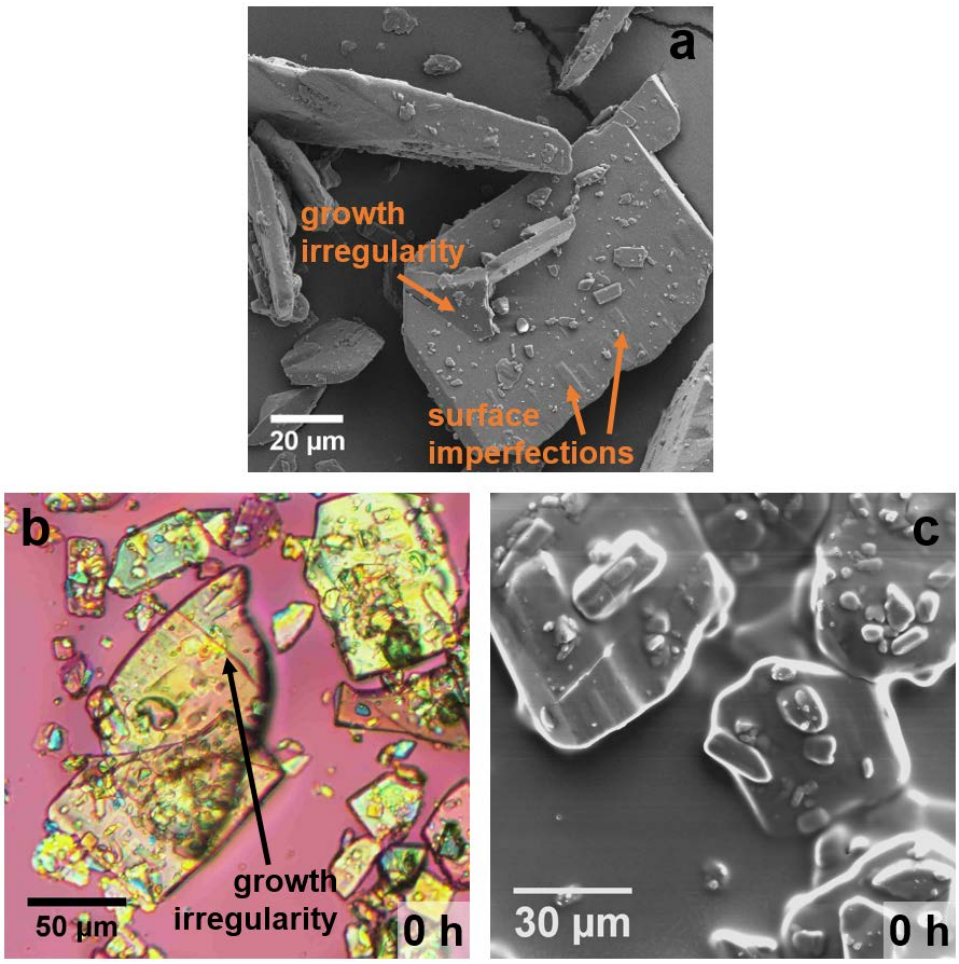

Figure 4.2. SEM and PLM images of (a) indomethacin crystals with surface imperfections, and (b,c) IDM crystals distributed in a copovidone film. The time notation in (b) and (c) refers to the duration of isothermal heating of the crystal in the polymer film (in this case no heating).

By imaging small indomethacin crystals with transmission electron microscopy (Figure 4.3), microstructure as well as the impact of the polymer film on the crystals can be observed. A drug crystal (no polymer film) has consistent internal microstructure, and gradual thickness changes as well as layers of crystal growth can be observed. The indomethacin crystal (dispersed in a copovidone film without heating) shown in Figure 4.3b shows the same smooth transition of thickness variation. In Figure 4.3c, grain boundaries divide a flat crystal into three distinct regions. During the imaging of this particle, the diffraction contrast from each region moved independently when focus was changed, confirming the crystallinity of the particle, as well as the different orientation of the three regions. In Figure 4.3d, thickness variations can again be observed, as well as discrete crystallites on the surface of the parent crystal. The presence of these surface crystallites and strain at the crystal-polymer interface leads to bend contours.

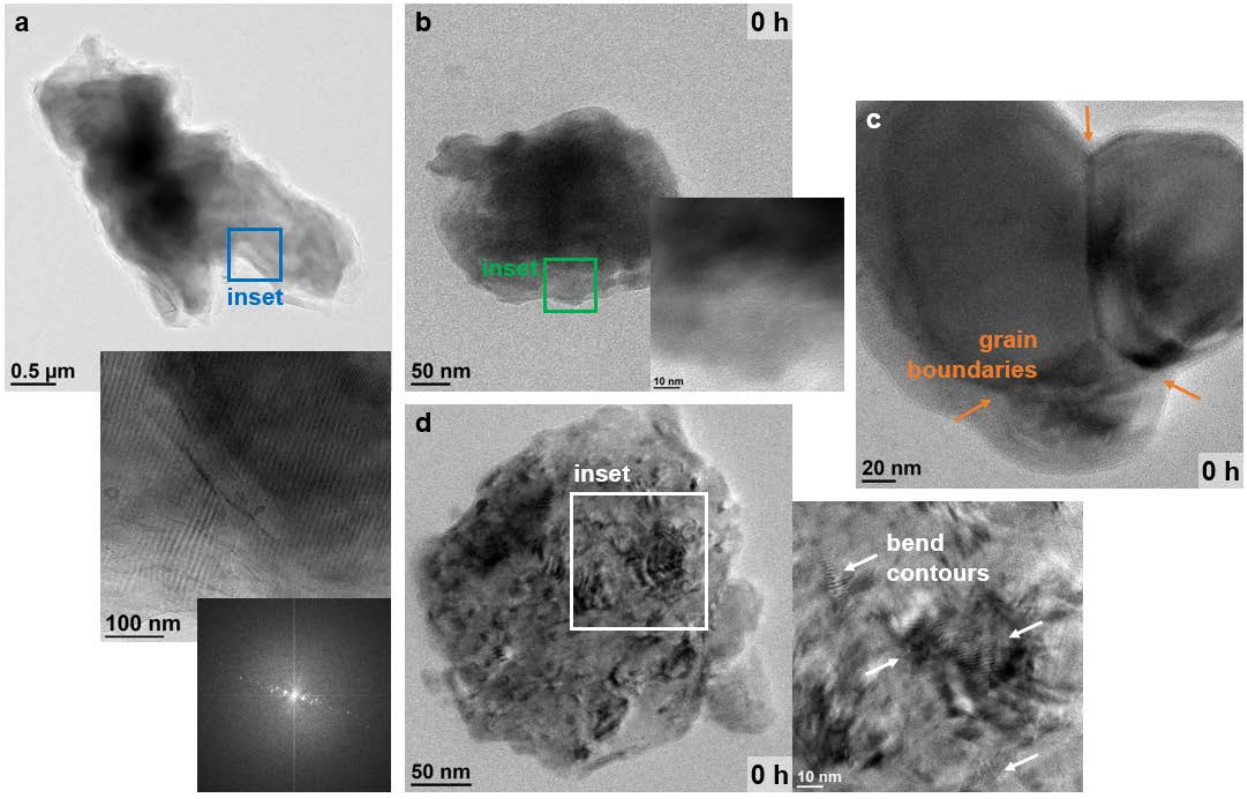

Figure 4.3. Bright field TEM images of (a) the internal microstructure of an indomethacin crystal, and (b-d) IDM crystals distributed in a copovidone film. The time notation in (b-d) refers to the duration of isothermal heating of the crystal in the polymer film (in this case no heating).

4.7.2 Dissolution of Drug Crystals in Polymer Films

4.7.2.1 Drug-Polymer Dissolution Monitored by Variable Temperature X-ray Diffraction

High temperature X-ray diffraction (XRD) has been used to study reaction kinetics and solid state changes,[210–212] and was used herein to monitor the in situ dissolution of indomethacin into molten copovidone under quiescent isothermal conditions. By heating the physical mixture to 130°C and monitoring the profile as the crystal dissolves into the polymeric matrix (Figure 4.4), the crystalline peak heights can be observed to decrease over time. The peak pattern at 130°C matches that of the physical mixture at room temperature, although a small shift can be observed attributable to the temperature difference. The detectable crystalline phase at the 20.7° 2θ has disappeared at approximately 120 minutes. Detectability of the crystalline phase may be limited by dilution of drug by the polymer, crystallite size, and crystal quality.[109,147–149,207,213]

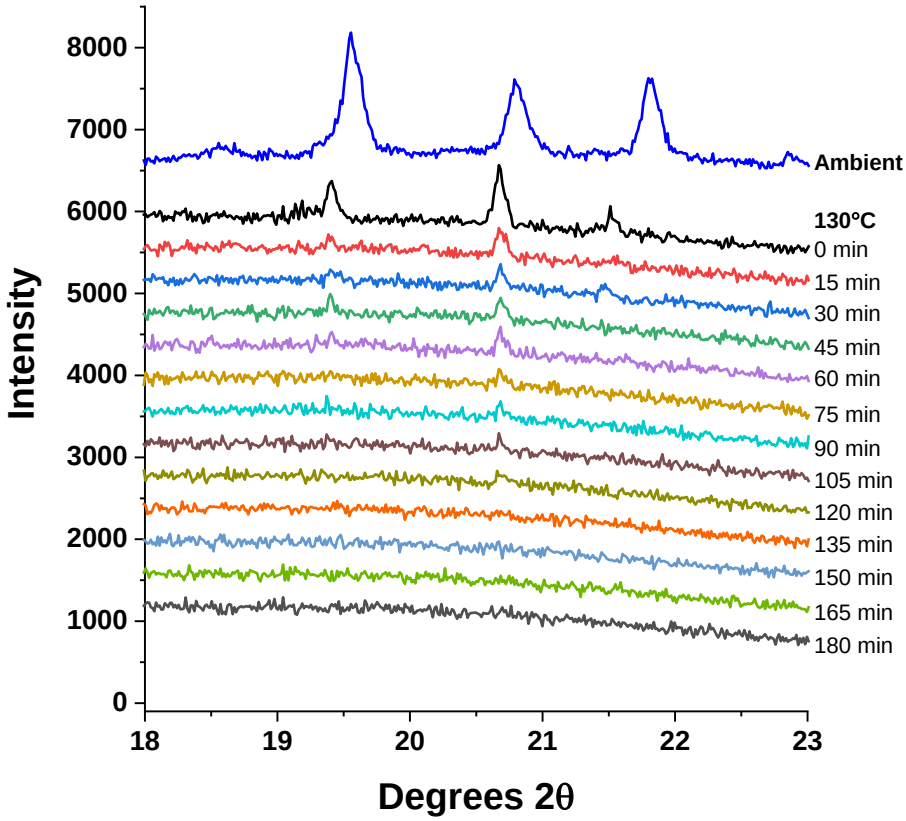

Figure 4.4. XRD patterns of indomethacin crystals dispersed in a copovidone film at ambient conditions and as the crystals dissolve over time at 130°C.

4.7.2.2 Polarized Light Microscopy

Indomethacin crystals distributed in a copovidone film were held under quiescent isothermal conditions at 130°C and crystal dissolution into the molten polymer was observed with time. The dissolution of three individual crystals under polarized light is shown in Figure 4.5. The smallest crystals dissolve quickly in under 30 minutes, leaving the larger crystals to be observed. Crystal A breaks up into at least 5 pieces within 30 minutes of isothermal treatment (black arrows), and then each of those individual fragments dissolve over the observation period. Crystal B shows evidence of an apparent growth imperfection to the crystal structure (blue arrows, also shown in Figure 4.2b). This disruption grows and separates the crystal into two pieces within 15-30 minutes. The small fragment dissolves within 60 minutes of observation, while the larger fragment continues to dissolve during the observation period. A channel can be seen forming from the left side of the crystal at around 45 minutes (white arrows), and irregularly grows as the crystal dissolves, ultimately dividing the fragment into two pieces around 105 minutes. Additionally, holes can be seen forming around 60 minutes in the center of crystal fragments which grow during the dissolution process. Similar to crystal B, a hole forms in crystal C around 30 minutes (purple arrows), which enlarges as dissolution continues. Because of the proximity of the hole to the edge of the crystal, the hole eventually merges with the amorphous matrix. In each image series, a boundary appears around the crystal where dissolved drug has joined the molten phase. This suggests that there is a refractive index difference to this area of film caused by a change in chemical composition and/or film thickness as the diffused drug migrates through the polymer melt.

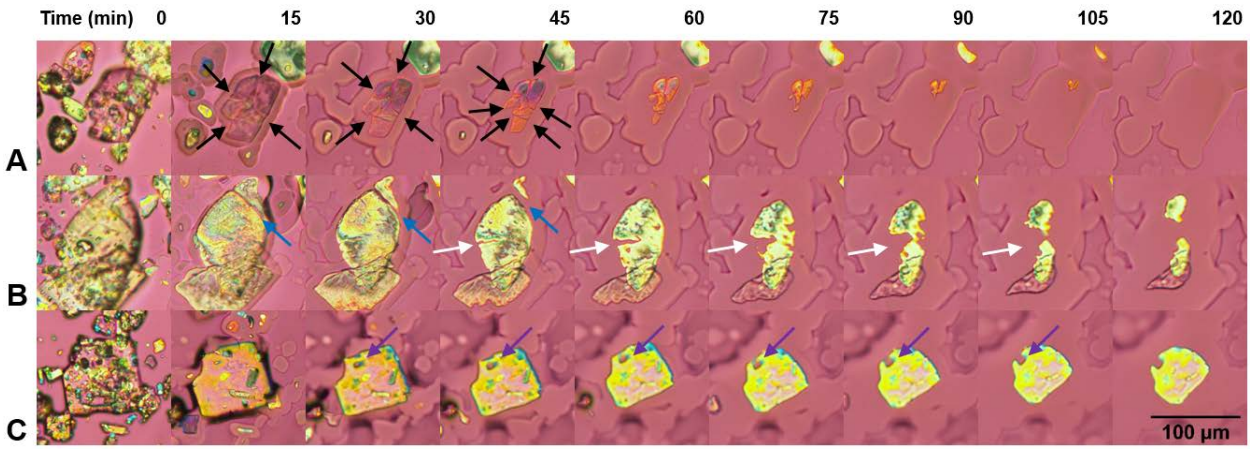

Figure 4.5. Time lapse polarized light micrographs of indomethacin crystals dissolving into copovidone held at 130°C. Arrows note the appearance and progression of hole and channel formation and fragmentation (discussed in the text).

4.7.2.3 Scanning Electron Microscopy

Copovidone films containing partially dissolved indomethacin crystals were observed by SEM, equipped with a backscatter detector. Crystals appear lighter (greater intensity) than the surrounding film, which indicates higher atomic number, presumably due to the chlorine atoms present in indomethacin. While the bulk crystals had generally smooth surfaces (Figure 4.2a), the partially dissolved crystals show irregular patterns on the crystal surface due to partial dissolution, as in Figure 4.6a. Figure 4.6b shows a small crystallite with channel formations prior to significant dissociation. In Figure 4.6c, the crystal fragments are found below the film surface, while they are found at the film surface in Figure 4.6d.

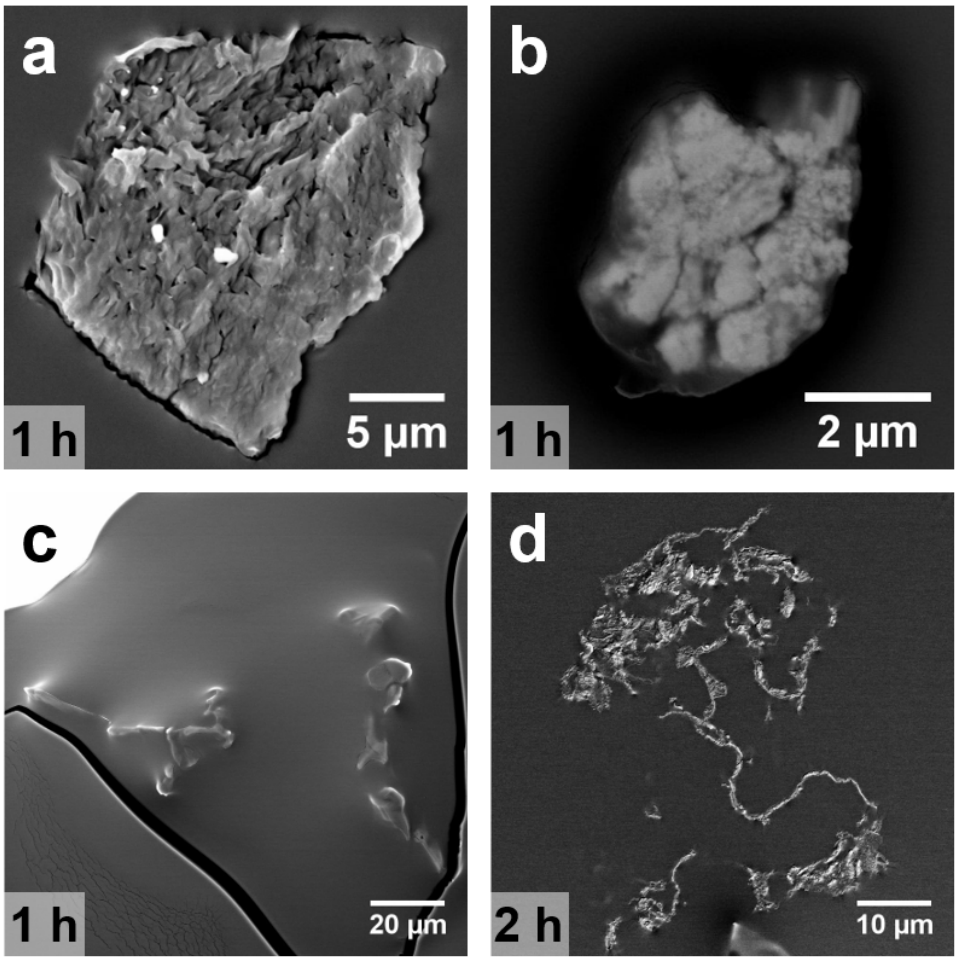

Figure 4.6. Backscatter SEM images of indomethacin drug crystals at various stages of dissolution into copovidone melt. The time notation refers to the duration of isothermal heating of the crystal in the polymer film (in this case 1 or 2 hours at 130°C).

The diffusion process was observed in crystals before (Figure 4.7a) and after heating and dissolution (Figure 4.7b) using elemental mapping. Indomethacin contains chlorine, while copovidone does not contain any unique elements. Thus, the appearance of chlorine indicates the presence of indomethacin, either as a crystal or molecularly dissolved into the film. Across the mapped area of the near-completely dissolved crystal (Figure 4.7b), a region of higher intensity in the backscattered image is observed around the remnants of a crystal which can be attributed to the presence of chlorine. The elemental mapping shows slight modulation of carbon, oxygen, and nitrogen signals in the polymer and drug-polymer diffusion areas, while distinct chlorine signals, corresponding to the increased intensity region in the electron image, are observed. A line scan was taken to provide elemental composition information across the region of interest, in the

polymer, drug-polymer diffusion, and crystal regions. Carbon, oxygen, and nitrogen show the expected trends of change in elemental composition across the line scan, based on consideration of the relative elemental compositions of drug and polymer. Interestingly, oxygen shows a distinct drop in quantity at the location of the crystal, corresponding to the lower overall oxygen content found in indomethacin relative to copovidone. In the outer areas of the film, no chlorine is detected indicating that only polymer is present. Moving inward, chlorine then appears and increases in concentration, maximizing across the majority of the drug-polymer diffusion and crystal regions. Due to the penetration depth of the electron beam, signal from the amorphous matrix is also seen in the area of the crystal, so the overall chlorine content appears lower than the theoretical level of a pure indomethacin crystal. In the undissolved crystal (Figure 4.7a), appearance of chlorine is observed which identifies the crystal in the film. No signal from indomethacin is seen outside of the crystal.

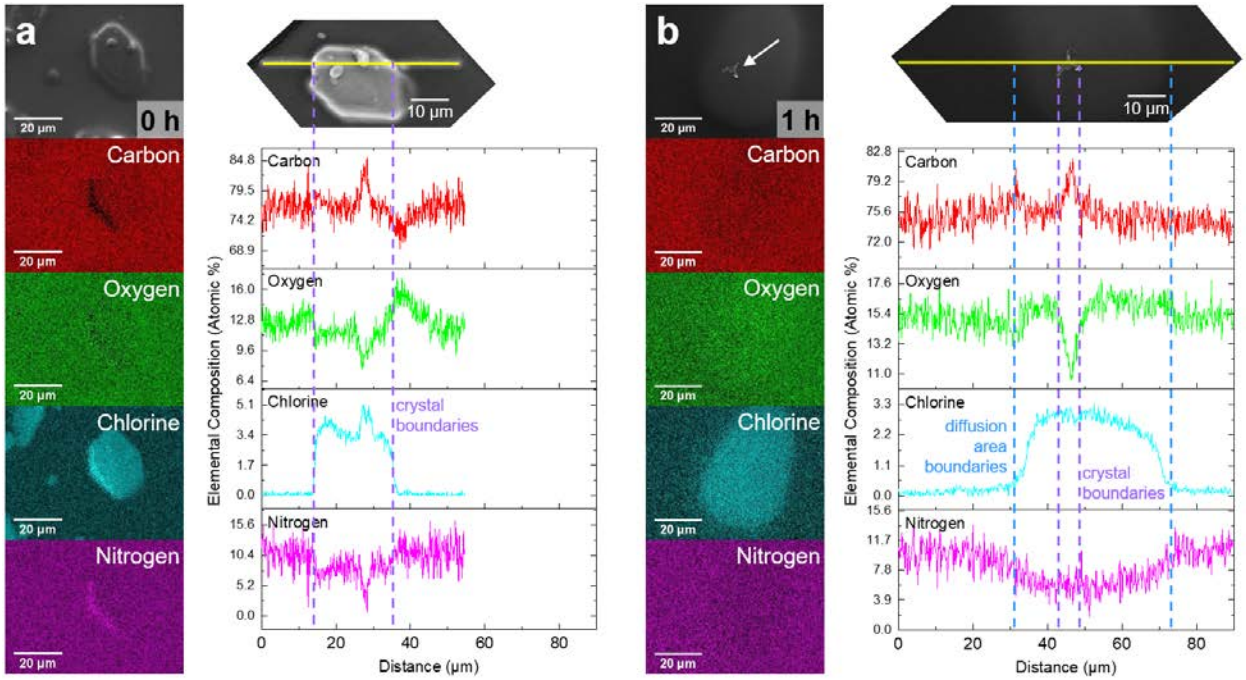

Figure 4.7. (a) SEM image and elemental maps and linescan of an undissolved crystal in the copovidone film. Distinct appearance of chlorine identifies the crystalline material. (b) Backscatter SEM image and elemental maps and line scan of a near completely dissolved indomethacin crystal into the copovidone film. The region of greater intensity surrounding the crystal (identified by a white arrow) indicates the change in atomic composition due to the diffusion of indomethacin into the polymer melt. Small modulations in carbon, oxygen, and nitrogen content across the map are observed, while distinct appearance of chlorine content is found in the diffusion area. The location of the line scan on the rotated SEM image is presented, and aligns with the scale on the panels shown in the chart. Vertical dashed lines indicate the location of the crystal and diffusion areas along the line scan. The time notation refers to the duration of isothermal heating of the crystal in the polymer film (in this case no heating or 1 hour at 130°C).

4.7.2.4 Transmission Electron Microscopy

TEM images allow the overall morphology and internal structure of the crystal to be visualized within the film following the heating process. However, the inherent challenge with this technique is in preparing an electron-transparent sample on the order of 100 nm thickness.[142,143,214] Amorphous domains appear as a homogenous continuous phase, while evidence of crystallinity include darker areas within the matrix, diffraction contrast, and lattice planes (at high magnification only).[103,141,144,207,215] Due to thickness variations of the crystal and film deposited on the grid and interference from the amorphous matrix, the crystal lattice could only be visualized

in some crystalline regions. When lattice planes can be visualized, crystallinity can be confirmed by Fast Fourier Transform (FFT) analysis.[207]

Bright field TEM images capture the stages of channel formation and fragmentation in the crystalline particles shown in Figure 4.8. Each of these particles has a rounded shape, indicating fairly uniform dissolution and reduction in crystal size by dissolution at all crystal surfaces. Figure 4.8a shows an example of the initiation of channel formation, where the channel has advanced <20 nm into the crystal. A more extensive channel, where the particle is fully divided, can be seen in Figure 4.8b. At an even more advanced stage of dissolution, separate fragments, presumably originating from a single particle with extensive channel formation, can be observed (Figure 4.8c). In each of these crystallites, the crystal lattice could not be imaged due to sample thickness and/or crystal orientation; however, crystallinity can be confirmed by the presence of diffraction contrast.

The intermediate stages of channel formation (Figure 4.9) were captured in a single particle, similar to what was seen under time lapse imaging with polarized light microscopy (Figure 4.5). A larger parent crystal (Figure 4.9a) has dissociated into three large fragments. Two of the smaller daughter fragments are separated by a narrow channel (Figure 4.9b), indicating they have more recently dissociated. Several small channels evolving from the left and right sides of the crystal are highlighted in Figure 4.9b. The channels at the bottom of the particle (Figure 4.9c) are nearly connected, whereby completion would eventually lead to crystal breakage. In Figure 4.9d, greater extent of dissolution is seen at the edge of the particle where the channel initiated; the channel becomes narrower as it advances into the particle. The heterogeneous appearance can be attributed to thickness variations across the crystal, as well as scattering effects from defects induced by the dissolution of the crystal.

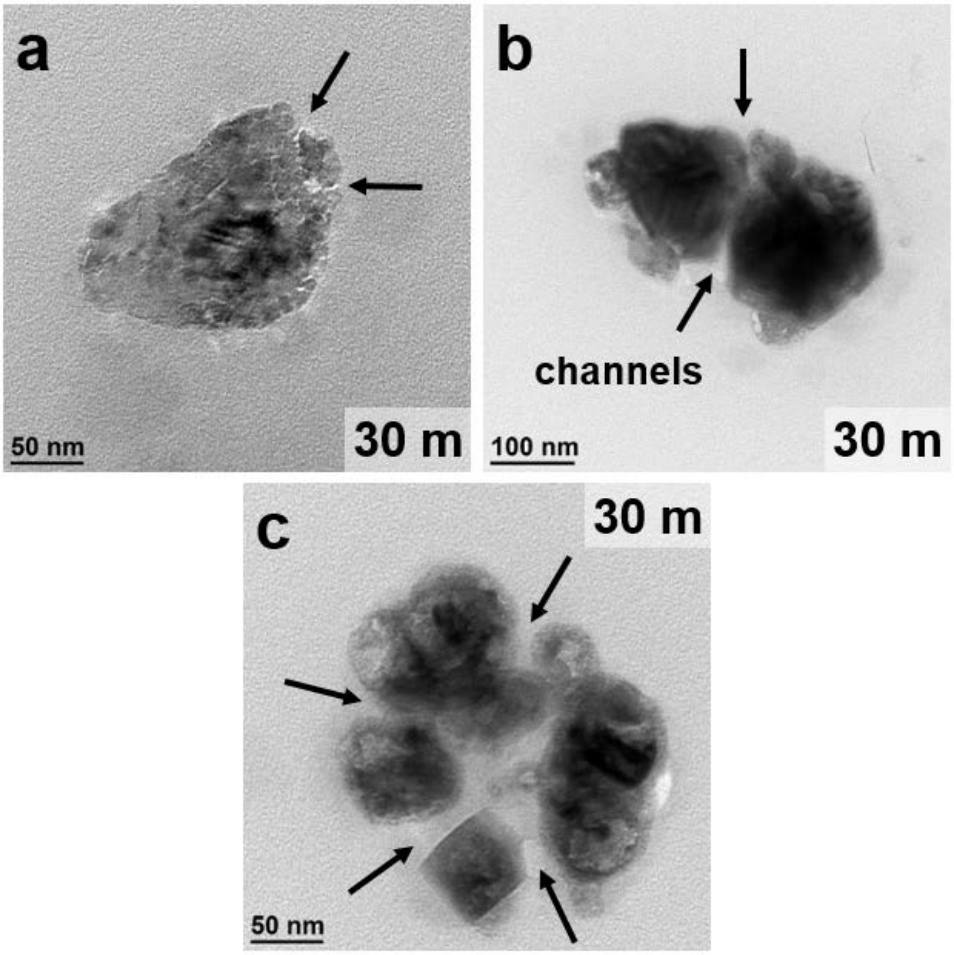

Figure 4.8. Bright field TEM images of indomethacin crystals with increasing degrees of channel formation and fragmentation. The arrows indicate channels where amorphous content is advancing into the crystal, dividing crystalline areas. The time notation refers to the duration of isothermal heating of the crystal in the polymer film (in this case 30 minutes at 130°C).

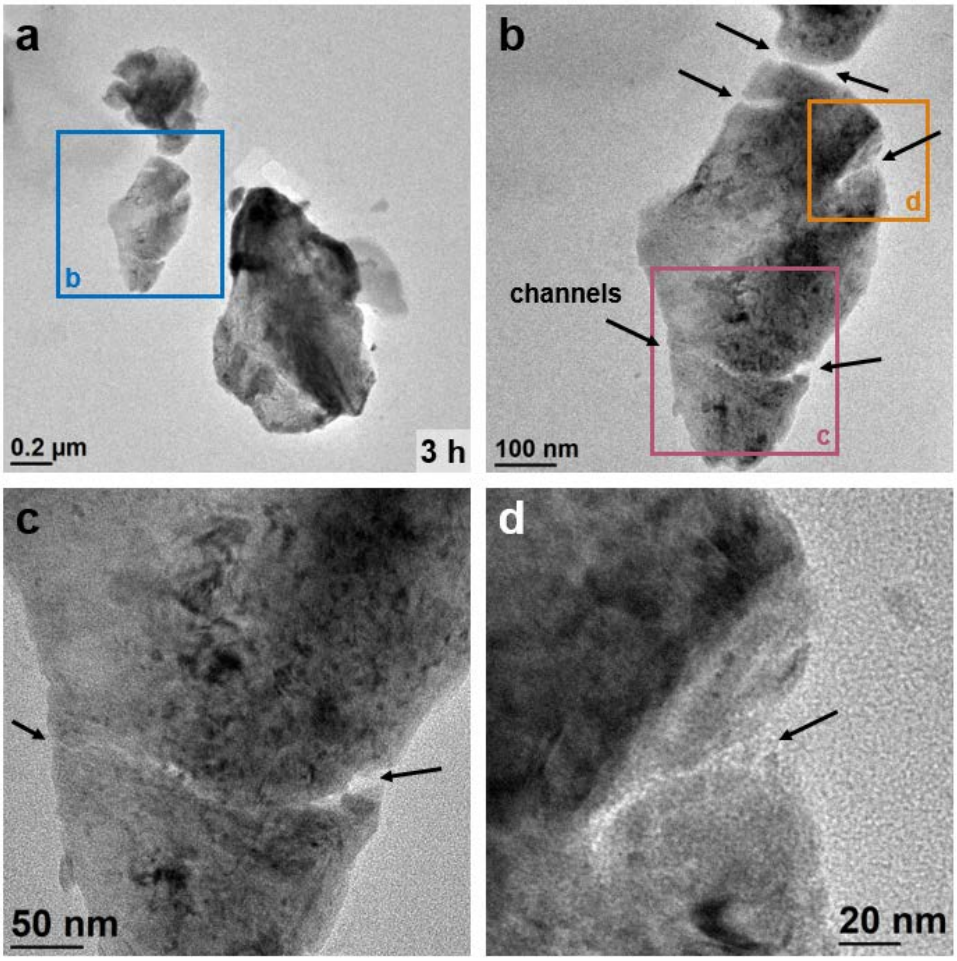

Figure 4.9. Bright field TEM images of indomethacin crystals with channel formations. The arrows indicate channels where amorphous content is advancing into the crystal, dividing crystalline areas. The time notation refers to the duration of isothermal heating of the crystal in the polymer film (in this case 3 hours at 130°C).

At a later stage of dissolution, a fragment field consisting of small, connected crystalline domains is observed (Figure 4.10a). Channels and wider regions of amorphous material are observed in interior areas. The highlighted region contains many crystallites, as noted by the presence of many spots at the same distance from the center of the FFT pattern (indicating that the spots arise from the same lattice spacing), but at multiple orientations (Figure 4.10b,inset). In this region, a channel is found which has separated a crystal fragment into two areas. The false color reconstruction was created from a single FFT spot, demonstrating a crystal lattice of a single orientation and lattice spacing (Figure 4.10c). Thus, this crystallite, now divided, has not changed

orientation or position as it is dissolving and breaking into two pieces. This observation provides evidence that the fragments are derived from a parent crystal.

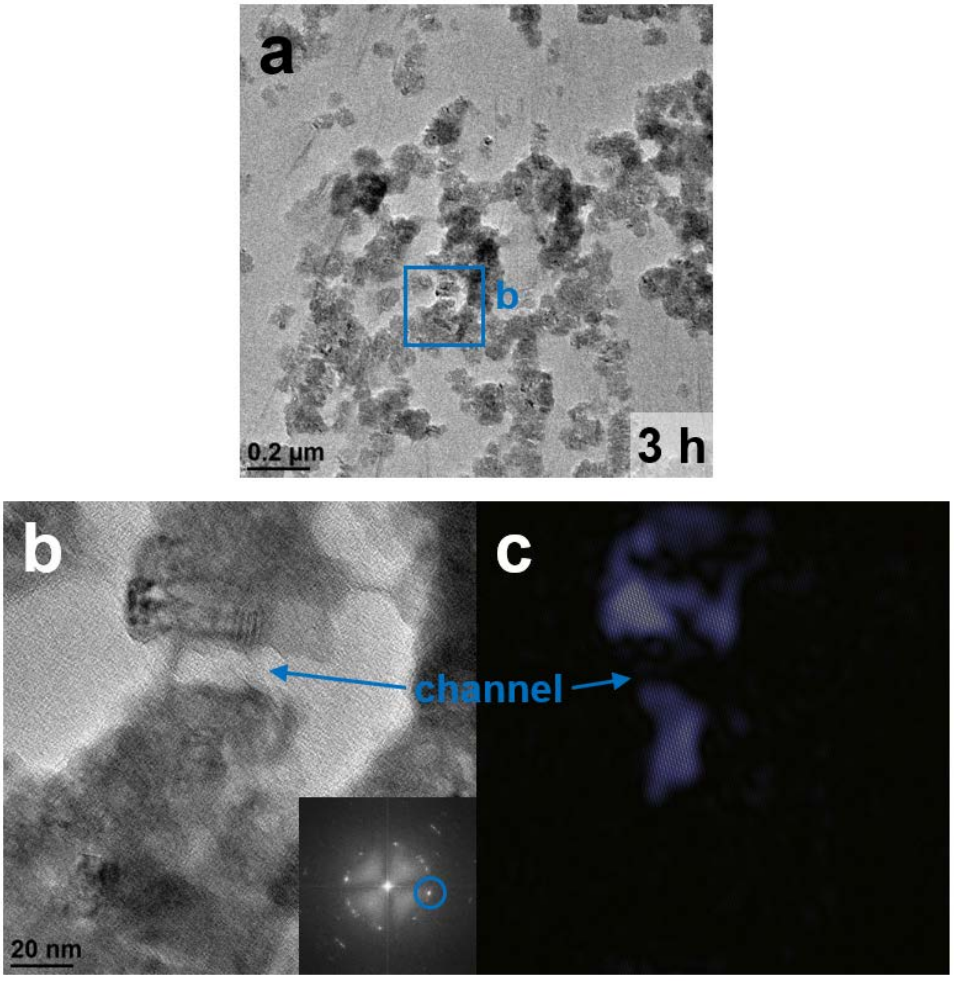

Figure 4.10. Bright field TEM images of a crystal fragment field of indomethacin crystals dissolving into a copovidone film at a later stage of dissolution (a). A channel has formed which separates two areas of a crystal fragment (b), highlighted by the false color reconstruction (c) generated from a single FFT spot (b, inset). The time notation refers to the duration of isothermal heating of the crystal in the polymer film (in this case 3 hours at 130°C).

Global dissolution by diffusion results in particle shrinkage, where the crystal dissolves from all surfaces. This is evidenced in Figure 4.11a, wherein a 40 nm crystallite with rounded shape has a single crystal lattice plane in focus throughout the entire area (Figure 4.11b), except in the lower right corner, where the lattice is obscured due to crystal thickness.

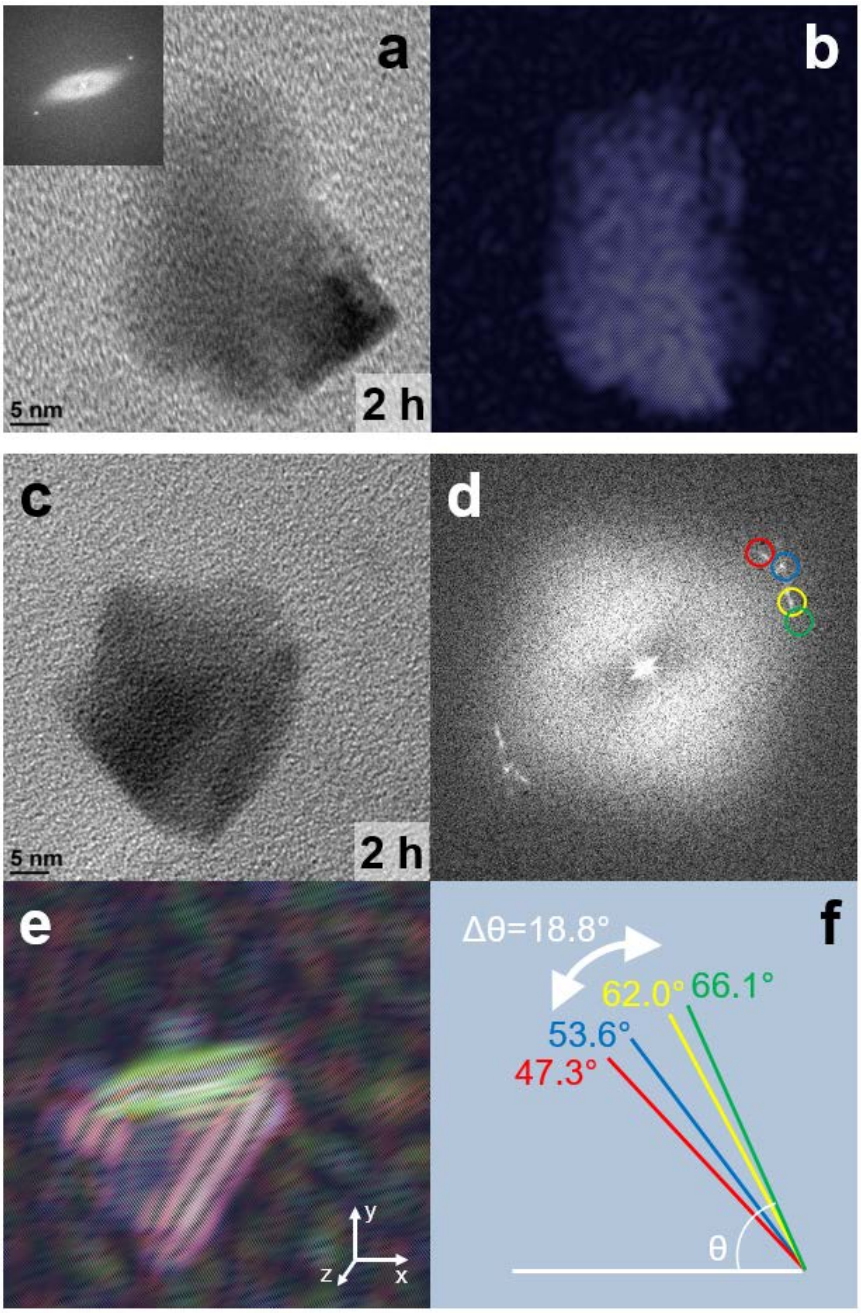

Figure 4.11. Bright field TEM images showing the dissolution by particle shrinkage (a-b) and fragmentation (c-f) mechanisms. In the crystallite in (a), the FFT pattern (a, inset) was reconstructed to reveal single lattice spacing. In the particle in (c), the four distinct spots with equivalent lattice spacing in FFT pattern (d) were reconstructed (e) to reveal a series of fragmentation and rotation events. The rotation of each false colorized lattice spacing is shown in (f). The time notation refers to the duration of isothermal heating of the crystal in the polymer film (in this case 2 hours at 130°C).

In Figure 4.11c, the mechanism of fragmentation of a 30 nm crystallite is observed. The FFT pattern shows four distinct spots with equivalent lattice spacing, which were individually reconstructed and false colorized with red, blue, yellow, and green. The spot indicated in blue is the sharpest, indicating that this is likely the original orientation of this lattice plane which has not shifted. The spot marked in red appears more as a smear rather than a crisp FFT spot, indicating slightly different orientation of areas of the lattice. The red fragment has rotated roughly 6° from the original placement, but covers approximately the same area in the x-y plane as the blue fragment. The red and blue lattice fragments are slightly obscured in the center due to crystal thickness. The spots marked in yellow and green cover roughly the same area in the x-y plane, but are approximately 8° and 12° shifted from the blue fragment. The overlay of these fragments reveals the layer-like structure of the crystal. Due to the size and spatial placement of each of the four fragments, there are three fragmentation sites where the crystal has delaminated or split apart. The first fragmentation site splits the yellow/green and red/blue fragments into top and bottom pieces. The red/blue and yellow/green fragments delaminated in the z-axis (i.e. parallel to the x-y plane). Rotation of each fragment presumably occurs as a result of slow dynamic motion of the crystallites in the amorphous matrix, diffusive movement of indomethacin into the amorphous matrix, and diffusive movement of copovidone into the area of the crystal, which functions to push the fragments apart. The crystal fragments, from red to green, rotate over a total of 18.8°.

When the crystal surface has dissolved sufficiently, discrete crystallites within the overall structure can be identified. In Figure 4.12, two daughter fragments of 150-300 nm in size are separated by a channel distance of 5 nm, suggesting their origin from a single parent crystalline particle. In each of these fragments, narrow channels can be seen penetrating from the edges and within the particulate structure (highlighted by the arrows in Figure 4.12b). These internal channels curve around crystalline formations. In Figure 4.12c, through FFT analysis, the lattice structure of the darker formations identifies crystalline domains of 6.4 ± 2.2 nm ($n = 18$) in size. The consistent lattice spacing indicates that a single lattice plane is being observed with multiple orientations. There are two possibilities for such an observation: (1) a parent crystal has fragmented, and the resultant crystallites have rotated in the x-y plane, or (2) the parent crystal was made up of multiple crystal orientations, which have now separated due to the dissolution process. Indeed, the crystallites in both daughter fragments are oriented primarily in the $1^{st}/3^{rd}$ quadrant, and have a

maximum rotation of 93°. Movement of the crystallites may also have taken place as a result of the cooling process from 130°C to room temperature.

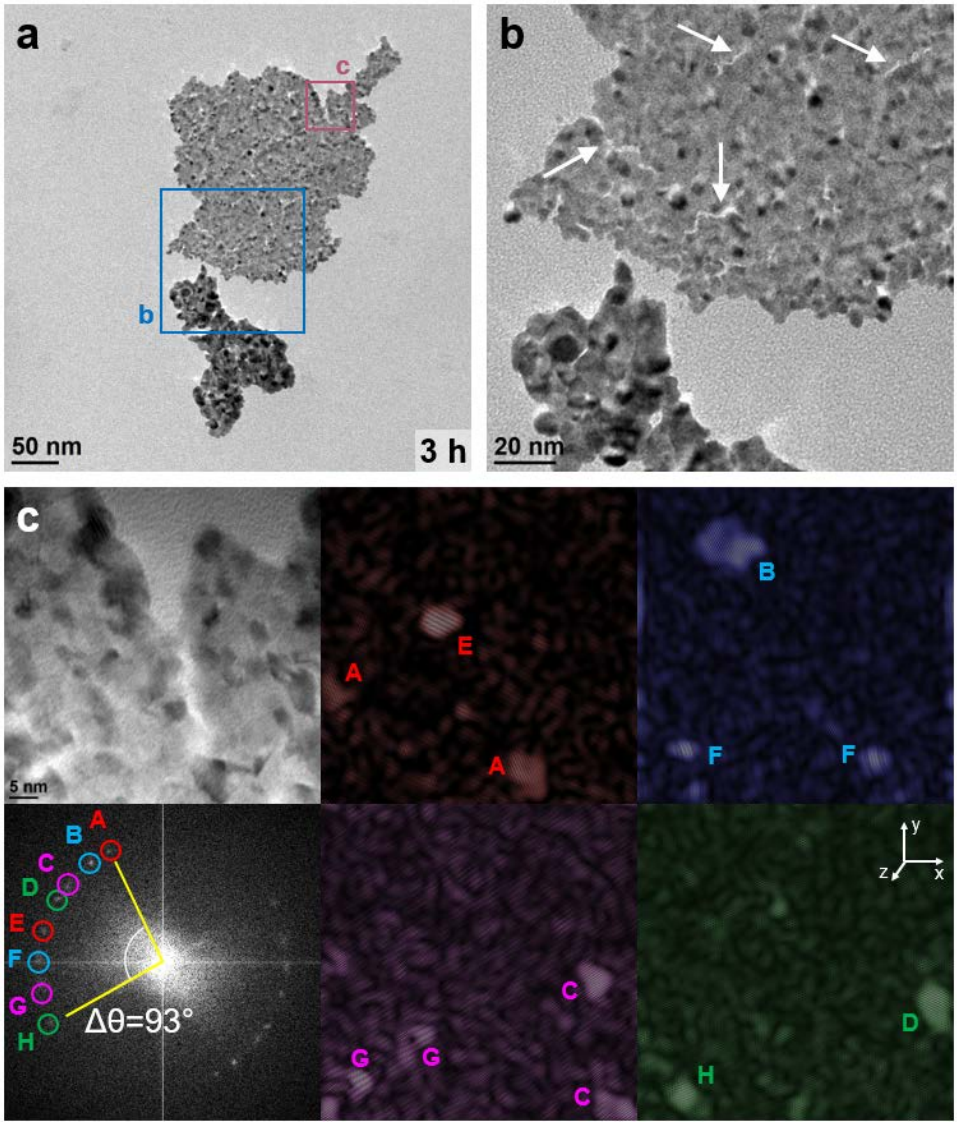

Figure 4.12. Bright field TEM images of an indomethacin crystal fragmented into two fragments 150-300 nm in size (a). Channel formations are observed (b), as well as discrete crystallites having rotated within the structure (c). False colorized reconstructions were generated from each FFT spot, with the crystallites spatially identified A-H corresponding to the FFT spot. The time notation refers to the duration of isothermal heating of the crystal in the polymer film (in this case 3 hours at 130°C).

4.7.2.5 Time Progression of Crystal Dissolution

Observation of crystalline material and its corresponding microstructure by TEM is inherently limited by the thickness requirement of the sample. In many of the images presented (Figure 4.8, Figure 4.11), even when lattice planes were visualized in one area, thickness variations obscured part of the crystalline area. Films were prepared and observed up to 3 hours of quiescent isothermal heating, and a different population of crystalline material would be expected to be observed at each time point, based on an extent of dissolution that translated to the specific thicknesses required for observation. While the dissolution mechanism is not expected to change overall based on the length of time, the observations that can be captured vary based on initial crystal size.

At an early time point (30 minutes), crystalline material from the smaller initial particles would be observable. For example, in Figure 4.8, the channel formation and fragmentation process is captured where the total area observed ranges from 100-300 nm. After 2 hours, the microstructure of 30-40 nm discrete crystals was observed (Figure 4.11), showing particle shrinkage and fragmentation dissolution mechanisms. After 2 and 3 hours, the highly heterogeneous nature of the particle surfaces could be observed in larger fragments (for example, Figure 4.9, Figure 4.10b, Figure 4.12). Discrete crystalline domains could be observed, as well as orientation changes.

At later time points, collections of small fragments are observed by both TEM and SEM techniques (Figure 4.10b, Figure 4.13). Because of the spatial proximity and similarity in extent of dissolution, these regions likely originated from a single particle, which has dissolved through the diffusion, particle shrinkage, channel formation, and fragmentation mechanisms. The particles do not migrate significantly from one another due to slow diffusivity in the highly viscous matrix. These fragment fields are seen over larger areas in SEM than can be observed in TEM due to the instrumental limitations of each technique. However, both techniques demonstrate the creation of new interfaces due to irregular dissolution, channel formation, and fragmentation.

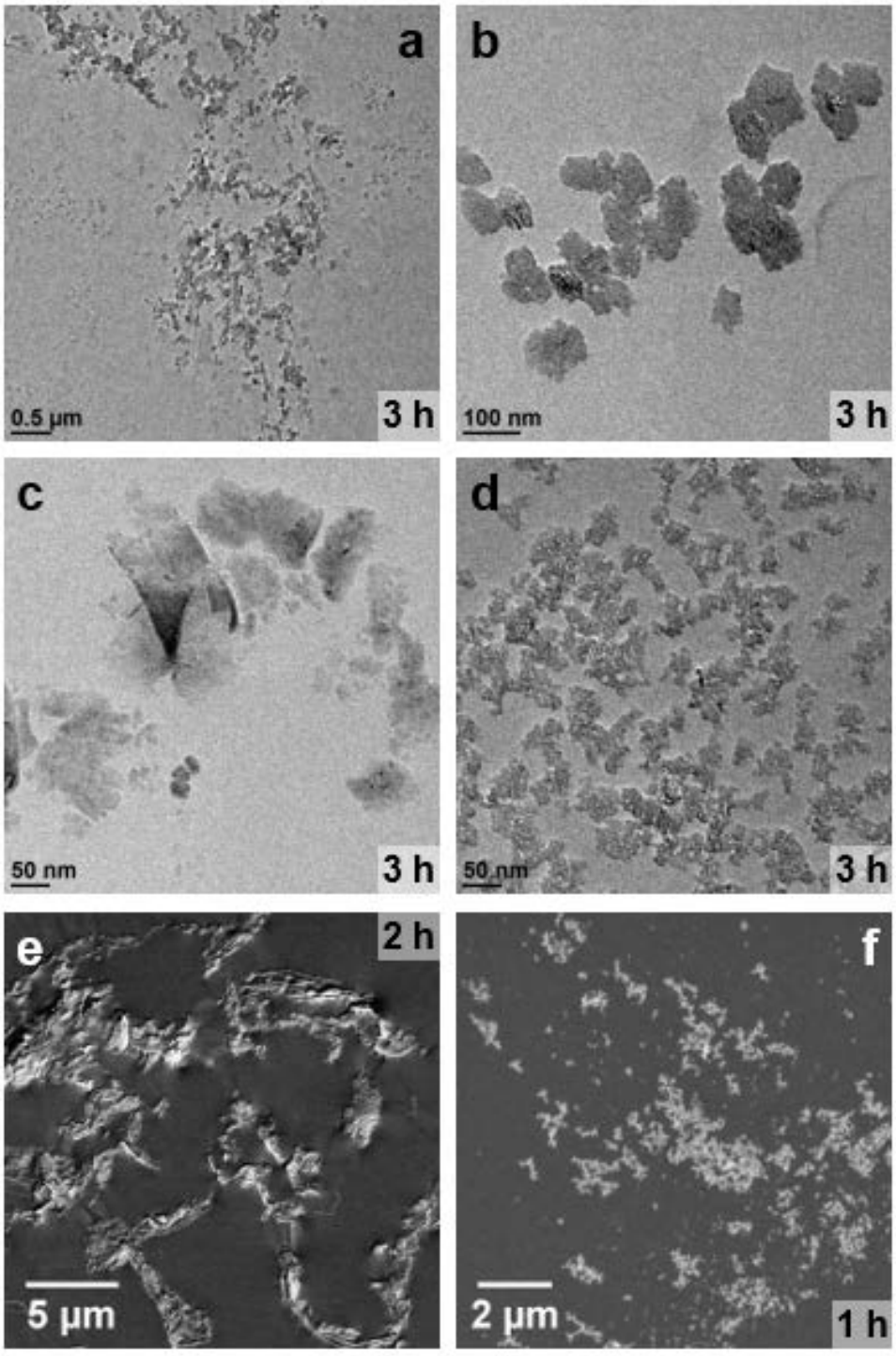

Figure 4.13. Crystal fragment fields observed by TEM (a-d) and SEM (e-f). Due to spatial proximity, and similarity in extent of dissolution, these regions likely originated from a single particle. The time notation refers to the duration of isothermal heating in the crystal in the polymer film (in this case 1-3 hours at 130°C).

4.7.3 Monte Carlo Simulation of Crystal Dissolution

Monte Carlo simulations of the probability of crystal dissolution were performed for systems representing various surface energy configurations. Figure 4.14 depicts three sample surface energy distributions with snapshots of the accompanying simulations. Figure 4.14a shows a uniform surface energy, representative of an ideal, defect free crystal. Figure 4.14b is a surface energy configuration containing a long diagonal region of high surface energy, representing the surface energy of a grain boundary between two crystallites. Figure 4.14c is more complex, containing randomly placed two-dimensional Gaussians of high surface energy along with two orthogonal lines originating from each of these high energy centers. The orientations of these pairs of orthogonal lines in space relative to the underlying 2D lattice were assigned randomly. This configuration is designed to represent point defects and the corresponding defect-induced strain in the crystal.

Beginning with the simplest energy configuration (Figure 4.14a), the snapshots reveal isotropic dissolution driven almost exclusively at the edges of the lattice. As expected, the crystallite seeks to minimize surface area by approaching a nearly circular (or spherical in 3D space) shape, as seen in Figure 4.14a-4. It can be noted, however, that the simulations deviate from circularity as the simulations progress, seen in Figure 4.14a-5 and Figure 4.14a-6. Most likely, this phenomenon is an artifact of the spatial discretization in the form of 2D Cartesian lattice sites of finite size. As the crystalline region shrinks, the dimensions of the lattice sites themselves influence the shape of the remaining domain, a consequence of forming a small circle from relatively large squares. In spite of this limitation, these results represent an idealized system and serve as a base case for comparison against more physically motivated and relevant simulations.

For the surface energy configuration in Figure 4.14b, the snapshots highlight interesting differences from those in Figure 4.14a. Dissolution is still driven to the edges of the lattice with a tendency to minimize surface area by approaching a circular shape (compare Figure 4.14a-4 with Figure 4.14b-5). However, the introduction of the high energy diagonal line in the surface energy distribution results is significant dissolution following this line. Dissolution along the diagonal begins forming a channel between the two halves (Figure 4.14b-1) which widens (Figure 4.14b-2) and eventually splits the crystal into two pieces (Figure 4.14b-3). These now disparate pieces each undergo dissolution originating at the edges and eventually working towards the center, similar to the dissolution for the single crystal in Figure 4.14a.

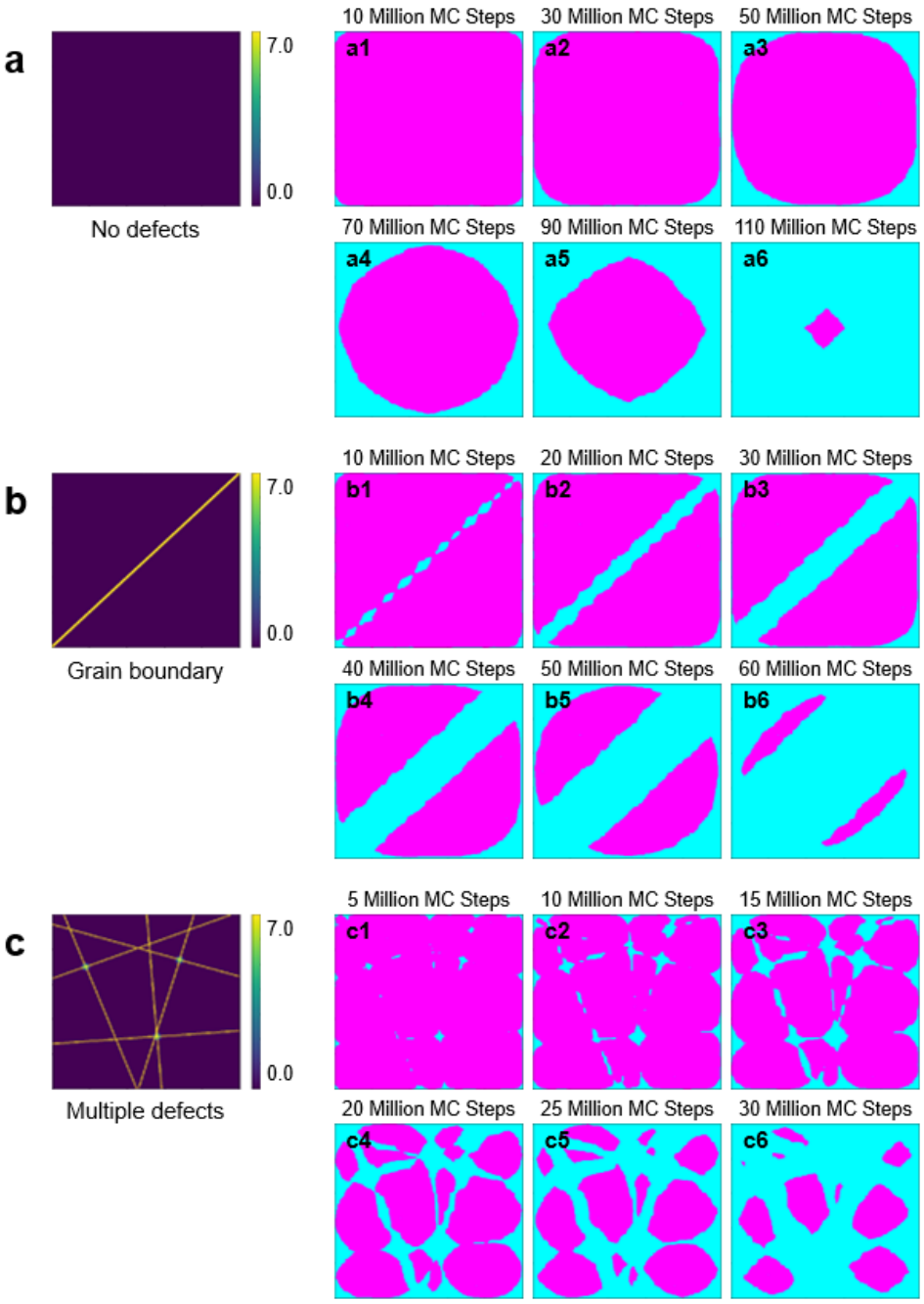

Figure 4.14. Surface energy distributions employed in MC simulations (a-c) and snapshots of MC simulations for the corresponding surface. Energy configurations represent (a) a defect-free crystal, (b) a crystal exhibiting a grain boundary, and (c) a crystal with randomly located defects and accompanying defect-induced strain. Number of MC steps refers to the number of trial steps of MC simulation.

The final system for consideration is a more complex surface energy distribution (Figure 4.14c), involving multiple localized high energy sites with high energy lines intersecting at these centers. Now, with significant regions of high surface energy, the initial crystal undergoes rapid dissolution emanating from these high energy sites/lines (Figure 4.14c-1,2) which leads to extensive channel formation (Figure 4.14c-3,4), and fragmentation (Figure 4.14c-4,5), as well as diffusion-based dissolution around the edges of the many resultant fragments (Figure 4.14c-6).

An interesting comparison between the three systems is revealed by the length of the simulation. While trial step count does not have a direct connection to any timescale, it is indicative of the relative probability of a particular dissolution event occurring. Hence, comparing the length of simulation to achieve a similar fractional dissolution proves to be a helpful surrogate to relative rate of dissolution (Figure 4.15). The presence of defects and high energy sites shortens simulation times and thus is thought to increase the rate (probability) of dissolution—new surfaces are quickly exposed, which then dissolve in the typical manner. Moreover, by comparing the extent of dissolution in Figure 4.14a-2, Figure 4.14c-3, and Figure 4.14c-6, where all three images depict simulations after 30 million trial MC steps, it is highlighted that the channel formation and fragmentation process is relatively rapid compared to the rate of diffusion-based dissolution alone.

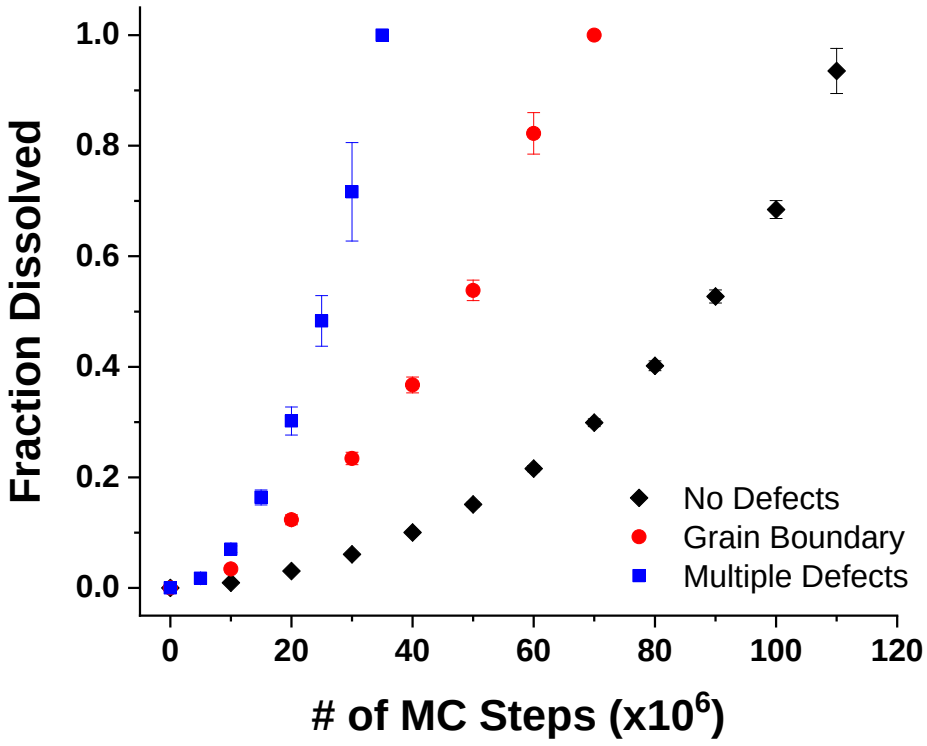

Figure 4.15. Relative extent of crystal dissolution per MC step of the three simulation conditions. Black diamonds represent the defect free simulation, red circles represent the grain boundary simulation, and blue squares represent the multiple random defects simulation. Error bars correspond to one standard deviation based on ten replicates for each simulation.

4.8 Discussion

4.8.1 Diffusion-Based Crystal Dissolution Model

Miscible drug-polymer systems will exhibit melting point depression, wherein the drug can be dissolved into the polymer at temperatures below the drug's melting point.[66,68,74,140] Indomethacin and copovidone are known to have favorable specific interactions, and be miscible at high temperatures.[61,65,68,105,137,140] The temperature-composition phase diagram of indomethacin and copovidone indicates that the solubility temperature of the composition (1:5 ratio) used in this investigation is approximately 78°C.[140] Thus, if taken to completion at 130°C, all of the drug would be able to dissolve in the polymer.

The Noyes-Whitney equation coupled with the Nernst-Brunner diffusion layer model forms the theoretical basis for understanding the dissolution mechanism of solutes into solvents (Eq. 2)

$$\frac{dC}{dt} = \frac{DA}{hV}\left(C_s - C\right) \quad \text{(Eq. 9)}$$

where *dC/dt* is the differential change in solute concentration in solution with time, *D* is the diffusion coefficient, *A* is the surface area available for dissolution, C_s is the equilibrium solubility of the crystalline drug in the molten polymer, *C* is the concentration of the dissolved drug in the liquid phase at time *t*, *h* represents the mass transfer boundary layer thickness at the solid-liquid interface, and *V* is the volume of the liquid phase. Drug and polymer dissolution models can be found in the literature which incorporate particle size, particle shape, diffusion layer thickness, impact of other formulation components, and sink vs. non-sink conditions on dissolution rates into (low viscosity) solvents or biological fluids.[194–196,216–220] In high viscosity environments, such as a polymer melt, the diffusivity of a solute molecule can be estimated by the Stokes-Einstein equation (Eq. 3)

$$D = \frac{k_B T}{6\pi\eta r} \quad \text{(Eq. 10)}$$

where k_B is the Boltzmann constant, *T* is the temperature, η is the viscosity, and *r* is the radius of the diffusing species. The dissolution rate is thus driven by diffusivity, temperature, viscosity, solubility, particle surface area, and boundary layer thickness.

Diffusion-based dissolution, schematically depicted in Figure 4.16a, represents the prevailing model for formation of a homogenous drug-polymer melt at temperatures above the polymer's glass transition.[125,138,140,186] First, the crystals are suspended within the polymer melt. A boundary layer will form on all crystal surfaces, across which the diffusing species will travel into the bulk. As the diffusion process proceeds, the crystal size reduces (particle shrinkage) uniformly from all surfaces until all crystals are completely dissolved, assuming the solubility limit has not been reached.

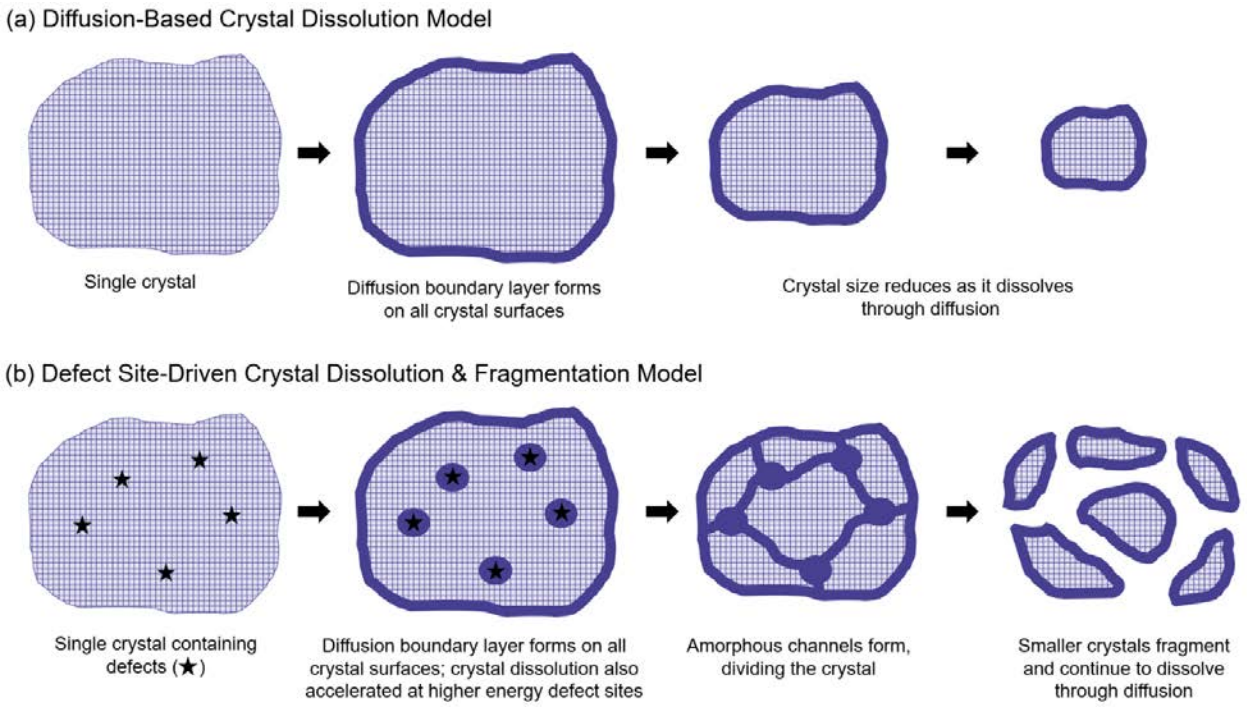

Figure 4.16. Models of crystal dissolution into polymer melts: (a) diffusion-based crystal dissolution and (b) defect-site driven crystal dissolution and fragmentation.

The diffusion process was readily visualized by SEM-EDX mapping, by tracking the location of the drug's chlorine signal. Under quiescent conditions, due to slow diffusivity in the viscous matrix, a gradient in chlorine signal arises on either side of a higher concentration plateau region (Figure 4.7b). The appearance of the plateau region suggests that ~30 μm was the initial width of the crystal being observed. Concentration, or (more accurately) activity gradients, provide the driving force for diffusion, whereby concentration is highest in the location of the (former) crystal. The driving force for diffusion decreases as the concentration gradient decreases further away from the crystal site. The observable gradient of molecularly dissolved indomethacin on each side of the plateau region is approximately 8 μm after 60 min of heating. In contrast, in the absence of heating, a sharp drop in chlorine content was observed, corresponding to the boundaries of the undissolved crystal (Figure 4.7a).

4.8.2 Defect Site-Driven Crystal Dissolution and Fragmentation Model

In addition to diffusion, a fragmentation process has been clearly identified. This mechanism was first suggested through the TEM imaging and microstructure characterization

performed on extrudates in our previous work[207] and is confirmed by the study of dissolution of crystals in films under quiescent isothermal conditions in this study. This crystal dissolution model is schematically depicted in Figure 4.16b. Upon formation of the diffusion boundary layer, diffusion rates are accelerated at higher energy defect sites at the crystal surface, likely due to a greater thermodynamic driving force for dissolution at these sites which results in a larger concentration gradient for diffusion. We propose that these higher energy sites are composed of defects intrinsic to the crystal, or representative of the typical surface energy heterogeneity associated with crystal surfaces. Channels form connecting these domains, due to the faster rates of dissolution and the stress fields associated with the defects. This channel formation process is the precursor to fragmentation of the crystal. Once the channels from different areas connect, the parent crystal breaks apart into smaller crystallites. The channel formation and fragmentation process forms new surfaces available for dissolution, which then continue to dissolve by diffusion and/or continued fragmentation by the same mechanism. Within the hot melt extrusion process, the stress fields may also be sites for particle breakage due to mechanical stresses imposed by mixing.

The MC simulations performed aid in interpreting the experimental results and validating the defect site-driven crystal dissolution and fragmentation model. The base case, presented in Figure 4.14a and Figure 4.14d, models the diffusion-based dissolution which would govern a relatively ideal crystal with no significant defects or variations in surface energy. As expected, simulations predict global dissolution which agrees well with the diffusion-based model from Figure 4.16a. Contrasted with this ideal system are the results from two cases which depict systems containing two common defect types. In Figure 4.14b and Figure 4.14e, a grain boundary is shown to facilitate dissolution at this crystal-crystal interface, leading to fragmentation and subsequent diffusion-based dissolution of the resulting fragments. Similarly, localized defects and accompanying stress fields (Figure 4.14c and Figure 4.14f) cause rapid dissolution emanating from the defect sites, channel formation and fragmentation, and diffusion-based dissolution of the various fragmented pieces. The excellent agreement between mathematical simulation results in Figure 4.14f and the conceptual model in Figure 4.16b supports the usefulness of the defect site-driven crystal dissolution and fragmentation model.

Fragmentation was observed at all length scales by various microscopy techniques. Surface imperfections and growth defects were observed in some crystalline starting material (Figure 4.2,

Figure 4.3), which is not unexpected, as such imperfections are common on the surface and in the bulk of organic crystals.[150,151] These growth imperfections served as sites for initiation of dissolution due to their higher surface energy, and dissolution would be accelerated at these sites. By polarized light microscopy (Figure 4.5), these growth imperfections served as sites for fragmentation early in the dissolution process. However, irregular dissolution (channel and hole formation) was observed even in the absence of visible growth imperfections, indicating that the defects do not need to be on the macro-scale in order to drive surface roughening and affect the dissolution process. By imaging with scanning electron microscopy, the partially dissolved crystallites showed little similarity to the bulk crystalline starting material (Figure 4.6). Crystal surfaces were often irregular and showed evidence of heterogeneous surface dissolution and channel formation.

Fragmented crystals were also observed showing a range of dissolution extent under transmission electron microscopy. Crystals were observed dissolving uniformly from all surfaces (particle shrinkage) as well as by channel formation, delamination, and fragmentation (Figure 4.8, Figure 4.9, Figure 4.10b, Figure 4.11). As the dissolution process proceeded, heterogeneity of the crystal surfaces were observed (Figure 4.12). Isolated crystallites were observed within the overall crystal structure, which showed evidence of rotation and orientation changes (Figure 4.12). Evidence that isolated crystallites from a single parent crystal dissolve at fairly uniform rates was observed through the appearance of fragment fields, consisting of similarly sized and structured particles, over significant distances (Figure 4.13).

4.8.3 Implications of a Fragmentation-Based Dissolution Mechanism

Imaging crystal dissolution in a viscous matrix under quiescent isothermal conditions allowed the fragmentation process to be captured because of the high viscosity of and consequently low diffusivity within the polymeric matrix. At the temperature condition selected, approximately 20°C above the glass transition temperature of the polymer and 30°C below the melting point of the drug, the dissolution process happened over a period of hours (depending on the size of the initial crystal). Also, because the crystal fragments don't move to any great extent, their microstructural progression could be observed. A fragmentation-based dissolution mechanism may be universally found in other solute-solvent systems, although it may not be observed because the particles disperse under typical experimental conditions. Similar dissolution mechanisms and

kinetics were demonstrated by Unwin and colleagues using atomic force microscopy (AFM) analysis of single crystals, which displayed surface roughening and increasing dissolution rates as dissolution progressed in an unstirred aqueous environment.[158,159] Alternatively, viscous solvents (e.g. polyethylene glycols, lipids, polymers) may have unique properties that bring about this mechanism.

Because of the exposure of new surfaces, fragmentation may enable dissolution to proceed more rapidly. Detection of the crystalline phase may also be hindered by the fragmentation process. For example, in powder x-ray diffraction, reduction in signal intensity due to decreased crystalline content and peak broadening due to decreased crystallite size (particularly into the low nanometer range) limit the detection of low levels of crystallinity.[109,147,148] In this system, the crystalline phase was detected through 2 hours by high temperature XRD (Figure 4.4), although crystals were observed by all microscopy techniques at longer dissolution times. Ultimately, the use of methods such as XRD may lead to an incorrect conclusion that the phase transformation is complete.

4.8.4 Application to Hot Melt Extrusion Process Modeling & Design

Modeling of HME is complex and has mainly focused on mass, energy, and momentum balances.[221] Recently, a HME process model has been developed which assumes a consistent number of particles and corresponding reduction of surface area during dissolution, and links process parameters with ASD formation.[222] The consideration of a fragmentation-based dissolution mechanism indicates that the number of particles, and thus surface area, may change during the dissolution process. A population balance-type model with a changing number of particles, due to both phase transformation and fragmentation, is therefore likely necessary to accurately capture the dynamics of the dissolution process.

Mechanical damage serves as a complementary source of lattice defects and particle breakage, which would accelerate the formation of dissolution surfaces. Mechanically-induced defects or particle breakage may arise due to mixing in the extruder.[140,207] Such mechanical contributions would be expected to have a significant impact on the dissolution mechanism of crystals within a hot melt extrusion process, particularly with screw configurations consisting of dispersive mixing/kneading elements.

Particle size distribution is known to play a significant kinetic role in a hot melt extrusion process.[126,140] The identification of a fragmentation mechanism driven by defects further suggests

that it is critical to have control of the crystal quality (i.e. defect density), in addition to the particle size distribution of the starting crystalline material, in order to have adequate control of an HME process. A crystallization process which produces particles with higher defect density yields a faster dissolution rate, as demonstrated by Burt and Mitchell.[154] Our work would further suggest that these defects served as sites for initiation of fragmentation, yielding more surfaces for dissolution, thus increasing dissolution rate.

4.9 Conclusion

A fragmentation-based mechanism for dissolution of organic crystals into a polymer melt was identified based on microscopic observation under multiple length scales. Defects intrinsic to the crystal, or induced by mechanical means, are hypothesized to be the sites of initiation of the crystal dissolution process. Stress fields from these defect sites further accelerate the dissolution process, forming channels and ultimately fragmenting the parent crystal into smaller crystallites. This fragmentation-based mechanism has implications for modeling of crystal dissolution into polymer melts, since the number of crystalline particles may change during the phase transformation, and not all surfaces may dissolve uniformly. In addition to the particle size distribution and corresponding available surface area for dissolution, the presence of intrinsic and induced defects affects the dissolution rate. Thus, crystal quality may be an unexplored critical material attribute.

CHAPTER 5. AMORPHOUS SOLID DISPERSIONS CONTAINING RESIDUAL CRYSTALLINITY: INFLUENCE OF SEED PROPERTIES AND POLYMER ADSORPTION ON DISSOLUTION PERFORMANCE

This chapter is a reprint with minor modifications of a manuscript published in *European Journal of Pharmaceutical Sciences* in February 2020 with the same title by: Dana E. Moseson, Andrew S. Parker, Stephen P. Beaudoin, and Lynne S. Taylor. Reprinted with permission from Elsevier. DOI: 10.1016/j.ejps.2020.105276

5.1 Abstract

The solubility advantage of amorphous solid dispersions (ASDs) is contingent upon supersaturation being generated and maintained. If crystals are present within an ASD, these crystals directly result in lost solubility advantage, and may also seed crystal growth leading to desupersaturation. The goal of this study was to evaluate the impact of residual crystals on ASD supersaturation profiles. Indomethacin-copovidone (PVPVA) ASDs with different levels of residual crystallinity were manufactured by hot melt extrusion (HME). PVPVA at 5 and 50 µg/mL was found to be a highly effective nucleation and crystal growth inhibitor of indomethacin at high supersaturation. Evidence of polymer adsorption onto indomethacin crystals was observed by atomic force microscopy and scanning electron microscopy. HME ASDs containing 0-25% residual crystallinity demonstrated lost solubility advantage, along with minimal desupersaturation during non-sink dissolution testing. While bulk seeds did not properly represent the impact of residual crystals, extensive polymer adsorption onto residual seed crystals resulted in poisoned crystal growth, limiting the potential dissolution performance consequences. Several risk factors related to the presence of residual crystallinity were identified: polymeric crystal growth inhibition effectiveness, seed properties, and supersaturation conditions.

5.2 Introduction

Accessing the solubility advantage of the amorphous form of a drug requires supersaturation to be generated and maintained.[31,93] Supersaturating formulations hold the promise of achieving bioavailability enhancement over their crystalline counterparts, as faster dissolution rates and higher solution concentrations can theoretically be achieved.[223,224] Supersaturated solutions are metastable and are prone to crystallization, thus prolonged maintenance of supersaturation in the gastrointestinal (GI) tract may be difficult.[225] Amorphous solid dispersions (ASDs) are a popular supersaturating formulation strategy, and consist of an amorphous drug and polymer formulated as a molecular-level dispersion.[226] The inclusion of a polymer in the ASD formulation can be used to inhibit crystallization from supersaturated solutions, even at low concentrations.[21,112,227–229] Proposed mechanisms for inhibition of nucleation or crystal growth by the polymeric precipitation inhibitor include specific interactions between the dissolved polymer and drug molecule and surface adsorption of polymer molecules onto crystalline drug particles.[21,230]

Non-sink conditions are essential for assessing the *in vitro* dissolution performance of a supersaturating system, as this allows the achievable supersaturation to be characterized, as well the kinetics of crystal nucleation and growth.[111,112,231,232] Non-sink dissolution behavior of ASDs is typically assessed by evaluating the release profile of a fresh sample, presumed to be completely amorphous, under non-sink conditions in simple or biorelevant media.[233] If crystals are present within an ASD, these crystals directly result in lost solubility advantage (i.e. it is assumed that they cannot dissolve due to rapid generation of supersaturation),[111] and may also impact dissolution performance in other ways. In solution, as a consequence of secondary nucleation or growth of seed crystals, desupersaturation results in a reduced amount of dissolved drug available for absorption.[17,100,101]

Crystallinity in the ASD may be residual from the manufacturing process or a result of recrystallization from the matrix. As it is not always practical to completely avoid residual crystallinity, or prevent crystallization upon product storage, specifications are set for allowable crystallinity, typically on a mass basis. However, % crystallinity is an arbitrary indicator of product quality, as many factors contribute to solid- and solution-state crystallization. For example, it has been shown that amorphous drugs have a wide range of crystallization tendencies and that the

intrinsic properties of crystal seeds drive crystal growth.[16,17,234] Further, a wide range of polymer properties play a role in stabilizing the solid state as well as inhibiting crystallization during dissolution.[18–21] Literature studies of crystalline content are principally concerned with crystals originating from the matrix, following manufacturing or storage.[92,96,99,235] As the origin of that crystallization (e.g. drug loading above the solubility/miscibility limit, moisture-induced phase separation) represents a nucleation-based failure mode, the potential product performance effects resulting from residual crystals, in which crystal growth would be the dominant pathway, may show different trends.

Non-sink dissolution tests offer a powerful way of detecting differences resulting from processing variation and critical quality attributes, such as residual crystallinity, and assessing product performance.[97,111,127,236–238] However, the impact of crystallinity within an ASD is inherently challenging to evaluate. Commonly, bulk crystal seeds or a physical mixture of fully amorphous with fully crystallized ASD fractions are often used as a surrogate for crystallinity that originated from within the matrix or is residual from the process.[17,127,128,238,239] In practice, crystal characteristics such as particle size, surface area, or defect density within the ASD matrix may not be properly represented by external bulk crystal seeds.[240,241] In our previous work, residual crystals embedded within hot melt extrusion (HME) samples or polymer films were imaged by transmission electron microscopy (TEM), and it was found that many crystals were on the order of 5-100 nm and highly defective.[207,242] Further, the use of bulk seeds or physical mixtures neglects the role of the polymer on the dissolution behavior. The intimate mixing achieved by a HME process may alter crystal growth behaviors, such as by polymer adsorption to crystal surfaces, thus altering kinetics.[230]

We seek to address several questions with respect to non-sink dissolution performance using indomethacin (IDM) and copovidone (PVPVA) as a model drug-polymer system: 1) Do residual crystals represent a failure mode of an ASD? 2) What are the consequences of these residual crystals on product performance? 3) Are there certain characteristics of the crystals or formulation which permit some degree of residual crystallinity in the ASD? 4) What impact does the polymer have on these crystals? Essentially, could crystallinity in an ASD ever be “inert” and have no impact on the dissolution performance of a supersaturating system? To address these questions, the impact of crystal seeds on non-sink dissolution performance of ASDs was assessed through two study designs. First, the impact of bulk IDM crystal seeds on maintenance of

supersaturation and the effect of polymeric additives (PVPVA) on crystal growth inhibition was studied. Second, non-sink dissolution performance of IDM/PVPVA ASDs prepared with various levels of residual crystallinity by a HME process was assessed and compared with dissolution performance of externally seeded samples. Atomic force microscopy (AFM) and scanning electron microscopy (SEM) imaging studies were utilized to characterize polymer adsorption and growth patterns of residual crystal seeds under non-sink conditions.

5.3 Experimental Section

5.3.1 Materials

Indomethacin (IDM, T_m = 160°C) was obtained from ChemShuttle (Hayward, CA) and copovidone, also known as polyvinylpyrrolidone/vinyl acetate copolymer (PVPVA, Kollidon VA64, T_g = 105°C), was a gift from BASF (Florham Park, NJ). All other materials used were of reagent grade.

5.3.2 Methods

5.3.2.1 Processing and Characterization of IDM Crystals

IDM crystals (bulk) were used after passing through a 60 mesh sieve (250 μm). A D_{50} particle size of 21.9 ± 0.3 μm was determined in triplicate using a Mastersizer 3000 particle size analyzer with Aero S attachment (Malvern Panalytical, Malvern, UK). BET surface area of 0.14 ± 0.08 m^2/g was determined in triplicate (TriStar II, Micromeritics, Norcross, GA).

For later dissolution and imaging studies, mechanical damage was applied to bulk crystals by cryomilling approximately 1 g of IDM crystals under liquid nitrogen using 5 minutes of pre-cooling time, followed by 2 minutes of grinding time at 10 Hz using a 6750 Freezer/Mill (SPEX, Metuchen, NJ).

5.3.2.2 Preparation of ASDs and Physical Mixtures

HME ASDs were prepared using an Xplore Pharma Melt Extruder (Geleen, The Netherlands), assembled with a 5 mL volume barrel with co-rotating conveying screw (refer to Appendix C Figure C.1a for a schematic of the extruder). Control of product melt temperature is

obtained through selection of operating set temperatures, and residence time is independently controlled through the use of the recirculation loop, thus ASDs of varying residual crystallinity were prepared by operating at different points within the process operating design space (Appendix C Figure C.1b). Specifically, operating conditions within the suspension regime were used wherein insufficient temperature and/or residence time was supplied in order to produce samples with residual crystallinity. Eight HME ASDs were used for this study, and basic process parameters and characterization are reported in Table 5.1. Full preparation details and solid state characterization were described previously.[140] Residence time is considered the point when the recirculation valve is opened and the melt begins extruding through the die. In all experiments, the total extrusion time ranged from the noted time until 2-4 minutes later, depending on the material flow characteristics (viscosity).

Table 5.1. Preparation details and crystallinity characterization of IDM/PVPVA HME ASDs used.

Sample ID	Process Set Temperature (°C)	Product Melt Temperature Range (°C)	Residence Time (min)	Appearance[1]	% Crystallinity by PXRD[1]
161-2	166	161 ± 1	2	Clear	0% (<LOD)
134-2	138	134 ± 1	2	Cloudy	1.8%
131-2	135	131 ± 1	2	Very cloudy	3%
131-5	135	131 ± 1	5	Cloudy	<LOQ
126-2	130	126 ± 1	2	Very cloudy	7%
121-2	126	121 ± 1	2	Opaque	16%
121-20	126	121 ± 1	20	Cloudy with visible crystals	1.9%
117-2	122	117 ± 1	2	Opaque	25%

[1] As determined in our previous publication; limits of detection and quantification were determined to be 0.4% and 1%. The % crystallinity reported refers to the drug total content.[140]

An amorphous solid dispersion of 1:1 weight ratio IDM/PVPVA was prepared by solvent evaporation (SE) out of methylene chloride and methanol (2:1 v:v) using a Brinkmann Rotavapor-R (Buchi, New Castle, DE) under reduced pressure at 60°C. The sample was then dried under vacuum and cryomilled for 60 seconds of grinding time at 10 Hz to form a fine powder. Additionally, a physical mixture (PM) of 1:1 IDM/PVPVA was prepared by tumble blending for

use in dissolution studies. A 60-140 mesh sieve fraction (106-250 μm) of all HME and SE ASDs was used for all dissolution studies.

All ASDs were stored in the refrigerator under desiccant immediately following production to arrest any possible crystal growth. No changes to crystallinity levels were observed over time by subsequent powder X-ray diffraction (PXRD) measurements.

5.3.2.3 Dissolution Studies and Solubility Measurements

5.3.2.3.1 Determination of Crystalline and Amorphous Solubility

The equilibrium solubility of IDM was determined by stirring excess IDM crystals in 50 mM pH 4.5 acetate buffer at 37°C for 72 hours (n = 3). This media reflects the buffer used for all dissolution studies. Concentrations were measured against a calibration curve (R^2 = 0.999) of the absorbance at 450 nm subtracted from absorbance at 317 nm using 10 mm UV fiber optic dip probe and SI Photonics 400 UV/Vis spectrophotometer (SI Photonics, Tuscan, AZ). The same procedure was performed in the presence of 50 μg/mL PVPVA to determine the influence (if any) of the polymer on the crystalline solubility.

The amorphous solubility was determined by a solvent shifting UV extinction method to detect the appearance of liquid-liquid phase separation (LLPS), as previously reported.[30,243] Briefly, a stock solution of IDM in methanol (5 mg/mL) was added to the 15 mL of buffer solution using a syringe pump at a rate of 80 μL/min (n = 3). Using the UV fiber optic dip probe, light scattering was monitored every 10 seconds and plotted against the concentration of drug in the vial. The formation of the colloidal phase results in an increase in scattering, and this concentration is reported as the amorphous solubility. The same procedure was performed in the presence of 50 μg/mL PVPVA added to the buffer solution to determine the influence (if any) of the polymer on the amorphous solubility. Paired, one-tailed student's t-test were performed in Microsoft Excel.

5.3.2.3.2 Dissolution Methods

All dissolution studies were conducted in triplicate using 200 mL jacketed beaker of 50 mM pH 4.5 acetate buffer at 37°C with a magnetic stir bar used at 300 rpm to provide a gentle vortex. A 10 mm UV fiber optic dip probe and SI Photonics 400 UV/Vis spectrophotometer (SI Photonics, Tuscan, AZ) were used to monitor concentrations over time. To account for scattering

induced by particulates in the dissolution media, concentrations were measured against a calibration curve (R^2 = 0.999) of the absorbance at 450 nm subtracted from absorbance at 317 nm. A maximum theoretical IDM concentration of 50 µg/mL representing a moderately high supersaturation condition (S = 6, where S is the ratio of the solution concentration to the equilibrium solubility), was selected for dissolution studies, as it would enable access to both dissolution and crystallization mechanisms as a robust non-sink condition (with respect to crystalline solubility). Dissolution experiments were monitored for 12 hours.

5.3.2.3.3 Nucleation and Crystal Growth Studies

A concentration of 50 µg/mL was created by anti-solvent addition of a concentrated methanolic solution of IDM into buffer. Crystal seeds (0-10 mg) were added to the solution, representing supplemental IDM concentrations of 0-50 µg/mL. The experiment was conducted for up to 12 hours to monitor either the nucleation induction time (in absence of seeds) or desupersaturation rate (in the presence of seeds). Experiments were repeated with 5 µg/mL and 50 µg/mL PVPVA added to the buffer.

5.3.2.3.4 Non-Sink Dissolution to Maintain Constant IDM Concentration

HME ASD powder was added into buffer to achieve a maximum theoretical concentration of IDM of 50 µg/mL.

Mixtures of SE ASD and PM powders were added in various ratios to achieve a maximum theoretical concentration of IDM of 50 µg/mL and PVPVA of 50 µg/mL. Ratios are reported in the % of crystalline drug (e.g. 0% represents 100% SE ASD, 10% represents 10% PM mixed with 90% SE ASD), 100% represents 100% PM).

Refer to Appendix C for detailed calculations.

5.3.2.3.5 Non-Sink Dissolution to Maintain Constant IDM Supersaturation

HME ASD powders containing high levels of residual crystallinity were added into buffer to achieve a maximum theoretical concentration of amorphous IDM of 50 µg/mL. Due to the

presence of crystallinity within the sample, the total dose of IDM (both amorphous and crystalline) was in excess of this amount.

SE ASD powder was added to achieve a maximum theoretical concentration of IDM of 50 µg/mL. Additional bulk crystal seeds were added, representing additional IDM concentrations of 10-50 µg/mL, equivalent to 20-100% crystals with respect to the amorphous dose.

Refer to Appendix C for detailed calculations.

5.3.2.4 Atomic Force Microscopy (AFM)

Crystal samples for AFM were prepared by affixing bulk IDM crystal powder onto a 15 mm steel AFM sample puck. Buffer solutions at 0 µg/mL, 5 µg/mL, and 50 µg/mL of PVPVA were added to the crystals on the pucks and equilibrated for 4 days prior to imaging. These solutions also contained 3 µg/mL IDM, which was prepared through anti-solvent addition out of ethanol into the buffer solutions. Crystal surfaces were probed by AFM using a MultiMode 8 (Bruker Corporation, Technology Forest, TX) operated in tapping mode with an NPG probe, cantilever C in all three media. Measurements were performed in the presence of buffer solutions using a fluid cell.

5.3.2.5 Crystal Dissolution and Crystal Growth Experiments for SEM Imaging

To examine the effect of the polymer on IDM crystals of multiple origins and seek microstructural information on residual crystal seeds found in HME ASDs, a series of experiments were performed to simulate crystal dissolution or crystal growth over a 24 hour period. Table 5.2 breaks down the amount of IDM or PVPVA added from the sample or directly to the solution. As the crystalline solubility of IDM in buffer is well below the amount of sample added, the crystal dissolution conditions allow the crystals to be isolated after a small amount of dissolution of the crystal or after the ASD has completely dissolved. The crystal growth conditions allow for the bulk crystals to grow from the high supersaturation added to the buffer solution. In the case of the ASD, the high supersaturation conditions are in addition to the ASD which dissolves during the experiment, which allows the residual crystals to grow. To retrieve crystals following the crystal dissolution or crystal growth experiments, the dissolution liquid was sampled, then the liquid was wicked away with filter paper to leave solids deposited on double-sided carbon tape. Concentration

vs time measurements were made for each of the crystal dissolution and crystal growth conditions to enable comparison of the SEM images to the dissolution/growth profiles.

Table 5.2. Crystal Dissolution and Crystal Growth Sample Matrix

Experiment	Sample	Sample Concentration		Solution Concentration		Condition
		IDM	PVPVA	IDM	PVPVA	
a2	IDM bulk crystal	50 µg/mL	---	---	---	Crystal Dissolution
a3	IDM bulk crystal	50 µg/mL	---	---	50 µg/mL	Crystal Dissolution
a4 (*)	IDM bulk crystal	50 µg/mL	---	50 µg/mL	---	Crystal Growth
a5 (*)	IDM bulk crystal	50 µg/mL	---	50 µg/mL	50 µg/mL	Crystal Growth
b1 (*)	HME ASD 117-2	50 µg/mL	50 µg/mL	---	---	Crystal Dissolution
b2 (*)	HME ASD 117-2	50 µg/mL	50 µg/mL	50 µg/mL	---	Crystal Growth
c2	IDM mechanically damaged crystal	50 µg/mL	---	---	---	Crystal Dissolution
c3	IDM mechanically damaged crystal	50 µg/mL	---	---	50 µg/mL	Crystal Dissolution
c4 (*)	IDM mechanically damaged crystal	50 µg/mL	---	50 µg/mL	---	Crystal Growth
c5 (*)	IDM mechanically damaged crystal	50 µg/mL	---	50 µg/mL	50 µg/mL	Crystal Growth

(*) Samples selected for chemical identification by Raman spectroscopy.

Crystals were imaged by SEM using a FEI TeneoVS scanning electron microscope (FEI Company, Hillsboro, Oregon) in OptiPlan mode with T1 and T2 detectors to capture backscatter and secondary electron images. Operating conditions were 5 kV accelerating voltage, 0.10 nA current, and ~2 mm working distance. Samples were fixed onto SEM stubs and sputter-coated with platinum for 60 seconds.

Chemical identification of a subset of crystal dissolution and crystal growth particles was performed with a Morphologi G3SE-ID Raman-coupled microscope (Malvern Panalytical, Malvern, UK). Liquid samples as described above were loaded onto microscope slides and particles were automatically identified with the Morphologi 8.20 software. A minimum of 5 particles for each sample were manually targeted for chemical identification. The presence of the γ and α forms of IDM are uniquely identified peaks at 1700 and 1650 cm^{-1}, respectively.[244,245]

5.3.2.6 Transmission Electron Microscopy (TEM)

Bright-field transmission electron micrographs were acquired in an FEI Tecnai G20 electron microscope (FEI, Hillsboro, Oregon, USA) equipped with a LaB6 source, X-max 80 mm^2 silicon drift detector (Oxford Instruments, Abingdon, Oxfordshire, UK), and operated at 200 keV, 100 µm aperture, and a spot size of 3. Extrudate pieces were placed on the 300 mesh carbon-coated copper TEM grid (SPI supplies, West Chester, PA) by gently touching/wiping the interior of the vial lid, which contained particulates fragmented from the bulk extrudate rods, with the carbon-coated side of the grid. Fast Fourier Transform (FFT) analysis was performed using the Gatan DigitalMicrograph 3.21 software suite (Pleasanton, CA).

5.4 Results

5.4.1 Crystalline and Amorphous Solubility

The crystalline and amorphous solubility of IDM in 50 mM pH 4.5 acetate buffer at 37°C was found to be approximately 8 and 80 µg/mL (Appendix C Figure C.2), and did not vary significantly in the presence of PVPVA (p-value > 0.05).

5.4.2 Nucleation and Crystal Growth Studies

Crystallization can be described into two separate rate processes: nucleation and growth.[227] In the absence of PVPVA, IDM nucleates in the pH 4.5 buffer system at S = 6 in under an hour, based on the loss of supersaturation observed after about 40 min (Table 5.1a). When crystal seeds are added, seed growth occurs, consuming the available supersaturation. As higher levels of seeds are added, the growth rates increase, as indicated by the steeper decline in the concentration as a function of time profile, indicating more rapid desupersaturation.

The rate of crystal growth is approximately proportional to the amount of crystal seeds added (Figure 5.2). The crystal growth rate, R_G, or the mass m deposited on crystal surface per unit time t, can be described by the following equation (Eq. 1)

$$R_G = Ak_G S^g = \frac{dm}{dt} \qquad \text{(Eq. 11)}$$

where S is the degree of supersaturation, A is the crystal surface area (proportional to seed amount), k_G is the growth rate coefficient, and g is the overall growth order.[230] Amongst other factors, the presence of polymer can alter both k_G and g.[246,247] Mechanical forces (such as those experienced during HME or cryomilling, as performed later in this study), can affect the surface area term by changing the particle size of crystals, creating defects, and generating new sites for growth.[248,249]

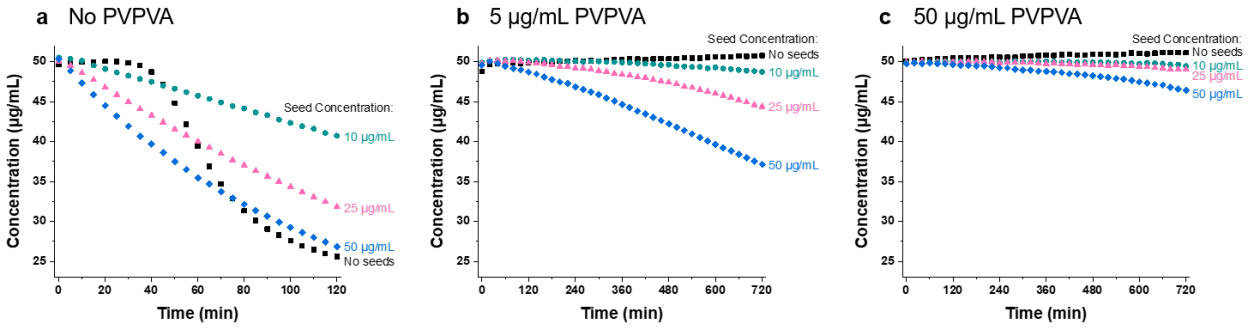

Figure 5.1. Supersaturation maintenance of 50 µg/mL IDM (S = 6) in the absence and presence of bulk crystal seeds in buffer with (a) 0 µg/mL, (b) 5 µg/mL, and (c) 50 µg/mL PVPVA.

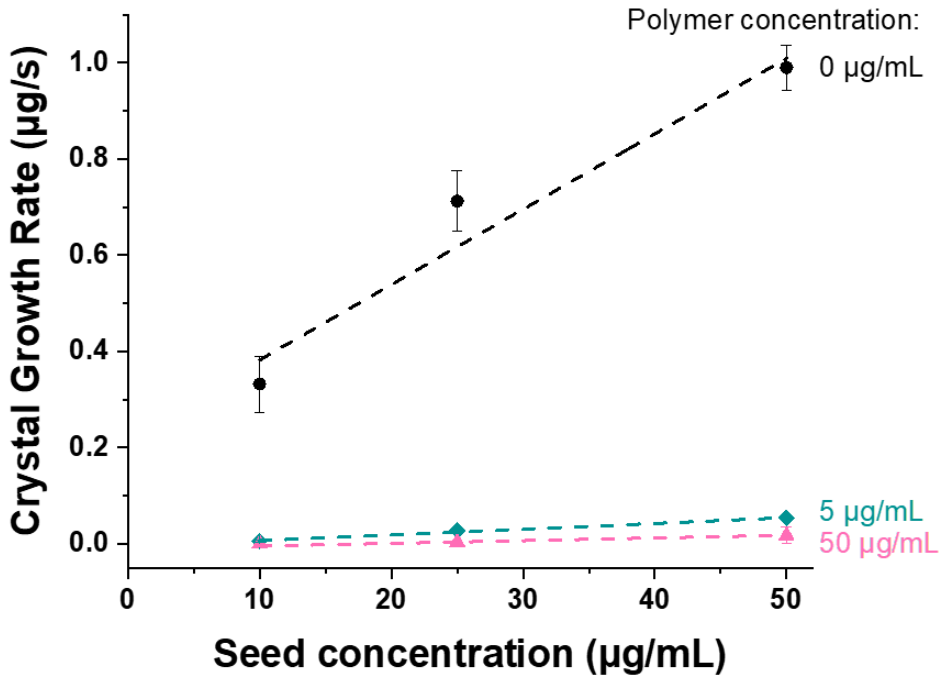

Figure 5.2. Crystal growth rates of IDM bulk seeds in the absence and presence of PVPVA. Dashed lines are added as a guide to the eye.

The supersaturation is maintained for >12 hours by PVPVA at polymer levels of 5-50 µg/mL (in the absence of crystal seeds), demonstrating that the polymer is a highly effective nucleation inhibitor of IDM at this degree of supersaturation, S = 6 (Figure 5.1b,c). When seeds are added to the solution, desupersaturation is observed, demonstrating that the crystal growth of seeds is occurring, albeit at reduced rates in the presence of PVPVA. The effectiveness (E_G) of the polymer at inhibiting the crystal growth of IDM seeds can be expressed using the following equation (Eq. 2)

$$E_G = \frac{R_{G,np}}{R_{G,p}} \qquad \text{(Eq. 12)}$$

where $R_{G,np}$ and $R_{G,p}$ are the crystal growth rates in the absence and presence of polymer.[250] A value of $E_G > 1$ indicates that the polymer is effective at disrupting growth. At the highest seed level (50 µg/mL), the polymer effectiveness ratio (E_G) was found to be 18 (for the low PVPVA concentration, 5 µg/mL) and 56 (for the high PVPVA concentration, 50 µg/mL), demonstrating that the polymer is a highly effective crystal growth inhibitor of IDM.

5.4.3 Non-Sink Dissolution of HME ASDs Containing Residual Crystallinity

The eight HME samples containing 0-25% crystallinity show dissolution profiles of similar shape (Figure 5.3), wherein the concentration increases at a similar rate, and then a near-plateau is reached. Concentrations continue increasing slightly during the remainder of the monitoring period for all samples of <2% crystalline content (Figure 5.3b). For samples of >3% crystalline content (Figure 5.3a), slight desupersaturation is noted over the monitoring period. Desupersaturation corresponds to the crystal growth rate being greater than that of the dissolution rate. Samples with higher levels of crystallinity reach lower maximum achieved concentrations.

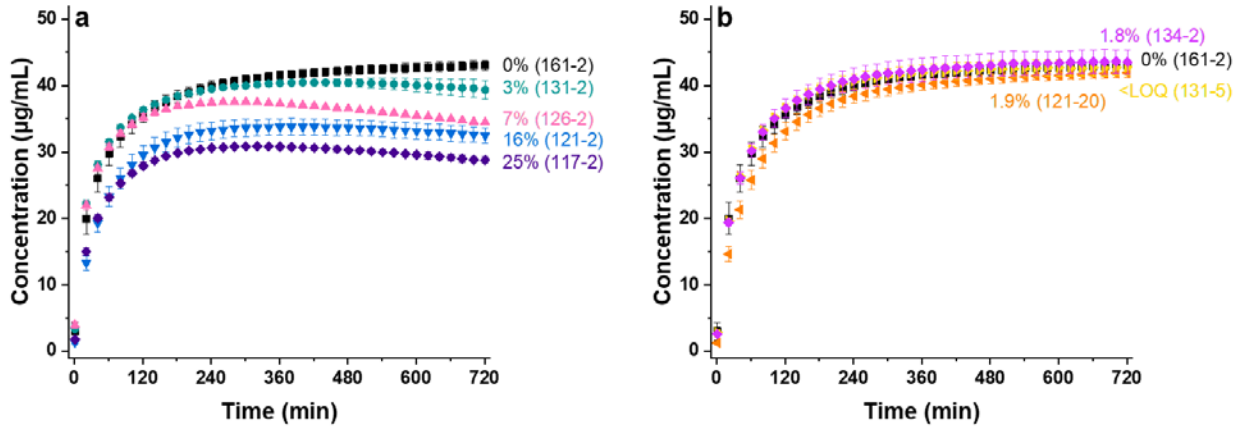

Figure 5.3. Non-sink dissolution of IDM/PVPVA HME ASDs containing (a) 0-25% and (b) <2% residual crystallinity.

5.4.4 Non-Sink Dissolution of SE ASDs and Bulk Crystal Seeds

Non-sink dissolution was performed on physical mixtures of SE ASD/PM prepared to yield a total amount of IDM and PVPVA of 50 µg/mL (compositionally equivalent to the HME samples), enabling direct comparison of dissolution profiles with those of the HME samples. Qualitatively equivalent dissolution profiles were obtained (Figure 5.4), with the maximum concentration achieved trending with the proportion of amorphous material. Therefore, the decrease in achievable concentration can be attributed to the proportion of crystalline content. Interestingly, desupersaturation is not observed during the monitoring period indicating that the dissolution rate is greater or equal to the crystal growth rate at all time points. This contrasts with the observation of the HME samples (Figure 5.3). The crystal-free SE ASD dissolution profile is equivalent to that of the HME ASD 161-2 (Appendix C Figure C.3).

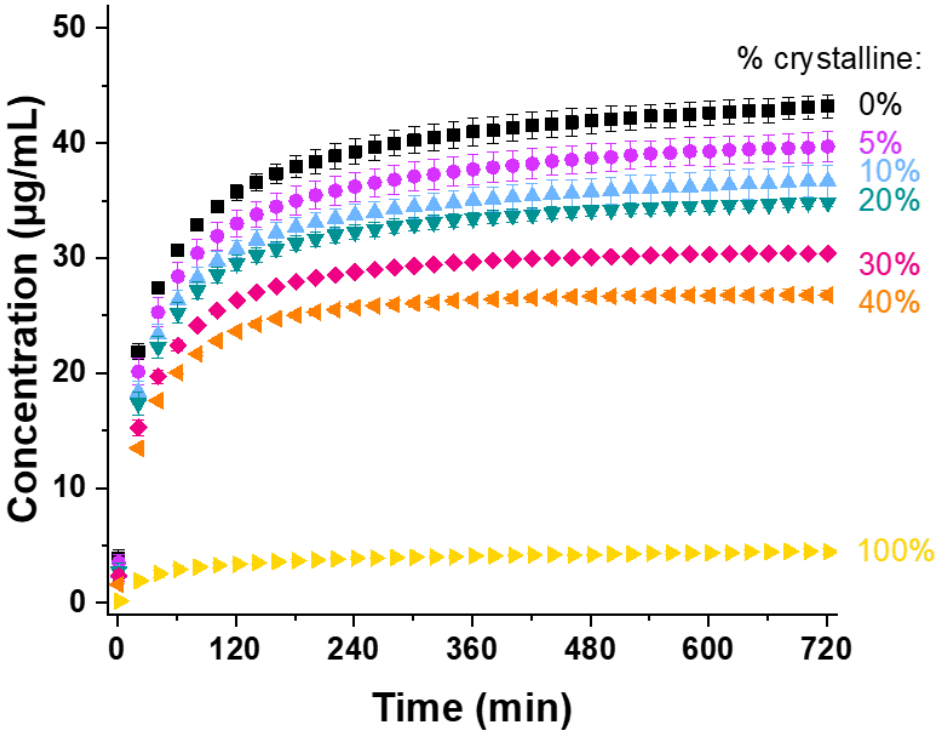

Figure 5.4. Non-sink dissolution of physical mixtures IDM/PVPVA SE ASD and PM yielding various levels of crystalline content. Total concentration of both IDM and PVPVA is maintained at 50 µg/mL.

To further investigate the observation of crystal growth rates varying between the HME samples and equivalent mixtures prepared from SE ASD/PM (from bulk IDM crystals), dissolution experiments were conducted at equivalent supersaturation conditions with varying crystalline content. The same quantity of SE ASD was added to each experiment to yield 50 µg/mL IDM, and additional bulk crystal seeds were added for an additional possible IDM concentration of 10-50 µg/mL. This scenario allows for a constant driving force for dissolution across all experiments based on a constant amount of amorphous IDM, a condition which was not met in the previous experiments. Although the total amorphous IDM does not dissolve during the monitoring period even in the absence of seeds, no (or minimal) desupersaturation is noted (Figure 5.5), indicating that the dissolution rate is greater than that of the crystal growth rate at all time points.

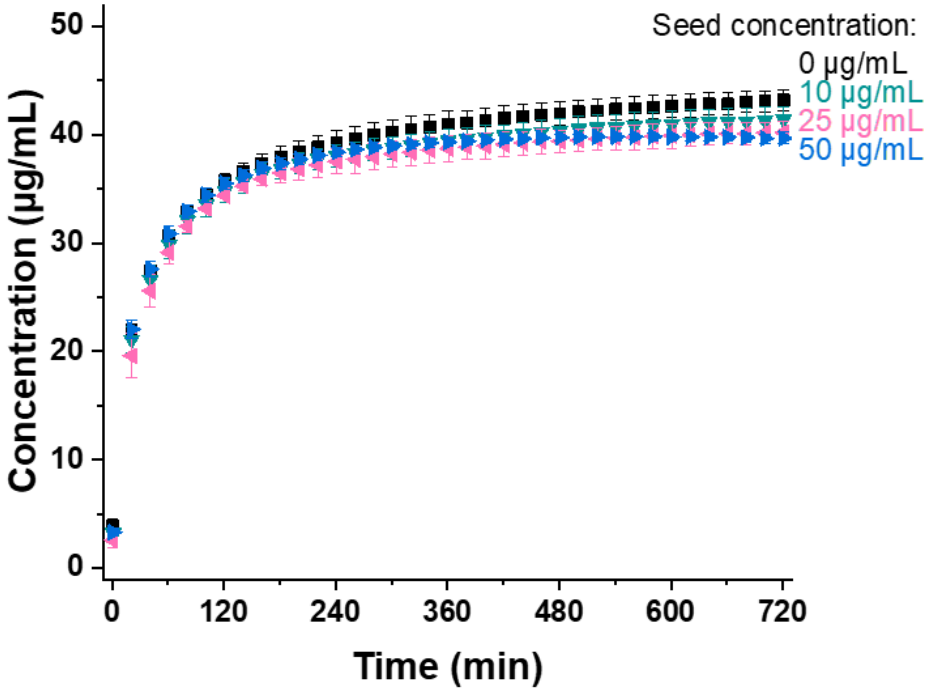

Figure 5.5. Non-sink dissolution of IDM/PVPVA SE ASD at a theoretical maximum concentration of 50 µg/mL. Additional bulk IDM crystal seeds added at concentrations of 10-50 µg/mL, corresponding to 20%, 50%, and 100% of the amorphous dose.

5.4.5 Non-Sink Dissolution of HME ASDs to Examine Supersaturation Effects

The impact of crystals on ASD dissolution under conditions of constant supersaturation potential were examined (Figure 5.6). This was accomplished using a crystal-free (161-2) HME ASD at 50 µg/mL and several HME ASDs containing high levels of crystalline content but altering the dose to keep the level of amorphous IDM constant (at 50 µg/mL). This has the effect of changing and controlling the supersaturation level generated as well as altering crystallization kinetics to gain further insight into crystal properties. (A comparison of the four samples with crystalline content at both dose levels used is found in Appendix C Figure C.4.) With increasing crystalline content, despite an equivalent amount of amorphous material available for dissolution, the dissolution rate and extent is reduced, suggesting that the crystals are consuming some of the available supersaturation. Desupersaturation is then observed for each sample containing crystalline content.

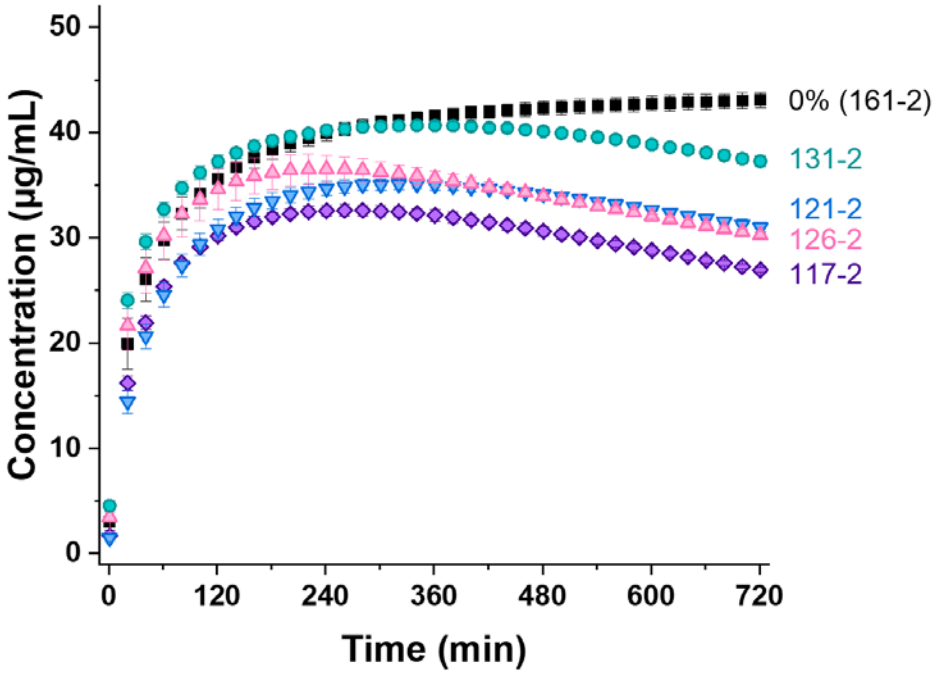

Figure 5.6. Dissolution profiles of ASDs at a constant supersaturation potential (where amorphous IDM is held constant at 50 ug/mL in the dose): crystal-free ASD 161-2 dosed at 50 µg/mL, 131-2 at 51.5 µg/mL, 126-2 at 60 µg/mL, 121-2 at 54 µg/mL, and 117-2 at 60 ug/mL.

5.4.6 Adsorbed Polymer Surface Coverage

Adsorption of PVPVA at different concentrations onto IDM crystals was observed via AFM (Figure 5.7). Bulk IDM crystal surfaces in the absence of polymer (Figure 5.7a,d) are generally smooth with occasional topographical features, consistent with SEM images (Figure 5.8a1). At lower polymer concentration (5 µg/mL, Figure 5.7b,e), spheroidal elevations in the topography, corresponding to contrast in the phase plot, indicate likely polymer adsorption, most clearly observed in the bottom left quadrant of the image. These polymer globules exhibit moderate surface coverage, with evidence of adsorption across much of the surface, yet are distinct and non-overlapping. In contrast, in the presence of higher PVPVA concentration (50 µg/mL), polymer adsorbs on the crystal surface with a high degree of surface coverage (Figure 5.7c,f). Measurements between the centers of adsorbed globules reveal mean distances of 160 ± 50 nm for the low polymer concentration (n = 30) and 70 ± 20 nm for the high polymer concentration (n = 100).

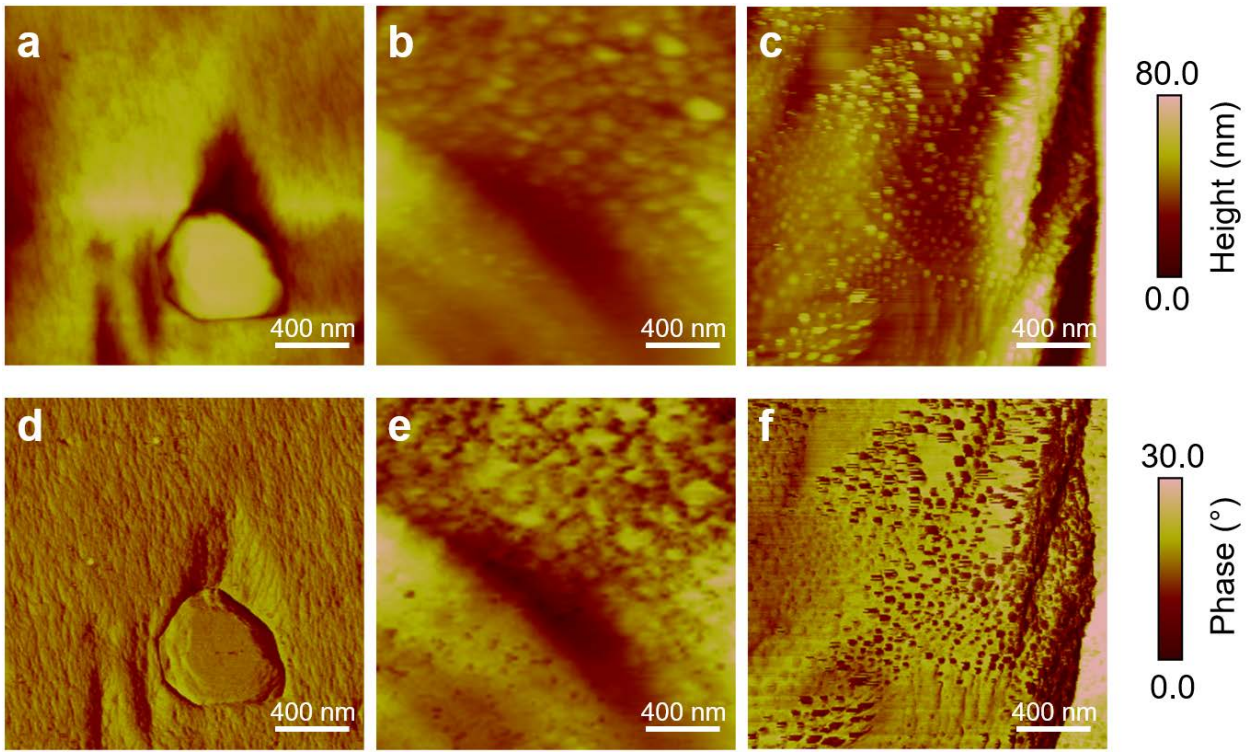

Figure 5.7. AFM topographical and phase lag plots showing adsorbed polymer surface coverage onto IDM crystal surfaces at (a,d) 0 µg/mL PVPVA, (b,e) 5 µg/mL PVPVA, and (c,f) 50 µg/mL PVPVA.

5.4.7 Polymer Impacts on Crystal Dissolution and Crystal Growth of Seeds of Different Origins

Differences in the microstructure of dissolving crystals and crystal seeds grown from supersaturated solutions are observed in the absence and presence of polymer (50 µg/mL). The impact of the polymer on bulk crystal surfaces under conditions of dissolution or growth was observed by SEM (Figure 5.8). Despite the generally smooth surfaces of the neat bulk IDM crystals (Figure 5.8a1), the crystal surface becomes much rougher, showing etching pits, when partially dissolved in the absence of polymer (Figure 5.8a2). In the presence of polymer (Figure 5.8a3), the etching pits have rounded features, indicating that polymer is interacting with the crystal surfaces during the dissolution process. At high supersaturation (an additional 50 µg/mL of IDM pre-dissolved in the media), IDM crystals grow as smooth, plate-like crystals in the absence of polymer (Figure 5.8a4) and show disrupted growth patterns consisting of striated surfaces and small needle-

like protrusions in the presence of polymer (Figure 5.8a5). The distance between step pinnings observed on the bulk crystal surface were measured at 270 ± 100 nm (n=20).

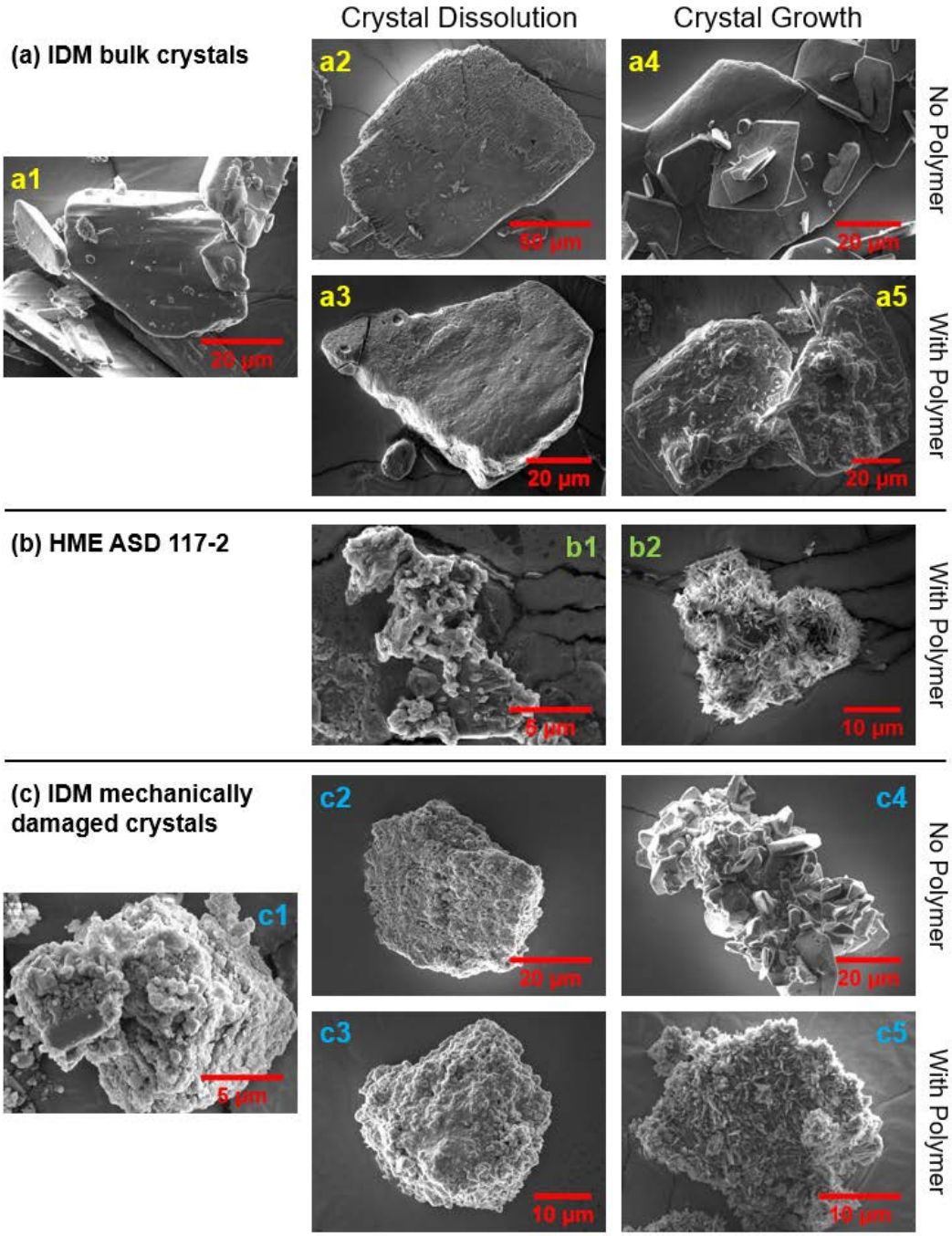

Figure 5.8. SEM images of IDM bulk crystals (A), residual crystals from 117-2 HME ASD (B), and mechanically damaged crystals (C), following 24 hours of dissolution or crystal growth. Representative dissolution profiles of each crystal dissolution or crystal growth sample are included in Figure S5.

Bulk crystals were then mechanically damaged by cryomilling, and subjected to the same dissolution and growth conditions. For dissolution, little difference is apparent based on the absence (Figure 5.8c2) or presence (Figure 5.8c3) of polymer, as the crystals retain the highly irregular appearance of the starting mechanically damaged crystals (Figure 5.8c1). However, when highly supersaturated conditions were applied (an additional 50 µg/mL of IDM), growth patterns are easily distinguished between the samples. In the absence of polymer (Figure 5.8c4), the sample is polycrystalline with multiple crystallites with reasonably well defined crystal facets. In the presence of polymer (Figure 5.8c5), small, irregular needle-like growth is observed from all surfaces, where the crystallites have widths of 170 ± 60 nm (n = 20). Thus, the presence of the polymer disrupts the growth patterns of both the bulk and mechanically damaged crystals, though with observable differences attributable to the polycrystalline nature of the seed crystals induced by mechanical damage. In both conditions, the γ polymorph is confirmed to be growing on the seed crystals, despite the difference in morphology (Appendix C Figure C.6).

Dissolution and growth patterns lend insight into the structure of the residual crystals present in the HME ASD. After dissolution of the surrounding amorphous material, a small residual crystal remains with rounded features, but a highly non-uniform structure (Figure 5.8b1). Residual crystals from the HME ASD exposed to higher supersaturation conditions, show needle-like growth protruding from all crystal surfaces, suggesting underlying disorder in the processed crystal such as was seen in the mechanically damaged crystal (Figure 5.8b2). Widths of needle-like crystallites were measured at 230 ± 80 nm (n = 20). Despite the needle-like growth pattern, the identity of crystals from both the dissolution and growth condition are confirmed to be the γ polymorph (Appendix C Figure C.6).

5.4.8 Transmission Electron Microscopy

IDM/PVPVA extrudate particles were imaged by TEM in order to observe the size/morphology of crystalline domains contained within the sample. Due to the time-intensive and emerging nature of the technique,[207,215,251] findings do not represent a statistically significant sample, but are intended to demonstrate characteristics of crystals found within the extrudates. A representative image showing amorphous and crystalline areas is found in Figure 5.9a. Small crystalline domains (<100 nm) are found within the homogenous continuous phase (amorphous area). The closer view of the 45x65 nm highlighted crystalline domain (Figure 5.9b) confirms the

crystalline character of the domain by the presence of diffraction contrast and lattice planes (the periodicity found in the image is confirmed by the FFT pattern in the inset).

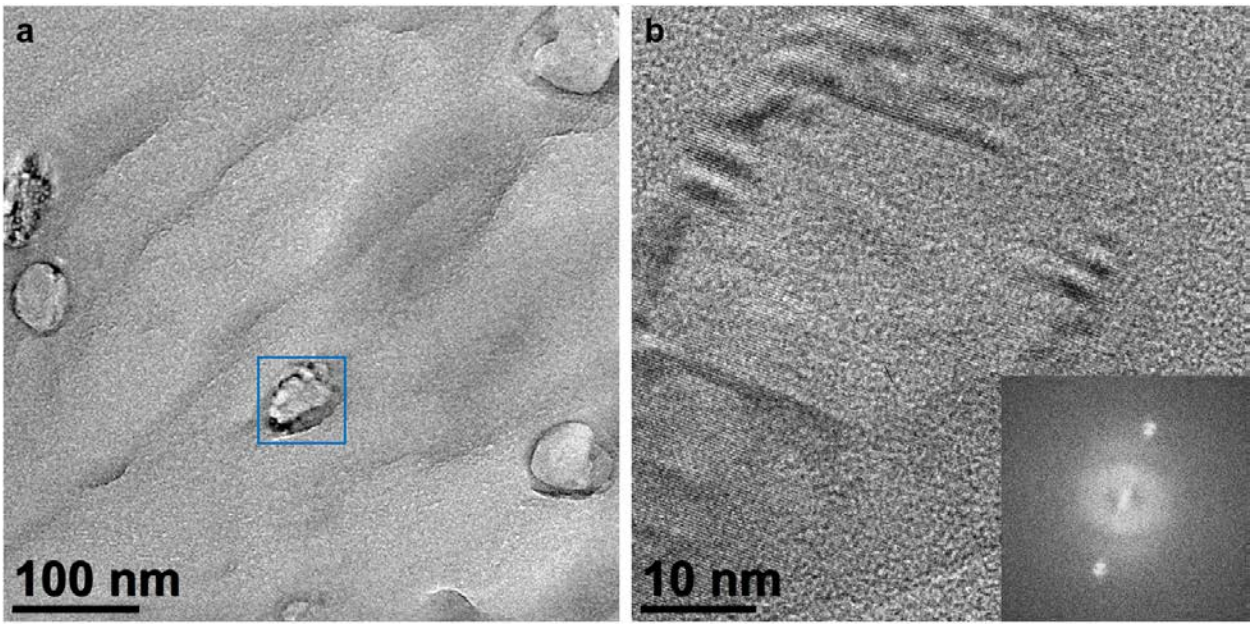

Figure 5.9. Bright field TEM image of an IDM/PVPVA ASD extrudate particle (HME sample 131-2) showing discrete crystalline domains embedded within the amorphous matrix. The crystalline domain highlighted in (a) is shown at higher magnification in (b), where the crystal lattice planes can be observed and crystallinity confirmed by FFT (inset) and presence of diffraction contrast.

5.5 Discussion

5.5.1 Non-Sink Dissolution Performance of ASDs Containing Residual Crystallinity

Supersaturation can be generated by dissolution of an amorphous solid dispersion under non-sink conditions. This leads to a competition between dissolution and crystallization, illustrated by Figure 5.10a.[112] The amorphous drug can dissolve and be absorbed across a biological membrane, or solution-mediated crystallization can occur and solution concentrations can be depleted. The amorphous drug can also crystallize directly from the solid state via matrix crystallization, ultimately decreasing the achievable supersaturation. In the presence of crystal seeds, the available supersaturation can be consumed by crystal growth of the seeds. These competing crystallization processes lead to a reduction in the amount of drug absorbed.[127,238,240,252]

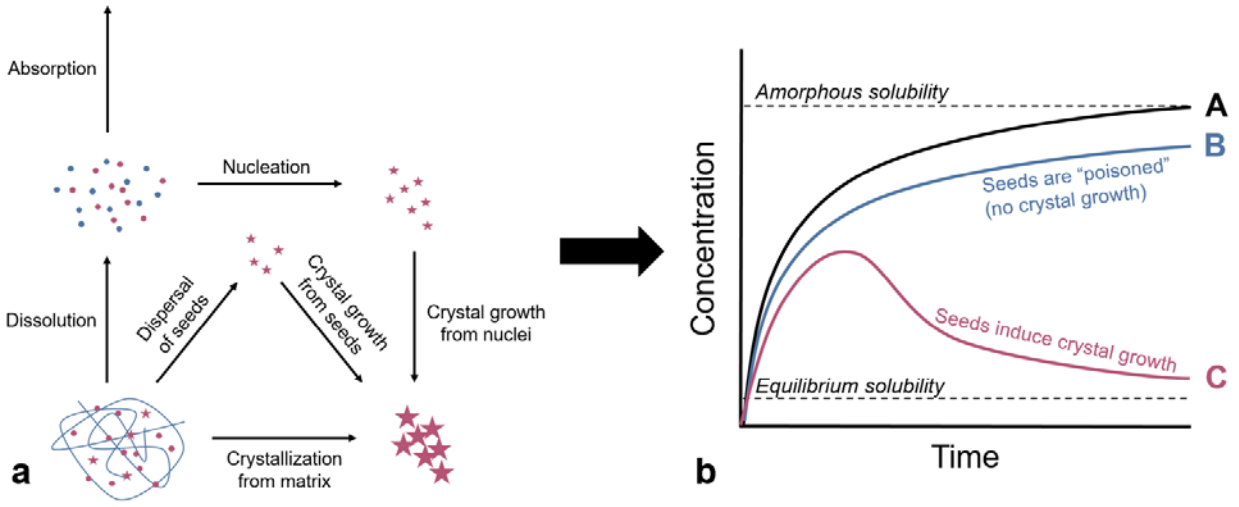

Figure 5.10. (a) Competition between dissolution and crystallization of an ASD system containing residual crystallinity under non-sink dissolution conditions (adapted in part from Alonzo et al.[112]). (b) Possible non-sink dissolution concentration vs. time profiles of ASD systems with and without crystalline content (A: complete dissolution, B: loss in solubility advantage, C: reduced dissolution rate and desupersaturation; discussed in text) (adapted from Sun et al.[111]).

Although dissolution testing for quality control purposes is traditionally conducted using sink conditions, where maximum concentrations do not exceed the crystalline solubility,[157] this does not adequately characterize supersaturating dosage forms, since both dissolution and crystallization kinetics, as well as supersaturation level, play an important role in impacting product quality and performance. A recent commentary by Sun et al. discussed the application of non-sink dissolution testing for assessing performance of these systems (Figure 5.10b).[111] In "at-sink" conditions with respect to amorphous solubility, if the ASD system does not nucleate, complete release of the amorphous drug can be achieved (scenario A). The authors then hypothesize several outcomes for ASD systems containing initial crystalline content. In one scenario (B), the crystal seeds may be inhibited from growth, or "poisoned" by the presence of the polymer, leading simply to a loss of solubility advantage (potency). However, if the crystal seeds can grow or induce secondary nucleation (C), a reduced dissolution rate and extent will be observed, along with desupersaturation due to crystal growth.

In the non-sink dissolution studies of the IDM/PVPVA ASDs containing residual crystal seeds resulting from incomplete amorphization during the HME process (Figure 5.3), the theoretical scenario B most closely matches the experimental outcomes. The HME ASD samples

contained crystallinity up to 25%, and near-complete release of the remaining amorphous content of the HME samples was achieved. (This observation is consistent at the concentration studied, 50 µg/mL, due to the minimal impact of crystallization. At higher supersaturation, where the kinetics of crystallization are increased, greater rates of desupersaturation were observed). The dissolution rate of the IDM/PVPVA system is drug-controlled, rather than polymer-controlled, due to the high drug loading of IDM in the PVPVA matrix.[253,254] In this regime, the highly soluble polymer is expected to dissolve quickly, leaving behind the amorphous drug in the solid amorphous particulates to be released at a relatively slower rate. In samples free of crystalline content, near-complete release of IDM is achieved after 12 hours, and the level continues to slowly increase. This observation is expected, as limited continued thermodynamic driving force for dissolution remains. Although the 12 hour monitoring period selected for this study is significantly longer than typical GI transit times, it allows for both dissolution and crystal growth mechanisms to be observed, thus allowing mechanistic information to be gained. In the HME ASD samples containing crystallinity, minimal desupersaturation was observed, despite the significant level of crystallinity contained within the ASDs. Additional studies were performed to further investigate the mechanisms involved in this observation.

By studying the dissolution performance outcomes from intrinsic residual crystals in comparison to control samples (i.e. physical mixtures of bulk IDM crystals and a fully amorphous ASD), the impact of the crystal properties and HME processing can be better understood. Figure 5.11 plots the total concentration after 12 hours dissolution against the amount (%) of crystalline content found in the HME and SE/PM samples (Figure 5.3 and Figure 5.4). A line joins the 100% amorphous (SE) vs. 100% crystalline (PM) samples, forming a theoretical maximum achievable concentration with respect to the level of crystallinity contained within the sample. This line represents scenario B, in which no crystal growth occurs, while deviation from this line provides some evidence of scenario C, in which dissolution rates are reduced or desupersaturation occurs due to crystallization. In the SE/PM mixtures, achieved concentrations reduce along this theoretical concentration line, in direct proportion with their percent (%) crystallinity, indicating that the crystal seeds present in the mixture do not grow. As the HME ASDs with residual crystallinity generate lower final concentrations at 12 hours than would be expected based on their reported % crystallinity (i.e. they fall below the theoretical maximum concentration line), this suggests that the crystal seeds have grown to some extent. This corresponds with the slight

desupersaturation observed during the plateau phase of the dissolution profile for HME ASD samples with crystallinity higher than 3%.

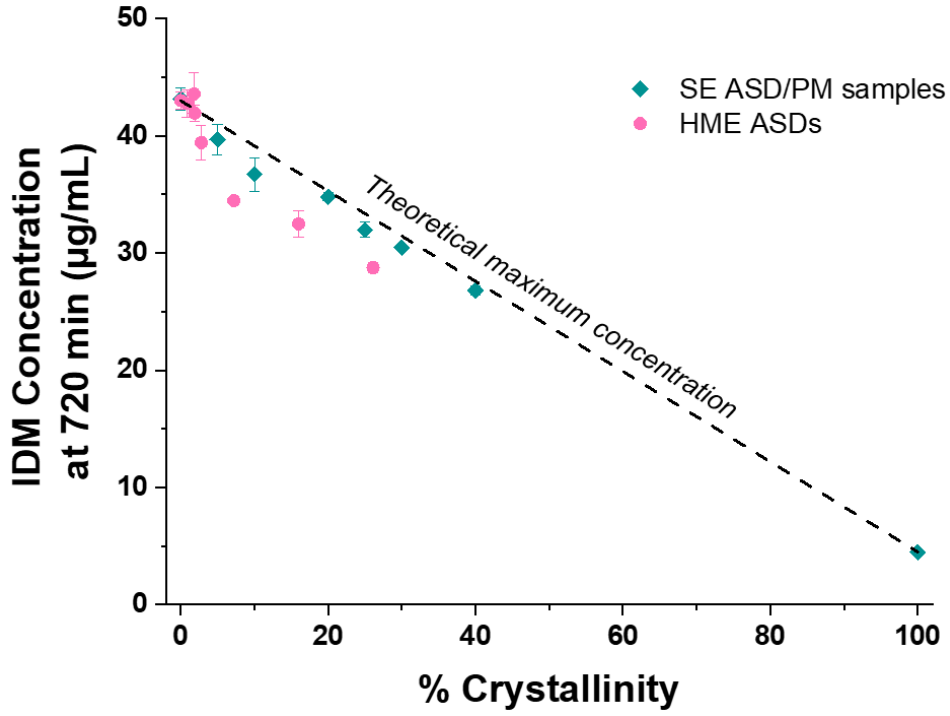

Figure 5.11. IDM concentration at t=720 min following dissolution of IDM/PVPVA HME ASDs or SE ASD/PM samples.

The HME ASDs with <2% crystallinity may follow the same pattern as those with higher levels of crystallinity, although it is not observable due to the small amount of crystallinity found within the ASDs. Alternately, due to the low level and crystal attributes (they can be inferred to be nanometer-sized and defective based on TEM studies[207]), these crystals may have higher solubility,[255,256] and dissolve. As the release profiles of these samples were indistinguishable from the crystal-free sample (Figure 5.3b), there may be some low level of crystallinity contained within an HME ASD that functionally performs like amorphous material, i.e. can dissolve instead of functioning as seeds for crystal growth. Through TEM characterization found in Figure 5.9 and in our previous publication,[207] we observed residual crystals in an IDM/PVPVA HME ASD <100 nm in size, including a population as small as 5-10 nm, generated by dissolution, fragmentation, and breakage effects. Based on the Gibbs-Thomson theory for size dependent-solubility,[255,256] crystals in this size range would be expected to show a non-negligible increase in solubility.

Experiments conducted to compare dissolution outcomes under constant supersaturation conditions enable additional insight into crystal properties, by altering dissolution and crystallization kinetics. Figure 5.12 plots the total concentration after 12 hours dissolution against the amount (%) of crystals present in the experiment, with a constant amorphous dose of 50 µg/mL. A line joins the concentrations found in the 0% and 100% crystallinity experiments (50 µg/mL of SE ASD with 0 or 50 µg/mL of added bulk crystal seeds). This level represents the expected decrease in solution concentration based on the level of bulk crystal seeds present (Figure 5.5), describing the rate of crystal growth over the course of the experiment as the fully amorphous ASD is dissolving. In comparison, the four HME samples containing 3-25% residual crystalline content (Figure 5.6) led to distinctly lower concentrations after 12 hours. This suggests that the crystals within these samples are better able to grow in the presence of polymer than the corresponding bulk crystalline seeds. The SEM images shown in Figure 5.8 support that there are different patterns of growth between the two crystal types, for an equivalent initial supersaturation level.

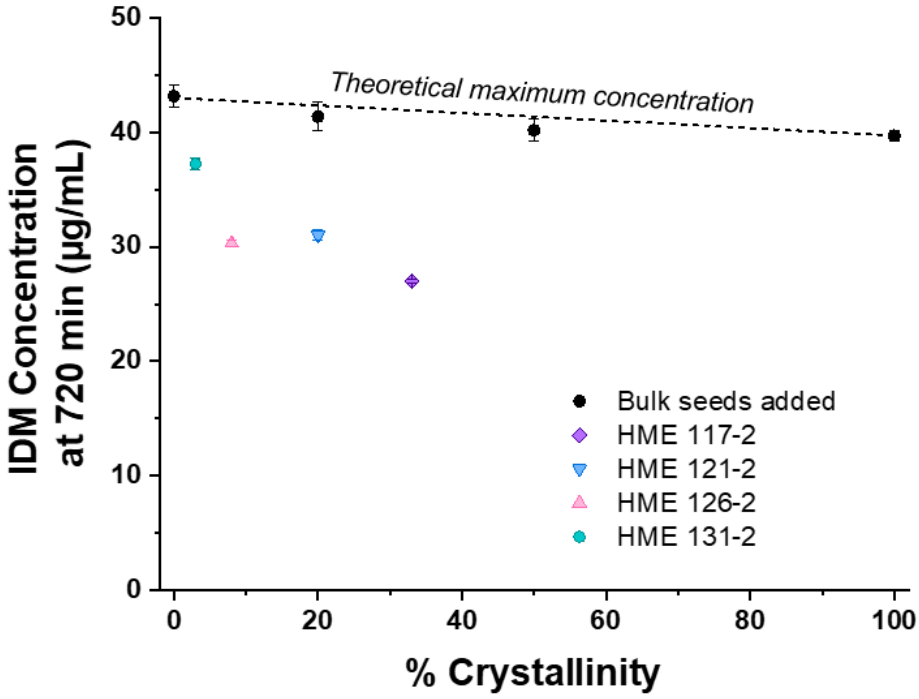

Figure 5.12. IDM concentration at t=720 min following dissolution of IDM/PVPVA ASDs under a constant supersaturation condition (amorphous IDM dose held constant at 50 µg/mL). The bulk seeds were added to the SE ASD, as shown in Figure 5.

Desupersaturation from the HME ASDs (Figure 5.3, Figure 5.6) but not the ASDs with added bulk crystals (Figure 5.4, Figure 5.5) has two primary causes. First, the residual crystals within the ASD are likely to have higher surface area for an equivalent amount of bulk crystal seeds, since the seeds have undergone size reduction due to mechanical breakage and partial dissolution during the HME process.[140,242] Second, the surface energy of the residual crystals is higher due to their underlying defect structure, caused by irregular dissolution, fragmentation, and mechanical breakage during the HME process,[207,242] which increases the likelihood for crystal growth during the non-sink dissolution experiments. The higher surface area and/or surface energy of residual crystals is supported by the comparative experiment at constant supersaturation conditions (Figure 5.6, Figure 5.12), wherein the HME samples containing residual crystallinity show a reduced net extent of dissolution (C_{max}), and then reduction in solution concentrations due to continued crystal growth. Essentially, the bulk crystal seeds do not provide an equivalent surrogate to the residual crystals for investigating the impact of crystallinity on non-sink dissolution performance. Although this is commonly mitigated by using micron-sized seeds,[237,238] we would speculate this size reduction would still not approximate the nanometer-scale size (<100 nm) and highly defective nature of HME residual crystals.[207,242] The crystallite size range found in this system is consistent with that observed by S'ari in felodipine ASDs prepared by HME, demonstrating the generalizable nature of this finding.[251] Another factor, beyond crystallization, that could cause deviation from the theoretical maximum concentration (dashed line in Figure 5.11) is if the reported % crystallinity is underestimated. The % crystallinity was determined by comparing PXRD peak areas of the samples against a standard curve prepared by spiking ASDs with bulk crystals.[140] As peak detection is influenced by crystal size and defects, along with instrument parameters, systematic underestimation of crystalline content may ultimately be common to HME ASDs.[148,149,207,257]

5.5.2 Impact of the Polymer Precipitation Inhibitor on Dissolution in the Presence of Crystal Seeds

Polymers are used to stabilize the amorphous drug in the solid state, and can inhibit crystallization processes during dissolution.[18,227] PVPVA was demonstrated to be a highly effective nucleation and crystal growth inhibitor of IDM (Figure 5.1b,c). Similar trends have been seen by other researchers using IDM, a range of polymers, and media conditions.[258–260] In the

presence of crystals seeds, rates of crystal growth were near zero in the presence of PVPVA (Figure 5.2), such that the crystal growth had almost no impact on the concentration of IDM in solution. The high level of PVPVA (50 µg/mL) corresponds with the amount of PVPVA found in the HME ASDs, suggesting that the high level of polymer could effectively "poison" crystal growth from crystal seeds during ASD dissolution. This was demonstrated in Figure 5.5, where bulk crystal seeds were added at levels of up to 100% of the initial amorphous dose in the ASD, and only a small decrease is observed in the final concentration at 12 hours (shown in Figure 5.12, along with a dashed line representing the theoretical maximum achievable concentration when bulk seeds are added).

As has been seen with other drug crystal and polymer systems,[230,250] AFM studies demonstrate the adsorption of PVPVA onto IDM crystals. A correlation can be observed between the polymer concentration and observed surface coverage on IDM bulk crystals (Figure 5.7), and the resulting impact on supersaturation maintenance/crystal growth rates (Figure 5.2), consistent with theoretical models of crystal growth in the presence of surface-poisoning species.[261,262] These data provide clear evidence that as polymer concentration increases, adsorbed polymer surface coverage is more extensive, which provides a mechanistic connection for crystal growth inhibition. Adsorption of PVPVA on the crystal serves to effectively "poison" the growth.

SEM imaging of crystals seeds after dissolution and growth conditions further support interaction of the polymer with the crystal surfaces (Figure 5.8). Under crystal growth conditions without PVPVA (Figure 5.8a4), the smooth surfaces of grown crystals suggest the single crystal origin of the as-received bulk crystals. No interference with surface integration of molecules into the crystal seeds is apparent. However, with PVPVA present in the dissolution media (Figure 5.8a5), surface growth is disrupted and fibrous or needle-like crystallites appear growing of the surfaces, which were confirmed to be the thermodynamically stable γ form, despite the difference in morphology. This suggests that the adsorbed polymeric network appears to limit the sites available for molecules to integrate into the crystal seeds, thus favoring growth in this needle-like arrangement. At lower polymer concentrations, suggesting lower levels of adsorption, the arrangement of polymer molecules at crystal surfaces has been described as a flatter "train" conformation, providing a thinner layer of coverage; while at higher polymer concentrations, a greater extent of adsorption would indicate a thicker layer of coverage providing greater barrier to surface diffusion.[263] Adsorption distances were found to be ~160 nm (at 5 µg/mL PVPVA) and

~70 nm (at 50 µg/mL PVPVA). As the amount of polymer has increased 10-fold, the thickness of the polymer surface coverage would be expected to increase. Other researchers have similarly observed that polymer adsorption disrupts the continuous, layer-by-layer growth of crystals observed in the polymer-free environment.[17,230] In this system, based on the near complete surface coverage and adsorption distances of ~70 nm, a needle-like crystal growth morphology was favored, as sites for growth were limited. Adsorption distances were found to be on the same order of magnitude as crystal widths and step pinning observations found by SEM imaging of crystals, demonstrating the link between polymer adsorption and growth patterns.

5.5.3 Risk Factors of Residual Crystalline Content Upon Dissolution

Non-sink dissolution performance of ASD systems containing residual crystallinity is drug-polymer system specific. The IDM/PVPVA system is categorized as being closest to scenario B, as strong evidence for the inhibition of crystal growth by the polymer has been observed. Other systems may trend toward scenario C, if the polymer does not sufficiently inhibit crystal growth of seeded systems. Examples of this in the literature include tacrolimus/hydroxypropyl methylcellulose (HPMC),[127] celecoxib/polyvinylpyrrolidone (PVP),[238] and indomethacin/Eudragit EPO.[138]

This study identifies several risk factors to the presence of residual crystallinity within an ASD.

(1) Crystal Growth Rates: Most importantly, by inhibiting crystal growth rates in the presence of the polymer, seed crystals have restricted ability to consume the available supersaturation, thus the amount of drug available for absorption is limited only by the amount of drug which is in the amorphous state. In a drug-polymer system such as IDM/PVPVA studied here, crystalline content poses a fairly low risk to the formulation, due to the highly effective nucleation and growth inhibition properties of PVPVA.

(2) Seed Properties: Crystal properties also drive the dissolution performance. Bulk seeds are routinely less potent at consuming supersaturation than HME residual crystalline seeds or seeds with higher relative surface energy or surface area,[17,237] as shown in Figure 5.11 and Figure 5.12 for the system studied herein. Residual crystals from the HME process are small and mechanically damaged, thus having

higher effective surface area available for growth in comparison to bulk crystals, despite their common origin.

(3) Supersaturation Conditions: Under higher supersaturation conditions, and thus higher crystal growth rates, the apparent potency of crystal seeds increased. This translates to a low fluid volume *in vivo* scenario, in which we would speculate that crystal seeds would be a greater formulation risk, in particular for faster crystallizing drugs.

5.6 Conclusion

By studying the dissolution performance of ASDs with residual crystals under non-sink conditions, the loss of solubility advantage (potency) was observed with the IDM/PVPVA model system. The impact of the polymer to maintain supersaturation and poison growth of seed crystals was also illustrated. The defective nature of residual crystals in the ASD was compared to bulk crystals through SEM imaging. While bulk seeds did not properly represent the impact of residual crystals, the potential dissolution performance consequences were limited due to polymer adsorption onto residual seed crystals, with subsequent poisoning of crystal growth.

We have demonstrated a provocative idea, that crystallinity intrinsic to an ASD formulation could have minimal impact on non-sink dissolution performance under controlled supersaturation conditions, beyond that of lost solubility advantage. In this model system, the polymer has two effects which are responsible for stabilizing the attained supersaturation: (1) preventing nucleation and (2) poisoning the growth of the seeds (both bulk or intrinsic to the HME samples). This work demonstrates the power of an effective polymeric inhibitor reducing nucleation and crystal growth of a drug during dissolution under non-sink conditions.

CHAPTER 6. APPLICATION AND LIMITATIONS OF THERMOGRAVIMETRIC ANALYSIS TO DELINEATE THE HOT MELT EXTRUSION CHEMICAL STABILITY PROCESSING WINDOW

This chapter is a reprint with minor modifications of a manuscript published in *International Journal of Pharmaceutics* in September 2020 with the same title by: Dana E. Moseson, Madison A. Jordan, Dishan D. Shah, Isaac D. Corum, Benedito R. Alvarenga Jr., and Lynne S. Taylor. Reprinted with permission from Elsevier. DOI: 10.1016/j.ijpharm.2020.119916

6.1 Abstract

Thermogravimetric analysis (TGA) is frequently used to define the threshold of acceptable processing temperatures for hot melt extrusion. Herein, evaluation of chemical stability of amorphous drug and polymer systems was assessed by a critical evaluation of TGA nonisothermal and isothermal methods. Nonisothermal analysis of three crystalline APIs of high glass-forming ability (posaconazole, indomethacin, and bicalutamide), as well as six common polymers, identified a degradation onset temperature that ranged from 52-170°C, depending on heating rate and degradation detection method employed. In particular, the tangent method significantly overestimated the onset of acceptable levels of degradation, while weight loss threshold criteria were more suitable. Isothermal analysis provided a more direct indication of chemical stability, however neat amorphous materials are likely to recrystallize. By forming an amorphous solid dispersion, the polymer can stabilize the amorphous drug against recrystallization, enabling isothermal analysis of chemical degradation. However, TGA mass loss of volatiles should be considered only as an approximate indicator of degradation, as actual potency loss is likely to be significantly higher; this was confirmed by high performance liquid chromatographic analysis of samples. TGA methods should be selected to generate highly sensitive outcomes, and caution should be applied when extrapolating suitability of processing conditions.

6.2 Introduction

Active pharmaceutical ingredients (APIs) and excipients are exposed to elevated temperatures during hot melt extrusion (HME) processing.[36] The thermal stability of these materials is essential to enable the preparation of a drug product with proper identity, strength, quality, purity, and potency characteristics, thus ensuring safety and efficacy.[264] When preparing

amorphous formulations by HME, the crystalline drug is converted to the amorphous form by melting or dissolving and mixing with the polymer.[140] Amorphous forms are known to be more reactive than their crystalline counterparts, so it is unsurprising that amorphous forms may be susceptible to thermal degradation at increased rates.[80,265,266] However, degradation of an amorphous form is inherently difficult to evaluate. Crystalline forms generally don't degrade significantly until they melt,[83] but amorphous forms are susceptible to recrystallization.[16]

Thermogravimetric analysis (TGA) is a common technique for evaluating degradation. TGA is used to measure changes in mass by: (1) heating the sample over a temperature range at a specified rate (nonisothermal method), or (2) heating the sample at a specified temperature for a selected time (isothermal method).[267] Mass decrease will occur upon solvent/water loss and when volatile degradation products are formed. A brief review of recent studies in which TGA was used to evaluate polymer or crystalline drug suitability for HME processing found that 100% of studies (n=30) used nonisothermal heating (10°C/min was the most common heating rate),[12,79,81,83,90,91,120,121,126,268–285] and 17% of studies (n=5) also included an isothermal test for 8-60 minutes.[79,269–272] Despite the popularity of the nonisothermal method, the degradation onset temperature, T_{onset}, generated (also commonly called T_{deg}) is frequently assigned based on qualitative curve interpretation, with little information provided based on the magnitude of degradation experienced at that specified temperature. A few studies reported % weight loss at a specified temperature during the heating ramp,[12,83,89,268,285,286] but little attempt has been made to reconcile these values with actual HME experiments. Ultimately, misleading information may be generated with the nonisothermal heating method regarding the thermal stability of the crystalline drug, polymer, or the drug-polymer system and subsequent suitability of these materials for HME. The impact of both time and temperature, or "cumulative exposure," must be considered when developing HME formulations and manufacturing processes.[79]

The study described herein has several objectives. First, TGA nonisothermal and isothermal methods were used to assess thermal degradation of crystalline APIs (and amorphous APIs, when possible) and common polymers used in HME processing. The potential for evaluating degradation profiles of amorphous APIs was probed by first running differential scanning calorimetry (DSC) experiments to evaluate crystallization tendency. Isothermal TGA was then used to assess degradation of amorphous drugs dispersed in polymers, reducing the potential for crystallization. Second, the thermal stability of common polymers was compared to literature

assessments, so as to enable descriptions of their acceptable processing window based on this expanded analysis. Lastly, degradation experienced during HME processing was quantified by HPLC and compared with the isothermal TGA results to assess the utility of the TGA degradation assessments. Ultimately, this research examines the application and limitations of TGA methods to assess the suitability of a drug for HME processing, polymer selection, and process design.

6.3 Experimental Section

6.3.1 Materials

Indomethacin (IDM, γ polymorph), posaconazole (PCZ, form I), and bicalutamide (BCL, form I) were selected as they have a high glass forming ability (class III molecules),[16,287,288] so as to enable degradation assessments in both the crystalline and amorphous state. IDM and BCL were obtained from ChemShuttle (Hayward, CA), and PCZ was gift from Dr. Reddy's Laboratories (Hyderabad, India). Six polymers were selected due to their frequent reported use in the literature for preparation of amorphous solid dispersions (ASDs) by HME.[289–291] Polyvinylpyrrolidone/vinyl acetate copolymer (PVPVA, Kollidon VA64), Soluplus, and polyvinylpyrrolidone (PVP, Kollidon K-30) were provided by BASF (Florham Park, NJ). Hydroxypropyl methylcellulose acetate succinate (HPMCAS, Aqoat MF) and hydroxypropyl methylcellulose (HPMC, Affinisol HME 100LV) were provided by Shin Etsu (Totowa, NJ). Eudragit EPO was provided by Evonik (Essen, Germany). Chemical structures of each material are found in Figure 6.1, and solid state properties of APIs, polymers, and ASDs are listed in Figure 6.2. A Rigaku SmartLab diffractometer (Rigaku Americas, The Woodlands, Texas) was operated in Bragg-Brentano mode with a Cu-kα radiation source and d/tex ultra detector using a scan rate of 4°/min over 5-40° 2θ and 0.02° step size to confirm the identity and solid state form of all crystalline drugs, polymers, and ASDs (data not shown).

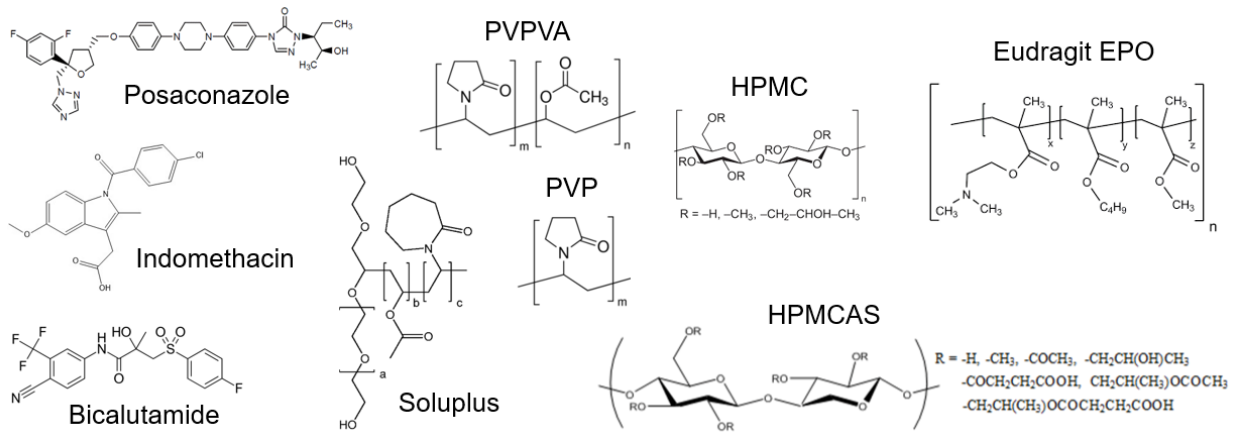

Figure 6.1. Chemical structures of APIs and polymers studied.

Table 6.1. Solid state properties of APIs, polymers, and ASDs studied.

Component	**MW (g/mol)**	T_m (°C)	T_g (°C)
Posaconazole (PCZ)	700.8	167	60
Indomethacin (IDM)	357.8	160	45
Bicalutamide (BCL)	430.4	193	54
PVPVA	55,000	---	109
PVP K-30	40,000	---	161
Soluplus	118,000	---	64
HPMCAS	18,000	---	122
HPMC	180,000	---	106
Eudragit EPO	47,000	---	55
25/75 PCZ/HPMCAS	---	---	97
25/75 PCZ/PVPVA	---	---	99
50/50 IDM/PVPVA	---	---	67
30/70 BCL/PVPVA	---	---	98

6.3.2 Sample Preparation

6.3.2.1 Preparation of Amorphous Drugs

Amorphous drugs were prepared in the TGA (Discovery 5500, TA Instruments, New Castle, DE) and DSC (Q2000, TA Instruments, New Castle, DE) *in situ* by heating to ~10°C degrees over their melting point and holding for 5 minutes before cooling to the temperature of the isothermal experiment.

6.3.2.2 ASD Preparation by Solvent Evaporation

Amorphous solid dispersions (ASDs) were prepared by solvent evaporation (SE) using a Brinkmann Rotavapor-R (Buchi, New Castle, DE) under reduced pressure at 60°C. The samples were then dried under vacuum and cryomilled for 60 seconds of grinding time at 10 Hz to form a fine powder using a 6750 Freezer/Mill (SPEX, Metuchen, NJ). IDM/PVPVA ASD was prepared with 50% drug loading out of methylene chloride and methanol (2:1 v:v). BCL/PVPVA ASD was prepared with 30% drug loading out of ethanol. PCZ/PVPVA and PCZ/HPMCAS were prepared with 25% drug loading out of methylene chloride and methanol (1:1 v:v).

6.3.2.3 Physical Mixtures and ASD Preparation by Hot Melt Extrusion

Crystalline physical mixtures of PCZ/HPMCAS, PCZ/PVPVA, and BCL/PVPVA were prepared by manual tumble blending. Two particle sizes of bicalutamide were used with D_{50} particle sizes of 3.5 and 93 µm.

HME ASDs of PCZ/HPMCAS, PCZ/PVPVA, IDM/PVPVA, and BCL/PVPVA were prepared by hot melt extrusion (HME) using an Xplore Pharma Melt Extruder (Geleen, The Netherlands), assembled with a 5mL volume barrel with co-rotating conveying screw (refer to Appendix Figure D.1 for a schematic of the extruder). The processing temperature was set to achieve the desired product melt temperature as monitored by an in-line thermocouple located between the screws and recirculation channel or die (approximately 5°C higher). Physical mixture blends were manually fed into the extruder. Residence time is considered the point when the recirculation valve is opened and the melt begins extruding through the die. Processing conditions for PCZ and IDM HME ASDs are found in Appendix D Tables D.1 and D.2. For BCL/PVPVA,

two HME batches were prepared the physical mixture prepared from micronized BCL crystals using product melt temperatures of 165°C and 180°C, 10 minutes of residence time, and a screw speed of 50 rpm. In particular, the BCL/PVPVA HME batches represent minimal mechanical input due to the extruder design and low polymer viscosity at the temperatures utilized.

6.3.3 Characterization Methods

6.3.3.1 Differential Scanning Calorimetry (DSC)

A Q2000 differential scanning calorimeter equipped with a refrigerated cooling accessory (TA Instruments, New Castle, DE) purged with nitrogen at 50 mL/min was used to analyze the thermal properties of the materials used in this study by heat/cool/heat methods. The melting point (T_m) and glass transition (T_g) temperature of the APIs was confirmed by heating crystalline API powder at 5°C/min to ~10°C above the melting point. The sample was then cooled at 10°C/min to 0°C and heated to ~20°C above its T_g. The polymers and ASDs were heated in modulated mode from 25°C (for polymers) or 0°C (for ASDs) below their T_g to at least 20°C above their T_g at 5°C/min ± 0.796°C every 60 sec. The sample was then cooled at 10°C/min to 0°C and heated to ~20°C above its T_g. A sample size of 3-5 mg was used for all experiments.

To assess the stability of amorphous APIs against recrystallization, isothermal holds were completed at a range of temperatures below the melting point to determine if recrystallization would be observed during the hold period. Crystalline API powders (3-5 mg) were heated at 20°C/min to ~10°C above T_m. This temperature was held for 2 min to ensure complete melting. The sample was then cooled at 20°C/min to the target isothermal hold temperature, which was maintained for 1 (for PCZ and BCL) or 4 hours (for IDM). After completion of the isothermal hold, the sample was cooled to 25°C at 20°C/min, then heated at 20°C/min to above the T_m. If a melting peak was detected upon the second heating cycle, this constituted evidence of nucleation during the isothermal hold period.

6.3.3.2 Thermogravimetric Analysis (TGA)

A Discovery TGA 5500 (TA Instruments, New Castle, DE) was used to assess the degradation by weight loss using nonisothermal and isothermal methods under a nitrogen purge. Nonisothermal heating was used to determine the T_{onset} of polymers, crystalline APIs, and ASD

samples (prepared by solvent evaporation) at 1, 2, 5, and 10°C/min from ambient conditions to 300°C (or higher, as needed for some materials) (Figure 6.2a). T_{onset} was calculated by two methods: (1) tangent intersection of the baseline and degradation curve, and (2) % weight loss. The tangent intersection method was performed within the TRIOS software. For the % weight loss method, data was normalized to 100% at 140°C for all polymer and ASD samples and just above the melting point for all crystalline drugs, then the temperature at which 0.1, 0.5%, and 1.0% weight loss was reached was considered the T_{onset}. Weight loss experienced up to 140°C was attributed to moisture/solvent loss.

To assess isothermal degradation kinetics, polymers, crystalline/amorphous APIs, and ASD samples prepared by solvent evaporation were heated at 50°C/min from ambient conditions to the target hold temperature under a nitrogen purge (Figure 6.2b). Samples remained at the target hold temperature for 4 hours and were monitored for weight loss. Experiments were conducted in duplicate. Raw data plots of isothermal weight loss can be found in Appendix D (Figures D.4-D.6).

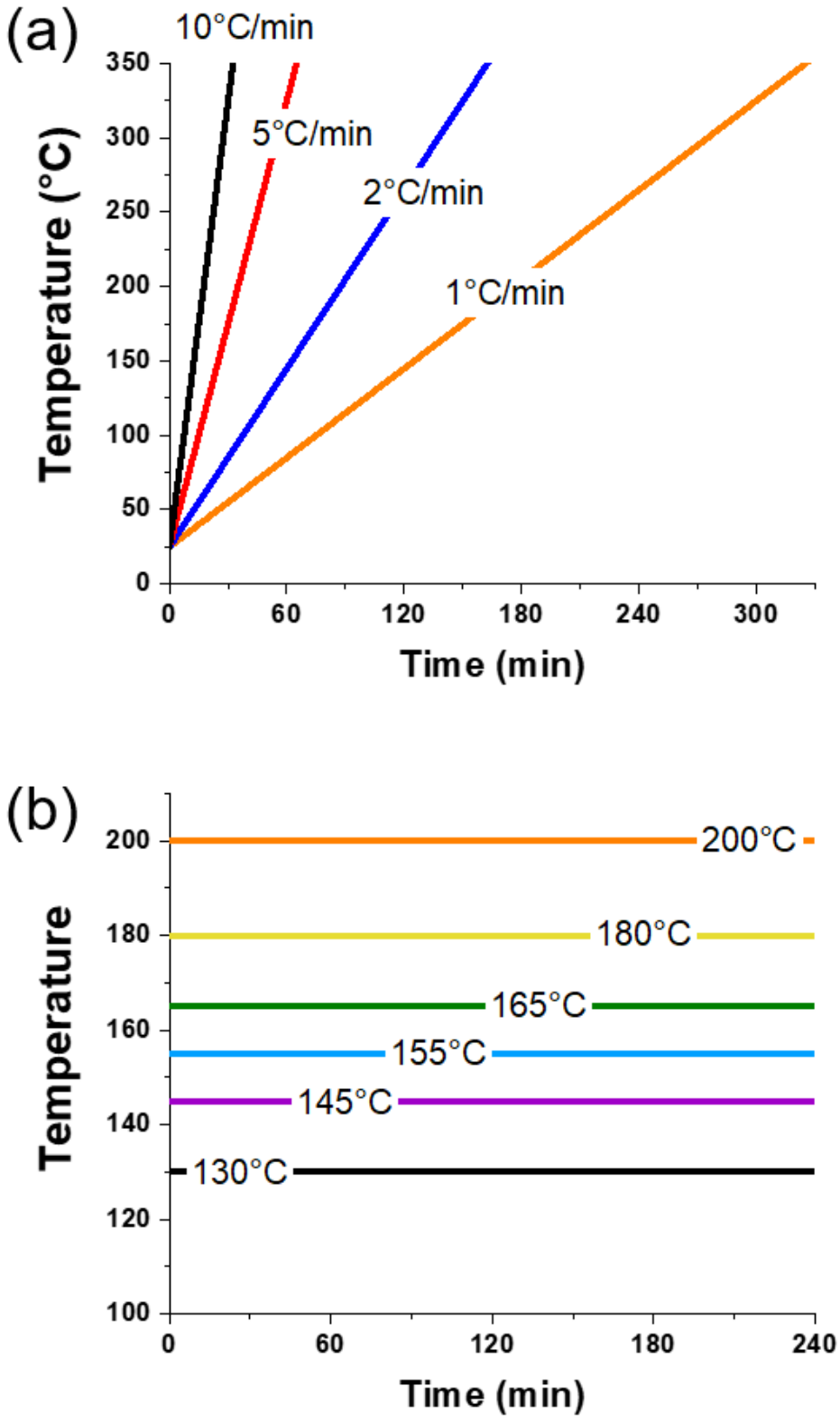

Figure 6.2. TGA methods for (a) nonisothermal and (b) isothermal heating depicted as temperature vs. time.

6.3.3.3 High Performance Liquid Chromatography (HPLC) Analysis

Posaconazole: HPLC analysis for quantification of PCZ in HME ASDs was carried out using an Agilent 1260 Infinity series HPLC equipped with an Agilent Eclipse Plus C18 (4.6×250 mm i.d., particle size 5 μm) and fluorescence detector (Agilent Technologies, Santa Clara, CA). Fluorescence detection conditions consisted of excitation and emission wavelengths of 240 nm and 385 nm, respectively. Chromatographic conditions consisting of 70% acetonitrile:30% water mobile phase with a flow rate of 1.0 mL/min, sample injection volume 20 μL, and run time of 6 min. The retention time of the PCZ peak was 4.3 minutes. Quantification of the amount of dissolved drug was performed against a standard calibration curve (R^2 = 0.999) over the range of 0.1-1000 μg/mL. Calibration standards and samples were dissolved in methanol. Assay preparations of HME samples were prepared in duplicate.

Indomethacin: HPLC analysis for quantification of IDM in HME ASDs was carried out using an Agilent 1100 series HPLC equipped with an Agilent Eclipse Plus C18 (4.6×150 mm i.d., particle size 5 μm) and utilized a UV wavelength of 240 nm for detection. The mobile phase consisted of 0.1 % (v/v) of formic acid (solvent A) and acetonitrile (solvent B), and the following gradient program was employed: 0 to 3 min, 65% B; 3.01 to 9 min, 65 to 95% B; 9.01 to 11 min, 95% B, 11 to 13 min, 95 to 65% B, and from 13.01 to 15 min, 65% B. The flow rate was 1.0 mL/min and the injection volume was 10 μL. The retention time of the IDM peak was 3.9 min. Quantification of the amount of dissolved drug was performed against a standard calibration curve (R^2 = 0.9995) over the range of 1-300 μg/mL. Calibration standards and samples were dissolved in acetonitrile. Assay preparations of HME samples were prepared in triplicate.

Bicalutamide: A reverse phase HPLC method was used to study the degradation of BCL following temperature exposure during TGA experiments and after HME. The method reported by Rao et al was used,[292] with a higher wavelength so as to avoid interference of PVPVA. An Agilent 1260 Infinity series HPLC with an Eclipse Plus C18 column (4.6×250 mm i.d., particle size 5 μm) was used with chromatographic conditions consisting of 50% acetonitrile:50% pH 3 0.01 M KH_2PO_4 mobile phase with a flow rate of 1.0 mL/min, sample injection volume 10 μL, and run time of 15 min. UV detection conditions utilized a wavelength of 270 nm. The retention time of the BCL peak was 9.3 min. Quantification of the amount of dissolved drug was performed against a standard calibration curve (R^2 = 0.998) over the range of 0.2-200 μg/mL. Calibration

standards and samples were dissolved in methanol. Assay preparations of HME and TGA-exposed samples were prepared in triplicate.

6.4 Results and Discussion

6.4.1 Thermal Stability of APIs

6.4.1.1 Nonisothermal Heating of Crystalline APIs

The three APIs used in this study are found in a commercial product manufactured by HME or are reported to have excellent thermal stability for HME processing:

(1) Posaconazole (PCZ) is found in an amorphous solid dispersion with HPMCAS and is manufactured by hot melt extrusion.[293] Posaconazole reportedly exhibits significant degradation when processed at temperatures above 160°C, thus the processing temperatures used are below the drug's melting point (T_m = 167°C) to offer protection against thermal degradation.[294] In another investigation, by an unspecified TGA method, degradation was not indicated below 325°C.[295]

(2) Indomethacin (IDM) has a single step of weight loss based on nonisothermal TGA analysis, which has been reported to begin at either 250°C [296] or 293°C.[297]

(3) Bicalutamide (BCL) has been reported to not undergo volatile degradation below 250°C (heating rate 10°C/min), and showed less than 0.5% weight loss when held at 160°C for 60 min (isothermal test of crystalline drug).[269]

Nonisothermal TGA analysis was performed on each of the three crystalline APIs at four heating rates: 1, 2, 5, and 10°C/min (Figure 6.3). In contrast to the thermal degradation properties described in the literature,[269,294,296,297] interpretation of the nonisothermal analysis curves paints an altered picture of degradation for each crystalline compound. Crystalline PCZ, which has a melting point of 167°C, appears highly stable against exposure to elevated temperatures within the range of typical HME conditions (130-200°C), and doesn't initiate mass loss until much higher temperatures. It is apparent that degradation initiates at low levels for crystalline IDM just above its melting point, 160°C. Significant levels of degradation are observed for crystalline BCL beginning near its melting point, 193°C, in contrast to a previous study in which it was reported as stable until 250°C.

These differences can largely be accounted for based on the methods used to make the degradation claims. In our experimental approach, several heating rates and degradation onset detection methods were used to characterize the nature of degradation. Each API shows a similar dependence of the volatile degradation on heating rate: degradation is initiated at lower temperatures when the scanning rate is slower (i.e. 1°C/min) and at higher temperatures when the heating rate is faster (i.e. 10°C/min). This trend clearly indicates that exposure time plays a role in thermal degradation, and justifies an isothermal approach to examining degradation kinetics.

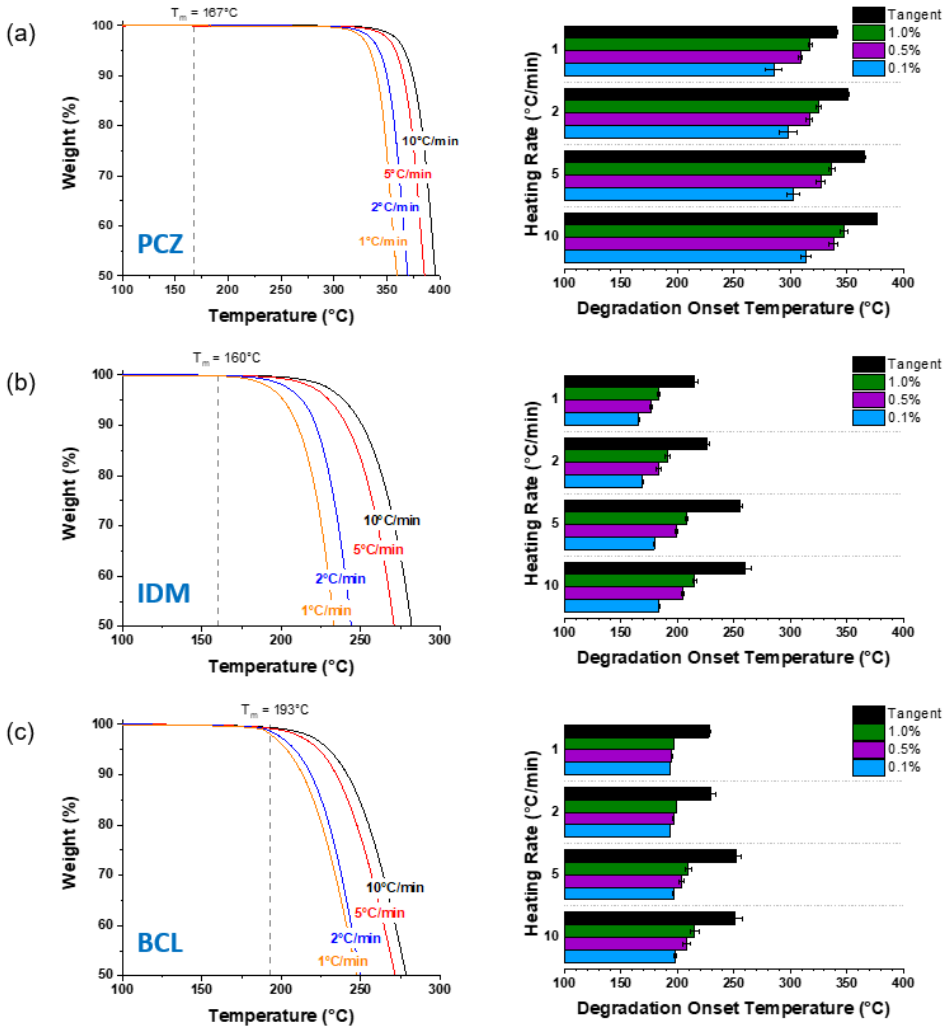

Figure 6.3. Nonisothermal TGA curves of crystalline APIs: (a) posaconazole (PCZ), (b) indomethacin (IDM), and (c) bicalutamide (BCL).

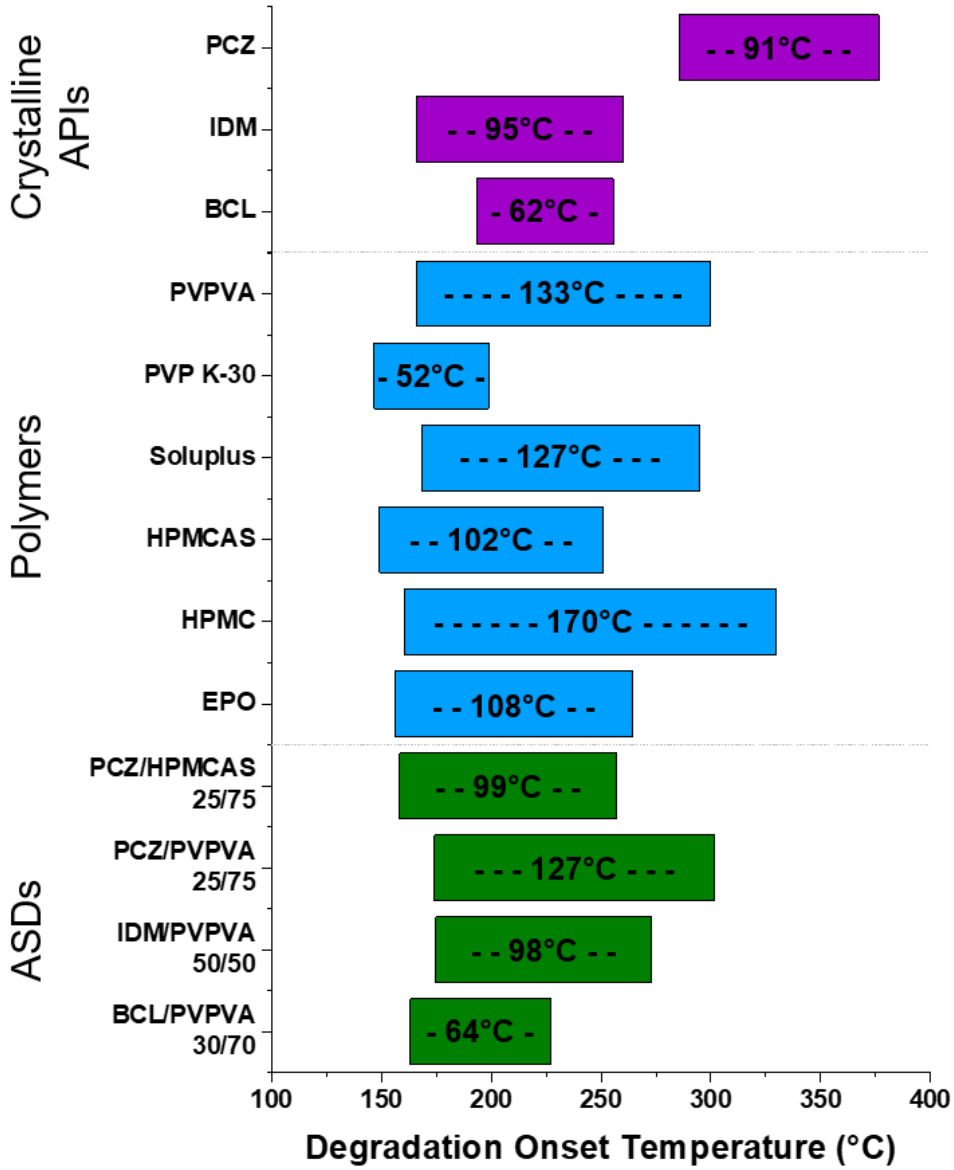

Figure 6.4. Range of degradation onset temperature as determined by % weight loss and tangent intersection methods for crystalline APIs, polymers, and ASDs.

These differences were quantified by determining the degradation onset temperature, T_{onset}, by the tangent intersection method and weight loss threshold (Figure 6.3). The T_{onset} values of crystalline PCZ, IDM, and BCL range from 285-376°C (range 91°C), 165-260°C (range 95°C), and 193-255°C (range 62°C), respectively (Figure 6.4). (Note: Figure 6.4 includes polymer and ASD range data, which will be discussed in Sections 3.2 and 3.3). The T_{onset} value for the low end of the range was selected from the slowest heating rate (1°C/min) and most stringent degradation criteria (0.1% weight loss threshold), while the high end of the range was selected from the fastest

heating rate (10°C/min) and most lenient criteria (tangent intersection). This wide range, generated by varying method parameters (i.e. heating rate) and detection method (tangent or weight loss threshold), indicates that the typical predictions of degradation onset temperature, made using fast heating rates and the tangent intersection or qualitative curve interpretation methods, are likely to overestimate acceptable processing temperatures, suggesting that the drug is thermally stable, when in practice significant degradation may be experienced. The tangent intersection method consistently identifies higher degradation temperatures than the weight loss threshold method, corresponding to percentage weight loss well above any pharmaceutically acceptable level (Figure 6.5). (Note: Figure 6.5 includes polymer and ASD range data, which will be discussed in Sections 3.2 and 3.3). For the three drugs, this corresponds to volatile weight loss greater than 10% at all heating rates tested.

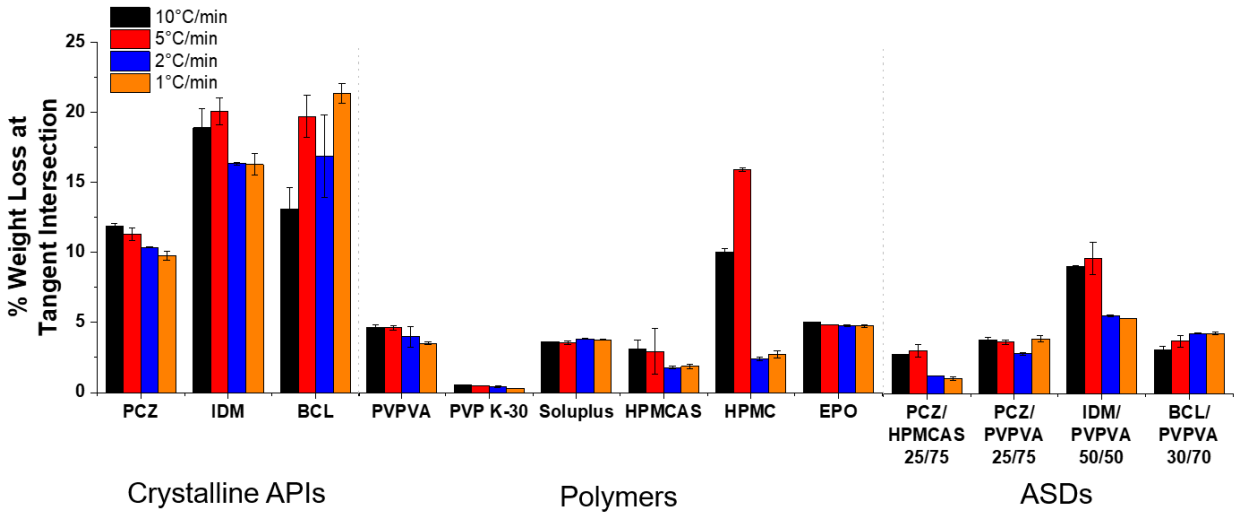

Figure 6.5. Percent weight loss at tangent intersection temperature for crystalline APIs, polymers, and ASDs.

Nonisothermal methods have additional limitations when being applied to the determination of acceptable hot melt extrusion processing windows for crystalline drugs. First, the greater reactivity of amorphous forms is not considered. Second, because only volatile degradation can be detected, degradation onset temperatures may falsely predict that a material is thermally stable within a particular temperature range, when in fact, non-volatile degradation occurs. In order to perform nonisothermal heating on an amorphous form, it must be stable against recrystallization

upon heating, which may pose significant experimental challenges, especially if slow heating rates are used (e.g. 1°C/min) in order to generate more accurate degradation assessments.

6.4.1.2 Suitability of APIs for Isothermal Heating

The hot melt extrusion process is conducted at elevated temperature, along with mechanical inputs. In HME processing to prepare amorphous solid dispersions, the intended goal of the process is to transform the crystalline drug into its amorphous state by a melting or dissolution mechanism,[36,140] Therefore, isothermal heating to investigate thermal degradation is directly translatable to the HME process, assuming degradation is not accelerated due to the shear inputs or localized heating. Limited degradation is expected for most crystalline materials,[265] and different degradation mechanisms are expected between the crystalline and amorphous states.[80] In the amorphous state, although increased degradation rates would be expected, the APIs would be susceptible to recrystallization, thus making degradation a challenging attribute to evaluate.

In order to determine if TGA can be used to study the degradation of the amorphous forms of the three APIs considered in this study, their isothermal stability against recrystallization was first evaluated. Even with APIs considered to have high glass forming ability as with the three considered here,[16,287,288] crystallization between T_g and T_m can be experimentally difficult to determine, especially with the complicating process of the potential for polymorph nucleation/growth.[98] Differential scanning calorimetry (DSC) results of the undercooled liquids of PCZ, IDM, and BCL following isothermal holds are found in Figure 6.6. Crystallization initiated in the undercooled liquid state within one hour for PCZ, evaluated from 130-160°C (T_m = 167°C, Figure 6.6a), and BCL, from 130-180°C (T_m = 193°C, Figure 6.6c). This indicates that a polymer additive would be necessary to stabilize the undercooled liquid state of these drugs in order to evaluate the isothermal degradation kinetics of these APIs below T_m.

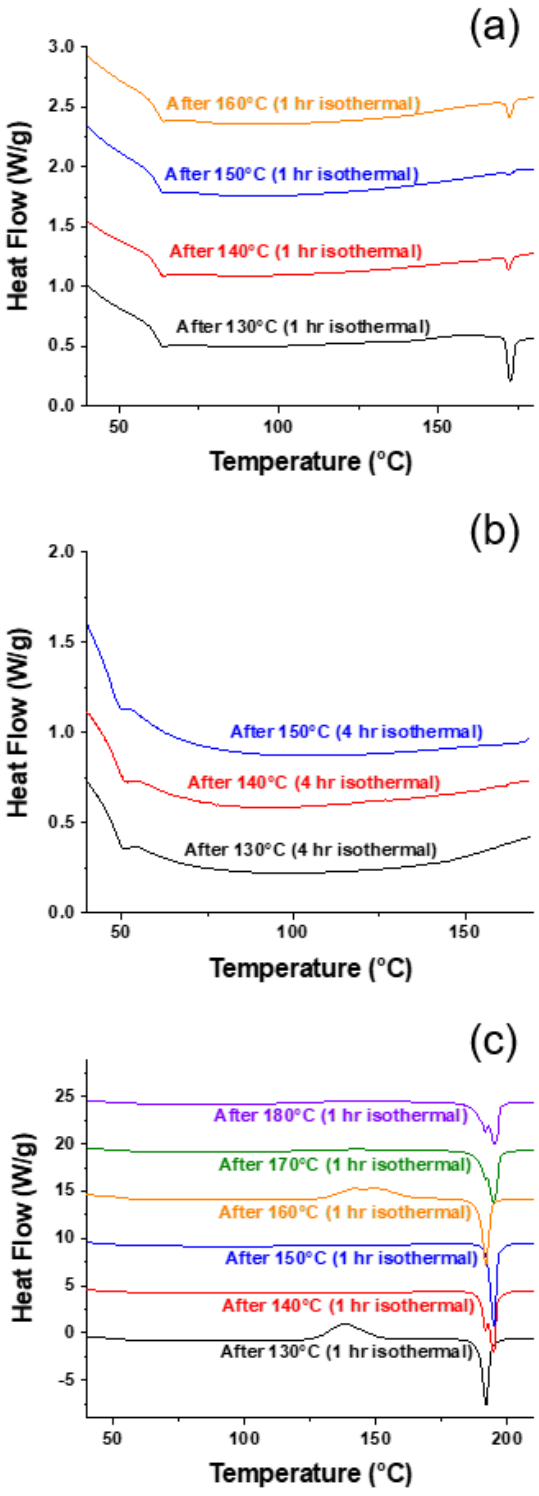

Figure 6.6. DSC traces showing the second heating cycle following isothermal hold of (a) PCZ (1 hour), (b) IDM (4 hours), and (c) BCL (1 hour). Recrystallization and/or melting events are observed for PCZ and BCL, indicating that the neat amorphous forms are not stable against recrystallization during isothermal holds as undercooled liquids.

Nucleation was not induced in the undercooled liquid of IDM over a four hour heating period at a range of 130-150°C (T_m = 160°C, Figure 6.6b), indicating that this API could be suitable for assessing degradation in its neat amorphous form at elevated temperatures over extended time periods. Such experiments were conducted by Carstensen and Morris,[80] where increased rates of degradation of the amorphous form were observed over the crystalline material. Similarly, as shown in Figure 6.7, weight loss over time is observed for crystalline and amorphous indomethacin in the 130-155°C temperature range. At all temperatures, the amorphous form degrades at a faster rate. Additionally, a different curve shape is observed between the forms, indicating a change in degradation mechanism.

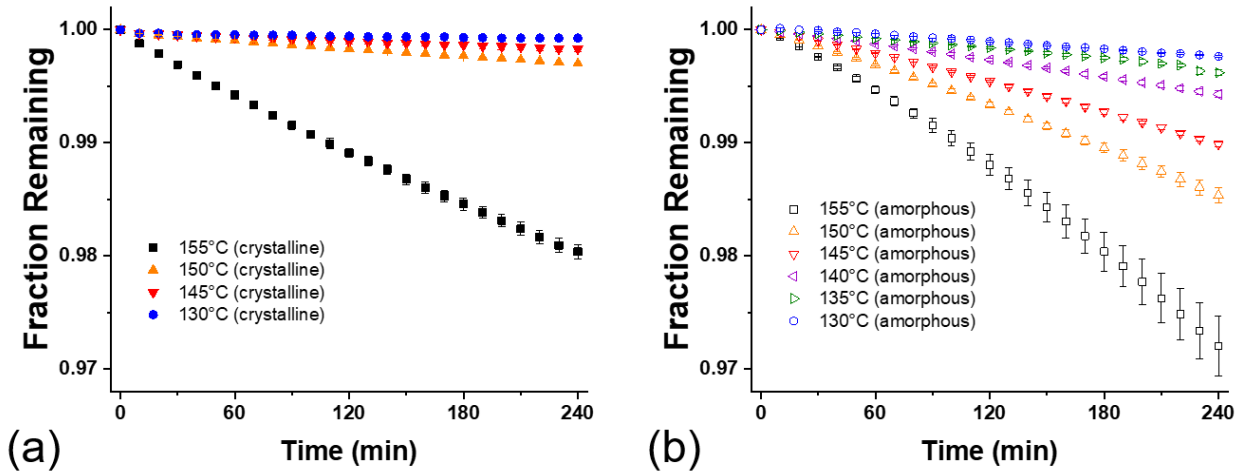

Figure 6.7. Isothermal degradation showing the weight loss curves of (a) crystalline and (b) amorphous IDM over the temperature range 130-155°C (below T_m).

6.4.2 Thermal Stability of Polymers

6.4.2.1 Nonisothermal Heating of Polymers

Three polyvinyl-based polymers (PVPVA, PVP, and Soluplus), two cellulosic polymers (HPMCAS, HPMC), and one methylacylate-based polymer (Eudragit EPO) were evaluated for their thermal stability by the nonisothermal method using four heating rates: 1, 2, 5, and 10°C/min. Nonisothermal degradation (Figure 6.8) resulted the same general trend seen in the crystalline APIs: degradation onset is dependent on heating rate and detection method used. The T_{onset} values of PVPVA, PVP, Soluplus, HPMCAS, HPMC, and Eudragit EPO ranged from 166-299°C (range 133°C), 147-199°C (range 52°C), 168-295°C (range 127°C), 149-251°C (range 102°C), 160-

330°C (range 170°C), and 156-264°C (range 108°C), respectively (Figure 6.4). The wide range of T_{onset} values found as a function of the TGA conditions and data analysis method further supports that the nonisothermal heating method does not provide suitable guide for selection HME processing conditions.

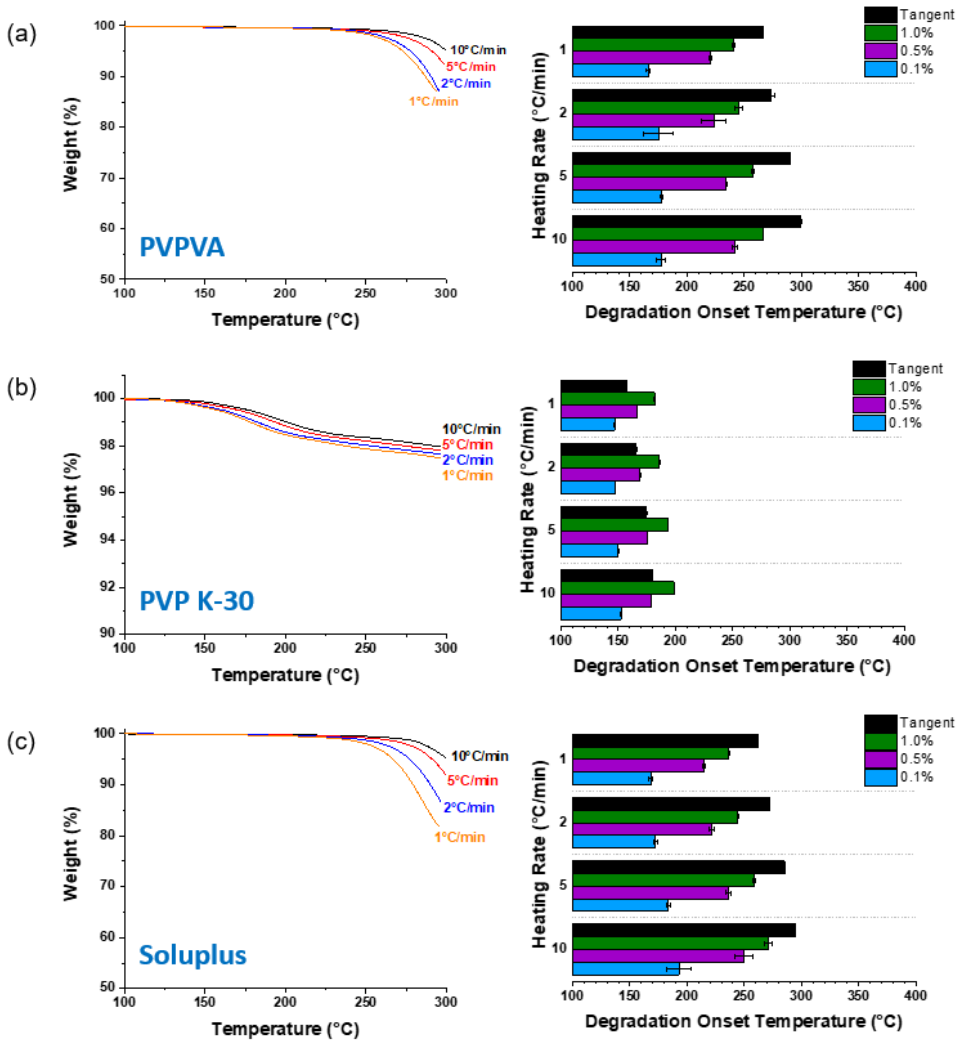

Figure 6.8. Nonisothermal TGA curves of polymers: (a) PVPVA, (b) PVP K-30, (c) Soluplus, (d) HPMCAS, (e) HPMC, and (f) Eudragit EPO.

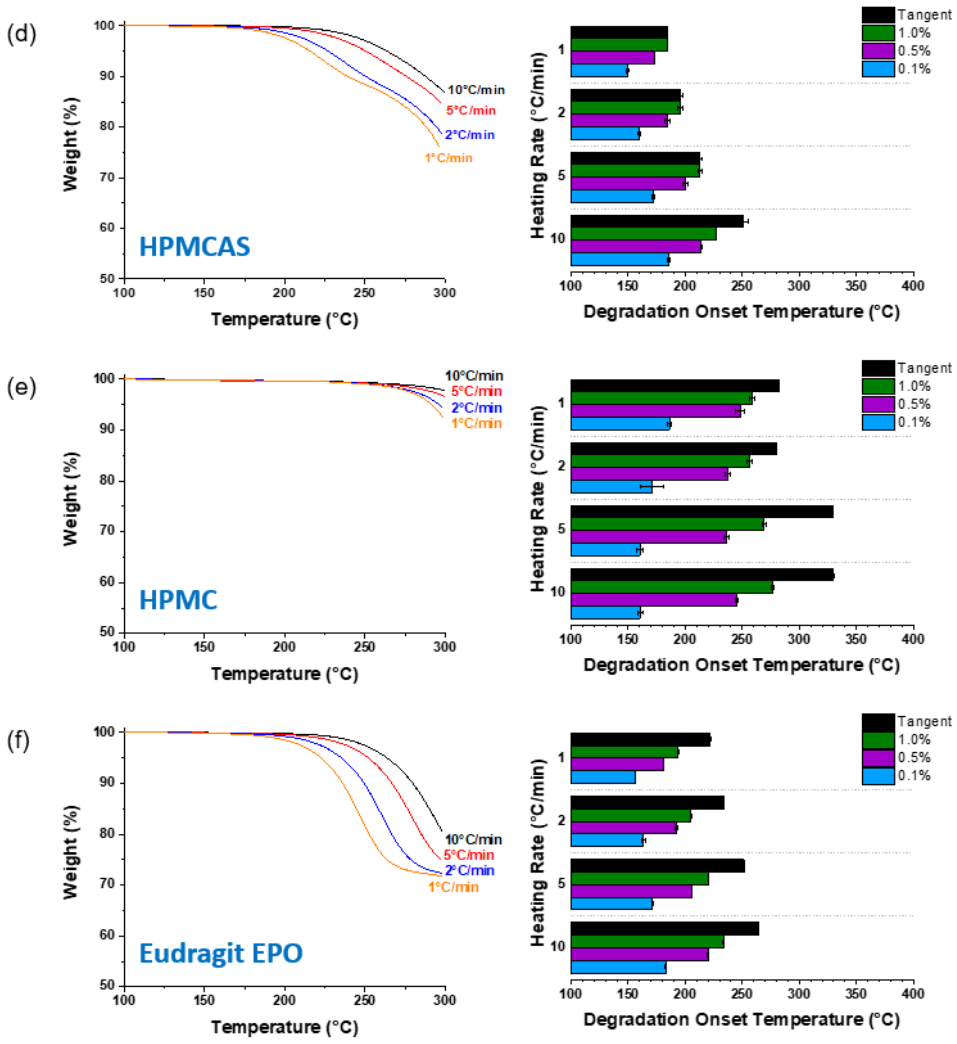

Figure 6.8 (continued). Nonisothermal TGA curves of polymers: (a) PVPVA, (b) PVP K-30, (c) Soluplus, (d) HPMCAS, (e) HPMC, and (f) Eudragit EPO.

In the series of research papers published by Serajuddin and coworkers, each of these families of polymers was studied for their thermal properties.[81,89–91] In these works, nonisothermal heating was performed at 5°C/min, and the tangent intersection method is assumed to have been used to determine the T_{onset}. The values determined herein (at 5°C/min using the tangent intersection method) are in approximate agreement with these works for all polymers except HPMC. In the Serajuddin studies,[89,91] different grades of HPMC were studied, and their heating ramp was discontinued at 300°C, while the value determined here exceeds 300°C.

With the exception of HPMC, the corresponding percentage of volatile weight loss experienced at the tangent intersection, T_{onset}, is quite consistent among the range of heating rates

tested (Figure 6.5). Interestingly, this observation is found despite the range of T_{onset} values based on heating rate.

Also of significant interest are the degradation curves of PVP K-30. In contrast to the other five polymers investigated, where the onset of degradation indicates a transition to a continued major mass loss event, a small level of degradation (~2%) occurs for PVP between ~150-200°C, and no other significant mass loss is observed up to 300°C. Jablonski and coworkers[298] have reported that the major mass loss event for PVP initiates around 380°C, and that the degree of initial small mass loss event is dependent on molecular weight. Ultimately, while 2% degradation may result in significant effects on product attributes, such as appearance, dissolution rate, or stability, the literature value of T_{onset} = 171°C reported by Serajuddin[81] likely does not reflect the major degradation event for this polymer.

6.4.2.2 Isothermal Heating of Polymers

Each polymer was subject to isothermal heating at the temperature range corresponding to typical HME processing conditions (130-200°C) for a four hour period. The plot of % weight loss (Figure 6.9) provides a simple assessment of degradation extent of the polymer based on cumulative exposure, i.e. the degradation kinetics generated by the combination of temperature and hold time. For neat polymers, this tool provides a guide for suitable HME processing conditions. PVPVA, PVP, Soluplus, and HPMC do not have significant degradation (<2%) within the range of cumulative exposure studied here. At higher temperature and longer hold times, HPMCAS and Eudragit EPO experience a greater degree of degradation. However, for both polymers, suitable conditions can be identified. HPMCAS has been observed to release acetic and succinic acid with more extreme HME processing conditions (higher temperature and screw speed), and the extrudates have a corresponding increase in yellowness.[299]

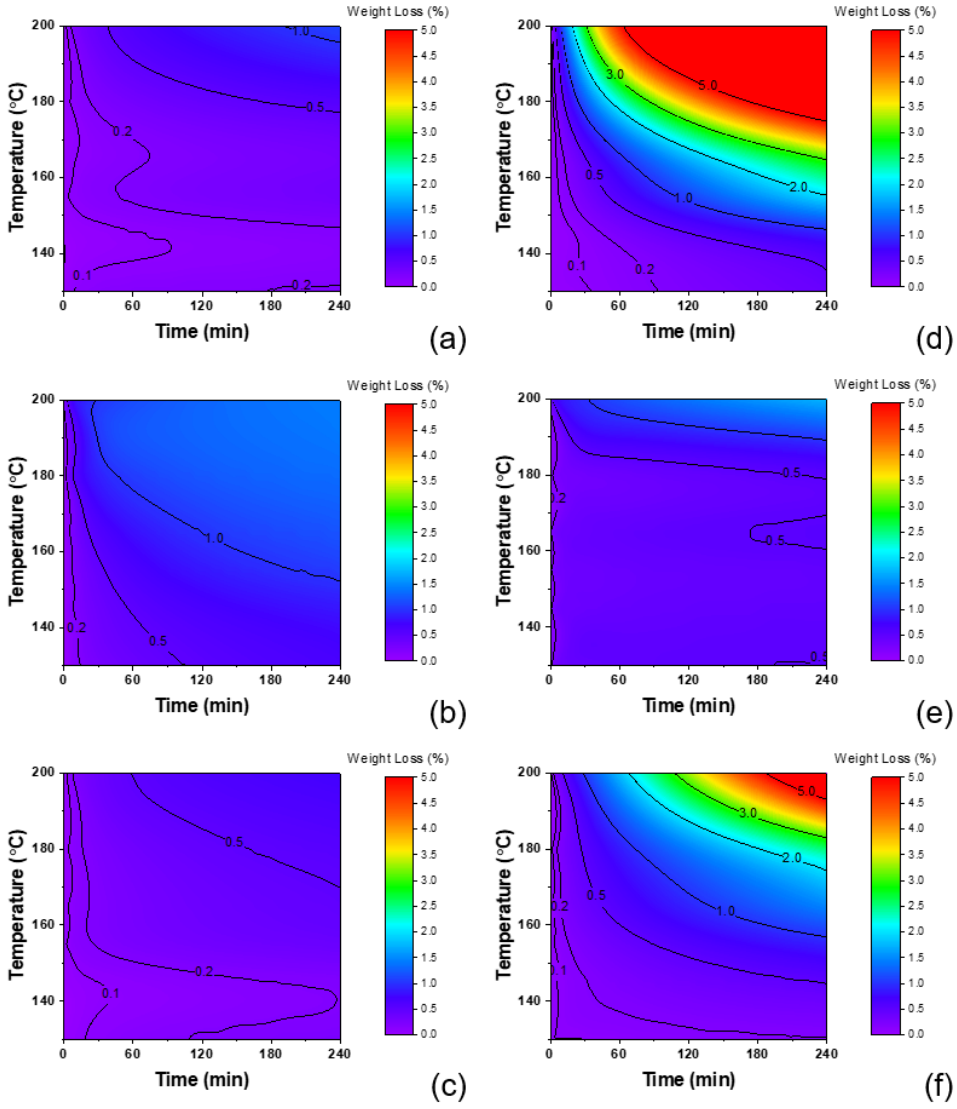

Figure 6.9. 2D contour plots showing % weight loss as a response to temperature (°C) and time (min) for polymers: (a) PVPVA, (b) PVP K-30, (c) Soluplus, (d) HPMCAS, (e) HPMC, and (f) Eudragit EPO.

Weight loss of polymers due to cumulative exposure of temperature and time may not be a comprehensive indication of suitability for HME processing. Mechanistic understanding of polymer degradation with respect to pharmaceutical formulations and processing is emerging. Several recent studies have examined polymer and formulation attributes after processing exposure, such as molecular weight (M_w), polydispersity index (PDI), rheology, and dissolution.[270,299–301] Polymer degradation is worthy of future investigation with a focus on relationship of TGA

predictions to degradation extent and product performance attributes (e.g. physical stability, dissolution performance).

6.4.3 Thermal Stability of Amorphous Drug-Polymer Systems

6.4.3.1 Nonisothermal Heating of ASDs

Drug-polymer ASDs were formulated in order to assess the suitability of TGA methods to assess the degradation of the amorphous form of the drug. The polymer has two functions for these experiments: (1) polymers may stabilize the melt against recrystallization[161,302] and (2) polymers have been reported to offer protection from thermal degradation (but may similarly destabilize them).[303,304] Further, the amorphous drug is likely to be formulated as an ASD, so the degradation assessment provides the opportunity for any interactions to present which might lead to chemical degradation issues.[125]

For such an experiment, physical mixtures of crystalline drug and polymer are likely unsuitable, as the system is unlikely to homogenize during the time frame of the experiment.[305] Homogenization reflects two phenomena: solubilization/dissolution and diffusion. At temperatures below the melting point, the crystalline drug must be first solubilized into the molten polymeric matrix to have equivalent reactivity to the amorphous form. This solubilization takes place as a crystal dissolution kinetic process, and the particle size of the crystalline drug is a key driver of dissolution rate per the Noyes-Whitney equation.[140] Second, the formation of a completely homogenous melt requires the drug to diffuse through the high viscosity environment of the molten polymer. In a recent study, the diffusion layer of an indomethacin crystal dissolving into a polymer film was found to be on the order of 8 μm,[242] reflecting the slow diffusivity of the drug molecule through the viscous polymer under high temperature quiescent conditions.

In the BCL/PVPVA model system, the delay in chemical reactivity was observed during a non-isothermal heating ramp (Figure 6.10). The weight loss curve of the physical mixture with micronized drug was similar to that of the ASD (reflecting faster crystal dissolution and drug diffusion kinetics due to the particle size), while the weight loss curve of the physical mixture with large drug crystals was delayed by approximately 10°C. This delay was similar for all heating rates 1-10°C/min. Essentially, because the solubilization/dissolution and diffusion mechanisms do not need to take place, the ASD provides a worst-case scenario for drug degradation, enabling

improved assessments for the drug-polymer system over a crystalline physical mixture. Additionally, as molecular interactions may form in an ASD, by forming the ASD prior to the TGA degradation assessment, this provides a best-case scenario for enabling an assessment of drug degradation (or stabilization) in the presence of a polymer.

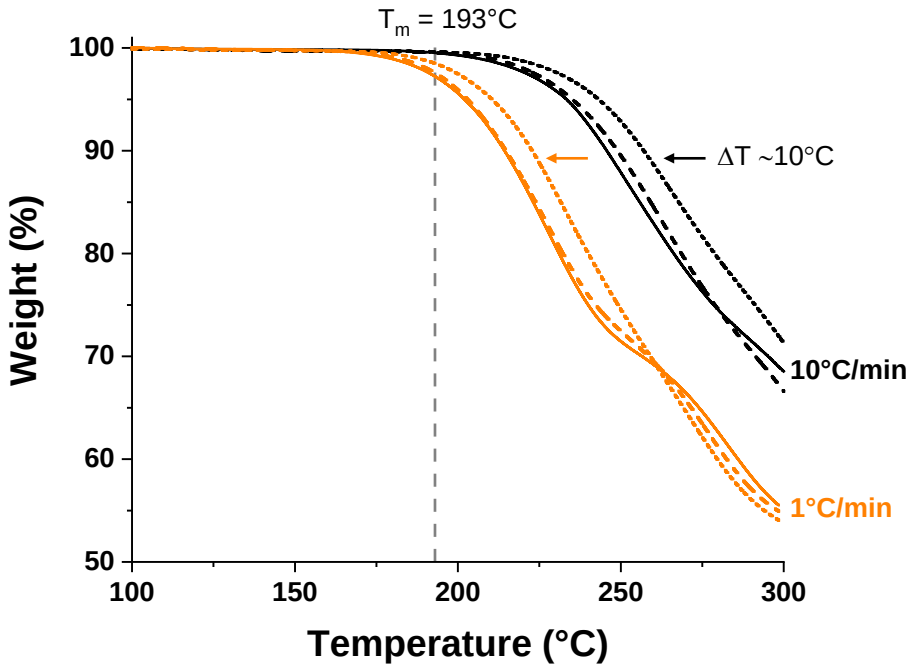

Figure 6.10. Nonisothermal TGA curves of BCL/PVPVA ASD (solid line) and crystalline physical mixtures (micronized particle size: dashed line, large particle size: short dashed line).

ASDs were evaluated for their thermal stability by the nonisothermal method using four heating rates: 1, 2, 5, and 10°C/min. Nonisothermal degradation (Figure 6.11) resulted the same general trend seen in the crystalline APIs and polymers: degradation onset is dependent on heating rate and detection method used. For PCZ, the T_{onset} values reduced by approximately 30°C from those found with the crystalline API, and further varied by the polymer used: 158-257°C (range 99°C) for PCZ/HPMCAS and 174-301°C (range 127°C) for PCZ/PVPVA. For IDM, the T_{onset} values ranged from 175-273°C (range 98°C) which is slightly higher than those found for the neat crystalline API. For BCL, the T_{onset} values ranged from 163-227°C (range 64°C), which is approximately 30°C lower than that found for the neat crystalline API.

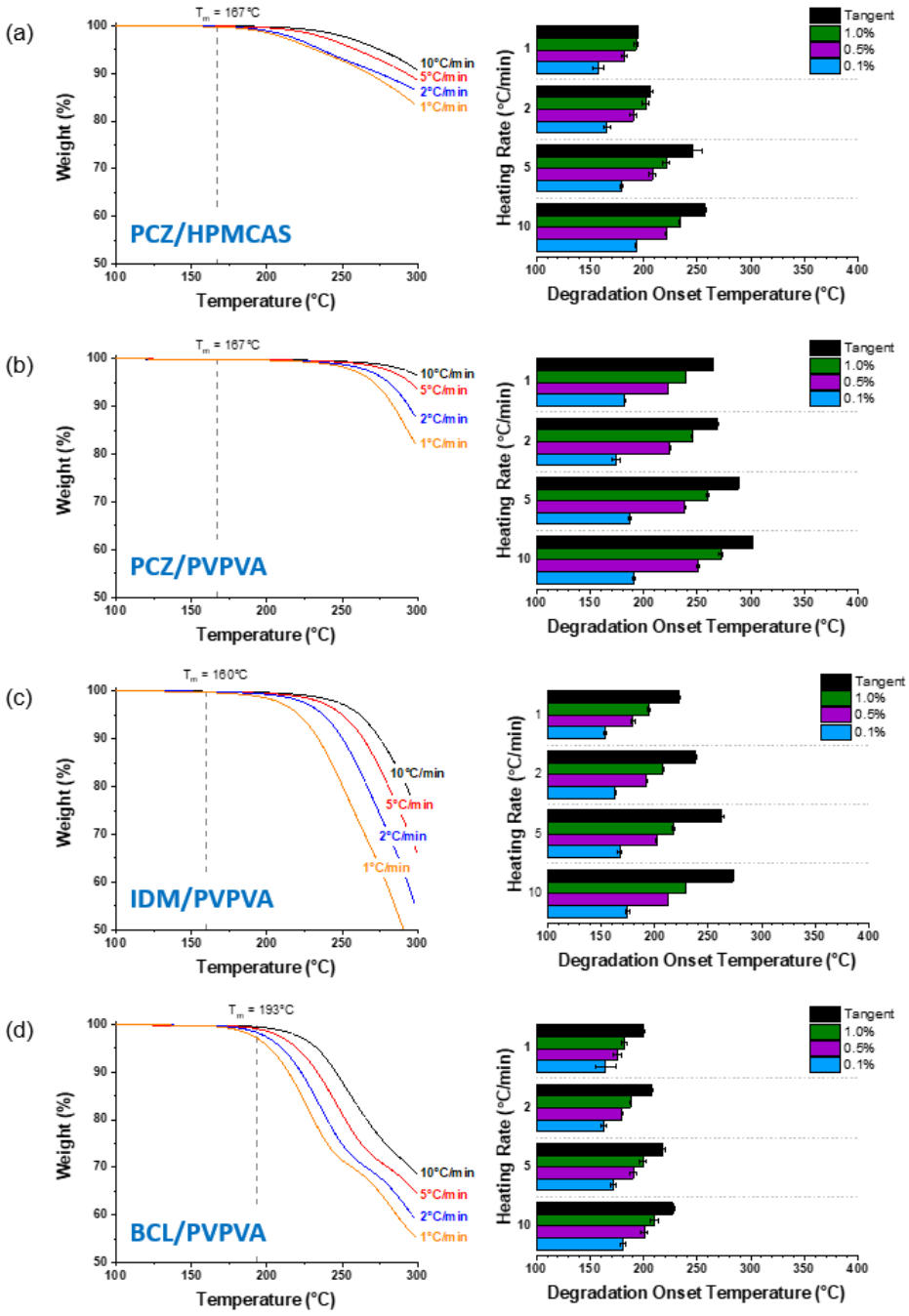

Figure 6.11. Nonisothermal TGA curves of ASDs: (a) PCZ/HPMCAS, (b) PCZ/PVPVA, (c) IDM/PVPVA, and (d) BCL/PVPVA.

For PCZ and BCL, the lower degradation onset results from a combination of effects. First, the polymer present in the sample is independently subject to thermal degradation, which was found to initiate at 149°C and 166°C for HPMCAS and PVPVA, respectively (based on lowest T_{onset} value found from the range of methods). Second, the API is in the amorphous state, and can

be expected to degrade at temperatures lower than those found for the crystalline samples. The different degradation temperature ranges found for PCZ with different polymers provides an interesting insight that PVPVA may be more protective to PCZ than HPMCAS.

The IDM/PVPVA provides a different case. Degradation onset was found to be delayed compared to the neat API sample. This suggests that PVPVA provides some protection against thermal degradation of IDM. Similar results were found by Vyazovkin and colleagues using PVP with IDM.[303,304] PVP was found to have both stabilizing or destabilizing effects based on the nature of intermolecular interactions, as well as the drug-polymer ratio. These works effectively demonstrate that the mechanism of stabilization offered by a polymer is complex, and worthy of investigation when developing drug formulations.

6.4.3.2 Isothermal Heating of ASDs and Comparison with HME Experiments

The ASD systems were subject to isothermal heating at the temperature range corresponding to typical HME processing conditions (130-200°C) for a four hour period. The plots of % weight loss vs. hold time and temperature found in Figure 6.12 enable assessment of the drug-polymer system and potential HME processing conditions. PCZ ASDs (Figure 6.12a,b) appear quite different in that the HPMCAS-formulated ASD experiences a high degree of degradation at greater exposure conditions, while the PVPVA-formulated ASD experiences degradation less than ~1% at the range of conditions. Upon close inspection, it is apparent that the level of degradation experienced by the formulation is driven by that of the polymer itself (compare Figure 6.12a with Figure 6.9d and Figure 6.12b with Figure 6.9a). Therefore, amorphous PCZ has a high degree of thermal stability at a wide range of exposure conditions, when stabilized by a polymer. Interpretation of the degradation contour plot confirms the volatile degradation experienced by HPMCAS, which has been studied in detail by Sarode et al.[299]

As degradation of posaconazole has not been extensively documented in the literature, HPLC analysis of extruded samples was performed. Samples of 25/75 PCZ/HPMCAS and 25/75 PCZ/PVPVA were produced at melt temperature conditions of 125-175°C. Regardless of extrusion temperature, all samples fell within 100-105% assay (Appendix D Table D.1), and no impurity peaks were observed beyond that observed in the standard solutions (Appendix D Figure D.2). This confirms the results observed by TGA: posaconazole has adequate thermal stability at a range of processing conditions.

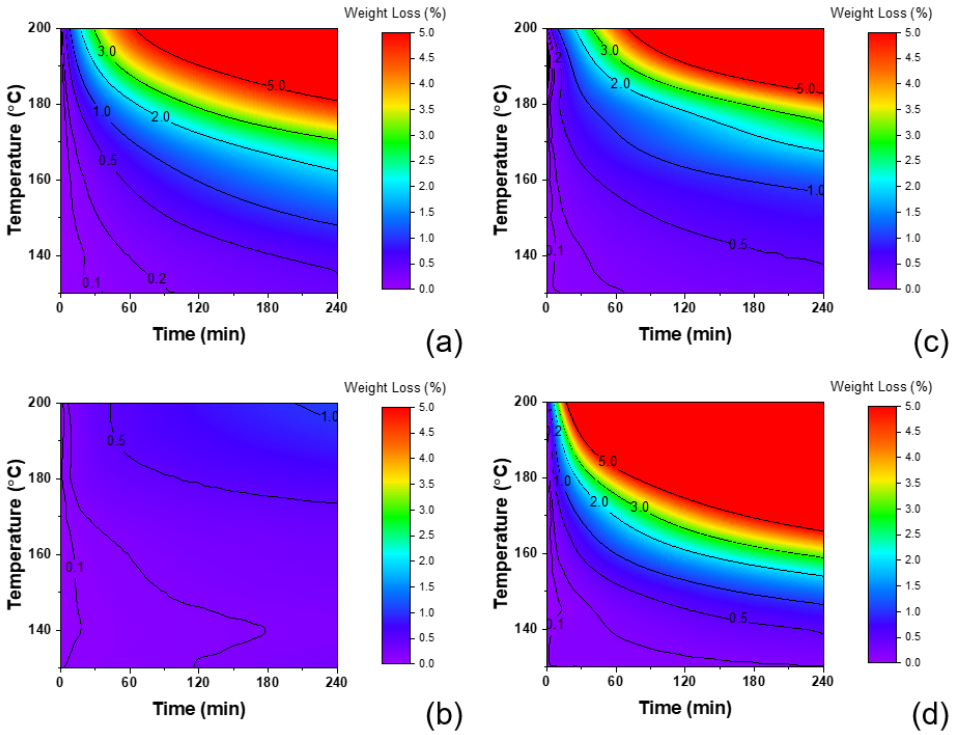

Figure 6.12. 2D contour plots showing % weight loss as a response to temperature (°C) and time (min) for ASDs: (a) PCZ/HPMCAS, (b) PCZ/PVPVA, (c) IDM/PVPVA, and (d) BCL/PVPVA.

Unlike the PCZ ASDs, the % weight loss as a response to hold time and temperature found for the IDM/PVPVA and BCL/PVPVA ASDs do not share similarity with that of their constituent polymer (compare Figure 6.12c,d with Figure 6.9a). Thus, their degradation must be primarily driven by the amorphous API. The 2D contour plots demonstrate that the IDM/PVPVA ASD (Figure 6.12c) has limited volatile degradation (<1%) at short exposure times (<10 min) for all temperatures (up to 200°C), and for extended times at temperatures of 160°C and below. Therefore, amorphous IDM has a high degree of thermal stability (demonstrated by TGA) which translates to stability at a wide range of processing conditions. The thermal stability of IDM during HME processing as has been observed in the literature[82,306–308] and confirmed in several HME samples prepared within our laboratory (refer to Appendix D Table D.2).

The BCL/PVPVA ASD (Figure 6.12d) experienced greater degradation rates than the other studied systems. Under 180°C, limited degradation (<1%) was experienced at short hold times (<10 minutes). At 165°C, the same degradation threshold (1%) was not experienced until 40 minutes. At 155°C, over 100 minutes of exposure were required to induce that level of degradation (1%). Clearly, for this drug, processing conditions of time and temperature must be chosen

carefully in order to generate a reasonable safety margin to translate TGA experiments to HME processing.

6.4.3.3 HPLC Analysis of TGA and Extrusion Samples of Bicalutamide/PVPVA ASD System

The BCL/PVPVA system was selected for comparative assessment of TGA weight loss and extent of degradation by HPLC analysis, as it had the most severe degradation profile among the systems studied. The extent of degradation (HPLC assay) experienced by samples exposed in the TGA was compared to that predicted by isothermal weight loss for BCL/PVPVA samples at two temperatures 180°C and 165°C (Figure 6.13). Assay values of samples exposed using the TGA (green diamonds) demonstrated significantly higher degradation beyond that of the corresponding weight loss value (black circles) at each timepoint. Clearly, loss of volatiles does not predict the complete degradation profile of bicalutamide. Huang et al. found the same trend for gliclazide: potency loss was significantly greater than the extent of weight loss.[87]

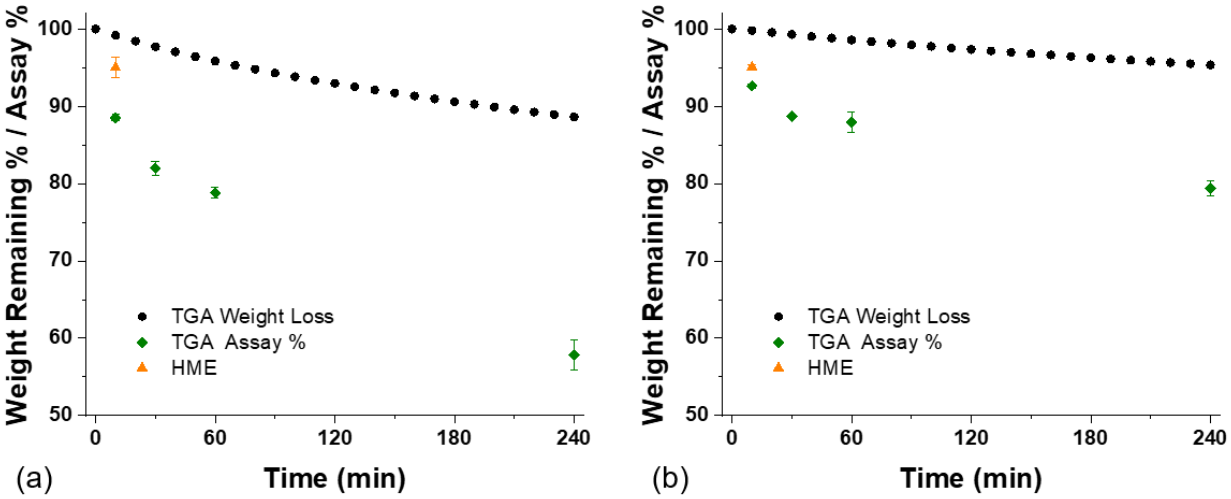

Figure 6.13. Comparison of degradation as record by TGA weight loss and assay of 30/70 BCL/PVPVA ASD samples exposed by TGA or HME at (a) 180°C and (b) 165°C. Error bars represent the standard deviation of triplicate preparations.

ASDs of BCL/PVPVA were prepared by HME in order to compare the level of degradation experienced under the quiescent conditions found in TGA. The level of degradation experienced by HME samples prepared at 180°C and 165°C for 10 minutes of processing time (orange triangles)

was compared to that found in samples of exposed in the TGA for 10 minutes-4 hours (green diamonds), as well as that predicted by weight loss recorded by TGA (black circles) (Figure 6.13). When exposed in the TGA for 10 minutes, limited degradation (<1%) was predicted by TGA weight loss data, while assay levels were found to be 88.5 ± 0.4% and 92.6 ± 0.2% at 180°C and 165°C, respectively. For the corresponding samples processed in the HME at 180°C and 165°C, assay values of 95.0 ± 1.3% and 95.0 ± 0.4% were found, respectively. Thus, the HME samples were found to be slightly less degraded than the samples exposed in the TGA at equivalent conditions. The appearance of degradants in the HME and TGA assay samples followed this trend. As seen in Figure 6.14, approximately 5-fold higher total peak area of degradant peaks is associated with the TGA assay samples (10 minutes isothermal hold) compared to the HME preparations at 10 minutes of processing time (1.5 ± 0.3% vs. 0.3 ± 0.1% peak area at 180°C, 0.34 ± 0.10% vs 0.07 ± 0.01% peak area at 165°C).

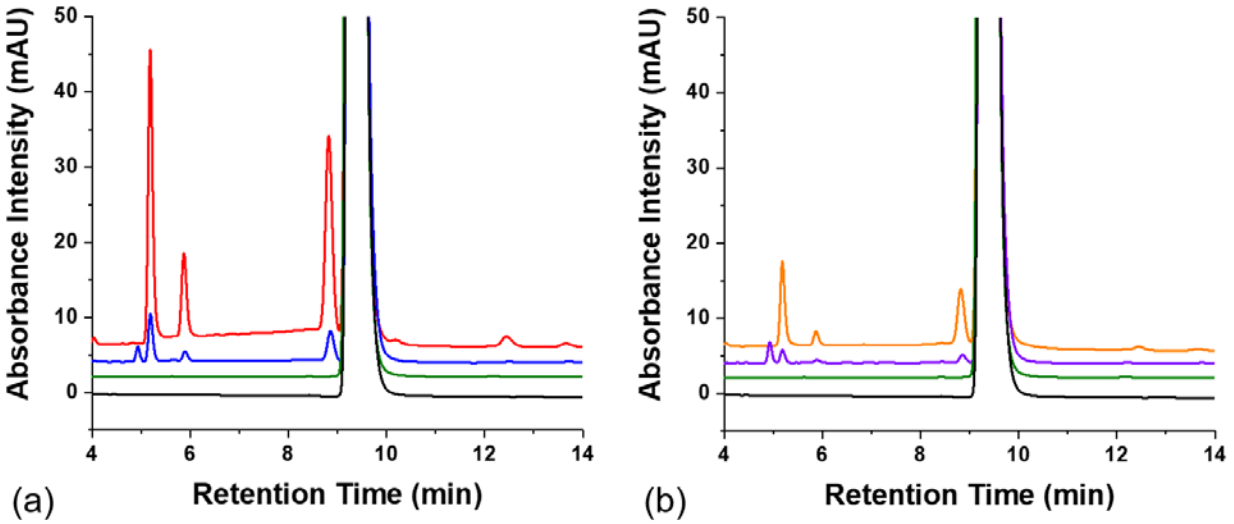

Figure 6.14. Representative chromatograms of BCL standard preparation (black), 30/70 BCL/PVPVA physical mixture (green), and 30/70 BCL/PVPVA ASD samples exposed by HME (blue, purple) or TGA (red, orange) for 10 minutes at (a) 180°C and (b) 165°C.

While unexpected, the harsher conditions found in the TGA may be due to the factors associated with the method. First, to achieve the target isothermal temperature, samples are heated at 50°C/min. To then reach room temperature after the isothermal hold, the samples are subjected to air cooling. Ultimately, the time of exposure at higher temperatures may be up to twice as long as the isothermal hold time. Second, the TGA samples are under a nitrogen purge, which may have

the effect of quickly removing volatile degradation products, and accelerating the reaction kinetics. Reduced degradation (by volatile weight loss) under air compared to nitrogen purge has been observed by Huang et al.[87]

Additionally, the processing conditions used in this study represent limited shear input. In larger scale continous extruders, increased specific mechanical energy can be found through extruder design and processing parameters (such as screw speed and feeding rate), and localized heating effects may be more pronounced.[86,87,309,310] Specific mechanical energy, in conjunction with process temperature, has found to promote to chemical degradation,[311] and is an important parameter when determining the acceptable processing window. When considering these shear effects, our results are even more surprising and significant. In our study, temperature effects experienced by the sample in both the TGA and in our HME (with limited shear input) is the primary factor driving degradation, and limited correlation between the two was observed for BCL/PVPVA samples. If the system were susceptible to degradation through associated mechanical inputs, degradation predictions by TGA weight loss measurements alone would be far from sufficient. This highlights the necessity of conducting assay measurements to determine the acceptability of processing conditions, related to both thermal and mechanical input, and not rely solely on TGA results.

6.5 Conclusion

The utility of nonisothermal and isothermal TGA methods to assess chemical stability of amorphous drug and polymer systems from the perspective of hot melt extrusion processing was critically examined. The primary limitation of TGA methods, namely that mass loss of volatiles is not equivalent to formation of degradants, significantly impedes its ability to provide consistent universal indicators of actual extent of degradation. Therefore, mass loss should be considered only an indicator of degradation, as actual potency loss is likely to be significantly higher than the mass loss. Thus, although TGA can provide a guide to identify temperature conditions and formulations that are susceptible to degradation, acceptable processing windows in terms of temperature range should be defined by assay experiments.

APPENDIX A. SUPPORTING INFORMATION FOR CHAPTER 2

Xplore Pharma Melt Extruder

A schematic of the Xplore Pharma Melt Extruder is presented in Figure A.1. The co-rotating conveying screws have a diameter of 14 mm and length of 120 mm. The thermocouple is positioned after the screws, and provides a real-time measurement of the product melt temperature. If the valve is closed, the melt continues into the recirculation channel. If the valve is open, the melt flows through the 3 mm die. Shear rate is controlled by the gap between the barrel and the top of the screw flight (0.1 mm). The instrument capabilities were demonstrated by Sakai et al.[134]

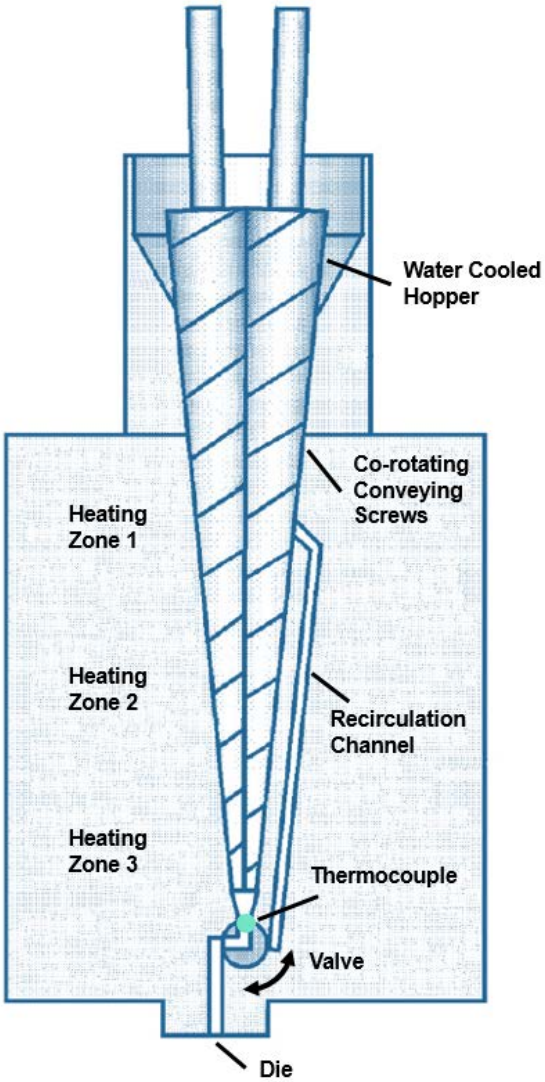

Figure A.1. Schematic of the Xplore Pharma Melt Extruder

Extrudate Appearance

Extrusion samples of the 50% drug loading composition were prepared at a range of product melt temperatures and residence times. The visual appearance of each extrudate is reported in Table 2.2, and a representative set of extrudates is pictured in Figure A.2. Samples produced at short residence times have more entrapped air, due to the extruder configuration. In contrast, samples produced with the recirculation loop (and thus longer residence times) have regular exposure to the input site, where air can escape, so these samples have fewer air bubbles. Due to the vertical extruder configuration and viscous flow, samples produced at lower temperatures have a larger diameter than those produced at higher temperatures. Amorphous indomethacin brings a yellow hue to all extrudates.

Extrudates produced at low melt temperatures and/or short residence times have visible crystals or are cloudy/opaque, corresponding to an increase in crystalline content. The clarity of the extrudate improves as temperature and/or residence time increases. Below the Tc, all samples produced are cloudy or opaque, consistent with residual crystalline content. At the Tc (131°C), 2 minutes of residence time produced a very cloudy extrudate. After 20 minutes, the extrudate produced is clear without visible crystals. Above the Tc, by providing sufficient thermal input, samples become clear. A clear extrudate may yet have residual crystalline content, detectable by higher resolution techniques.

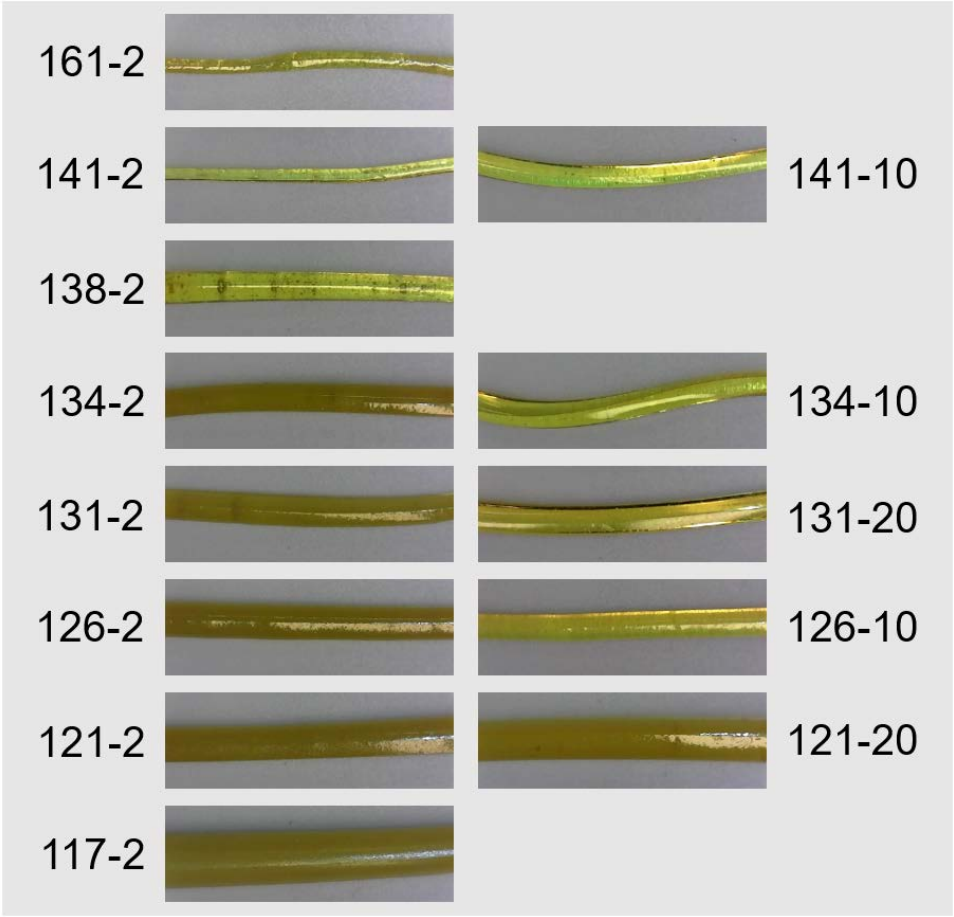

Figure A.2. Representative IDM:PVPVA extrudates. Extrudates produced at lower temperatures and/or shorter residence times have visible crystals or are cloudy/opaque, corresponding to an increase in crystalline content. Extrudate clarity improves with increasing temperature and/or residence time.

XRPD Raw Data

The raw XRPD diffractograms of the HME samples, constituent components (IDM, PVPVA), physical mixture (PM5050), and solvent evaporation preparation (SE5050) are presented in Figure A.3.

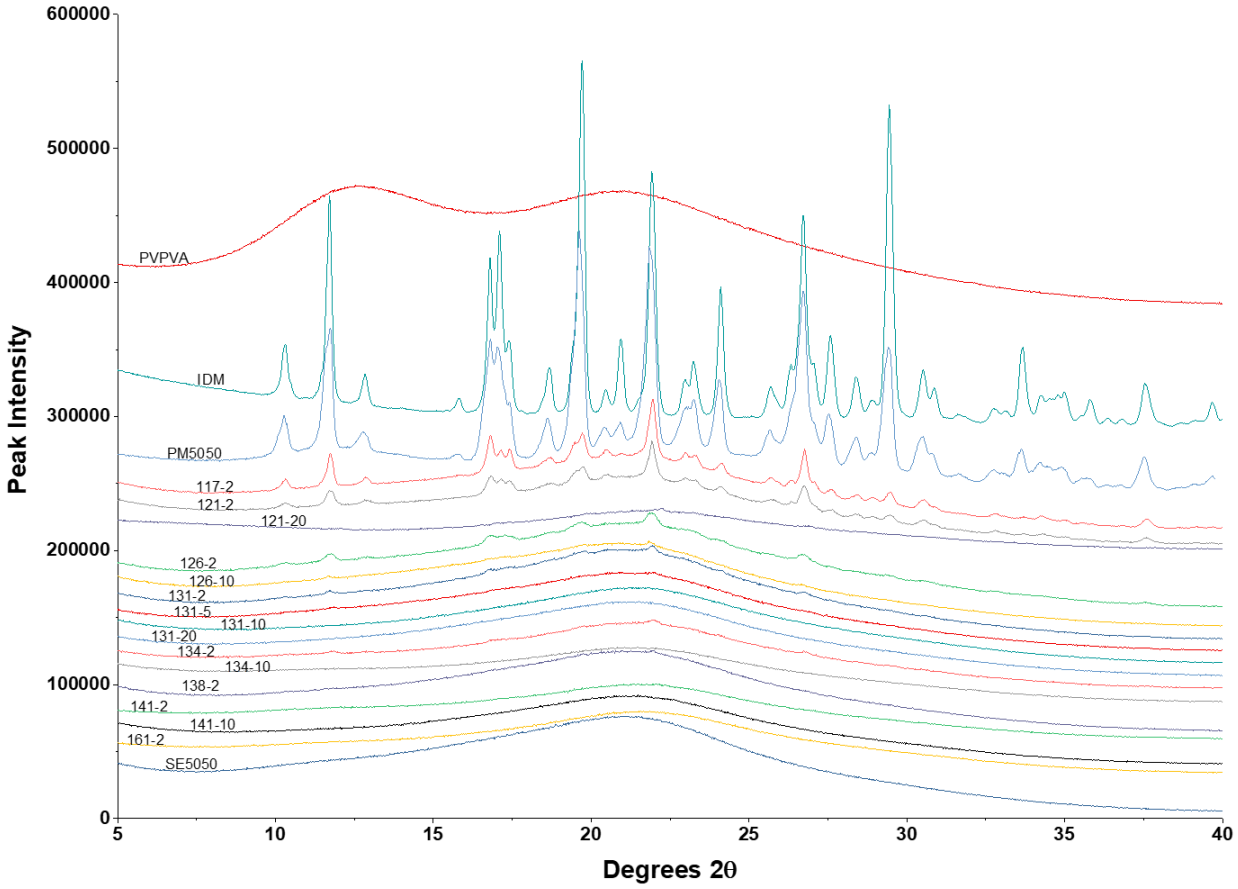

Figure A.3. XRPD diffractograms of IDM, PVPVA, 1:1 IDM:PVPVA physical mixture (PM), and 1:1 IDM:PVPVA ASDs prepared by HME.

DSC Analysis

DSC thermograms showing reversing heat flow (Figure A.4a) and non-reversing heat flow (Figure A.4b) of the first heating cycle. In the reversing heat flow, the glass transitions of several of the 1:1 IDM:PVPVA ASDs prepared by HME are compared to PVPVA, the 1:1 IDM:PVPVA physical mixture (PM5050), and the 1:1 IDM:PVPVA ASDs prepared by solvent evaporation (SE5050). The glass transition of each of the HME ASDs are located in the same temperature range as that of the solvent evaporation sample. The glass transition of the physical mixture corresponds to that of PVPVA. In the non-reversing heat flow, the water evaporation endotherm can be seen in each sample from approximately 40-80°C. Several of the 1:1 IDM:PVPVA ASDs prepared by HME (2 minutes residence time) are compared to the 1:1 IDM:PVPVA physical mixture (PM5050), and the 1:1 IDM:PVPVA ASDs prepared by solvent evaporation (SE5050). The physical mixture shows the largest dissolution endotherm between approximately 105-160°C. The size of the dissolution endotherm decreases for each HME ASD as the operating melt temperature decreases, with equivalent residence time, up to 131°C. Above this operating melt temperature, the dissolution endotherm is not observed.

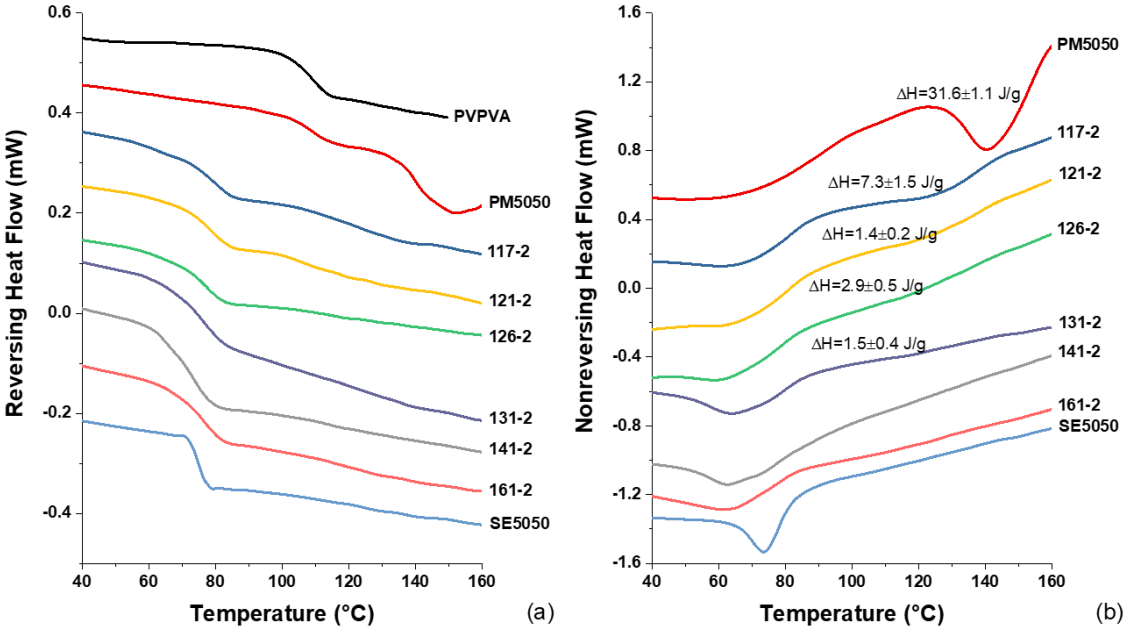

Figure A.4. DSC thermograms showing (a) reversing heat flow and (b) non-reversing heat flow of the first heating cycle.

APPENDIX B. SUPPORTING INFORMATION FOR CHAPTER 4

Code used for Monte Carlo Simulations

```
## ================= MC Crystal Dissolution - Version 1.0 ============== ##
# ========================================================================
#  Version 1.0 is a stochastic, 2D-lattice crystal dissolution simulation,
#  applying a pseduo-Metropolis method to evaluate trial MC moves. Energy
#  penalties are assigned for forming new interfaces when crystal units are
#  removed. Underlying surface energy distribution of the crystal surface is
#  also tuned to control diffusion-limited dissolution and dissolution
#  driven by surface defects.
# ========================================================================
import numpy as np # Library used for mathematical operations
import matplotlib.pyplot as plt # Library used for simulation visualization

## ========================= Initialize Parameters ====================== ##
MC_samples = 30000000 # Number of trial MC steps
Accepted = 0 # Tracks number of accepted MC moves
Rejected = 0 # Tracks number of rejected MC moves
seed = np.random.randint(0, 4294967296, dtype = 'uint32') # Generate seed
MC_seed = np.random.seed(seed) # Seed random number generation
#MC_seed = np.random.seed(5400) # Used for repeatability/troubleshooting

## ============================ Generate Grids ========================== ##
# ========================================================================
#  Variable 'grid' stores if a given "lattice" location
#  contains a crystallite unit (1 for yes, 0 for no)
# ========================================================================
dimensionality = 500 # Desired simulation size
total_lattice_sites = int((dimensionality - 2)**2)
grid = np.ones((dimensionality, dimensionality), dtype='int')
# Following lines cause the outer edge sites to be vacant
grid[0,:] = 0
grid[:,0] = 0
grid[dimensionality - 1,:] = 0
grid[:,dimensionality - 1] = 0
indices = np.indices((dimensionality, dimensionality))

## ============================== Energetics ============================ ##
# ========================================================================
#  Assign energy benefits and penalties associated with dissolution and forming
#  interfaces. The base energy (surface energy) for each site is set
#  initially and then multiple defect sites can be added. Defects can take the
#  form of grain boundaries or 2D Gaussians with accompanying orthogonal stress
#  lines of random spatial orientation
# ========================================================================
```

```
vert_interface = 4 # Energy penalty from forming verical interface
horz_interface = 4 # Energy penalty from forming horizontal interface

# Surface Energy Distribution - 1 corresponds to no defect
#                               2 corresponds to grain boundary
#                               3 corresponds to multiple small defects
configuration = 1

# No defects
if configuration == 1:
    surface_energy_distribution = np.zeros((dimensionality, dimensionality))

# Grain boundary
elif configuration == 2:
    width = 11 # Odd number giving the width of the score
    amp_max = 7 # Max surface energy at peak of defect
    base = amp_max*np.ones((dimensionality, dimensionality))
    upper = np.triu(base, (width-1)/2)
    lower = np.tril(base, -(width-1)/2)
    surface_energy_distribution = np.subtract(np.subtract(base, upper), lower)

# Multiple small defects
else:
    # Generate random locations for defects and random orientations for the
    # pairs of orthongonal lines
    defects = 3
    x_center = np.transpose(np.random.randint(1, dimensionality - 1, defects))
    y_center = np.transpose(np.random.randint(1, dimensionality - 1, defects))
    angles = 90.0 - 180*np.random.rand(defects,1)

    spread = dimensionality/10 # Spread of effect of defect
    amp_max = 7 # Max surface energy at peak of defect
    surface_energy_distribution = np.zeros((dimensionality, dimensionality))

    # Generates a suface containing various randomly placed defect sites
    for counter in range(0, defects):
        x_diff = np.power(x_center[counter] - indices[1], 2)
        y_diff = np.power(y_center[counter] - indices[0], 2)
        diff_sum = x_diff+y_diff
        surface_energy_distribution += amp_max*np.exp(-diff_sum/spread)
        grid[y_center[counter], x_center[counter]] = 0

    width = 3 # Thickness of orthogonal lines
    # Generate orthgonal lines originating from each defect. By convention
    # below, line 1 and line 2 are colinear while line 3 and line 4 are
    # colinear, each traveling in opposite directions from the center of the
    # defect
    for counter in range(defects):
        main_slope = np.tan(np.radians(angles[counter]))
        if main_slope < 0:
```

```
    off_slope = np.tan(np.radians(angles[counter] + 90.0))
else:
    off_slope = np.tan(np.radians(angles[counter] - 90.0))


if np.fabs(angles[counter]) > 45.0:
    slope1 = main_slope
    slope2 = off_slope
else:
    slope2 = main_slope
    slope1 = off_slope

# Line 1
y1_line = -np.arange(-y_center[counter],0)
run_over_rise_1 = np.floor((1/slope1)*np.indices(( \
                  len(y1_line),))).astype('int')
x1_line =  np.multiply(np.ones((1,len(y1_line)), dtype='int'), \
           x_center[counter], dtype='int') - run_over_rise_1
x1_line_adj = np.trim_zeros(np.ndarray.flatten(np.multiply (\
              np.multiply(x1_line, np.greater_equal( \
              x1_line, 1, dtype = 'int')), np.less_equal( \
              x1_line,dimensionality-2, dtype = 'int')).astype('int')))
y1_line_adj = np.trim_zeros(np.ndarray.flatten(np.multiply( \
              np.multiply(y1_line, np.greater_equal( \
              x1_line, 1, dtype = 'int')), np.less_equal( \
              x1_line,dimensionality-2, dtype = 'int')).astype('int')))
y1_ind = np.transpose(np.concatenate( \
         (y1_line_adj, y1_line_adj, y1_line_adj)))
x1_ind = np.transpose(np.concatenate( \
         (x1_line_adj - 1, x1_line_adj, x1_line_adj + 1)))

# Line 2
y2_line = np.arange(y_center[counter], dimensionality-1)
run_over_rise_2 = np.floor((1/slope1)*np.indices(( \
                  len(y2_line),))).astype('int')
x2_line = np.multiply(np.ones((1,len(y2_line)), dtype='int'), \
          x_center[counter], dtype='int') + run_over_rise_2
x2_line_adj = np.trim_zeros(np.ndarray.flatten(np.multiply( \
              np.multiply(x2_line, np.less_equal( \
              x2_line,dimensionality-2, dtype = 'int')), \
              np.greater_equal(x2_line, 1, dtype = 'int')) \
              .astype('int')))
y2_line_adj = np.trim_zeros(np.ndarray.flatten(np.multiply( \
              np.multiply(y2_line, np.less_equal( \
              x2_line,dimensionality-2, dtype = 'int')), \
              np.greater_equal(x2_line, 1, dtype = 'int')) \
              .astype('int')))
y2_ind = np.transpose(np.concatenate( \
         (y2_line_adj, y2_line_adj, y2_line_adj)))
x2_ind = np.transpose(np.concatenate( \
```

```
                (x2_line_adj - 1, x2_line_adj, x2_line_adj + 1)))

        # Line 3
        x3_line = -np.arange(-x_center[counter], 0)
        rise_over_run_3 = np.floor(slope2*np.transpose( \
                          np.indices((len(x3_line),)))).astype('int')
        y3_line = np.transpose(np.multiply(np.ones((len(x3_line),1), \
                  dtype='int'), y_center[counter], dtype='int') \
                  - rise_over_run_3)
        y3_line_adj = np.trim_zeros(np.ndarray.flatten(np.multiply( \
                      np.multiply(y3_line, np.less_equal( \
                      y3_line,dimensionality-2, dtype = 'int')), \
                      np.greater_equal(y3_line, 1, dtype = 'int')) \
                      .astype('int')))
        x3_line_adj = np.trim_zeros(np.ndarray.flatten(np.multiply( \
                      np.multiply(x3_line, np.less_equal( \
                      y3_line,dimensionality-2, dtype = 'int')), \
                      np.greater_equal(y3_line, 1, dtype = 'int')) \
                      .astype('int')))
        x3_ind = np.concatenate((x3_line_adj, x3_line_adj, x3_line_adj))
        y3_ind = np.concatenate((y3_line_adj - 1,y3_line_adj, y3_line_adj + 1))

        # Line 4
        x4_line = np.arange(x_center[counter], dimensionality-1)
        rise_over_run_4 = np.floor(slope2*np.transpose(np.indices( \
                          (len(x4_line),)))).astype('int')
        y4_line =  np.transpose(np.multiply(np.ones((len(x4_line),1), \
                   dtype='int'), y_center[counter], dtype='int') \
                   + rise_over_run_4)
        y4_line_adj = np.trim_zeros(np.ndarray.flatten(np.multiply( \
                      np.multiply(y4_line, np.greater_equal(y4_line, 1, \
                      dtype  =  'int')),  np.less_equal(y4_line,dimensionality-
2,\
                      dtype = 'int')).astype('int')))
        x4_line_adj = np.trim_zeros(np.ndarray.flatten(np.multiply( \
                      np.multiply(x4_line, np.greater_equal(y4_line, 1, \
                      dtype  =  'int')),  np.less_equal(y4_line,dimensionality-
2,\
                      dtype = 'int')).astype('int')))
        x4_ind = np.concatenate((x4_line_adj, x4_line_adj, x4_line_adj))
        y4_ind = np.concatenate((y4_line_adj - 1,y4_line_adj, y4_line_adj + 1))

        # Incorporate lines into surface energy configuration
        np.put(surface_energy_distribution, np.ravel_multi_index( \
              [[y1_ind], [x1_ind]], (dimensionality, dimensionality)), amp_max)
        np.put(surface_energy_distribution, np.ravel_multi_index( \
              [[y2_ind], [x2_ind]], (dimensionality, dimensionality)), amp_max)
        np.put(surface_energy_distribution, np.ravel_multi_index( \
              [[y3_ind], [x3_ind]], (dimensionality, dimensionality)), amp_max)
        np.put(surface_energy_distribution, np.ravel_multi_index( \
```

```
            [[y4_ind], [x4_ind]], (dimensionality, dimensionality)), amp_max)

# Surface Energy Distribution Plot
plt.figure()
plt.pcolormesh(surface_energy_distribution)
plt.colorbar()
plt.title('Surface Energy Distribution')
plt.clim(0, amp_max)

## ==================== Crystal Dissolution Simulation ================= ##
for counter in range(MC_samples):

    # End simulation if entire surface crystallizes
    if Accepted == total_lattice_sites:
        print('Surface completely dissolved')
        break

    # Pring extent of dissolution and save surface plot every specified number
    # of steps, with appropriate axis labels, title, and file identifier
    if (counter + 1) % 10000000 == 0:
        fig = plt.figure()
        power = np.int(np.floor(np.log10(counter + 1)))
        value = (counter + 1) / pow(10, power)
        file_name = 'ColorSet1_E{:d}_{:.1f}.png'.format(power, value)
        plt.pcolormesh(grid, cmap='cool')
        plt.colorbar()
        plt.title(format('%d Trial Monte Carlo Steps' % (counter + 1)))
        fig.savefig(file_name)
        plt.close(fig)
        print(Accepted / total_lattice_sites)

    # Pick a crystallized spot at random
    [trial_x_index, trial_y_index] = np.random.randint(
                                    1, dimensionality - 1, size=2)
    while grid[trial_y_index, trial_x_index] == 0:
        [trial_x_index, trial_y_index] = np.random.randint(
                                        1, dimensionality - 1, size=2)

    # Determine neighboring sites
    up_neighbor = grid[trial_y_index - 1, trial_x_index]
    down_neighbor = grid[trial_y_index + 1, trial_x_index]
    left_neighbor = grid[trial_y_index, trial_x_index - 1]
    right_neighbor = grid[trial_y_index, trial_x_index + 1]
    all_neighbors = np.array([up_neighbor, down_neighbor,
                              left_neighbor, right_neighbor])
    [filled_neighbors] = np.nonzero(all_neighbors)

    # Evaluate energetics
    delta_E = -surface_energy_distribution[trial_y_index, trial_x_index]
```

```
# If down site is occupied, penalize for new vertical interface; otherwise
# give benefit for removing interface
if down_neighbor == 1:
    delta_E += vert_interface
else:
    delta_E -= vert_interface

# If up site is occupied, penalize for new vertical interface; otherwise
# give benefit for removing interface
if up_neighbor == 1:
    delta_E += vert_interface
else:
    delta_E -= vert_interface

# If left site is occupied, penalize for new horizontal interface;
# otherwise give benefit for removing interface
if left_neighbor == 1:
    delta_E += horz_interface
else:
    delta_E -= horz_interface

# If right site is occupied, penalize for new horizontal interface;
# otherwise give benefit for removing interface
if right_neighbor == 1:
    delta_E += horz_interface
else:
    delta_E -= horz_interface

# Calculate probability of removing unit then compare against random
# number between 0.0 and 1.0, accepting move if probability exceeds it
exp_E = np.exp(-delta_E)
if exp_E >= 1.0:
    grid[trial_y_index, trial_x_index] = 0
    Accepted += 1
else:
    test = np.random.random()
    if exp_E > test:
        grid[trial_y_index, trial_x_index] = 0
        Accepted += 1
    else:
        Rejected += 1
```

APPENDIX C. SUPPORTING INFORMATION FOR CHAPTER 5

Hot Melt Extrusion

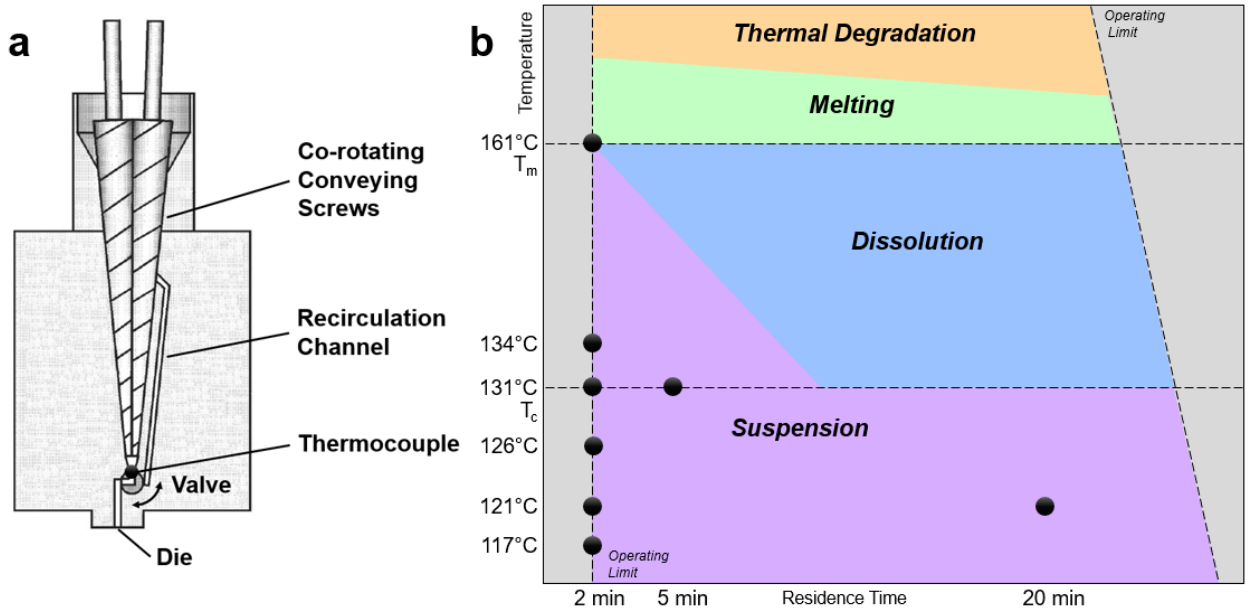

Figure C.1. (a) Schematic of the Xplore hot melt extruder. (b) The process conditions of the eight IDM:PVPVA HME ASDs (black dots) are represented within a process operating space diagram, constructed based on solid state characterization of many samples found in our previous work.[140]

Solubility Determination

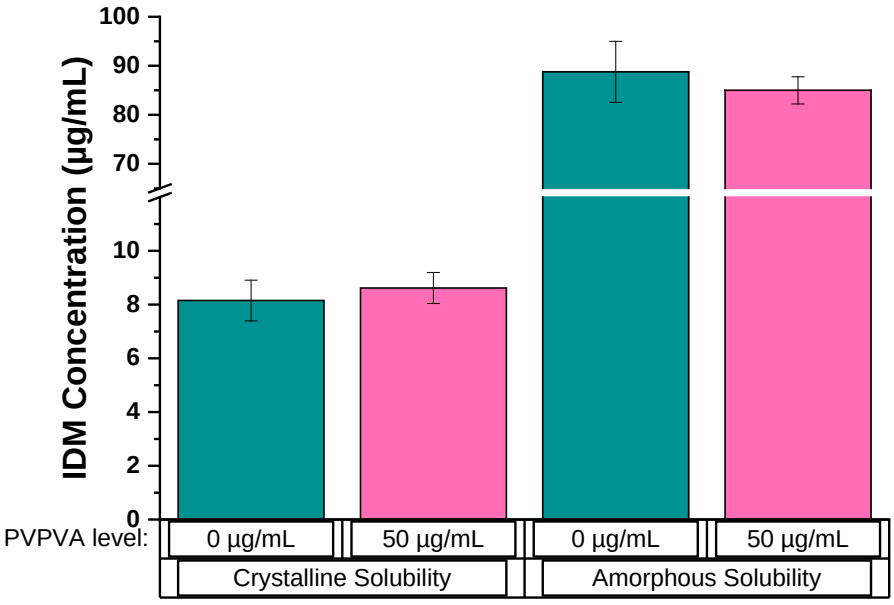

Figure C.2. Amorphous and crystalline solubility of indomethacin in buffer in the absence and presence of PVPVA (0-50 µg/mL). Error is reported as one standard deviation of triplicate preparations.

Dissolution Sample Preparation

Example calculations:

- To achieve a total IDM concentration of 50 µg/mL for HME powders (Figure 5.3) or physical mixtures (Figure 5.4), 20 mg of powder was added.

$$P = \frac{C \times V}{F_{DL} \times 1000}$$

$$20 = \frac{50 \times 200}{0.5 \times 1000}$$

P = powder amount (mg)

C = target IDM solution concentration (µg/mL)

V = dissolution volume (mL)

F_{DL} = formulation drug loading (50%)

In the body of the manuscript, the concentration of these samples will be noted by the total drug substance dose included in the experiment, 50 µg/mL, and this amount represents the sum of both amorphous and crystalline IDM.

- For experiments where bulk seeds were added (as found in Figure 5.5), 20 mg of ASD powder was used. The levels noted as 10, 25, and 50 µg/mL crystalline reflect the use of 2, 5, or 10 mg bulk seeds, corresponding to levels of crystallinity 20%, 50%, and 100% with respect to the reference 100% concentration of 50 µg/mL.

- To achieve a concentration of amorphous IDM of 50 µg/mL (Figure 5.6), the following calculation was applied to adjust for residual crystalline content of HME powders.

$$P = \frac{C \times V}{F_{DL} \times (1 - R) \times 1000}$$

$$26.7 = \frac{50 \times 200}{0.5 \times 0.75 \times 1000}$$

$$23.8 = \frac{50 \times 200}{0.5 \times 0.84 \times 1000}$$

$$21.5 = \frac{50 \times 200}{0.5 \times 0.93 \times 1000}$$

$$20.6 = \frac{50 \times 200}{0.5 \times 0.97 \times 1000}$$

P = powder amount (mg)

C = target IDM solution concentration (µg/mL)

V = dissolution volume (mL)

F_{DL} = formulation drug loading (50%)

R = residual crystalline content (25% for HME 117-2, 16% for HME 121-2, 7% for HME 126-2, 3% for HME 131-2)

In the body of the manuscript, the concentration of these samples will be noted by the total drug substance dose included in the experiment: 67 µg/mL for HME 117-2, 60 µg/mL for HME 121-2, 54 µg/mL for HME 126-2, and 51.5 µg/ mL for HME 131-2. It then follows that the dose of crystals in these experiments is 17 µg/mL, 10 µg/mL, 4 µg/mL, and 1.5 µg/mL, representing 33%, 20%, 8%, and 3% crystallinity with respect to the reference 100% concentration of 50 µg/mL.

Comparative profiles for HME ASDs

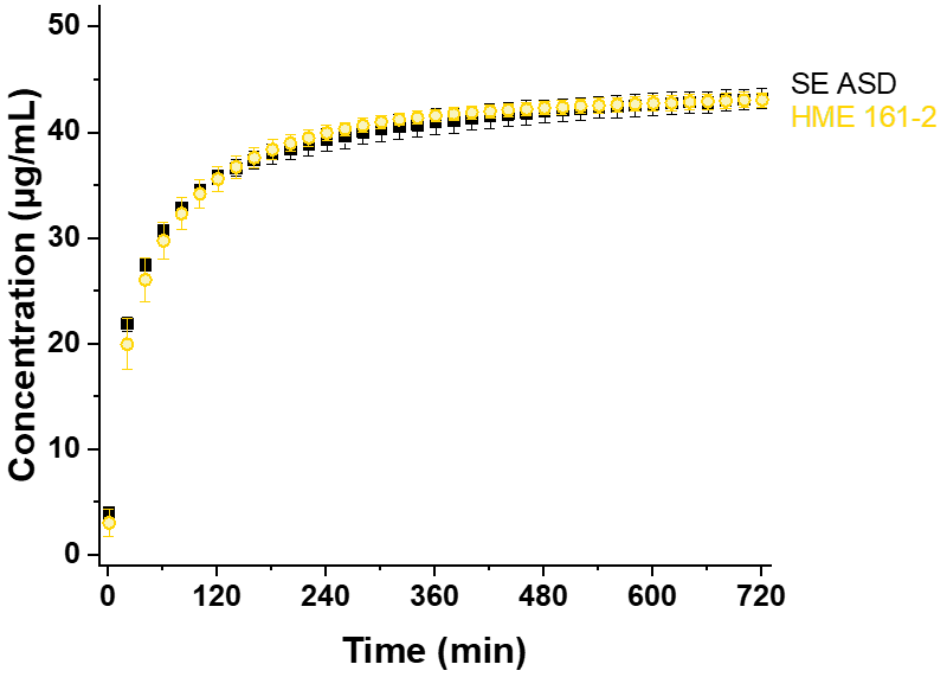

Figure C.3. Comparative dissolution profiles of crystal-free samples: SE ASD and HME ASD 161-2.

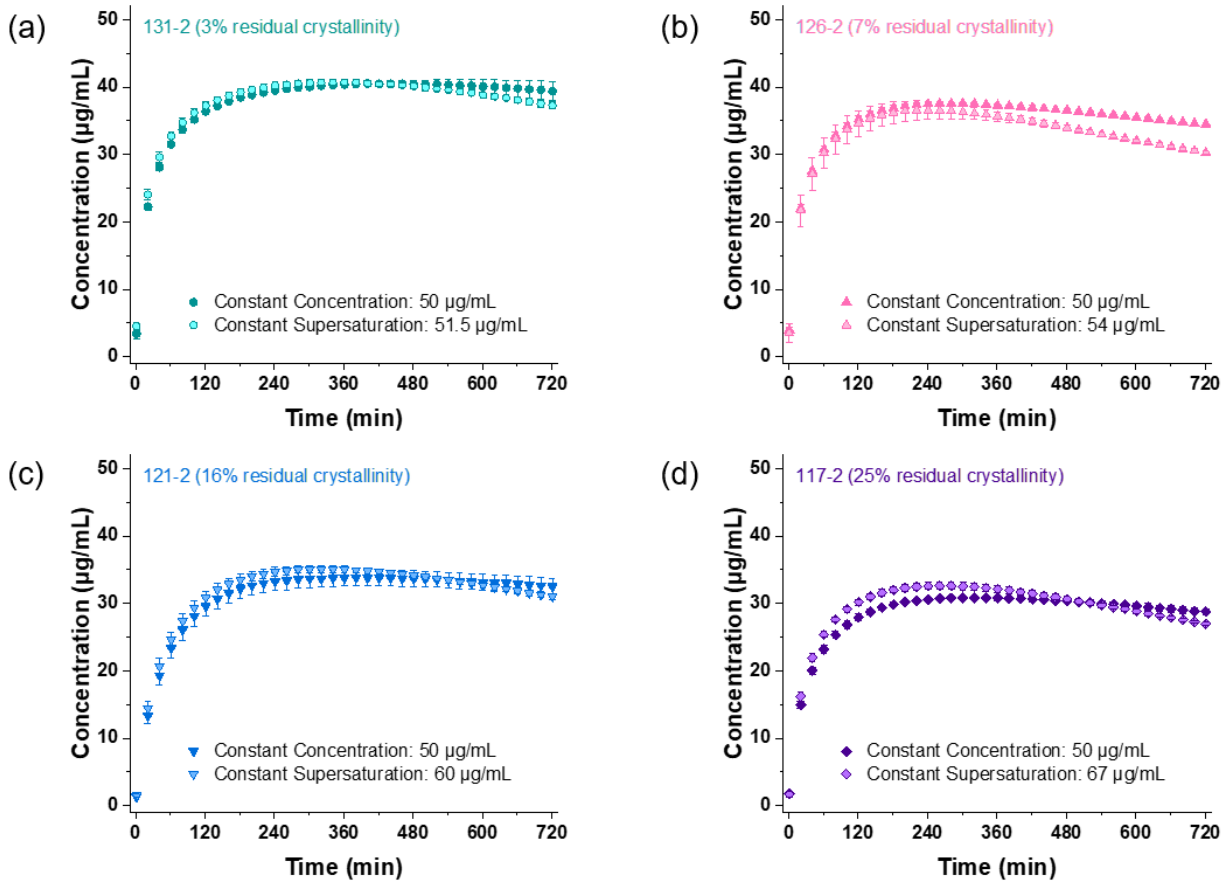

Figure C.4. Comparative dissolution profiles of HME ASDs containing 3-25% residual crystallinity: constant concentration vs. constant supersaturation.**Supporting data for crystal dissolution and crystal growth experiments**

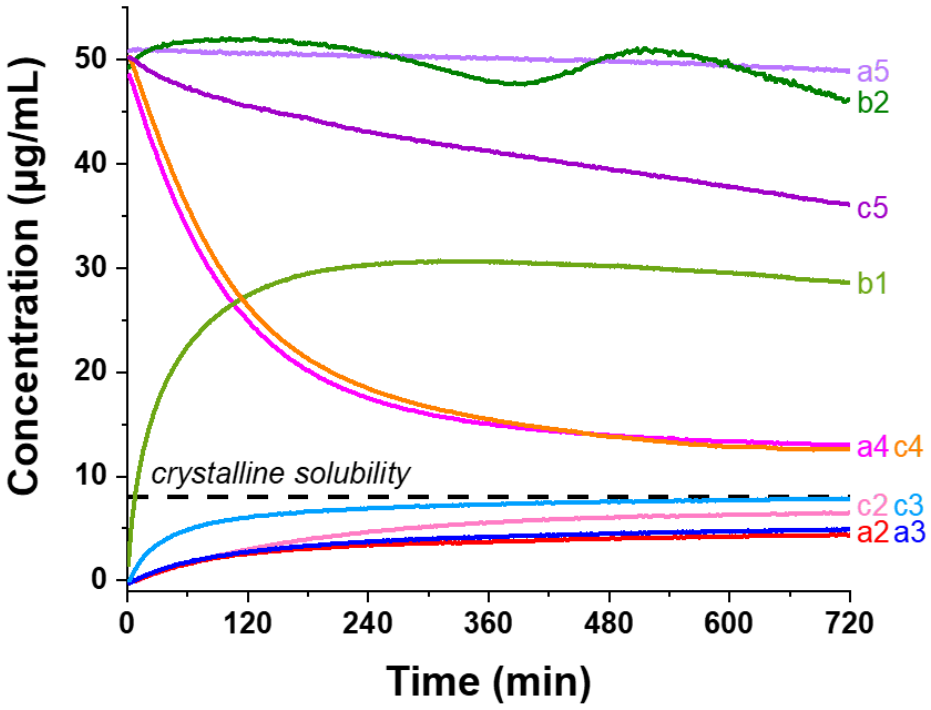

Figure C.5. Representative dissolution profiles of the SEM imaging samples of crystal dissolution and crystal growth.

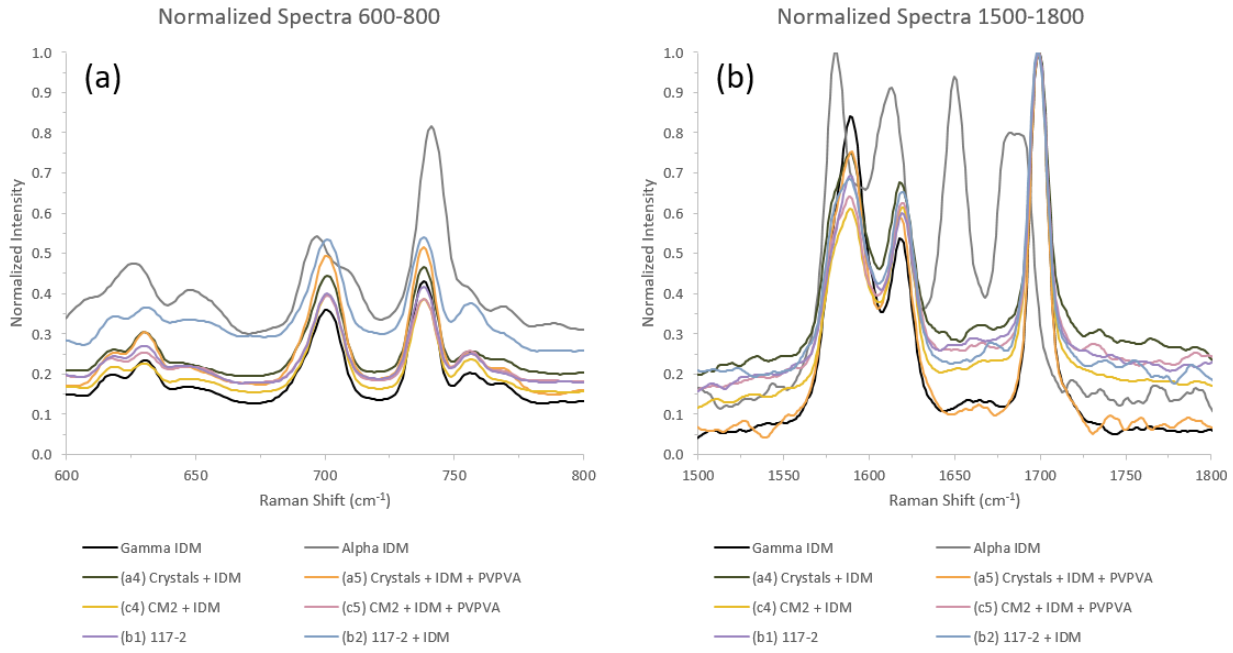

Figure C.6. Normalized Raman spectra over a Raman shift range of (a) 600-800 cm-1 and (b) 1500-1800 cm-1 for select crystal dissolution and growth samples along with gamma and alpha IDM reference spectra.

APPENDIX C. SUPPORTING INFORMATION FOR CHAPTER 6

Hot Melt Extrusion & Assay Results

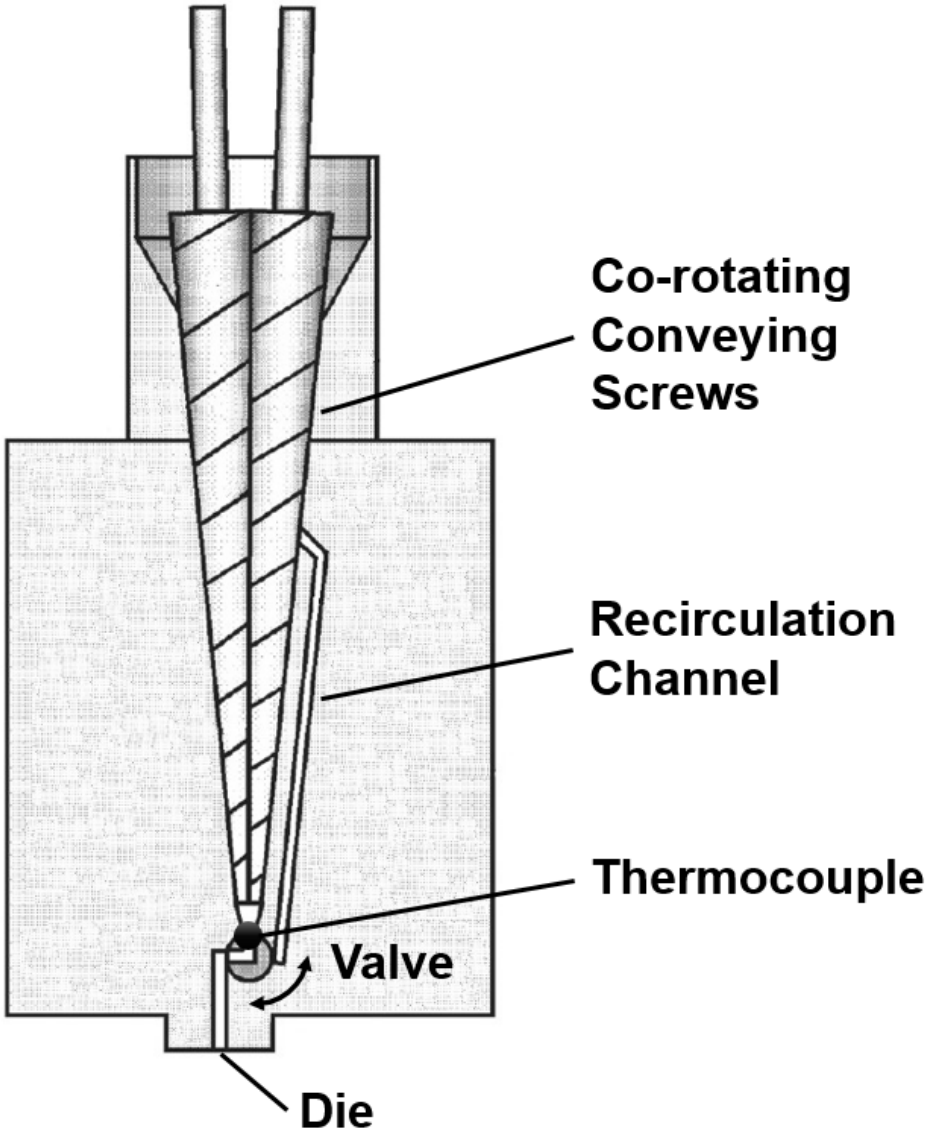

Figure D.1. Schematic of the Xplore hot melt extruder.

Table D.1. Processing conditions and assay results of PCZ/HPMCAS and PCZ/PVPVA HME ASDs. Assay results were conducted in duplicate, with standard deviation reported in parenthesis.

Formulation	Product Melt Temperature (°C)	Residence Time (min)	Screw Speed (RPM)	Assay (%) of PCZ peak RT 4.3
25/75 PCZ/HPMCAS	175	5	100	104.3 (3.7)
25/75 PCZ/HPMCAS	155	2	100	102.3 (3.8)
25/75 PCZ/HPMCAS	145	2	100	104.5 (1.3)
25/75 PCZ/HPMCAS	125	2	100	101.5 (4.4)
25/75 PCZ/PVPVA	175	5	100	101.7 (2.1)
25/75 PCZ/PVPVA	125	2	100	100.1 (1.8)

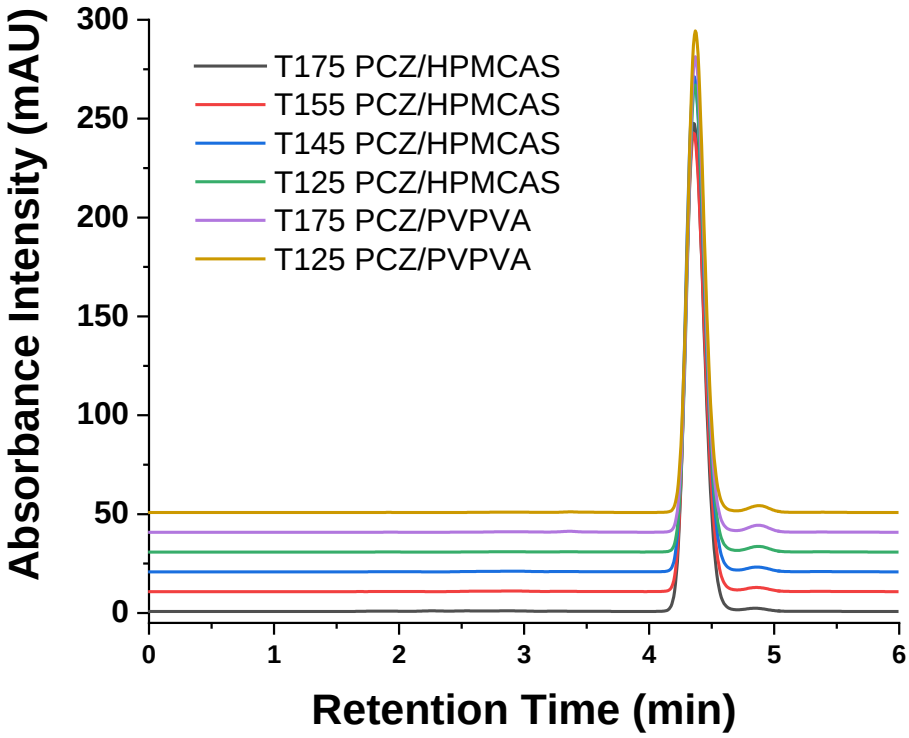

Figure D.2. Representative chromatograms of PCZ/HPMCAS and PCZ/PVPVA HME ASDs. The small peak found at RT 4.8 is also found in the standard solutions (not shown).

Table D.2. Processing conditions and assay results of IDM/PVPVA HME ASDs. Assay results were conducted in triplicate, with standard deviation reported in parenthesis.

Formulation	Product Melt Temperature (°C)	Residence Time (min)	Screw Speed (RPM)	Assay (%) of IDM peak RT 3.9	% area of impurity peak at RT 8.9
50/50 IDM/PVPVA	161	2	20	95.0 (1.0)	0.1
50/50 IDM/PVPVA	131	2	20	95.7 (1.1)	0.1
50/50 IDM/PVPVA	131	20	20	98.7 (1.7)	0.0
50/50 IDM/PVPVA	121	2	20	95.1 (0.9)	0.0
50/50 IDM/PVPVA	121	20	20	95.1 (1.1)	0.0

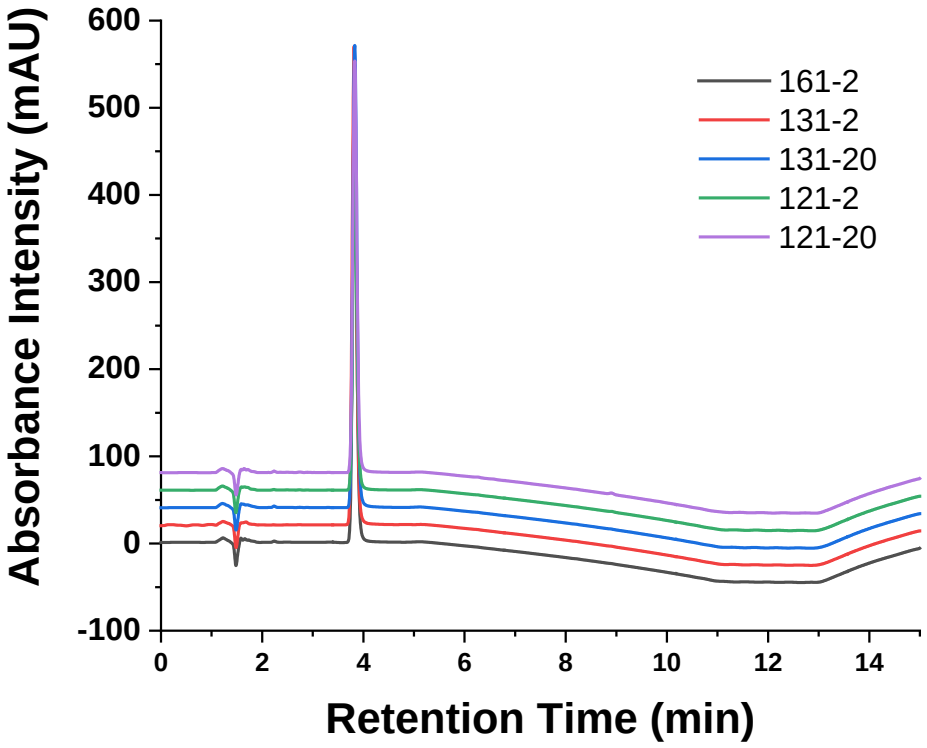

Figure D.3. Representative chromatograms of IDM/PVPVA HME ASDs.

Isothermal TGA Plots

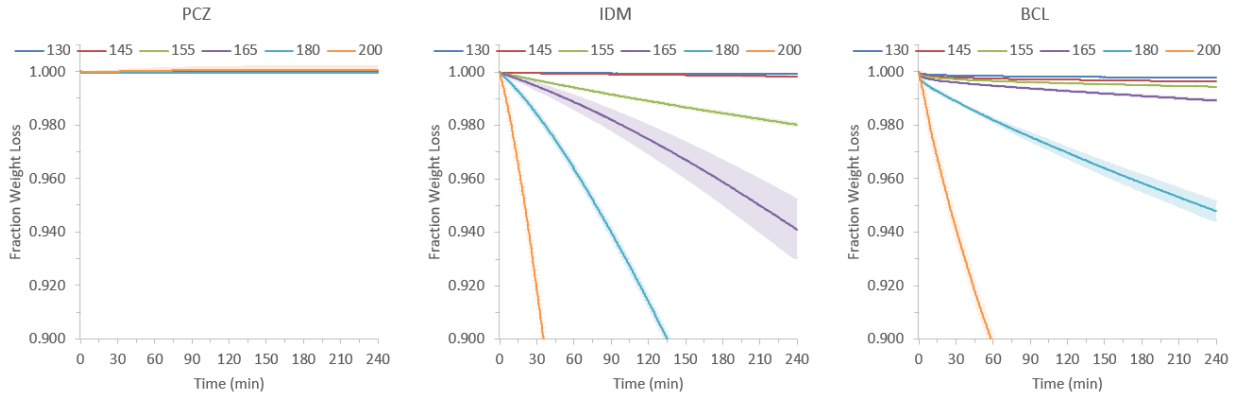

Figure D.4. Raw data of isothermal TGA weight loss experiments for crystalline APIs (PCZ, IDM, and BCL).

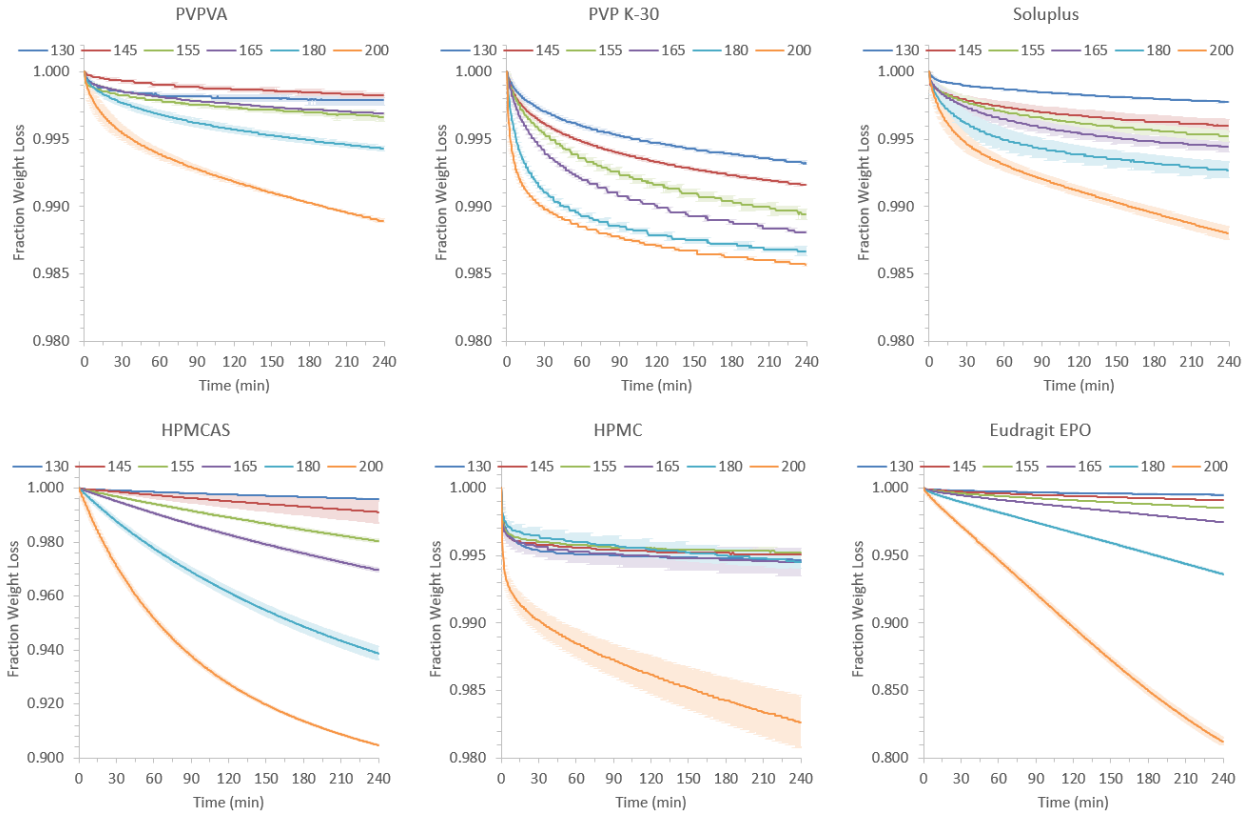

Figure D.5. Raw data of isothermal TGA weight loss experiments for polymers (PVPVA, PVP K-30, Soluplus, HPMCAS, HPMC, and Eudragit EPO).

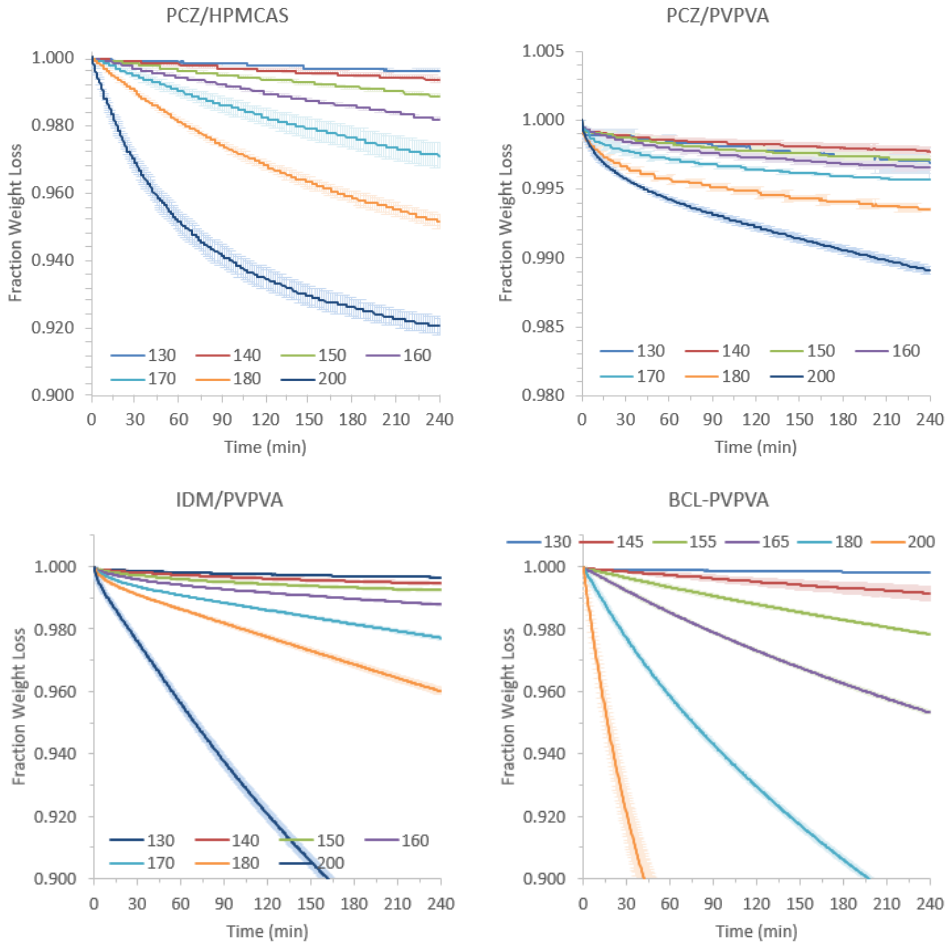

Figure D.6. Raw data of isothermal TGA weight loss experiments for ASDs (PCZ/HPMCAS, PCZ/PVPVA, IDM/PVPVA, and BCL/PVPVA).

REFERENCES

(1) Newman, A.; Knipp, G.; Zografi, G. Assessing the Performance of Amorphous Solid Dispersions. *J. Pharm. Sci.* **2012**, *101*, 1355–1377.

(2) Lipinski, C. A. Drug-like Properties and the Causes of Poor Solubility and Poor Permeability. *J. Pharmacol. Toxicol. Methods* **2000**, *44* (1), 235–249.

(3) Palucki, M.; Higgins, J. D.; Kwong, E.; Templeton, A. C. Strategies at the Interface of Drug Discovery and Development: Early Optimization of the Solid State Phase and Preclinical Toxicology Formulation for Potential Drug Candidates. *J. Med. Chem.* **2010**, *53* (16), 5897–5905.

(4) Bennett-Lenane, H.; O'Shea, J. P.; O'Driscoll, C. M.; Griffin, B. T. A Retrospective Biopharmaceutical Analysis of >800 Approved Oral Drug Products: Are Drug Properties of Solid Dispersions and Lipid-Based Formulations Distinctive? *J. Pharm. Sci.* **2020**, *109* (11), 3248–3261.

(5) Leeson, P. D. Molecular Inflation, Attrition and the Rule of Five. *Adv. Drug Deliv. Rev.* **2016**, *101*, 22–33.

(6) Lipinski, C. A.; Lombardo, F.; Dominy, B. W.; Feeney, P. J. Experimental and Computational Approaches to Estimate Solubility and Permeability in Drug Discovery and Development Settings. *Adv. Drug Deliv. Rev.* **1997**, *23*, 3–25.

(7) Van Den Mooter, G. The Use of Amorphous Solid Dispersions: A Formulation Strategy to Overcome Poor Solubility and Dissolution Rate. *Drug Discov. Today Technol.* **2012**, *9* (2), e79–e85.

(8) Jermain, S. V.; Brough, C.; Williams, R. O. Amorphous Solid Dispersions and Nanocrystal Technologies for Poorly Water-Soluble Drug Delivery – An Update. *Int. J. Pharm.* **2018**, *535*, 379–392.

(9) Terefe, H. The Origins of HME as a Solubility Enhancement Manufacturing Technology. *Am. Pharm. Rev.* **2017**.

(10) Chen, B.; Zhu, L.; Zhang, F.; Qiu, Y. Process Development and Scale-Up: Twin-Screw Extrusion. In *Developing Solid Oral Dosage Forms*; Elsevier Inc., 2017; pp 821–868.

(11) Vigh, T.; Drávavölgyi, G.; Sóti, P. L.; Pataki, H.; Igricz, T.; Wagner, I.; Vajna, B.; Madarász, J.; Marosi, G.; Nagy, Z. K. Predicting Final Product Properties of Melt Extruded Solid Dispersions from Process Parameters Using Raman Spectrometry. *J. Pharm. Biomed. Anal.* **2014**, *98*, 166–177.

(12) Keen, J. M.; Martin, C.; MacHado, A.; Sandhu, H.; McGinity, J. W.; Dinunzio, J. C. Investigation of Process Temperature and Screw Speed on Properties of a Pharmaceutical

Solid Dispersion Using Corotating and Counter-Rotating Twin-Screw Extruders. *J. Pharm. Pharmacol.* **2014**, *66* (2), 204–217.

(13) Liu, H.; Zhu, L.; Wang, P.; Zhang, X.; Gogos, C. G. Effects of Screw Configuration on Indomethacin Dissolution Behavior in Eudragit E PO. *Adv. Polym. Technol.* **2012**, *31* (4), 331–342.

(14) Pharmaceutical Development Q8(R2). *ICH Harmonised Tripartite Guideline*. 2009.

(15) Crowley, M. M.; Zhang, F.; Repka, M. A.; Thumma, S.; Upadhye, S. B.; Kumar Battu, S.; McGinity, J. W.; Martin, C. Pharmaceutical Applications of Hot-Melt Extrusion: Part I. *Drug Dev. Ind. Pharm.* **2007**, *33*, 909–926.

(16) Baird, J. A.; Van Eerdenbrugh, B.; Taylor, L. S. A Classification System to Assess the Crystallization Tendency of Organic Molecules from Undercooled Melts. *J. Pharm. Sci.* **2010**, *99* (9), 3787–3806.

(17) Que, C.; Gao, Y.; Raina, S. A.; Zhang, G. G. Z.; Taylor, L. S. Paclitaxel Crystal Seeds with Different Intrinsic Properties and Their Impact on Dissolution of Paclitaxel-HPMCAS Amorphous Solid Dispersions. *Cryst. Growth Des.* **2018**, *18* (3), 1548–1559.

(18) Van Duong, T.; Van den Mooter, G. The Role of the Carrier in the Formulation of Pharmaceutical Solid Dispersions. Part II: Amorphous Carriers. *Expert Opin. Drug Deliv.* **2016**, *13*, 1681–1694.

(19) Lin, X.; Hu, Y.; Liu, L.; Su, L.; Li, N.; Yu, J.; Tang, B.; Yang, Z. Physical Stability of Amorphous Solid Dispersions : A Physicochemical Perspective with Thermodynamic , Kinetic and Environmental Aspects. *Pharm. Res.* **2018**, *35*.

(20) Xie, T.; Gao, W.; Taylor, L. S. Impact of Eudragit EPO and Hydroxypropyl Methylcellulose on Drug Release Rate, Supersaturation, Precipitation Outcome and Redissolution Rate of Indomethacin Amorphous Solid Dispersions. *Int. J. Pharm.* **2017**.

(21) Raghavan, S. L.; Trividic, A.; Davis, A. F.; Hadgraft, J. Crystallization of Hydrocortisone Acetate: Influence of Polymers. *Int. J. Pharm.* **2001**, *212* (2), 213–221.

(22) Marsac, P. J.; Munson, E. J. Advanced Characterization of Solid Oral Dosage Forms: Linking Physical Changes to Measures of Performance and Quality. *AAPS Newsmag.* **2016**, No. January.

(23) Zhang, G. G. Z.; Zhou, D. Crystalline and Amorphous Solids. In *Developing Solid Oral Dosage Forms*; 2017; pp 23–57.

(24) Byrn, S. R.; Zografi, G.; Chen, X. (Sean). Polymorphs. In *Solid State Properties of Pharmaceutical Materials*; 2017; pp 22–37.

(25) Bates, S.; Zografi, G.; Engers, D.; Morris, K.; Crowley, K.; Newman, A. Analysis of Amorphous and Nanocrystalline Solids from Their X-Ray Diffraction Patterns. *Pharm. Res.*

2006, *23* (10), 2333–2349.

(26) Hancock, B. C.; Zografi, G. Characteristics and Significance of the Amorphous State in Pharmaceutical Systems. *J. Pharm. Sci.* **1997**, *86* (1), 1–12.

(27) Byrn, S. R.; Zografi, G.; Chen, X. (Sean). Solid-State Properties and Pharmaceutical Development. In *Solid State Properties of Pharmaceutical Materials*; 2017; pp 1–21.

(28) Byrn, S. R.; Zografi, G.; Chen, X. (Sean). Amorphous Solids. In *Solid State Properties of Pharmaceutical Materials*; 2017; pp 69–88.

(29) Jain, N.; Yalkowsky, S. H. Estimation of the Aqueous Solubility I: Application to Organic Nonelectrolytes. *J. Pharm. Sci.* **2001**, *90* (2), 234–252.

(30) Taylor, L. S.; Zhang, G. G. Z. Physical Chemistry of Supersaturated Solutions and Implications for Oral Absorption. *Adv. Drug Deliv. Rev.* **2016**, *101*, 122–142.

(31) Hancock, B. C.; Parks, M. What Is the True Solubility Advantage for Amorphous Pharmaceuticals? *Pharm. Res.* **2000**, *17* (4), 397–404.

(32) Trasi, N. S.; Baird, J. A.; Kestur, U. S.; Taylor, L. S. Factors Influencing Crystal Growth Rates from Undercooled Liquids of Pharmaceutical Compounds. *J. Phys. Chem. B* **2014**, *118* (33), 9974–9982.

(33) Newman, A.; Zografi, G. What We Need to Know about Solid-State Isothermal Crystallization of Organic Molecules from the Amorphous State below the Glass Transition Temperature. *Mol. Pharm.* **2020**.

(34) Ilevbare, G. A.; Marsac, P. J.; Mitra, A. Performance and Characterization of Amorphous Solid Dispersions: An Overview. In *Discovering and Developing Molecules with Optimal Drug-Like Properties*; 2015; pp 287–343.

(35) Yamashita, K.; Nakate, T.; Okimoto, K.; Ohike, A.; Tokunaga, Y.; Ibuki, R.; Higaki, K.; Kimura, T. Establishment of New Preparation Method for Solid Dispersion Formulation of Tacrolimus. *Int. J. Pharm.* **2003**, *267* (1–2), 79–91.

(36) Huang, S.; Williams, R. O. Effects of the Preparation Process on the Properties of Amorphous Solid Dispersions. *AAPS PharmSciTech* **2017**, *19*.

(37) Sandhu, H.; Shah, N.; Chokshi, H.; Malick, A. W. Overview of Amorphous Solid Dispersion Technologies. In *Amorphous Solid Dispersions: Theory and Practice*; Sandhu, H., Shah, N., Chokshi, H., Malick, A. W., Choi, D. S., Eds.; 2014; pp 91–122.

(38) Paudel, A.; Worku, Z. A.; Meeus, J.; Guns, S.; Van Den Mooter, G. Manufacturing of Solid Dispersions of Poorly Water Soluble Drugs by Spray Drying: Formulation and Process Considerations. *Int. J. Pharm.* **2013**, *453* (1), 253–284.

(39) Singh, A.; Van den Mooter, G. Spray Drying Formulation of Amorphous Solid Dispersions.

Adv. Drug Deliv. Rev. **2016**, *100*, 27–50.

(40) Repka, M. A.; Bandari, S.; Kallakunta, V. R.; Vo, A. Q.; McFall, H.; Pimparade, M. B.; Bhagurkar, A. M. Melt Extrusion with Poorly Soluble Drugs – An Integrated Review. *Int. J. Pharm.* **2018**, *535* (1–2), 68–85.

(41) Patil, H.; Tiwari, R. V.; Repka, M. A. Hot-Melt Extrusion: From Theory to Application in Pharmaceutical Formulation. *AAPS PharmSciTech* **2016**, *17* (1), 20–42.

(42) Shah, S.; Maddineni, S.; Lu, J.; Repka, M. A. Melt Extrusion with Poorly Soluble Drugs. *Int. J. Pharm.* **2013**, *453* (1), 233–252.

(43) Brown, C.; Dinunzio, J.; Eglesia, M.; Forster, S.; Lamm, M.; Lowinger, M.; Marsac, P.; McKelvey, C.; Meyer, R.; Schenck, L.; Terife, G.; Troup, G.; Smith-Goettler, B.; Starbuck, C. Hot-Melt Extrusion for Solid Dispersions: Composition and Design Considerations. In *Amorphous Solid Dispersions: Theory and Practice*; 2014; pp 197–230.

(44) Martin, C. Twin Screw Extrusion for Pharmaceutical Processes. In *Melt Extrusion: Materials, Technology and Drug Product Design*; 2013; pp 47–79.

(45) Gogos, C. G.; Liu, H. Laminar Dispersive and Distributive Mixing with Dissolution and Applications to Hot-Melt Extrusion. In *Hot-Melt Extrusion: Pharmaceutical Applications2*; 2012; pp 261–284.

(46) Sun, C. C. Materials Science Tetrahedron - A Useful Tool for Pharmaceutical Research and Development. *J. Pharm. Sci.* **2009**, *98* (5), 1671–1687.

(47) Evans, R. C.; Bochmann, E. S.; Kyeremateng, S. O.; Wagner, K. G. Holistic QbD Approach for Hot-Melt Extrusion Process Design Space Evaluation : Linking Materials Science , Experimentation and Process. *Eur. J. Pharm. Biopharm.* **2019**.

(48) Thiry, J.; Krier, F.; Evrard, B. A Review of Pharmaceutical Extrusion: Critical Process Parameters and Scaling-Up. *Int. J. Pharm.* **2015**, *479* (1), 227–240.

(49) DiNunzio, J. C.; Zhang, F.; Martin, C.; McGinity, J. W. Melt Extrusion. In *Formulating Poorly Water Soluble Drugs*; 2012; pp 311–362.

(50) DiNunzio, J. C.; Miller, D. A. Formulation Development of Amorphous Solid Dispersions Prepared by Melt Extrusion. In *Melt Extrusion: Materials, Technology and Drug Product Design*; 2013; pp 161–203.

(51) Ayenew, Z.; Paudel, A.; Van Den Mooter, G. Can Compression Induce Demixing in Amorphous Solid Dispersions? A Case Study of Naproxen-PVP K25. *Eur. J. Pharm. Biopharm.* **2012**, *81* (1), 207–213.

(52) Démuth, B.; Nagy, Z. K.; Balogh, A.; Vigh, T.; Marosi, G.; Verreck, G.; Van Assche, I.; Brewster, M. E. Downstream Processing of Polymer-Based Amorphous Solid Dispersions to Generate Tablet Formulations. *Int. J. Pharm.* **2015**, *486* (1–2), 268–286.

(53) Yang, Z.; Nollenberger, K.; Albers, J.; Qi, S. Molecular Implications of Drug-Polymer Solubility in Understanding the Destabilization of Solid Dispersions by Milling. *Mol. Pharm.* **2014**, *11* (7), 2453–2465.

(54) Marsac, P. J.; Shamblin, S. L.; Taylor, L. S. Theoretical and Practical Approaches for Prediction of Drug-Polymer Miscibility and Solubility. *Pharm. Res.* **2006**, *23* (10), 2417–2426.

(55) Nishi, T.; Wang, T. T.; Kwei, T. K. Thermally Induced Phase Separation Behavior of Compatible Polymer Mixtures. *Macromolecules* **1975**, *8* (2), 227–234.

(56) Greco, P.; Martuscelli, E. Crystallization and Thermal Behaviour of Poly(d(-)-3-Hydroxybutyrate)-Based Blends. *Polymer (Guildf).* **1989**, *30* (8), 1475–1483.

(57) Avella, M.; Martuscelli, E. Poly-d-(-)(3-Hydroxybutyrate)/Poly(Ethylene Oxide) Blends: Phase Diagram, Thermal and Crystallization Behaviour. *Polymer (Guildf).* **1988**, *29* (10), 1731–1737.

(58) Painter, P. C.; Shenoy, S. L.; Bhagwagar, D. E.; Fishburn, J.; Coleman, M. M. Effect of Hydrogen Bonding on the Melting Point Depression in Polymer Blends Where One Component Crystallizes. *Macromolecules* **1991**, *24* (20), 5623–5629.

(59) Hoei, Y.; Yamaura, K.; Matsuzawa, S. A Lattice Treatment of Crystalline Solvent-Amorphous Polymer Mixtures on Melting-Point Depression. *J. Phys. Chem.* **1992**, *96* (26), 10584–10586.

(60) Tian, B.; Tang, X.; Taylor, L. S. Investigating the Correlation between Miscibility and Physical Stability of Amorphous Solid Dispersions Using Fluorescence-Based Techniques. *Mol. Pharm.* **2016**, *13* (11), 3988–4000.

(61) Zhao, Y.; Inbar, P.; Chokshi, H. P.; Malick, A. W.; Choi, D. S. Prediction of the Thermal Phase Diagram of Amorphous Solid Dispersions by Flory-Huggins Theory. *J. Pharm. Sci.* **2011**, *100*, 3196–3207.

(62) Anderson, B. D. Predicting Solubility/Miscibility in Amorphous Dispersions: It Is Time to Move Beyond Regular Solution Theories. *J. Pharm. Sci.* **2017**, *107* (1), 24–33.

(63) Potter, C. B.; Davis, M. T.; Albadarin, A. B.; Walker, G. M. Investigation of the Dependence of the Flory-Huggins Interaction Parameter on Temperature and Composition in a Drug-Polymer System. *Mol. Pharm.* **2018**.

(64) Knopp, M. M.; Olesen, N. E.; Huang, Y.; Holm, R.; Rades, T. Statistical Analysis of a Method to Predict Drug-Polymer Miscibility. *J. Pharm. Sci.* **2016**, *105*, 362–367.

(65) Sun, Y.; Tao, J.; Zhang, G. G. Z.; Yu, L. Solubilities of Crystalline Drugs in Polymers: An Improved Analytical Method and Comparison of Solubilities of Indomethacin and Nifedipine in PVP, PVP/VA, and PVAc. *J. Pharm. Sci.* **2010**, *99*, 4023–4031.

(66) Tao, J.; Sun, Y.; Zhang, G. G. Z.; Yu, L. Solubility of Small-Molecule Crystals in Polymers: D-Mannitol in PVP, Indomethacin in PVP/VA, and Nifedipine in PVP/VA. *Pharm. Res.* **2009**, *26*, 855–864.

(67) Mahieu, A.; Willart, J.-F.; Dudognon, E.; Dane, F.; Descamps, M. A New Protocol To Determine the Solubility of Drugs into Polymer Matrixes. *Mol. Pharm.* **2013**, *10*, 560–566.

(68) Knopp, M. M.; Tajber, L.; Tian, Y.; Olesen, N. E.; Jones, D. S.; Kozyra, A.; Löbmann, K.; Paluch, K.; Brennan, C. M.; Holm, R.; Healy, A. M.; Andrews, G. P.; Rades, T. Comparative Study of Different Methods for the Prediction of Drug-Polymer Solubility. *Mol. Pharm.* **2015**, *12*, 3408–3419.

(69) Lehmkemper, K.; Kyerematen, S. O.; Heinzerling, O.; Degenhardt, M.; Sadowski, G. Long-Term Physical Stability of PVP- and PVPVA-Amorphous Solid Dispersions. *Mol. Pharm.* **2017**, *14* (1), 157–171.

(70) Kyerematen, S. O.; Pudlas, M.; Woehrle, G. H. A Fast and Reliable Empirical Approach for Estimating Solubility of Crystalline Drugs in Polymers for Hot Melt Extrusion Formulations. *J. Pharm. Sci.* **2014**, *103* (9), 2847–2858.

(71) Babu, J. R.; Brostow, W.; Kalogeras, I. M.; Sathigari, S. Glass Transitions in Binary Drug + Polymer Systems. *Mater. Lett.* **2009**, *63* (30), 2666–2668.

(72) Chokshi, R. J.; Sandhu, H. K.; Iyer, R. M.; Shah, N. H.; Malick, A. W.; Zia, H. Characterization of Physico-Mechanical Properties of Indomethacin and Polymers to Assess Their Suitability for Hot-Melt Extrusion Processs as a Means to Manufacture Solid Dispersion/Solution. *J. Pharm. Sci.* **2005**, *94* (11), 2463–2474.

(73) Hancock, B. C.; Zografi, G. The Relationship Between the Glass Transition Temperature and the Water Content of Amorphous Pharmaceutical Solids. *Pharm. Res.* **1994**, *11* (4), 471–477.

(74) Marsac, P. J.; Shamblin, S. L.; Taylor, L. S. Theoretical and Practical Approaches for Prediction of Drug-Polymer Miscibility and Solubility. *Pharm. Res.* **2006**, *23*, 2417–2426.

(75) Marsac, P. J.; Li, T.; Taylor, L. S. Estimation of Drug-Polymer Miscibility and Solubility in Amorphous Solid Dispersions Using Experimentally Determined Interaction Parameters. *Pharm. Res.* **2009**, *26*, 139–151.

(76) Lehmkemper, K.; Kyerematen, S. O.; Heinzerling, O.; Degenhardt, M.; Sadowski, G. Impact of Polymer Type and Relative Humidity on the Long-Term Physical Stability of Amorphous Solid Dispersions. *Mol. Pharm.* **2017**, *14* (12), 4374–4386.

(77) Pajula, K.; Taskinen, M.; Lehto, V.; Ketolainen, J.; Korhonen, O. Predicting the Formation and Stability of Amorphous Small Molecule Binary Mixtures from Computationally Determined Flory-Huggins Interaction Parameter and Phase Diagram. **2010**, *7* (3), 795–804.

(78) Wlodarski, K.; Sawicki, W.; Kozyra, A.; Tajber, L. Physical Stability of Solid Dispersions

with Respect to Thermodynamic Solubility of Tadalafil in PVP-VA. *Eur. J. Pharm. Biopharm.* **2015**, *96*, 237–246.

(79) DiNunzio, J. C.; Brough, C.; Hughey, J. R.; Miller, D. A.; Williams, R. O.; McGinity, J. W. Fusion Production of Solid Dispersions Containing a Heat-Sensitive Active Ingredient by Hot Melt Extrusion and Kinetisol Dispersing. *Eur. J. Pharm. Biopharm.* **2010**, *74* (2), 340–351.

(80) Carstensen, J. T.; Morris, T. Chemical Stability of Indomethacin in the Solid Amorphous and Molten States. *J. Pharm. Sci.* **1993**, *82* (6), 657–659.

(81) Gupta, S. S.; Meena, A. K.; Parikh, T.; Serajuddin, A. T. M. Investigation of Thermal and Viscoelastic Properties of Polymers Relevant to Hot Melt Extrusion - I: Polyvinylpyrrolidone and Related Polymers. *J Excipients Food Chem.* **2014**, *5* (1), 32–45.

(82) Forster, A.; Hempenstall, J.; Rades, T. Characterization of Glass Solutions of Poorly Water-Soluble Drugs Produced by Melt Extrusion with Hydrophilic Amorphous Polymers. *J. Pharm. Pharmacol.* **2001**, *53* (3), 303–315.

(83) Evans, R. C.; Kyerematen, S. O.; Asmus, L.; Degenhardt, M.; Rosenberg, J.; Wagner, K. G. Development and Performance of a Highly Sensitive Model Formulation Based on Torasemide to Enhance Hot-Melt Extrusion Process Understanding and Process Development. *AAPS PharmSciTech* **2018**, *19* (4), 1592–1605.

(84) Verreck, G.; Decorte, A.; Li, H.; Tomasko, D.; Arien, A.; Peeters, J.; Rombaut, P.; Van den Mooter, G.; Brewster, M. E. The Effect of Pressurized Carbon Dioxide as a Plasticizer and Foaming Agent on the Hot Melt Extrusion Process and Extrudate Properties of Pharmaceutical Polymers. *J. Supercrit. Fluids* **2006**, *38* (3), 383–391.

(85) Guo, Z.; Lu, M.; Li, Y.; Pang, H.; Lin, L.; Liu, X.; Wu, C. The Utilization of Drug-Polymer Interactions for Improving the Chemical Stability of Hot-Melt Extruded Solid Dispersions. *J. Pharm. Pharmacol.* **2014**, *66* (2), 285–296.

(86) Haser, A.; Huang, S.; Listro, T.; White, D.; Zhang, F. An Approach for Chemical Stability during Melt Extrusion of a Drug Substance with a High Melting Point. *Int. J. Pharm.* **2017**, *524* (1–2), 55–64.

(87) Huang, S.; O'Donnell, K. P.; Delpon de Vaux, S. M.; O'Brien, J.; Stutzman, J.; Williams, R. O. Processing Thermally Labile Drugs by Hot-Melt Extrusion: The Lesson with Gliclazide. *Eur. J. Pharm. Biopharm.* **2017**, *119*, 56–67.

(88) Ghosh, I.; Vippagunta, R.; Li, S.; Vippagunta, S. Key Considerations for Optimization of Formulation and Melt-Extrusion Process Parameters for Developing Thermosensitive Compound. *Pharm. Dev. Technol.* **2012**, *17* (4), 502–510.

(89) Gupta, S. S.; Solanki, N.; Serajuddin, A. T. M. Investigation of Thermal and Viscoelastic Properties of Polymers Relevant to Hot Melt Extrusion, IV: Affinisol™ HPMC HME Polymers. *AAPS PharmSciTech* **2016**, *17* (1), 148–157.

(90) Parikh, T.; Gupta, S. S.; Meena, A.; Serajuddin, A. T. M. Investigation of Thermal and Viscoelastic Properties of Polymers Relevant to Hot Melt Extrusion - III: Polymethacrylates and Polymethacrylic Acid Based Polymers. *J. Excipients Food Chem.* **2014**, *5* (1), 56–64.

(91) Meena, A.; Parikh, T.; Gupta, S. S.; Serajuddin, A. T. M. Investigation of Thermal and Viscoelastic Properties of Polymers Relevant to Hot Melt Extrusion - II: Cellulosic Polymers. *J. Excipients Food Chem.* **2014**, *5* (1), 46–55.

(92) Haser, A.; Cao, T.; Lubach, J.; Listro, T.; Acquarulo, L.; Zhang, F. Melt Extrusion vs. Spray Drying: The Effect of Processing Methods on Crystalline Content of Naproxen-Povidone Formulations. *Eur. J. Pharm. Sci.* **2017**, *102*, 115–125.

(93) Murdande, S. B.; Pikal, M. J.; Shanker, R. M.; Bogner, R. H. Solubility Advantage of Amorphous Pharmaceuticals: I. A Thermodynamic Analysis. *J. Pharm. Sci.* **2010**, *99* (3), 1254–1264.

(94) Mistry, P.; Amponsah-Efah, K. K.; Suryanarayanan, R. Rapid Assessment of the Physical Stability of Amorphous Solid Dispersions. *Cryst. Growth Des.* **2017**, *17* (5), 2478–2485.

(95) Hancock, B. C.; Shamblin, S. L.; Zografi, G. Molecular Mobility of Amorphous Pharmaceutical Solids Below Their Glass Transition Temperatures. *Pharm. Res.* **1995**, *12* (6), 799–806.

(96) Rumondor, A. C. F.; Stanford, L. A.; Taylor, L. S. Effects of Polymer Type and Storage Relative Humidity on the Kinetics of Felodipine Crystallization from Amorphous Solid Dispersions. *Pharm. Res.* **2009**, *26* (12), 2599–2606.

(97) Trasi, N. S.; Purohit, H. S.; Taylor, L. S. Evaluation of the Crystallization Tendency of Commercially Available Amorphous Tacrolimus Formulations Exposed to Different Stress Conditions. *Pharm. Res.* **2017**, 1–14.

(98) Baird, J. A.; Taylor, L. S. Evaluation of Amorphous Solid Dispersion Properties Using Thermal Analysis Techniques. *Adv. Drug Deliv. Rev.* **2012**, *64* (5), 396–421.

(99) Ivanisevic, I. Physical Stability Studies of Miscible Amorphous Solid Dispersions. *J. Pharm. Sci.* **2010**, *99* (9), 4005–4012.

(100) Frawley, P. J.; Mitchell, N. A.; Ó'Ciardhá, C. T.; Hutton, K. W. The Effects of Supersaturation, Temperature, Agitation and Seed Surface Area on the Secondary Nucleation of Paracetamol in Ethanol Solutions. *Chem. Eng. Sci.* **2012**, *75*, 183–197.

(101) Ilevbare, G. A.; Liu, H.; Edgar, K. J.; Taylor, L. S. Effect of Binary Additive Combinations on Solution Crystal Growth of the Poorly Water-Soluble Drug, Ritonavir. *Cryst. Growth Des.* **2012**, *12* (12), 6050–6060.

(102) Qian, F.; Huang, J.; Zhu, Q.; Haddadin, R.; Gawel, J.; Garmise, R.; Hussain, M. Is a Distinctive Single Tg a Reliable Indicator for the Homogeneity of Amorphous Solid Dispersion? *Int. J. Pharm.* **2010**, *395*, 232–235.

(103) Mugheirbi, N. A.; Marsac, P. J.; Taylor, L. S. Insights into Water-Induced Phase Separation in Itraconazole-Hydroxypropylmethyl Cellulose Spin Coated and Spray Dried Dispersions. *Mol. Pharm.* **2017**, *14*, 4387–4402.

(104) Janssens, S.; De Zeure, A.; Paudel, A.; Van Humbeeck, J.; Rombaut, P.; Van Den Mooter, G. Influence of Preparation Methods on Solid State Supersaturation of Amorphous Solid Dispersions: A Case Study with Itraconazole and Eudragit E100. *Pharm. Res.* **2010**, *27* (5), 775–785.

(105) Yuan, X.; Xiang, T. X.; Anderson, B. D.; Munson, E. J. Hydrogen Bonding Interactions in Amorphous Indomethacin and Its Amorphous Solid Dispersions with Poly(Vinylpyrrolidone) and Poly(Vinylpyrrolidone-Co-Vinyl Acetate) Studied Using 13C Solid-State NMR. *Mol. Pharm.* **2015**, *12*, 4518–4528.

(106) Savolainen, M.; Heinz, A.; Strachan, C.; Gordon, K. C.; Yliruusi, J.; Rades, T.; Sandler, N. Screening for Differences in the Amorphous State of Indomethacin Using Multivariate Visualization. *Eur. J. Pharm. Sci.* **2007**, *30* (2), 113–123.

(107) Hanada, M.; Jermain, S. V.; Lu, X.; Su, Y.; Williams, R. O. Predicting Physical Stability of Ternary Amorphous Solid Dispersions Using Specific Mechanical Energy in a Hot Melt Extrusion Process. *Int. J. Pharm.* **2018**, *548* (1), 571–585.

(108) Shah, B.; Kakumanu, V. K.; Bansal, A. K. Analytical Techniques for Quantification of Amorphous/Crystalline Phases in Pharmaceutical Solids. *J. Pharm. Sci.* **2006**, *95* (8), 1641–1665.

(109) Rumondor, A. C. F.; Taylor, L. S. Application of Partial Least-Squares (PLS) Modeling in Quantifying Drug Crystallinity in Amorphous Solid Dispersions. *Int. J. Pharm.* **2010**, *398*, 155–160.

(110) Rohrs, B. R. Dissolution Method Development for Poorly Soluble Compounds. *Dissolution Technol.* **2001**, *8* (3), 1–5.

(111) Sun, D. D.; Wen, H.; Taylor, L. S. Non-Sink Dissolution Conditions for Predicting Product Quality and In Vivo Performance of Supersaturating Drug Delivery Systems. *J. Pharm. Sci.* **2016**, *105* (9), 2477–2488.

(112) Alonzo, D. E.; Zhang, G. G. Z.; Zhou, D.; Gao, Y.; Taylor, L. S. Understanding the Behavior of Amorphous Pharmaceutical Systems during Dissolution. *Pharm. Res.* **2010**, *27* (4), 608–618.

(113) GUZMAN, H. R.; TAWA, M.; ZHANG, Z.; RATANABANANGKOON, P.; SHAW, P.; GARDNER, C. R.; CHEN, H.; MOREAU, J.-P.; ALMARSSON, O. R.; REMENAR, U. F. Combined Use of Crystalline Salt Forms and Precipitation Inhibitors to Improve Oral Absorption of Celecoxib from Solid Oral Formulations. *J. Pharm. Sci.* **2007**, *96* (10), 2686–2702.

(114) Indulkar, A. S.; Gao, Y.; Raina, S. A.; Zhang, G. G. Z.; Taylor, L. S. Exploiting the

Phenomenon of Liquid-Liquid Phase Separation for Enhanced and Sustained Membrane Transport of a Poorly Water-Soluble Drug. *Mol. Pharm.* **2016**, *13* (6), 2059–2069.

(115) LaFountaine, J. S.; Prasad, L. K.; Brough, C.; Miller, D. A.; McGinity, J. W.; Williams, R. O. Thermal Processing of PVP- and HPMC-Based Amorphous Solid Dispersions. *AAPS PharmSciTech* **2016**, *17* (1), 120–132.

(116) Yang, F.; Su, Y.; Zhang, J.; DiNunzio, J.; Leone, A.; Huang, C.; Brown, C. D. Rheology Guided Rational Selection of Processing Temperature to Prepare Copovidone-Nifedipine Amorphous Solid Dispersions via Hot Melt Extrusion (HME). *Mol. Pharm.* **2016**, *13* (10), 3494–3505.

(117) Aho, J.; Boetker, J. P.; Baldursdottir, S.; Rantanen, J. Rheology as a Tool for Evaluation of Melt Processability of Innovative Dosage Forms. *Int. J. Pharm.* **2015**, *494*, 623–642.

(118) Bochmann, E. S.; Üstüner, E. E.; Gryczke, A.; Wagner, K. G. Predicting Melt Rheology for Hot-Melt Extrusion by Means of a Simple Tg-Measurement. *Eur. J. Pharm. Biopharm.* **2017**, *119*, 47–55.

(119) Yang, F.; Su, Y.; Zhu, L.; Brown, C. D.; Rosen, L. A.; Rosenberg, K. J. Rheological and Solid-State NMR Assessments of Copovidone/Clotrimazole Model Solid Dispersions. *Int. J. Pharm.* **2016**, *500* (1–2), 20–31.

(120) Mitra, A.; Li, L.; Marsac, P.; Marks, B.; Liu, Z.; Brown, C. Impact of Polymer Type on Bioperformance and Physical Stability of Hot Melt Extruded Formulations of a Poorly Water Soluble Drug. *Int. J. Pharm.* **2016**, *505* (1–2), 107–114.

(121) Lang, B.; Liu, S.; McGinity, J. W.; Williams, R. O. Effect of Hydrophilic Additives on the Dissolution and Pharmacokinetic Properties of Itraconazole-Enteric Polymer Hot-Melt Extruded Amorphous Solid Dispersions. *Drug Dev. Ind. Pharm.* **2016**, *42* (3), 429–445.

(122) Sarode, A. L.; Sandhu, H.; Shah, N.; Malick, W.; Zia, H. Hot Melt Extrusion (HME) for Amorphous Solid Dispersions: Predictive Tools for Processing and Impact of Drug-Polymer Interactions on Supersaturation. *Eur. J. Pharm. Sci.* **2013**, *48* (3), 371–384.

(123) Hitzer, P.; Bäuerle, T.; Drieschner, T.; Ostertag, E.; Paulsen, K.; van Lishaut, H.; Lorenz, G.; Rebner, K. Process Analytical Techniques for Hot-Melt Extrusion and Their Application to Amorphous Solid Dispersions. *Anal. Bioanal. Chem.* **2017**, *409* (18), 4321–4333.

(124) Van Renterghem, J.; Kumar, A.; Vervaet, C.; Remon, J. P.; Nopens, I.; Vander Heyden, Y.; De Beer, T. Elucidation and Visualization of Solid-State Transformation and Mixing in a Pharmaceutical Mini Hot Melt Extrusion Process Using in-Line Raman Spectroscopy. *Int. J. Pharm.* **2017**, *517* (1–2), 119–127.

(125) Boersen, N.; Brown, C.; DiNunzio, J.; Johnson, D.; Marsac, P.; Meyer, R.; McKelvey, C. Hot-Melt Extrusion: The Process-Product-Performance Interplay. In *Discovering and Developing Molecules with Optimal Drug-Like Properties*; 2015; pp 345–381.

(126) Li, M.; Gogos, C. G.; Ioannidis, N. Improving the API Dissolution Rate during Pharmaceutical Hot-Melt Extrusion I: Effect of the API Particle Size, and the Co-Rotating, Twin-Screw Extruder Screw Configuration on the API Dissolution Rate. *Int. J. Pharm.* **2015**, *478*, 103–112.

(127) Purohit, H. S.; Trasi, N. S.; Sun, D. D.; Chow, E. C. Y.; Wen, H.; Zhang, X.; Gao, Y.; Taylor, L. S. Investigating the Impact of Drug Crystallinity in Amorphous Tacrolimus Capsules on Pharmacokinetics and Bioequivalence Using Discriminatory In Vitro Dissolution Testing and Physiologically Based Pharmacokinetic Modeling and Simulation. *J. Pharm. Sci.* **2018**, *107* (5), 1330–1341.

(128) Koyama, H.; Ito, M.; Terada, K.; Sugano, K. Effect of Seed Particles on Precipitation of Weak Base Drugs in Physiological Intestinal Conditions. *Mol. Pharm.* **2016**, *13* (8), 2711–2717.

(129) Pitzer, K. S.; Peiper, J. C.; Busey, R. H. Thermodynamic Properties of Aqueous Sodium Chloride Solutions. *J. Phys. Chem. Ref. Data* **1984**, *13* (1), 1–102.

(130) Tian, Y.; Booth, J.; Meehan, E.; Jones, D. S.; Li, S.; Andrews, G. P. Construction of Drug-Polymer Thermodynamic Phase Diagrams Using Flory-Huggins Interaction Theory: Identifying the Relevance of Temperature and Drug Weight Fraction to Phase Separation within Solid Dispersions. *Mol. Pharm.* **2013**, *10* (1), 236–248.

(131) Prudic, A.; Ji, Y.; Sadowski, G. Thermodynamic Phase Behavior of API/Polymer Solid Dispersions. *Mol. Pharm.* **2014**, *11* (7), 2294–2304.

(132) Li, S.; Tian, Y.; Jones, D. S.; Andrews, G. P. Optimising Drug Solubilisation in Amorphous Polymer Dispersions: Rational Selection of Hot-Melt Extrusion Processing Parameters. *AAPS PharmSciTech* **2016**, *17* (1), 200–213.

(133) Matsumoto, T.; Zografi, G. Physical Properties of Solid Molecular Dispersions of Indomethacin with Poly(Vinylpyrrolidone) and Poly(Vinylpyrrolidone-Co-Vinylacetate) in Relation to Indomethacin Crystallizatoin. *Pharm. Res.* **1999**, *16* (11), 1722–1728.

(134) Sakai, T.; Thommes, M. Investigation into Mixing Capability and Solid Dispersion Preparation Using the DSM Xplore Pharma Micro Extruder. *J. Pharm. Pharmacol.* **2014**, *66* (2), 218–231.

(135) Lamm, M. S.; DiNunzio, J.; Khawaja, N. N.; Crocker, L. S.; Pecora, A. Assessing Mixing Quality of a Copovidone-TPGS Hot Melt Extrusion Process with Atomic Force Microscopy and Differential Scanning Calorimetry. *AAPS PharmSciTech* **2016**, *17* (1), 89–98.

(136) Aho, J.; Van Renterghem, J.; Arnfast, L.; De Beer, T.; Rantanen, J. The Flow Properties and Presence of Crystals in Drug-Polymer Mixtures: Rheological Investigation Combined with Light Microscopy. *Int. J. Pharm.* **2017**, *528* (1–2), 383–394.

(137) Pezzoli, R.; Lyons, J. G.; Gately, N.; Higginbotham, C. L. Investigation of Miscibility Estimation Methods between Indomethacin and Poly(Vinylpyrrolidone-Co-Vinyl Acetate).

Int. J. Pharm. **2018**, *549*, 50–57.

(138) Liu, H.; Wang, P.; Zhang, X.; Shen, F.; Gogos, C. G. Effects of Extrusion Process Parameters on the Dissolution Behavior of Indomethacin in Eudragit E PO Solid Dispersions. *Int. J. Pharm.* **2010**, *383*, 161–169.

(139) Schittny, A.; Ogawa, H.; Huwyler, J.; Puchkov, M. A Combined Mathematical Model Linking the Formation of Amorphous Solid Dispersions with Hot-Melt-Extrusion Process Parameters. *Eur. J. Pharm. Biopharm.* **2018**.

(140) Moseson, D. E.; Taylor, L. S. The Application of Temperature-Composition Phase Diagrams for Hot Melt Extrusion Processing of Amorphous Solid Dispersions to Prevent Residual Crystallinity. *Int. J. Pharm.* **2018**, *553*, 454–466.

(141) Ricarte, R. G.; Lodge, T. P.; Hillmyer, M. A. Detection of Pharmaceutical Drug Crystallites in Solid Dispersions by Transmission Electron Microscopy. *Mol. Pharm.* **2015**, *12*, 983–990.

(142) Thomas, J.; Gemming, T. *Analytical Transmission Electron Microscopy: An Introduction for Operators*; 2014.

(143) Kolb, U.; Gorelik, T. E.; Mugnaioli, E.; Stewart, A. Structural Characterization of Organics Using Manual and Automated Electron Diffraction. *Polym. Rev.* **2010**, *50*, 385–409.

(144) Li, N.; Gilpin, C. J.; Taylor, L. S. Understanding the Impact of Water on the Miscibility and Microstructure of Amorphous Solid Dispersions: An AFM-LCR and TEM-EDX Study. *Mol. Pharm.* **2017**, *14*, 1691–1705.

(145) Reimer, L.; Kohl, H. Imaging of Crystalline Specimens and Their Defects. In *Transmission Electron Microscopy: Physics of Image Formation*; 2008; pp 359–418.

(146) Eddleston, M. D.; Jones, W. Observation and Characterization of Crystal Defects in Pharmaceutical Solids. In *Disordered Pharmaceutical Materials*; 2016; pp 103–134.

(147) Rahman, Z.; Siddiqui, A.; Bykadi, S.; Khan, M. A. Determination of Tacrolimus Crystalline Fraction in the Commercial Immediate Release Amorphous Solid Dispersion Products by a Standardized X-Ray Powder Diffraction Method with Chemometrics. *Int. J. Pharm.* **2014**, *475*, 462–470.

(148) Langford, J. I.; Wilson, A. J. C. Scherrer after Sixty Years: A Survey and Some New Results in the Determination of Crystallite Size. *J. Appl. Crystallogr.* **1978**, *11*, 102–113.

(149) Ungar, T. Microstructure Parameters from X-Ray Line Profile Analysis. In *Advanced X-ray Techniques in Research and Industry*; 2005; pp 268–286.

(150) Jones, W.; Eddleston, M. D. Crystal Imperfections in Molecular Crystals: Physical and Chemical Consequences. In *Disordered Pharmaceutical Materials*; 2016; pp 85–102.

(151) Newman, A.; Zografi, G. Critical Considerations for the Qualitative and Quantitative Determination of Process-Induced Disorder in Crystalline Solids. *J. Pharm. Sci.* **2014**, *103*, 2595–2604.

(152) Keith, R. E.; Gilman, J. J. Dislocation Etch Pits and Plastic Deformation in Calcite. *Acta Metall.* **1960**, *8*, 1–10.

(153) Vasilchenko, M. A.; Shakhtshneider, T. P.; Boldyrev, V. V. The Morphology of Etch Pits During Thermal Treatment of Drugs and Its Dependence on the Features of Their Crystallochemical Structure. *J. Therm. Anal.* **1999**, *57*, 157–164.

(154) Burt, H. M.; Mitchell, A. G. Crystal Defects and Dissolution. *Int. J. Pharm.* **1981**, *9*, 137–152.

(155) Wen, H.; Li, T.; Morris, K. R.; Park, K. Dissolution Study on Aspirin and α-Glycine Crystals. *J. Phys. Chem. B* **2004**, *108* (30), 11219–11227.

(156) Li, T. L.; Morris, K. R.; Park, K. Influence of Solvent and Crystalline Supramolecular Structure on the Formation of Etching Patterns on Acetaminophen Single Crystals: A Study with Atomic Force Microscopy and Computer Simulation. *J. Phys. Chem. B* **2000**, *104* (9), 2019–2032.

(157) Gray, V.; Kelly, G.; Xia, M.; Butler, C.; Thomas, S.; Mayock, S. The Science of USP 1 and 2 Dissolution: Present Challenges and Future Relevance. *Pharm. Res.* **2009**, *26*, 1289–1302.

(158) Maddar, F. M.; Adobes-Vidal, M.; Hughes, L. P.; Wren, S. A. C.; Unwin, P. R. Dissolution of Bicalutamide Single Crystals in Aqueous Solution: Significance of Evolving Topography in Accelerating Face-Specific Kinetics. *Cryst. Growth Des.* **2017**, *17*, 5108–5116.

(159) Adobes-Vidal, M.; Maddar, F. M.; Momotenko, D.; Hughes, L. P.; Wren, S. A. C.; Poloni, L. N.; Ward, M. D.; Unwin, P. R. Face-Discriminating Dissolution Kinetics of Furosemide Single Crystals: In Situ Three-Dimensional Multi-Microscopy and Modeling. *Cryst. Growth Des.* **2016**, *16*, 4421–4429.

(160) Mullin, J. W. Crystal Growth. In *Crystallization*; 2001; pp 216–288.

(161) Tian, B.; Gao, W.; Tao, X.; Tang, X.; Taylor, L. S. Impact of Polymers on the Melt Crystal Growth Rate of Indomethacin Polymorphs. *Cryst. Growth Des.* **2017**, *17*, 6467–6476.

(162) Peruffo, M.; Mbogoro, M. M.; Edwards, M. A.; Unwin, P. R. Holistic Approach to Dissolution Kinetics: Linking Direction-Specific Microscopic Fluxes, Local Mass Transport Effects and Global Macroscopic Rates from Gypsum Etch Pit Analysis. *Phys. Chem. Chem. Phys.* **2013**, *15*, 1956–1965.

(163) Lasaga, A. C. Variation of Crystal Dissolution Rate Based on a Dissolution Stepwave Model. *Science (80-.).* **2002**, *291*, 2400–2404.

(164) Siepmann, F.; Siepmann, J.; Walther, M.; MacRae, R. J.; Bodmeier, R. Polymer Blends for

Controlled Release Coatings. *J. Control. Release* **2008**, *125*, 1–15.

(165) Maderuelo, C.; Zarzuelo, A.; Lanao, J. M. Critical Factors in the Release of Drugs from Sustained Release Hydrophilic Matrices. *J. Control. Release* **2011**, *154*, 2–19.

(166) Peppas, N. A.; Bures, P.; Leobandung, W.; Ichikawa, H. Hydrogels in Pharmaceutical Formulations. *Eur. J. Pharm. Biopharm.* **2000**, *50*, 27–46.

(167) Ahuja, A.; Khar, R. K.; Ali, J. Mucoadhesive Drug Delivery Systems. *Drug Dev. Ind. Pharm.* **1997**, *23*, 489–515.

(168) Andrews, G. P.; Laverty, T. P.; Jones, D. S. Mucoadhesive Polymeric Platforms for Controlled Drug Delivery. *Eur. J. Pharm. Biopharm.* **2009**, *71*, 505–518.

(169) Wang, Y.; Zheng, Y.; Zhang, L.; Wang, Q.; Zhang, D. Stability of Nanosuspensions in Drug Delivery. *J. Control. Release* **2013**, *172*, 1126–1141.

(170) Kumari, P.; Ghosh, B.; Biswas, S. Nanocarriers for Cancer-Targeted Drug Delivery. *J. Drug Target.* **2016**, *24*, 179–191.

(171) Gothwal, A.; Khan, I.; Gupta, U. Polymeric Micelles: Recent Advancements in the Delivery of Anticancer Drugs. *Pharm. Res.* **2016**, *33*, 18–39.

(172) Mitragotri, S.; Burke, P. A.; Langer, R. Overcoming the Challenges in Administering Biopharmaceuticals: Formulation and Delivery Strategies. *Nat. Rev. Drug Discov.* **2014**, *13*, 655–672.

(173) Valenta, C.; Auner, B. G. The Use of Polymers for Dermal and Transdermal Delivery. *Eur. J. Pharm. Biopharm.* **2004**, *58*, 279–289.

(174) Baghel, S.; Cathcart, H.; O'Reilly, N. J. Polymeric Amorphous Solid Dispersions: A Review of Amorphization, Crystallization, Stabilization, Solid-State Characterization, and Aqueous Solubilization of Biopharmaceutical Classification System Class II Drugs. *J. Pharm. Sci.* **2016**, *105*, 2527–2544.

(175) Van Duong, T.; Van den Mooter, G. The Role of the Carrier in the Formulation of Pharmaceutical Solid Dispersions. Part I: Crystalline and Semi-Crystalline Carriers. *Expert Opin. Drug Deliv.* **2016**, *13*, 1583–1594.

(176) Haser, A.; Zhang, F. New Strategies for Improving the Development and Performance of Amorphous Solid Dispersions. *AAPS PharmSciTech* **2018**, *19*, 978–990.

(177) Andrews, G. P.; Jones, D. S.; Diak, O. A.; McCoy, C. P.; Watts, A. B.; McGinity, J. W. The Manufacture and Characterisation of Hot-Melt Extruded Enteric Tablets. *Eur. J. Pharm. Biopharm.* **2008**, *69*, 264–273.

(178) Zhang, F.; McGinity, J. W. Properties of Sustained-Release Tablets Prepared by Hot-Melt Extrusion. *Pharm. Dev. Technol.* **1999**, *4*, 241–250.

(179) Crowley, M. M.; Schroeder, B.; Fredersdorf, A.; Obara, S.; Talarico, M.; Kucera, S.; McGinity, J. W. Physicochemical Properties and Mechanism of Drug Release from Ethyl Cellulose Matrix Tablets Prepared by Direct Compression and Hot-Melt Extrusion. *Int. J. Pharm.* **2004**, *269*, 509–522.

(180) Maniruzzaman, M.; Boateng, J. S.; Bonnefille, M.; Aranyos, A.; Mitchell, J. C.; Douroumis, D. Taste Masking of Paracetamol by Hot-Melt Extrusion: An in Vitro and in Vivo Evaluation. *Eur. J. Pharm. Biopharm.* **2012**, *80*, 433–442.

(181) Lowinger, M. B.; Su, Y.; Lu, X.; Williams, R. O.; Zhang, F. Can Drug Release Rate from Implants Be Tailored Using Poly(Urethane) Mixtures? *Int. J. Pharm.* **2018**, *557*, 390–401.

(182) Stewart, S.; Domínguez-Robles, J.; Donnelly, R.; Larrañeta, E. Implantable Polymeric Drug Delivery Devices: Classification, Manufacture, Materials, and Clinical Applications. *Polymers (Basel).* **2018**, *10*, 1379.

(183) Leuner, C.; Dressman, J. Improving Drug Solubility for Oral Delivery Using Solid Dispersions. *Eur. J. Pharm. Biopharm.* **2000**, *50*, 47–60.

(184) Serajuddin, A. T. M. Solid Dispersion of Poorly Water-Soluble Drugs: Early Promises, Subsequent Problems, and Recent Breakthroughs. *J. Pharm. Sci.* **1999**, *88*, 1058–1066.

(185) Lipp, R. The Innovator Pipeline: Bioavailability Challenges and Advanced Oral Drug Delivery Opportunities. *Am. Pharm. Rev.* **2013**, *16*, 2–7.

(186) Noyes, A. A.; Whitney, W. R. The Rate of Solution of Solid Substances in Their Own Solutions. *J. Am. Chem. Soc.* **1897**, *19*, 930–934.

(187) Feng, T.; Pinal, R.; Carvajal, M. T. Process Induced Disorder in Crystalline Materials: Differentiating Defective Crystals from the Amorphous Form of Griseofulvin. *J. Pharm. Sci.* **2008**, *97*, 3207–3221.

(188) Koivisto, M.; Heina, P.; Tanninen, V. P.; Lehto, V. Depth Profiling of Compression-Induced Disorders and Polymorphic Transition on Tablet Surfaces with Grazing Incidence X-Ray Diffraction. **2006**, *23*.

(189) Mah, P. T.; Laaksonen, T.; Rades, T.; Aaltonen, J.; Peltonen, L.; Strachan, C. J. Unravelling the Relationship between Degree of Disorder and the Dissolution Behavior of Milled Glibenclamide. *Mol. Pharm.* **2014**, *11*, 234–242.

(190) McBride, J. M. The Role of Local Stress in Solid-State Radical Reactions. *Acc. Chem. Res.* **1983**, *16*, 304–312.

(191) Mcbride, J. M.; Segmuller, B. E.; Hollingsworth, M. D.; Mills, D. E.; Weber, B. A. Mechanical Stress and Reactivity in Organic Solids. *Science (80-.).* **1986**, *234*, 830–835.

(192) Luty, T.; Fouret, R. On Stability of Molecular Solids '"under Chemical Pressure."' *J. Chem. Phys.* **1989**, *90*, 5696–5703.

(193) Herms, M.; Wagner, M.; Kayser, S.; Kießling, F. M.; Poklad, A.; Zhao, M.; Kretzer, U. Defect-Induced Stress Imaging in Single and Multi-Crystalline Semiconductor Materials. *Mater. Today Proc.* **2018**, *5*, 14748–14756.

(194) Mosharraf, M.; Nystrom, C. The Effect of Particle Size and Shape on the Surface Specific Dissolution Rate of Microsized Practically Insoluble Drugs. *Int. J. Pharm.* **1995**, *122*, 35–47.

(195) Wang, J.; Flanagan, D. R. General Solution for Diffusion-Controlled Dissolution of Spherical Particles. 2. Evaluation of Experimental Data. *J. Pharm. Sci.* **2002**, *91*, 534–542.

(196) Wang, J.; Flanagan, D. R. General Solution for Diffusion-Controlled Dissolution of Spherical Particles. 1. Theory. *J. Pharm. Sci.* **1999**, *88*, 731–738.

(197) Yu, W.; Liao, L.; Bharadwaj, R.; Hancock, B. C. What Is the "Typical" Particle Shape of Active Pharmaceutical Ingredients? *Powder Technol.* **2017**, *313*, 1–8.

(198) van der Eerden, J. P.; Bennema, P.; Cherepanova, T. A. Survey of Monte Carlo Simulations of Crystal Surfaces and Crystal Growth. *Prog. Cryst. Growth Charact.* **1978**, *1*, 219–254.

(199) Beatty, K. M.; Jackson, K. A. Monte Carlo Modeling of Silicon Crystal Growth. *J. Cryst. Growth* **2000**, *211*, 13–17.

(200) German, R. M. Thermodynamics of Sintering. In *Sintering of Advanced Materials*; Woodhead Publishing Limited, 2010; pp 3–32.

(201) Ho, R.; Wilson, D. A.; Heng, J. Y. Y. Crystal Habits and the Variation in Surface Energy Heterogeneity. *Cryst. Growth Des.* **2009**, *9*, 4907–4911.

(202) MacInnis, I. N.; Brantley, S. L. The Role of Dislocations and Surface Morphology in Calcite Dissolution. *Geochim. Cosmochim. Acta* **1992**, *56*, 1113–1126.

(203) Lasaga, C. A Model for Crystal Dissolution. *Eur. J. Mineral.* **2003**, *15*, 603–615.

(204) Douglass, I.; Harrowell, P. Kinetics of Dissolution of an Amorphous Solid. *J. Phys. Chem. B* **2018**, *122*, 2425–2433.

(205) Meakin, P.; Rosso, K. M. Simple Kinetic Monte Carlo Models for Dissolution Pitting Induced by Crystal Defects. *J. Chem. Phys.* **2008**, *129*, 204106.

(206) Kurganskaya, I.; Luttge, A. Kinetic Monte Carlo Approach To Study Carbonate Dissolution. *J. Phys. Chem. C* **2016**, *120*, 6482–6492.

(207) Moseson, D. E.; Mugheirbi, N. A.; Stewart, A. A.; Taylor, L. S. Nanometer-Scale Residual Crystals in a Hot Melt Extruded Amorphous Solid Dispersion: Characterization by Transmission Electron Microscopy. *Cryst. Growth Des.* **2018**, *18*, 7633–7640.

(208) Oliphant, T. E. *A Guide to NumPy*; Trelgol Publishing, 2006.

(209) Hunter, J. D. Matplotlib: A 2D Graphics Environment. *Comput. Sci. Eng.* **2007**, *9*, 90–95.

(210) Karjalainen, M.; Airaksinen, S.; Rantanen, J.; Aaltonen, J.; Yliruusi, J. Characterization of Polymorphic Solid-State Changes Using Variable Temperature X-Ray Powder Diffraction. *J. Pharm. Biomed. Anal.* **2005**, *39*, 27–32.

(211) Rastogi, S.; Zakrzewski, M.; Suryanarayanan, R. Investigation of Solid-State Reactions Using Variable Temperature X-Ray Powder Diffractrometry. I. Aspartame Hemihydrate. *Pharm. Res.* **2001**, *18*, 267–273.

(212) Bergese, P.; Colombo, I.; Gervasoni, D.; Depero, L. E. Melting of Nanostructured Drugs Embedded into a Polymeric Matrix. *J. Phys. Chem. B* **2004**, *108*, 15488–15493.

(213) Stephenson, G. A.; Forbes, R. A.; Reutzel-Edens, S. M. Characterization of the Solid State: Quantitative Issues. *Adv. Drug Deliv. Rev.* **2001**, *48*, 67–90.

(214) Eddleston, M. D.; Bithell, E. G.; Jones, W. Transmission Electron Microscopy of Pharmaceutical Materials. *J. Pharm. Sci.* **2010**, *99*, 4072–4083.

(215) S'ari, M.; Cattle, J.; Hondow, N.; Brydson, R.; Brown, A. Low Dose Scanning Transmission Electron Microscopy of Organic Crystals by Scanning Moire Fringes. *Micron* **2019**, *120*, 1–9.

(216) Galli, C. Experimental Determination of the Diffusion Boundary Layer Width of Micron and Submicron Particles. *Int. J. Pharm.* **2006**, *313*, 114–122.

(217) Jiao, S.; Fan, W.; Yue, S.; Zhennan, S.; Wenjun, Z.; Chunling, W.; Yihui, D. Effect of Particle Size on Solubility, Dissolution Rate and Oral Bioavailability. *Int. J. Nanomedicine* **2012**, *12*, 5733–5744.

(218) Chu, K. R.; Lee, E.; Jeong, S. H.; Park, E. S. Effect of Particle Size on the Dissolution Behaviors of Poorly Water-Soluble Drugs. *Arch. Pharm. Res.* **2012**, *35*, 1187–1195.

(219) Narasimhan, B. Mathematical Models Describing Polymer Dissolution: Consequences for Drug Delivery. *Adv. Drug Deliv. Rev.* **2001**, *48*, 195–210.

(220) Craig, D. Q. M. The Mechanisms of Drug Release from Solid Dispersions in Water-Soluble Polymers. *Int. J. Pharm.* **2002**, *231*, 131–144.

(221) Grimard, J.; Dewasme, L.; Vande Wouwer, A. A Review of Dynamic Models of Hot-Melt Extrusion. *Processes* **2016**, *4*, 19.

(222) Schittny, A.; Ogawa, H.; Huwyler, J.; Puchkov, M. A Combined Mathematical Model Linking the Formation of Amorphous Solid Dispersions with Hot-Melt-Extrusion Process Parameters. *Eur. J. Pharm. Biopharm.* **2018**, *132*, 127–145.

(223) Brouwers, J.; Brewster, M. E.; Augustijns, P. Supersaturating Drug Delivery Systems: The Answer to Solubility-Limited Oral Bioavailability? *J. Pharm. Sci.* **2009**, *98* (8), 2549–2572.

(224) Buckley, S. T.; Frank, K. J.; Fricker, G.; Brandl, M. Biopharmaceutical Classification of Poorly Soluble Drugs with Respect to "Enabling Formulations." *Eur. J. Pharm. Sci.* **2013**, *50* (1), 8–16.

(225) Ilevbare, G. A.; Liu, H.; Edgar, K. J.; Taylor, L. S. Maintaining Supersaturation in Aqueous Drug Solutions: Impact of Different Polymers on Induction Times. *Cryst. Growth Des.* **2013**, *13* (2), 740–751.

(226) Williams, H. D.; Trevaskis, N. L.; Charman, S. A.; Shanker, R. M.; Charman, W. N.; Pouton, C. W.; Porter, C. J. H. Strategies to Address Low Drug Solubility in Discovery and Development. *Pharmacol. Rev.* **2013**, *65* (1), 315–499.

(227) Price, D. J.; Ditzinger, F.; Koehl, N. J.; Jankovic, S.; Tsakiridou, G.; Nair, A.; Holm, R.; Kuentz, M.; Dressman, J. B.; Saal, C. Approaches to Increase Mechanistic Understanding and Aid in the Selection of Precipitation Inhibitors for Supersaturating Formulations - a PEARRL Review. *J. Pharm. Pharmacol.* **2018**, *71*, 483–509.

(228) Lindfors, L.; Forssén, S.; Westergren, J.; Olsson, U. Nucleation and Crystal Growth in Supersaturated Solutions of a Model Drug. *J. Colloid Interface Sci.* **2008**, *325* (2), 404–413.

(229) Ozaki, S.; Kushida, I.; Yamashita, T.; Hasebe, T.; Shirai, O.; Kano, K. Inhibition of Crystal Nucleation and Growth by Water-Soluble Polymers and Its Impact on the Supersaturation Profiles of Amorphous Drugs. *J. Pharm. Sci.* **2013**, *102* (7), 2273–2281.

(230) Schram, C. J.; Beaudoin, S. P.; Taylor, L. S. Polymer Inhibition of Crystal Growth by Surface Poisoning. *Cryst. Growth Des.* **2016**, *16* (4), 2094–2103.

(231) Knopp, M. M.; Chourak, N.; Khan, F.; Wendelboe, J.; Langguth, P.; Rades, T.; Holm, R. Effect of Polymer Type and Drug Dose on the in Vitro and in Vivo Behavior of Amorphous Solid Dispersions. *Eur. J. Pharm. Biopharm.* **2016**, *105*, 106–114.

(232) Thiry, J.; Broze, G.; Pestieau, A.; Tatton, A. S.; Baumans, F.; Damblon, C.; Krier, F.; Evrard, B. Investigation of a Suitable in Vitro Dissolution Test for Itraconazole-Based Solid Dispersions. *Eur. J. Pharm. Sci.* **2016**, *85*, 94–105.

(233) O'Dwyer, P. J.; Litou, C.; Box, K. J.; Dressman, J. B.; Kostewicz, E. S.; Kuentz, M.; Reppas, C. In Vitro Methods to Assess Drug Precipitation in the Fasted Small Intestine – a PEARRL Review. *J. Pharm. Pharmacol.* **2019**, *71* (4), 536–556.

(234) Rodríguez-Hornedo, N.; Murphy, D. Significance of Controlling Crystallization Mechanisms and Kinetics in Pharmaceutical Systems. *J. Pharm. Sci.* **1999**, *88* (7), 651–660.

(235) Purohit, H. S.; Taylor, L. S. Phase Behavior of Ritonavir Amorphous Solid Dispersions during Hydration and Dissolution. *Pharm. Res.* **2017**, *34* (12), 2842–2861.

(236) Greco, K.; Bogner, R. Crystallization of Amorphous Indomethacin during Dissolution: Effect of Processing and Annealing. *Mol. Pharm.* **2010**, *7* (5), 1406–1418.

(237) Hermans, A.; Kesisoglou, F.; Xu, W.; Dewitt, K.; Marota, M.; Colace, T. Possibilities And Limiting Factors For Use Of Dissolution As A Quality Control Tool To Detect Presence Of Crystallinity For Amorphous Solid Dispersions: An Experimental And Modeling Investigation Andre. *J. Pharm. Sci.* **2019**.

(238) Knopp, M. M.; Wendelboe, J.; Holm, R.; Rades, T. Effect of Amorphous Phase Separation and Crystallization on the in Vitro and in Vivo Performance of an Amorphous Solid Dispersion. *Eur. J. Pharm. Biopharm.* **2018**, *130* (May), 290–295.

(239) Zidan, A. S.; Rahman, Z.; Sayeed, V.; Raw, A.; Yu, L.; Khan, M. A. Crystallinity Evaluation of Tacrolimus Solid Dispersions by Chemometric Analysis. *Int. J. Pharm.* **2012**, *423* (2), 341–350.

(240) Purohit, H. S.; Trasi, N. S.; Osterling, D. J.; Stolarik, D. F.; Jenkins, G. J.; Gao, W.; Zhang, G. G. Z.; Taylor, L. S. Assessing the Impact of Endogenously Derived Crystalline Drug on the in Vivo Performance of Amorphous Formulations. *Mol. Pharm.* **2019**.

(241) Theil, F.; Milsmann, J.; Anantharaman, S.; Van Lishaut, H. Manufacturing Amorphous Solid Dispersions with a Tailored Amount of Crystallized API for Biopharmaceutical Testing. *Mol. Pharm.* **2018**, *15* (5), 1870–1877.

(242) Moseson, D. E.; Parker, A. S.; Gilpin, C. J.; Stewart, A. A.; Beaudoin, S. P.; Taylor, L. S. Dissolution of Indomethacin Crystals into a Polymer Melt: Role of Diffusion and Fragmentation. *Cryst. Growth Des.* **2019**, *19*, 3315–3328.

(243) Almeida E Sousa, L.; Reutzel-Edens, S. M.; Stephenson, G. A.; Taylor, L. S. Assessment of the Amorphous “Solubility” of a Group of Diverse Drugs Using New Experimental and Theoretical Approaches. *Mol. Pharm.* **2015**, *12* (2), 484–495.

(244) Taylor, L. S.; Zografi, G. Spectroscopic Characterization of Interactions between PVP and Indomethacin in Amorphous Molecular Dispersions. *Pharmaceutical Research*. 1997, pp 1691–1698.

(245) Malwade, C. R.; Qu, H. Cooling Crystallization of Indomethacin: Effect of Supersaturation, Temperature, and Seeding on Polymorphism and Crystal Size Distribution. *Org. Process Res. Dev.* **2018**, *22* (6), 697–706.

(246) Schram, C. J.; Smyth, R. J.; Taylor, L. S.; Beaudoin, S. P. Understanding Crystal Growth Kinetics in the Absence and Presence of a Polymer Using a Rotating Disk Apparatus. *Cryst. Growth Des.* **2016**, *16* (5), 2640–2645.

(247) Alonzo, D. E.; Raina, S. A.; Zhou, D.; Gao, Y.; Zhang, G. G. Z.; Taylor, L. S. Characterizing the Impact of Hydroxypropylmethyl Cellulose on the Growth and Nucleation Kinetics of Felodipine from Supersaturated Solutions. *Cryst. Growth Des.* **2012**, *12* (3), 1538–1547.

(248) Price, R.; Young, P. M. On the Physical Transformations of Processed Pharmaceutical Solids. *Micron* **2005**, *36* (6), 519–524.

(249) Luisi, B. S.; Medek, A.; Liu, Z.; Mudunuri, P.; Moulton, B. Milling-Induced Disorder of Pharmaceuticals: One-Phase or Two-Phase System? *J. Pharm. Sci.* **2012**, *101* (4), 1475–1485.

(250) Schram, C. J.; Taylor, L. S.; Beaudoin, S. P. Influence of Polymers on the Crystal Growth Rate of Felodipine: Correlating Adsorbed Polymer Surface Coverage to Solution Crystal Growth Inhibition. *Langmuir* **2015**, *31* (41), 11279–11287.

(251) S'ari, M. Structural Integrity of Active Pharmaceutical Ingredients in Formulations by Electron Microscopy Techniques, University of Leeds, 2018.

(252) Wilson, V.; Lou, X.; Osterling, D. J.; Stolarik, D. F.; Jenkins, G.; Gao, W.; Zhang, G. G. Z.; Taylor, L. S. Relationship between Amorphous Solid Dispersion In Vivo Absorption and In Vitro Dissolution: Phase Behavior during Dissolution, Speciation, and Membrane Mass Transport. *J. Control. Release* **2018**, *292* (October), 172–182.

(253) Indulkar, A. S.; Lou, X.; Zhang, G. G. Z.; Taylor, L. S. Insights into the Dissolution Mechanism of Ritonavir-Copovidone Amorphous Solid Dispersions: Importance of Congruent Release for Enhanced Performance. *Mol. Pharm.* **2019**, *16* (3), 1327–1339.

(254) Saboo, S.; Mugheirbi, N. A.; Zemlyanov, D. Y.; Kestur, U. S.; Taylor, L. S. Congruent Release of Drug and Polymer: A "Sweet Spot" in the Dissolution of Amorphous Solid Dispersions. *J. Control. Release* **2019**, *298* (January), 68–82.

(255) Hammond, R. B.; Pencheva, K.; Roberts, K. J.; Auffret, T. Quantifying Solubility Enhancement Due to Particle Size Reduction and Crystal Habit Modification: Case Study of Acetyl Salicylic Acid. *J. Pharm. Sci.* **2007**, *96* (8), 1967–1973.

(256) Byrn, S. R.; Zografi, G.; Chen, X. (Sean). Crystal Mesophases and Nanocrystals. In *Solid State Properties of Pharmaceutical Materials*; 2017; pp 89–98.

(257) Dedroog, S.; Pas, T.; Vergauwen, B.; Huygens, C.; Mooter, G. Van den. SOLID-STATE ANALYSIS OF AMORPHOUS SOLID DISPERSIONS: WHY DSC AND XRPD MAY NOT BE REGARDED AS STAND-ALONE TECHNIQUES. *J. Pharm. Biomed. Anal.* **2019**, No. Accepted, 10.1016/j.jpba.2019.112937.

(258) Patel, D. D.; Joguparthi, V.; Wang, Z.; Anderson, B. D. Maintenance of Supersaturation I: Indomethacin Crystal Growth Kinetic Modeling Using an Online Second-Derivative Ultraviolet Spectroscopic Method. *J. Pharm. Sci.* **2011**, *100* (7), 2623–2641.

(259) Patel, D. D.; Anderson, B. D. Effect of Precipitation Inhibitors on Indomethacin Supersaturation Maintenance: Mechanisms and Modeling. *Mol. Pharm.* **2014**, *11* (5), 1489–1499.

(260) Cheng, H.; Mao, L.; Zhang, S.; Lv, H. Impacts of Polymeric Additives on Nucleation and Crystal Growth of Indomethacin from Supersaturated Solutions. *AAPS PharmSciTech* **2019**, *20* (193).

(261) Kubota, N.; Mullin, J. W. A Kinetic Model for Crystal Growth from Aqueous Solution in the Presence of Impurity. *J. Cryst. Growth* **1995**, *152* (3), 203–208.

(262) Kubota, N. Effect of Impurities on the Growth Kinetics of Crystals. *Cryst. Res. Technol.* **2001**, *36*, 749–769.

(263) Patel, D. D.; Anderson, B. D. Adsorption of Polyvinylpyrrolidone and Its Impact on Maintenance of Aqueous Supersaturation of Indomethacin via Crystal Growth Inhibition. *J. Pharm. Sci.* **2015**, *104* (9), 2923–2933.

(264) *Q3B(R2): Impurities in New Drug Products*; 2006; p 12.

(265) Pikal, M. J.; Lukes, A. L.; Lang, J. E. Thermal Decomposition of Amorphous B-lactam Antibacterials. *J. Pharm. Sci.* **1977**, *66* (9), 1312–1316.

(266) Byrn, S. R.; Xu, W.; Newman, A. W. Chemical Reactivity in Solid-State Pharmaceuticals: Formulation Implications. *Adv. Drug Deliv. Rev.* **2001**, *48* (1), 115–136.

(267) Vyazovkin, S.; Wight, C. A. Model-Free and Model-Fitting Approaches to Kinetic Analysis of Isothermal and Nonisothermal Data. *Thermochim. Acta* **1999**, *340–341*, 53–68.

(268) Djuris, J.; Nikolakakis, I.; Ibric, S.; Djuric, Z.; Kachrimanis, K. Preparation of Carbamazepine-Soluplus?? Solid Dispersions by Hot-Melt Extrusion, and Prediction of Drug-Polymer Miscibility by Thermodynamic Model Fitting. *Eur. J. Pharm. Biopharm.* **2013**, *84* (1), 228–237.

(269) Andrews, G. P.; Abudiak, O. A.; Jones, D. S. Physicochemical Characterization of Hot Melt Extruded Bicalutamide- Polyvinylpyrrolidone Solid Dispersions. *J. Pharm. Sci.* **2010**, *99* (3), 1322–1335.

(270) Karandikar, H.; Ambardekar, R.; Kelly, A.; Gough, T.; Paradkar, A. Systematic Identification of Thermal Degradation Products of HPMCP during Hot Melt Extrusion Process. *Int. J. Pharm.* **2015**, *486* (1–2), 252–258.

(271) Lu, J.; Obara, S.; Ioannidis, N.; Suwardie, J.; Gogos, C.; Kikuchi, S. Understanding the Processing Window of Hypromellose Acetate Succinate for Hot-Melt Extrusion, Part I: Polymer Characterization and Hot-Melt Extrusion. *Adv. Polym. Technol.* **2018**, *37* (1), 154–166.

(272) Feng, X.; Vo, A.; Patil, H.; Tiwari, R. V.; Alshetaili, A. S.; Pimparade, M. B.; Repka, M. A. The Effects of Polymer Carrier, Hot Melt Extrusion Process and Downstream Processing Parameters on the Moisture Sorption Properties of Amorphous Solid Dispersions. *J. Pharm. Pharmacol.* **2016**, *68* (5), 692–704.

(273) Liu, J.; Cao, F.; Zhang, C.; Ping, Q. Use of Polymer Combinations in the Preparation of Solid Dispersions of a Thermally Unstable Drug by Hot-Melt Extrusion. *Acta Pharm. Sin. B* **2013**, *3* (4), 263–272.

(274) Albarahmieh, E.; Qi, S.; Craig, D. Q. M. Hot Melt Extruded Transdermal Films Based on Amorphous Solid Dispersions in Eudragit RS PO: The Inclusion of Hydrophilic Additives to Develop Moisture-Activated Release Systems. *Int. J. Pharm.* **2016**, *514* (1), 270–281.

(275) Hughey, J. R.; Keen, J. M.; Brough, C.; Saeger, S.; McGinity, J. W. Thermal Processing of a Poorly Water-Soluble Drug Substance Exhibiting a High Melting Point: The Utility of KinetiSol ® Dispersing. *Int. J. Pharm.* **2011**, *419* (1–2), 222–230.

(276) Hughey, J. R.; DiNunzio, J. C.; Bennett, R. C.; Brough, C.; Miller, D. a; Ma, H.; Williams, R. O.; McGinity, J. W. Dissolution Enhancement of a Drug Exhibiting Thermal and Acidic Decomposition Characteristics by Fusion Processing: A Comparative Study of Hot Melt Extrusion and KinetiSol Dispersing. *AAPS PharmSciTech* **2010**, *11* (2), 760–774.

(277) Dedroog, S.; Huygens, C.; Van den Mooter, G. Chemically Identical but Physically Different: A Comparison of Spray Drying, Hot Melt Extrusion and Cryo-Milling for the Formulation of High Drug Loaded Amorphous Solid Dispersions of Naproxen. *Eur. J. Pharm. Biopharm.* **2018**.

(278) Abu-Diak, O. A.; Jones, D. S.; Andrews, G. P. An Investigation into the Dissolution Properties of Celecoxib Melt Extrudates: Understanding the Role of Polymer Type and Concentration in Stabilizing Supersaturated Drug Concentrations. *Mol. Pharm.* **2011**, *8* (4), 1362–1371.

(279) DiNunzio, J. C.; Brough, C.; Miller, D. A.; Williams, R. O.; McGinity, J. W. Fusion Processing of Itraconazole Solid Dispersions by KinetiSol Dispersing: A Comparative Study to Hot Melt Extrusion. *J. Pharm. Sci.* **2010**, *99* (3), 1239–1253.

(280) Fan, W.; Zhu, W.; Zhang, X.; Xu, Y.; Di, L. Application of the Combination of Ball-Milling and Hot-Melt Extrusion in the Development of an Amorphous Solid Dispersion of a Poorly Water-Soluble Drug with High Melting Point. *RSC Adv.* **2019**, *9* (39), 22263–22273.

(281) Alshehri, S. M.; Tiwari, R. V.; Alsulays, B. B.; Ashour, E. A.; Alshetaili, A. S.; Almutairy, B.; Park, J. B.; Morott, J.; Sandhu, B.; Majumdar, S.; Repka, M. A. Investigation of the Combined Effect of MgO and PEG on the Release Profile of Mefenamic Acid Prepared via Hot-Melt Extrusion Techniques. *Pharm. Dev. Technol.* **2017**, *22* (6), 740–753.

(282) Kulkarni, C.; Kelly, A. L.; Gough, T.; Jadhav, V.; Singh, K. K.; Paradkar, A. Application of Hot Melt Extrusion for Improving Bioavailability of Artemisinin a Thermolabile Drug. *Drug Dev. Ind. Pharm.* **2018**, *44* (2), 206–214.

(283) Maru, S. M.; De Matas, M.; Kelly, A.; Paradkar, A. Characterization of Thermal and Rheological Properties of Zidovidine, Lamivudine and Plasticizer Blends with Ethyl Cellulose to Assess Their Suitability for Hot Melt Extrusion. *Eur. J. Pharm. Sci.* **2011**, *44* (4), 471–478.

(284) Albadarin, A. B.; Potter, C. B.; Davis, M. T.; Iqbal, J.; Korde, S.; Pagire, S.; Paradkar, A.; Walker, G. Development of Stability-Enhanced Ternary Solid Dispersions via Combinations of HPMCP and Soluplus® Processed by Hot Melt Extrusion. *Int. J. Pharm.*

2017, *532* (1), 603–611.

(285) Liu, X.; Lu, M.; Guo, Z.; Huang, L.; Feng, X.; Wu, C. Improving the Chemical Stability of Amorphous Solid Dispersion with Cocrystal Technique by Hot Melt Extrusion. *Pharm. Res.* **2012**, *29* (3), 806–817.

(286) Monschke, M.; Wagner, K. G. Amorphous Solid Dispersions of Weak Bases with PH-Dependent Soluble Polymers to Overcome Limited Bioavailability Due to Gastric PH Variability – An in-Vitro Approach. *Int. J. Pharm.* **2019**, *564* (April), 162–170.

(287) Wyttenbach, N.; Kuentz, M. Glass-Forming Ability of Compounds in Marketed Amorphous Drug Products. *Eur. J. Pharm. Biopharm.* **2017**, *112*, 204–208.

(288) Alhalaweh, A.; Alzghoul, A.; Kaialy, W.; Mahlin, D.; Bergström, C. A. S. Computational Predictions of Glass-Forming Ability and Crystallization Tendency of Drug Molecules. *Mol. Pharm.* **2014**, *11* (9), 3123–3132.

(289) McKelvey, C. A.; Kesisoglou, F. Enabling an HCV Treatment Revolution and the Frontiers of Solid Solution Formulation. *J. Pharm. Sci.* **2019**, *108* (1), 50–57.

(290) LaFountaine, J. S.; McGinity, J. W.; Williams, R. O. Challenges and Strategies in Thermal Processing of Amorphous Solid Dispersions: A Review. *AAPS PharmSciTech* **2016**, *17* (1), 43–55.

(291) Huang, S.; O'Donnell, K. P.; Keen, J. M.; Rickard, M. A.; McGinity, J. W.; Williams, R. O. A New Extrudable Form of Hypromellose: AFFINISOL™ HPMC HME. *AAPS PharmSciTech* **2016**, *17* (1), 106–119.

(292) Nageswara Rao, R.; Narasa Raju, A.; Narsimha, R. Isolation and Characterization of Process Related Impurities and Degradation Products of Bicalutamide and Development of RP-HPLC Method for Impurity Profile Study. *J. Pharm. Biomed. Anal.* **2008**, *46* (3), 505–519.

(293) Haser, A.; DiNunzio, J. C.; Martin, C.; McGinity, J. W.; Zhang, F. Melt Extrusion. In *Formulating Poorly Water Soluble Drugs*; 2016; pp 383–436.

(294) Fang, L. Y.; Harris, D.; Krishna, G.; Moton, A. E. J.; Prestipino, R. C.; Steinman, M.; Wan, J.; Waskin, H. A. HIGH DENSITY COMPOSITIONS CONTAINING POSACONAZOLE AND FORMULATIONS COMPRISING THE SAME. US 2011/0123627 A1, 2011.

(295) Din, S. U.; Hughes, H.; Reilly, N. J. O.; Cathcart, H.; Ceallaigh, T. O.; Ndzie, E.; Mcloughlin, P. Investigation into the Stability , Crystallization Kinetics , and Heating Rate Dependent Crystallization of Amorphous Posaconazole. **2020**.

(296) Azevedo, M. L. S.; Silveira, B. M.; Novack, K. M.; Barboza, A. P. M.; Neves, B. R. A.; dos Santos, V. M. R. Study of Controlled Release of PMMA-g-PEG Copolymer and Derivatives Incorporated with the Indomethacin Drug. *Macromol. Symp.* **2018**, *381* (1), 1–8.

(297) Dalmoro, A.; Bochicchio, S.; Nasibullin, S. F.; Bertoncin, P.; Lamberti, G.; Barba, A. A.; Moustafine, R. I. Polymer-Lipid Hybrid Nanoparticles as Enhanced Indomethacin Delivery Systems. *Eur. J. Pharm. Sci.* **2018**, *121* (May), 16–28.

(298) Jablonski, A. E.; Lang, A. J.; Vyazovkin, S. Isoconversional Kinetics of Degradation of Polyvinylpyrrolidone Used as a Matrix for Ammonium Nitrate Stabilization. *Thermochim. Acta* **2008**, *474* (1–2), 78–80.

(299) Sarode, A. L.; Obara, S.; Tanno, F. K.; Sandhu, H.; Iyer, R.; Shah, N. Stability Assessment of Hypromellose Acetate Succinate (HPMCAS) NF for Application in Hot Melt Extrusion (HME). *Carbohydr. Polym.* **2014**, *101* (1), 146–153.

(300) Mathers, A.; Hassouna, F.; Malinová, L.; Merna, J.; Růžička, K.; Fulem, M. Impact of Hot-Melt Extrusion Processing Conditions on Physicochemical Properties of Amorphous Solid Dispersions Containing Thermally Labile. *J. Pharm. Sci.* **2019**.

(301) Auch, C.; Harms, M.; Mäder, K. How Changes in Molecular Weight and PDI of a Polymer in Amorphous Solid Dispersions Impact Dissolution Performance. *Int. J. Pharm.* **2018**.

(302) Sun, Y.; Zhu, L.; Wu, T.; Cai, T.; Gunn, E. M.; Yu, L. Stability of Amorphous Pharmaceutical Solids: Crystal Growth Mechanisms and Effect of Polymer Additives. *AAPS J.* **2012**, *14* (3), 380–388.

(303) Jelić, D.; Liavitskaya, T.; Vyazovkin, S. Thermal Stability of Indomethacin Increases with the Amount of Polyvinylpyrrolidone in Solid Dispersion. *Thermochim. Acta* **2019**, *676* (April), 172–176.

(304) Ben Osman, Y.; Liavitskaya, T.; Vyazovkin, S. Polyvinylpyrrolidone Affects Thermal Stability of Drugs in Solid Dispersions. *Int. J. Pharm.* **2018**, *551* (1–2), 111–120.

(305) Tao, J.; Sun, Y.; Zhang, G. G. Z.; Yu, L. Solubility of Small-Molecule Crystals in Polymers: D-Mannitol in PVP, Indomethacin in PVP/VA, and Nifedipine in PVP/VA. *Pharm. Res.* **2009**, *26*, 855–864.

(306) Patterson, J. E.; James, M. B.; Forster, A. H.; Lancaster, R. W.; Butler, J. M.; Rades, T. Preparation of Glass Solutions of Three Poorly Water Soluble Drugs by Spray Drying, Melt Extrusion and Ball Milling. *Int. J. Pharm.* **2007**, *336* (1), 22–34.

(307) Forster, A.; Hempenstall, J.; Tucker, I.; Rades, T. The Potential of Small-Scale Fusion Experiments and the Gordon-Taylor Equation to Predict the Suitability of Drug/Polymer Blends for Melt Extrusion. *Drug Dev. Ind. Pharm.* **2001**, *27* (6), 549–560.

(308) Pezzoli, R.; Lyons, J. G.; Gately, N.; Higginbotham, C. L. Stability Studies of Hot-Melt Extruded Ternary Solid Dispersions of Poorly-Water Soluble Indomethacin with Poly(Vinyl Pyrrolidone-Co-Vinyl Acetate)and Polyethylene Oxide. *J. Drug Deliv. Sci. Technol.* **2019**, *52* (March), 248–254.

(309) Pas, T.; Bergonzi, A.; Michiels, E.; Rousseau, F.; Schymkowitz, J.; Koekoekx, R.; Clasen,

C.; Vergauwen, B.; Mooter, G. Van Den. Preparation of Amorphous Solid Dispersions by Cryomilling: Chemical and Physical Concerns Related to APIs and Carriers. *Mol. Pharm.* **2020**, *17*, 1001–1013.

(310) Kaushik, R.; O'Donnell, K. P.; Singh, G. *Impact of Extrusion Process Parameters on Drug Recovery and Dissolution Performance of Solid Dispersions of Ritonavir and AFFINISOL TM HPMC HME*.

(311) Ma, X.; Huang, S.; Lowinger, M. B.; Liu, X.; Lu, X.; Su, Y.; Williams, R. O. Influence of Mechanical and Thermal Energy on Nifedipine Amorphous Solid Dispersions Prepared by Hot Melt Extrusion: Preparation and Physical Stability. *Int. J. Pharm.* **2019**, *561* (January), 324–334.

VITA

Dana Moseson received a Bachelor's of Science degree in Life Science from Pennsylvania State University (University Park, PA) in 2005. She worked at Emerson Resources, Inc. (Norristown, PA) from 2006-2016 in solid dose formulation development and clinical supplies manufacturing. In the fall of 2016, Dana joined the department of Industrial and Physical Pharmacy at Purdue University (West Lafayette, IN). She was awarded a fellowship from the National Science Foundation Graduate Research Fellowship Program from 2018-2020. In addition, her research won several prestigious awards, including the International Pharmaceutical Excipients Council of the Americas (IPEC-Americas) Graduate Student Award (2019) and National Institute for Pharmaceutical Technology and Education (NIPTE) Outstanding Student Research Scholarship (2020).